

**RHODIUM AND IRON COMPLEXES
AND TRANSITION STATES:
A COMPUTATIONAL,
SPECTROSCOPIC AND
ELECTROCHEMICAL STUDY.**

M.M. CONRADIE

**RHODIUM AND IRON COMPLEXES
AND TRANSITION STATES:
A COMPUTATIONAL,
SPECTROSCOPIC AND
ELECTROCHEMICAL STUDY.**

A thesis submitted to meet the requirements for the degree of
Philosophiae Doctor

in the
Department of Chemistry
Faculty of Natural and Agricultural Sciences

at the
University of the Free State

by
Marrigje Marianne Conradie

promotor
Prof. J. Conradie

March 2010

I will be with you. I will not fail you nor forsake you.

Joshua 1:5

Acknowledgments

My further gratitude hereby expressed to:

Prof. Jeanet Conradie,

my mother and promoter, thank you for your devotion, support and late night discussions.

Mr. Hans Koorts,

my grandfather, who read this thesis for language and grammar editing.

Family and friends,

especially my sister Susan and my friend Liesel, for motivation and support.

Prof. Jannie Swarts and colleagues,

for valuable inputs and discussions.

The Chemistry Department and the University of the Free State,

for available facilities.

Prof. Abhik Gosh and the bioinorganic chemistry group,

for research opportunities and teaching me valuable computational skills.

CTCC and the University of Tromsø,

for available facilities.

The National Research Foundation,

for financial support.

Table of contents

Chapter 1

Introduction and aim of study	1
1.1 Introduction	1
1.2 Aim of study	7

Chapter 2

Survey of literature and fundamental aspects	9
2.1 Computational chemistry	9
2.1.1 Introduction	9
2.1.2 Basic Quantum Chemistry	12
2.1.3 Density Functional Theory (DFT)	13
2.1.4 Amsterdam Density Functional (ADF)	14
2.1.5 Gaussian03	15
2.1.6 Exchange-and-correlation (XC) Functional	15
2.1.7 Database	17
2.2 Fundamental Concepts	19
2.2.1 Basic Point Group Theory	19
2.2.2 Transition Metal Coordination	23
2.2.3 Crystal Field Theory (CFT)	25
2.2.4 Molecular Orbital (MO) Theory	30
2.2.5 Ligand Field Theory (LFT)	33
2.2.6 Spin Crossover (SCO)	33
2.2.7 Potential Energy Surface (PES)	35
2.3 Electrochemistry	39
2.3.1 Introduction	39
2.3.2 Cyclic Voltammetry (CV)	40
2.3.3 Spectroelectrochemistry (SEC)	45
2.4 Rhodium complexes	47
2.4.1 Square planar Rh(I) and octahedral Rh(III) chemistry	47
2.4.2 The Monsanto Process: $[\text{Rh}(\text{CO})_2\text{I}_2]^- + \text{CH}_3\text{I}$	61
2.4.3 $[\text{Rh}(\beta\text{-diketonato})(\text{CO})(\text{PPh}_3)] + \text{CH}_3\text{I}$	69
2.4.4 $[\text{Rh}(\text{acac})(\text{P}(\text{OPh})_3)_2] + \text{CH}_3\text{I}$	74
2.5 Iron complexes	77
2.5.1 $[\text{Fe}(\beta\text{-diketonato})_3]$	77
2.5.2 $[\text{Fe}(\text{salen})(\text{CH}_3)_2(\text{COCH}_3)_2(\text{py})_2]$	82
2.5.3 $[\text{Fe}(\text{porphyrin})(\text{Ar})]$	85

Chapter 3

Results and discussion	95
3.1 Rhodium complexes	95
3.1.1 Introduction	95
3.1.2 [Rh(acac)(CO)(PPh ₃)] + CH ₃ I	97
3.1.3 [Rh(β-diketonato)(CO)(PPh ₃)] + CH ₃ I	120
3.1.4 [Rh(acac)(P(OPh) ₃) ₂] + CH ₃ I	129
3.1.5 Crystal structure of [Rh(bth)(CO) ₂]	144
3.2 Iron complexes	152
3.2.1 [Fe(β-diketonato) ₃]	152
3.2.2 [Fe(salen)(CH ₃) ₂ (COCH ₃) ₂ (py) ₂]	168
3.2.3 [Fe(porphyrin)(Ar)]	179

Chapter 4

Experimental	193
4.1 Materials	193
4.2 Techniques and apparatus	193
4.2.1 Melting point (m.p.) determination	193
4.2.2 Analysis	193
4.2.3 Spectroscopic measurements	193
4.2.4 Spectrophotometric measurements	194
4.2.5 Electrochemistry	194
4.3 Synthesis	195
4.3.1 β-diketones	195
4.3.2 Rhodium complexes	195
4.3.3 [Fe(β-diketonato) ₃] complexes { 1 }-{ 10 }	195
4.4 Crystallography	202
4.4.1 Structure determination of [Rh(bth)(CO) ₂]	202
4.5 Computational	203
4.5.1 Resources	203
4.5.2 Rhodium complexes	206
4.5.3 Iron complexes	208

Chapter 5

Concluding remarks and future perspectives	211
5.1 Concluding remarks	211
5.2 Future perspectives	216

TABLE OF CONTENTS

Appendix A

Infrared spectrophotometry (IR)	A-1
Ultraviolet spectrophotometry (UV)	A-6
Mass spectrometry (MS)	A-11
Cyclic voltammetry (CV)	A-16

Appendix B

Crystallography: supporting information	CD
---	----

Appendix C

Computational: supporting information	CD
---	----

Abstract and keywords

Opsomming en sleutelwoorde

1 Introduction and aim of study

1.1 Introduction.

The formation and breaking of metal-carbon bonds have become an important and versatile tool in synthetic organic chemistry.¹ Transition metal assisted reactions used for the manufacture of organic compounds on an industrial scale include the oxidation, hydrogenation, hydroformylation, isomerization and polymerization of alkenes, diene cyclooligomerization and alcohol carbonylation. Other reactions, such as the asymmetric hydrogenation of prochiral alkenes, the activation of C-H bonds for hydrogen/deuterium exchange, the reduction of ketones by hydrosilation and the decarbonylation of aldehydes are also catalyzed by complexes of transition metals. These reactions have a wide application in laboratory-scale preparations and some are also used in the manufacture of pharmaceuticals.

The reactions of the types just mentioned, and indeed, a majority of all organic reactions, are controlled by kinetic rather than thermodynamic factors. The addition of transition metal complexes that can become intimately involved in the reaction sequence is an effective way of increasing the reaction rates. The transition metal catalyst lowers the energy of activation of the reaction by changing the mechanism² and in some cases it relaxes restrictions imposed by orbital symmetry control.³

The scope of this thesis focuses mainly on rhodium and iron based catalysts. Below are selected examples of industrial processes involving rhodium complex or iron complex assisted reactions.

¹ (a) H. Alper (Editor), *Transition Metal Organometallics in Organic Synthesis*, Academic press, New York, **1978**, Vol. 2. (b) D.C. Black, W.R. Jackson, J.M. Swan, In: D.N. Jones (Editor), *Comprehensive Organic Chemistry*, Pergamon, Oxford, **1979**, Vol. 3, Parts 15 and 16. (c) J.P. Collman, L.S. Hegedus, *Principles and Applications of Organotransition Metal Chemistry*, University Science Books, CA, **1980**.

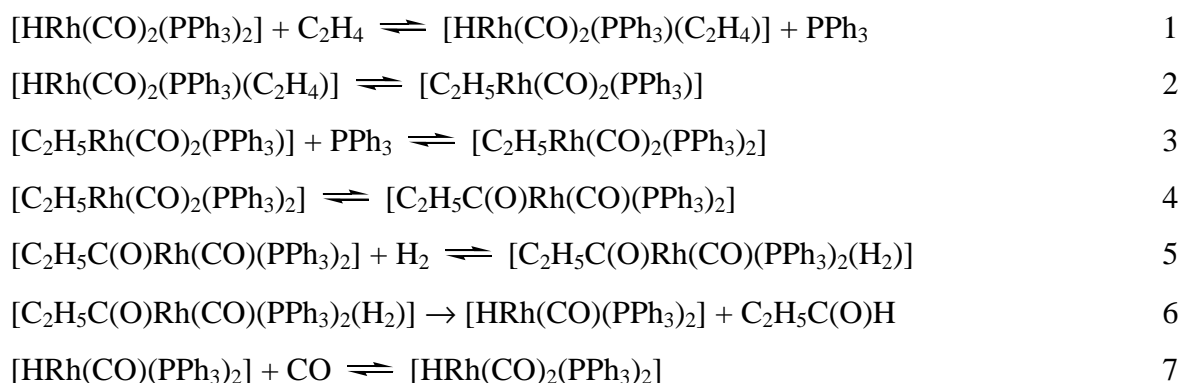
² J.K. Kochi, *Organometallic Mechanisms and Catalysis*, Academic Press, New York, **1978**.

³ (a) J. Halpern, in: I. Wender, P. Pino (Eds.), *Organic Synthesis via Metal Carbonyls*, Wiley, New York, 1977. (b) F.D. Mango, *Coord. Chem. Rev.* **1975** (15) 109-205. (c) R.G. Pearson, *Symmetry Rules for Chemical Reactions*, Wiley, New York, **1976**.

Rhodium based catalysts.

During the last 50 years, industrial organic chemistry has been based largely on petroleum products. Most petrochemical processes use heterogeneous rather than homogeneous catalysts. This is principally because heterogeneous catalysts are generally more stable at higher temperatures and are less troublesome to separate from the substrate phase. However, over the past 30 years, there has been a growing interest in homogeneous catalysts because they often show higher selectivity and greater catalytic activity and they also provide greater control of temperature on the catalyst site. For some commercial processes it has been determined that the advantage of soluble catalysts outweigh the economic problems associated with catalyst recovery. Examples include the hydroformylation of alkenes and olefins catalyzed by rhodium phosphine/phosphite complexes and the carbonylation of methanol to acetic acid with $[\text{Rh}(\text{CO})_2\text{I}_2]^-$ as the active catalyst.⁴

Each catalytic cycle is composed of several steps; the hydroformylation of C_2H_4 by $[\text{HRh}(\text{CO})_2(\text{PPh}_3)_2]$ to liberate ethyl aldehyde, $\text{C}_2\text{H}_5\text{C}(\text{O})\text{H}$, can serve as an example:⁵



The above reactions may be classified as ligand addition to the sixteen electron rhodium complex (reactions 3 and 7), ligand substitution (reaction 1), insertion within the co-ordination sphere (reactions 2 and 4), oxidative addition (reaction 5) and reductive elimination (reaction 6). During catalysis, reactions such as 1-7 often occur so rapidly that they may not be individually observed. Thus, the importance of model complexes to demonstrate and study the individual steps of

⁴ R.S. Dickson, *Homogeneous Catalysis with Compounds of Rhodium and Iridium*, D. Reidel Publishing Company, Dordrecht, **1985**, Chapter 1.

⁵ J.D. Atwood, *Coord. Chem. Rev.* **1988** (83) 93-114.

catalytic reactions is apparent. In South Africa, two world scale hydroformylation plants, one at Sasolburg and one at Secunda, use rhodium catalysts for the production of alcohols for Sasol.

The rhodium complexes $[\text{Rh}(\text{acac})(\text{CO})(\text{PPh}_3)]$ and $[\text{Rh}(\text{acac})(\text{P}(\text{OPh})_3)_2]$ (Hacac = acetylacetonate), in the presence of triphenylphosphine (PPh_3) or triphenylphosphite ($\text{P}(\text{OPh})_3$) respectively, are catalyst precursors for the hydroformylation of olefins under mild conditions (10 atm and 80 °C).⁶ Hydroformylation of 1,5-hexadiene catalyzed by the $[\text{Rh}(\text{acac})(\text{P}(\text{OPh})_3)_2]/\text{P}(\text{OPh})_3$ system leads to the formation of mono- and dialdehydes 4-heptenal, 2-Me-3-hexenal and octane-1,8-dial, 2,5-Me₂-hexanedial respectively. The reaction catalyzed by the $[\text{Rh}(\text{acac})(\text{CO})(\text{PPh}_3)]/\text{PPh}_3$ system produces, besides dialdehydes, monoaldehydes with a terminal double bond, namely 6-heptenal and 2-Me-5-hexenal.

Among the most representative examples of an industrial process catalyzed by a rhodium complex in solution is certainly the rhodium-iodide catalyzed carbonylation of methanol to acetic acid.⁷ The original $[\text{Rh}(\text{CO})_2\text{I}_2]^-$ catalyst, developed at the Monsanto laboratories⁸ and studied in detail by Forster and co-workers,⁹ is largely used for the industrial production of acetic acid with a selectivity greater than 99%. Acetic acid's global production in 2005 was about 9 million tons and the demand grows annually by nearly 5%. More than 60% of this is being produced by the Monsanto process.¹⁰ This process is illustrated in Figure 1.1.

⁶ (a) A.M. Trzeciak, J.J. Ziolkowski, *J. Organomet. Chem.* **1994** (464) 107-111. (b) A.M. Trzeciak, J.J. Ziolkowski, *J. Organomet. Chem.* **1994** (479) 213-216. (c) A.M. Trzeciak, J.J. Ziolkowski, *J. Mol. Catal.* **1988** (48) 319-324. (d) H. Janecko, A.M. Trzeciak, J.J. Ziolkowski, *J. Mol. Catal.* **1984** (26) 355-361.

⁷ P.M. Maitlis, A. Haynes, G.J. Sunley, M.J. Howard, *J. Chem. Soc., Dalton Trans.* **1996** 2187-2196.

⁸ (a) K.K. Robinson, A. Hershman, J.H. Craddock, J.F. Roth, *J. Catal.* **1972** (27) 389-396. (b) F.E. Paulik, J.F.J. Roth, *Chem. Soc., Chem. Commun.* **1968** 1578a.

⁹ (a) D. Forster, *J. Am. Chem. Soc.* **1976** (98) 846-848. (b) D. Forster, *Adv. Organomet. Chem.* **1979** (17) 255-267. (c) D. Forster, T.C. Singleton, *J. Mol. Catal.* **1982** (17) 299-314.

¹⁰ Annual report, Indian Petrochemicals Corporation Ltd, Baroda, **2005**, p68.

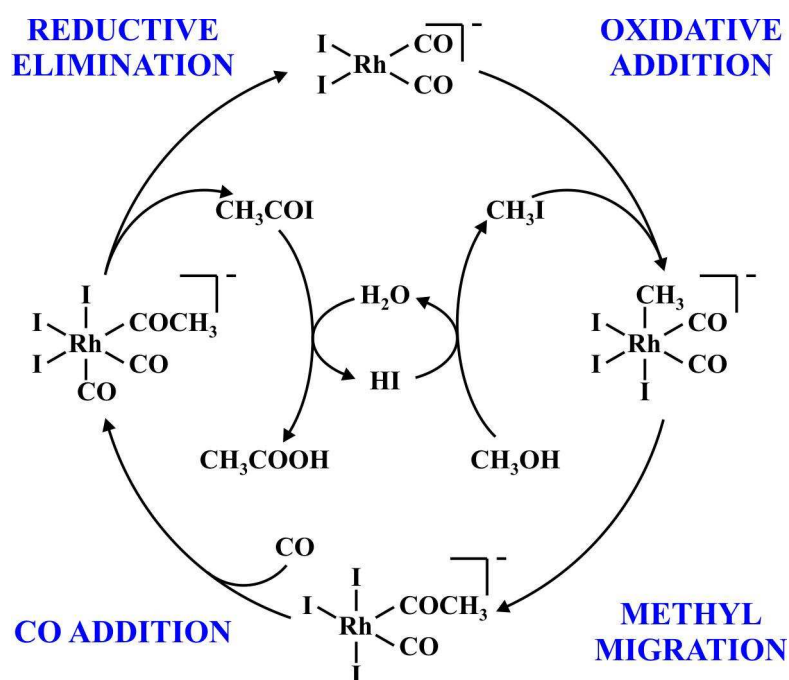


Figure 1.1: The Monsanto process.

The Monsanto process, however, has some drawbacks. The conditions used industrially (30-60 atm and 150-200 °C)¹¹ have spurred the search for new catalysts which could work in milder conditions.^{12,13,14} The rate determining step of the catalytic cycle is the oxidative addition of methyl iodide (Figure 1.1), therefore a catalyst design should focus on the improvement of this reaction. The basic idea is that ligands which increase the electron density at the rhodium centre should promote oxidative addition, and consequently the overall rate of production. For this purpose, several other rhodium compounds have been synthesized in the last few years and have been demonstrated to be active catalysts of comparable or better performances than the original Monsanto catalyst.^{12,15,16,17} One of the most important classes is based on rhodium complexes containing simple phosphines,¹⁸ biphosphine ligands¹⁹ and more recently also mixed bidentate

¹¹ J.F. Roth, J.H. Craddock, A. Hershman, F.E. Paulik, *Chem. Technol.* **1971** 600-605.

¹² J.R. Dilworth, J.R. Miller, N. Wheatley, M.J. Baker, J.G. Sunley, *J. Chem. Soc., Chem. Commun.* **1995** 1579-1581.

¹³ T. Ghaffar, H. Adams, P.M. Maitlis, A. Haynes, G.J. Sunley, M. Baker, *Chem. Commun.* **1998** 1023-1024.

¹⁴ R.W. Wegman, *Chem. Abstr.* **1986** (105) 78526g.

¹⁵ J. Rankin, A.D. Poole, A.C. Benyei, D. Cole-Hamilton, *Chem. Commun.* **1997** 1835-1836.

¹⁶ K.V. Katti, B.D. Santarsiero, A.A. Pinkerton, R.G. Cavell, *Inorg. Chem.* **1993** (32) 5919-5925.

¹⁷ M.J. Baker, M.F. Giles, A.G. Orpen, M.J. Taylor, R.J. Watt, *J. Chem. Soc., Chem. Commun.* **1995** 197-198.

¹⁸ J. Rankin, A.C. Benyei, A.D. Poole, D.J. Cole-Hamilton, *J. Chem. Soc., Dalton Trans.* **1999** 3771-3782.

ligands.^{14,16,17} Indeed, all these new ligands enhance oxidative addition but as a consequence they usually retard the subsequent CO migratory insertion because the increased electron density at the rhodium centre also leads to a stronger Rh-CO bond.

Due to the cost of rhodium (~R600 per gram),²⁰ and the fact that rhodium catalysts can only be used in reactors made of hastaloy (much more expensive than stainless steel), the development of rhodium catalysts with a higher activity will be profitable - lower concentration rhodium catalyst and smaller reactor. In the catalyst design, it is also of economic importance that loss of rhodium due to decomposition must be minimized.

Effective catalyst design should focus on the acceleration of all steps in the catalytic cycle and stability over the long term. It is therefore necessary to study each step of a catalytic cycle in detail and to test the stability of the rhodium catalyst.

Iron based catalysts.

Metal atoms, especially iron, are present at the active catalytic centre in almost a third of all known enzymes.²¹ Iron is especially important and occurs in relatively high concentrations in the human body (5.4 g per 70 kg) of which most of this is involved in the enzyme function.²² This metal is involved in a number of processes, including binding of substrates to orientate them properly for the subsequent reaction, mediating oxidation/reduction and electron transport reactions through reversible changes in the metal oxidation state and electrostatically stabilizing negative charges.

An important example of industrial processes catalyzed by an iron complex is certainly the iron-catalyzed cross-coupling reaction (Figure 1.2). The importance of iron-catalyzed cross-coupling reactions for the formation of carbon-carbon bonds as well as carbon-heteroatom

¹⁹ K.G. Moloy, R.W. Wegman, *Organometallics* **1989** (8) 2883-2892.

²⁰ www.kitco.com

²¹ I. Diaz-Acosta, J. Baker, J.F. Hinton, P. Pulay, *Spectrochimica Acta Part A* **2003** (59) 363-377.

²² H. Douglas, *Bioorganic Chemistry*, Third Edition, Springer, New York, **1996**.

bonds can hardly be overestimated.²³ Within a few decades, this methodology evolved into a routine tool for the preparation of fine chemicals and pharmaceutically active compounds in the laboratory. On the industrial scale,²⁴ it is widely appreciated in the context of parallel synthesis and combinatorial chemistry,²⁵ and plays a prominent role in a rapidly growing number of highly impressive total syntheses of target molecules of utmost complexity.²⁶ As synthetic organic methods are increasingly concerned with the growing importance of sustainable chemistry, iron-catalyzed cross-coupling reactions are one of the promising research areas for the construction of C-C bonds, since iron is inexpensive and more environmentally friendly than the usual metals used - palladium, cobalt or nickel.²⁷ After the pioneering works of Kochi and co-workers in the 1970s,^{27,28} the groups of Cahiez,²⁹ Fürstner,^{30,31} and Nakamura³² have recently

-
- ²³ (a) F. Diederich, P.J. Stang (Editors), *Metal-catalyzed Cross-coupling Reactions*, Wiley-VCH: Weinheim, Germany, **1998**. (b) N. Miyaura (Editor), *Cross-Coupling Reactions. A Practical Guide, Topics in Current Chemistry*, Springer: Berlin, **2002**, Vol. 219. (c) D.W. Knight, In: B.M. Trost, I. Fleming (Editors), *Comprehensive Organic Synthesis*, Pergamon: Oxford, U.K., **1991**, Vol. 3, p481. (d) J.J. Li, G.W. Gribble, (Editors), *Palladium in Heterocyclic Chemistry: A Guide for the Synthetic Chemist*, Elsevier: Oxford, U.K., **2000**.
- ²⁴ M. Beller, A. Zapf, W. Mägerlein, *Chem. Eng. Technol.* **2001** (24) 575-582.
- ²⁵ K.C. Nicolaou, R. Hanco, W. Hartwig (Editors), *Handbook of Combinatorial Chemistry: Drugs, Catalysts, Materials*, Wiley-VCH: Weinheim, Germany, **2002**.
- ²⁶ (a) A. Fürstner, H. Weintritt, *J. Am. Chem. Soc.* **1998** (120) 2817-2825. (b) A. Fürstner, I. Konetzki, *J. Org. Chem.* **1998** (63) 3072-3080. (c) A. Fürstner, J. Grabowski, C.W. Lehmann, *J. Org. Chem.* **1999** (64) 8275-8280. (d) A. Fürstner, O.R. Thiel, N. Kindler, B. Bartkowska, *J. Org. Chem.* **2000** (65) 7990-7995. (e) A. Fürstner, T. Dierkes, O.R. Thiel, G. Blanda, *Chem.-Eur. J.* **2001** (7) 5286-5298.
- ²⁷ (a) C. Bolm, J. Legros, J. Le Pailh, L. Zani, *Chem. Rev.* **2004** (104) 6217-6254. (b) A. Fürstner, R. Martin, *Chem. Lett.* **2005** (34) 624-629.
- ²⁸ (a) M. Tamura, J. K. Kochi, *J. Am. Chem. Soc.* **1971** (93) 1487-1489. (b) M. Tamura, J.K. Kochi, *J. Org. Chem.* **1975** (40) 599-606.
- ²⁹ (a) G. Cahiez, P.Y. Chavant, E. Metais, *Tetrahedron Lett.* **1992** (33) 5245-5248. (b) G. Cahiez, S. Marquais, *Tetrahedron Lett.* **1996** (37) 1773-1776. (c) G. Cahiez, H. Avedissian, *Synthesis* **1998** 1199-1205. (d) C. Duplais, F. Bures, T. Korn, I. Sapountzis, G. Cahiez, P. Knochel, *Angew. Chem. Int. Ed.* **2004** (43) 2968-2970. (e) G. Cahiez, V. Habiak, C. Duplais, A. Moyeux, *Angew. Chem. Int. Ed.* **2007** (46) 4364-4366.
- ³⁰ A. Fürstner, A. Leitner, M. Méndez, H. Krause, *J. Am. Chem. Soc.* **2002** (124) 13856-13863.
- ³¹ (a) R. Martin, A. Fürstner, *Angew. Chem. Int. Ed.* **2004** (43) 3955-3957. (b) A. Fürstner, H. Krause, C.W. Lehmann, *Angew. Chem. Int. Ed.* **2006** (45) 440-444. (c) B. Scheiper, M. Bonnekessel, H. Krause, A. Fürstner, *J. Org. Chem.* **2004** (69) 3943-3949.
- ³² M. Nakamura, K. Matsuo, S. Ito, E. Nakamura, *J. Am. Chem. Soc.* **2004** (126) 3686-3687.

extended the scope of iron-catalyzed processes, notably by developing efficient cross-coupling reactions between aromatic Grignard reagents and alkyl halides.³³

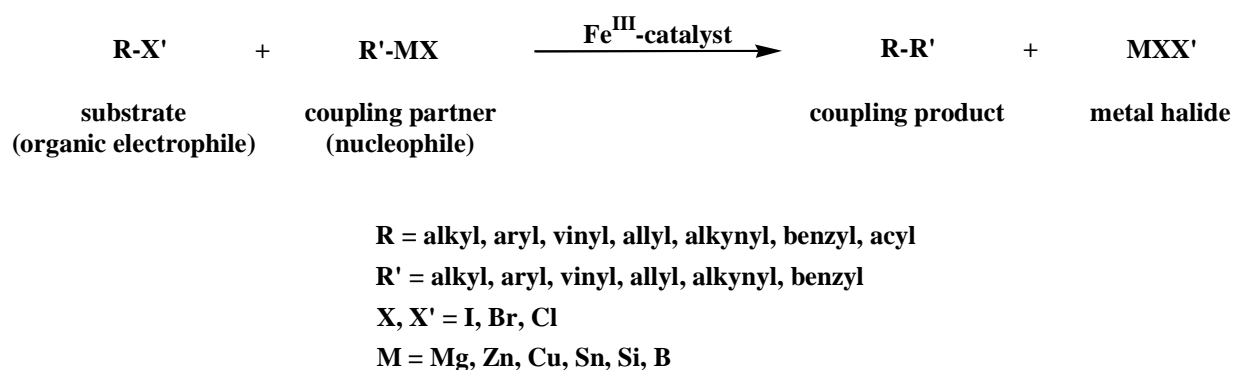


Figure 1.2: General iron-catalyzed cross-coupling reaction.

Simple iron salts such as FeCl₃, Fe(β-diketonato)₃ or the salen complex turned out to be highly efficient, cheap, toxicologically benign and environmentally friendly pre-catalysts for a host of cross-coupling reactions of alkyl or aryl Grignard reagents, zincates or organomanganese species with aryl and heteroaryl chlorides, triflates, and even tosylates.³⁰ Although iron-catalyzed cross-coupling is not yet nearly as mature as its palladium- or nickel-catalyzed counterparts, this transformation provides efficient and scalable solutions for many types of C-C-bond formations.³⁴

1.2 Aim of study.

The following goals were set for the rhodium study:

- (i) The determination of the stereochemistry of the reaction products of the oxidative addition of CH₃I to [Rh(acac)(CO)(PPh₃)], by means of ¹H NMR spectroscopy and DFT computational methods.
- (ii) The determination of the detailed reaction mechanism of the oxidative addition of CH₃I to [Rh(acac)(CO)(PPh₃)], by means of DFT computational methods.

³³ (a) T. Nagano, T. Hayashi, *Org. Lett.* **2004** (6) 1297-1299. (b) R.B. Bedford, D.W. Bruce, R.M. Frost, J.W. Goodby, M. Hird, *Chem. Commun.* **2004** 2822-2823. (c) R.B. Bedford, M. Betham, D.W. Bruce, A.A. Danopoulos, R.M. Frost, M. Hird, *Chem. Commun.* **2005** 4161-4163. (d) Y. Hayashi, H. Shinokubo, K. Oshima, *Tetrahedron Lett.* **1998** (39) 63-66.

³⁴ A. Guérinot, S. Reymond, J. Cossy, *Angew. Chem. Int. Ed.* **2007** (46) 6521-6524.

INTRODUCTION AND AIM OF STUDY

- (iii) To investigate the electronic effects of the R₁ and R₂ side groups of the β-diketonato ligand, coordinated to the [Rh(β-diketonato)(CO)(PPh₃)] complexes, on the DFT calculated activation energy of the oxidative addition reaction of methyl iodide to the [Rh(β-diketonato)(CO)(PPh₃)] complexes. Different R side groups, with electronic properties ranging from electron withdrawing (CF₃) to electron donating (C₄H₃S), were chosen.
- (iv) The determination of the stereochemistry of the reaction product and the detailed reaction mechanism of the oxidative addition of CH₃I to [Rh(acac)(P(OPh)₃)₂], by means of DFT computational methods.
- (v) To investigate the performance of simplified models *versus* the full experimental model of the oxidative addition reaction of CH₃I to [Rh(acac)(P(OPh)₃)₂], by means of DFT computational methods.

The following goals were set for the iron study:

- (i) The optimized synthesis of new and known [Fe(β-diketonato)₃] complexes.
- (ii) To characterize the synthesized [Fe(β-diketonato)₃] complexes with a variety of methods, UV spectrophotometry, mass spectroscopy, elemental analysis, melting points, etc.
- (iii) The electrochemical characterization of the [Fe(β-diketonato)₃] complexes using cyclic voltammetry and spectroelectrochemistry. To evaluate the formal reduction potential (E⁰), as well as the electrochemical and chemical reversibility/irreversibility, of the redox active iron(III) centre. To determine the effect of the electron donation/withdrawal of the different R side groups of the β-diketonato ligands on the formal reduction potential (E⁰).
- (iv) To identify the three dimensional geometry of the [Fe(β-diketonato)₃] complexes utilizing DFT computational methods.
- (v) To determine relationships between experimentally determined and DFT calculated properties, such as the acid dissociation constant (pK_a) of the β-diketone coordinated to the iron complex, the total group electronegativities (χ_{R1} + χ_{R2}) of the R₁ and R₂ side groups on the β-diketonato ligand, the formal reduction potentials (E⁰) of the redox active metal Fe(III)/Fe(II) in [Fe^{III}(β-diketonato)₃] and the calculated ionization potentials.
- (vi) To test the performance of different functionals in relation to the energetics of different spin states of transition metal complexes, such as the spin crossover complex [Fe(salen)(CH₃)₂(COCH₃)₂(py)₂] and five-coordinate iron(III) porphyrins.

2

Survey of literature and fundamental aspects

2.1 Computational chemistry.

2.1.1 Introduction.^{1,2,3}

Computational chemistry has become a powerful tool for the study of a molecular system prior to synthesizing the system in the lab. Properties like geometric arrangements, relative energies and vibration frequencies can be accurately predicted. One of its strengths is the opportunity to study species, processes and/or conditions that are difficult, dangerous, impossible or too expensive to study experimentally. Computational chemistry can also be used for a better understanding of some chemical problems by making it more visual, for instance molecular orbitals.

Originally, computational quantum chemistry suffered from severe limitations with respect to the size of the molecules. The development of more efficient computers and more elaborate mathematical tools has overcome parts of this limitation, thus enabling researchers to look at real- or almost real-sized systems. However, because computational chemistry methods employ a number of approximations, the results obtained from computational calculations should always be treated with some degree of caution.

Quantum chemistry is a branch of theoretical chemistry, which applies quantum mechanics and quantum field theory to address issues and problems in chemistry. A brief introduction to quantum chemistry is given in section 2.1.2.

¹ E Lewars, *Computational Chemistry, Introduction to the theory and Applications of Molecular and Quantum Mechanics*, Kluwer Academic Publishers, Boston, **2003**, p1-7.

² A. Ghosh, P.R. Taylor, *Curr. Opi. Chem. Biol.* **2003**, 7, 113-124.

³ C. Bo, F. Maseras, *Dalton Trans.* **2008**, 2911-2919.

The broad classes of computational chemistry are:

- **Ab Initio:** *Ab initio* calculations involve a full quantum mechanical calculation from first principles, based on the Schrödinger equation. It is limited to small systems and the calculations are very time consuming, but the most accurate that can be performed. Example: Gaussian03, CCSD(T), CASPT2 etc.
- **Density Functional Theory (DFT):** DFT is also based on the Schrödinger equation. In DFT, the many-body electronic wave function is replaced with the electronic density as the basic quantity. Thus, DFT does not calculate a wave function, but rather derives the electron distribution (electron density function) directly. Examples: ADF, Q-Chem, Gaussian03, GAMESS, DALTON, etc.
- **Empirical:** These calculations are based on a database of experimental observations and work best at determining molecules of the same class or type as those previously well characterized. Fast and Cheap. Example: AMBER, OPLS, etc.
- **Semi-Empirical:** These calculations take advantage of the predictive power of a true quantum mechanical calculation, but use empirically determined or fit values for parts of the calculation that are too difficult to perform. It is thus the mixing of theory (Schrödinger equation) and experiment (empirical means experimental). This plugging of experimental values into a mathematical procedure to get the best calculated values is called parameterization. This method is faster than *ab initio* and more accurate and predictive than the empirical. The drawback of this method is that the parameters for many systems, especially larger transition metal complexes, are not available. Example ZINDO, AM1, etc.
- **Molecular Mechanics (MM):** The term MM refers to the use of Newtonian mechanics to model molecular systems. Typically, MM models consist of spherical balls (atoms) connected by springs (bonds). Internal forces experienced in the model structure are described by using simple mathematical functions (*e.g.* Hooke's law). If we know what the normal spring lengths are and how much energy it takes to stretch and bend the springs, we can calculate the energy of a given collection of balls and springs, *i.e.* of a given molecule. Changing the geometry until the lowest energy is found enables one to do a geometrical optimization. Example: AMBER, Hyperchem.
- **Molecular Dynamics (MD):** MD simulation numerically solves Newton's equations of *motion* on an atomistic or similar model of a molecular system to obtain information about its time-dependent properties. For example, one can simulate the motion of an enzyme as it changes shape on binding to a substrate. Example: AMBER.

CHAPTER 2

Ab initio means “from the origin” in Latin. The simplest qualitative model is the Hartree-Fock (HF) approximation, also called the self-consistent field method (SCF). The HF approximation is a method for the determination of the ground-state wave function and ground-state energy of a quantum many-body system. Here the N-body wave function can be described by a single Slater determinant of N spin orbitals. The HF method accounts for a large part of the electron-electron interaction, including the exchange energy. The exchange interaction is a quantum mechanical effect which increases or decreases the expectation value of the energy between two or more identical particles when their wave functions overlap. The single-determinant approximation does not take into account Coulomb correlation, leading to a total electronic energy different from the exact solution of the non-relativistic Schrödinger equation within the Born-Oppenheimer approximation. Therefore the HF limit is always above this exact energy. The difference in energy is called the correlation energy. Calculating the correlation energy is very resource-consuming. To account for the correlation energy, several different approaches are in use of which selected methods are listed in Table 2.1.

Table 2.1: A brief list of electronic structural calculation methods.

Method	Class	Description	Performance
HF or SCF	<i>ab initio</i>	Wave function based approximation using a single electron configuration.	Modest accuracy for structures and vibrational frequencies, poor for energetics.
MP2 ⁱ	high-quality <i>ab initio</i>	Improvement on HF using perturbation theory.	Good for structures and frequencies, modest for energetics.
CCSD(T) ⁱⁱ	high-quality <i>ab initio</i>	Improvement of HF theory including excited Slater determinants in the wave function.	Excellent structures, frequencies and energetics in case of a single electronic configuration. Is a good initial approximation.
CASSCF ⁱⁱⁱ	high-quality <i>ab initio</i>	Wave function approximation using several electron configurations.	Modest to reasonably good accuracy for structures, frequencies and energetics.
CASPT2 ^{iv}	high-quality <i>ab initio</i>	Improvement of CASSCF theory using second-order perturbation theory.	Good structures and frequencies, good excitation energies, reaction energies of modest accuracy.
DFT	not purely <i>ab initio</i>	Density-based methods, taking exchange and correlation parameters into account.	Good structures and frequencies; more variable on energetics; significantly dependent on the functional used (see section 2.1.6).

ⁱ Second-order Møller-Plesset perturbation theory.

ⁱⁱ Coupled-cluster SD(T).

ⁱⁱⁱ Complete active space SCF.

^{iv} Complete active space SCF second-order perturbation theory.

2.1.2 Basic Quantum Chemistry.^{4,5,6}

Quantum mechanics mathematically describes the behaviour of electrons and thus of chemistry. In quantum mechanics the state of a system is not described by particle characteristics, but by a wave function. Therefore, the goal in all quantum chemical methods is to solve (approximate) the time-independent Schrödinger equation, which describes how the quantum state of a physical system changes in time. For a single particle, the one dimensional equation can be presented as follows:

$$-\frac{\hbar^2}{2m} \frac{d^2\psi(x)}{dx^2} + V(x)\psi(x) = E\psi(x)$$

This can more generally be written as:

$$H\psi = E\psi$$

where H is the Hamiltonian operator, E the total energy of the state and ψ denotes the molecular wave function. The wave function ψ is a function of the electron and nuclear positions. As the name implies, this is the description of an electron as a wave. As such, it can describe the probability of electrons being in certain locations, but it cannot predict exactly where the electrons are. The wave function is often called "a probability amplitude" because the square of the wave function yields probabilities. The Hamiltonian (H) for an N-particle system is generally given by:

$$H = - \sum_i^{\text{particles}} \frac{\hbar^2 \nabla_i^2}{2m_i} + \sum_{i<j}^{\text{particles}} \frac{q_i q_j}{r_{ij}}$$

or in atomic units

$$H = - \sum_i^{\text{particles}} \frac{\nabla_i^2}{2m_i} + \sum_{i<j}^{\text{particles}} \frac{q_i q_j}{r_{ij}}$$

with

$$\nabla_i^2 = \frac{\partial^2}{\partial x_i^2} + \frac{\partial^2}{\partial y_i^2} + \frac{\partial^2}{\partial z_i^2}$$

⁴ D.C. Young, *Computational Chemistry - A practical Guide for applying techniques to real-world problems*, Wiley-Interscience, New York, **2001**, p10-11.

⁵ W. Koch, M.C. Holthausen, *A Chemist's guide to density functional theory*, Second Edition, Wiley-VCH, Weinheim, **2002**, p3-6.

⁶ G.H. Grant, W.G. Richards, *Computational Chemistry*, Oxford University Press, Oxford, **1995**, p5-6.

where ∇_i^2 is the Laplacian operator acting on particle i . m_i and q_i are the mass and charge of particle i respectively and r_{ij} is the distance between the particles. Both nuclei and electrons are particles.

The Hamiltonian operator contains the kinetic (described by the first term) and potential (described by the second term) energy terms for the whole system. Once the correct wave function is known, it is in principle possible to extract all information on the system. Unfortunately, it is only possible to solve the Schrödinger equation exactly for one particle systems. And because of this, a variety of methods for obtaining approximate solutions have been developed for multiple electron systems. These methods range from methods having adjusted parameters (semi-empirical methods) to highly advanced analytical methods based on different mathematical formalisms (coupled cluster, configuration interaction, many-body perturbation theory).

2.1.3 Density Functional Theory (DFT).^{7,8,9,10}

The foundation behind DFT is that the energy of a molecule can be determined from the electron density instead of a wave function. This was first stated by Hohenberg and Kohn. But the original theorem only applied to the finding of the ground-state electronic energy of a molecule. A practical application of this theory was developed by Kohn and Sham who formulated a method similar in structure to the HF method.

In this formalism, Kohn and Sham introduced the concept of a non-interacting reference system (*i.e.* a system with non-interacting electrons) described by a set of one-electron orbitals (KS-orbitals). This made it possible to compute the major part of the kinetic energy to a high degree of accuracy. The KS-orbitals are used to provide an electron density for further calculations of the energy, whereas the orbitals in wave function methods (*e.g.* HF methods) are

⁷ D.C. Young, *Computational Chemistry - A practical Guide for applying techniques to real-world problems*, Wiley-Interscience, New York, **2001**, p42-43.

⁸ C.J. Cramer, *Essentials of Computational chemistry - theories and models*, Second Edition, Wiley, Chichester, **2004**, p249-303.

⁹ W.J. Hehre, *A guide to molecular mechanics and quantum chemical calculations*, Wavefunction, Irvine, **2003**, p30-32.

¹⁰ U. von Barth, *Physica Scripta*, **2004**, T109, 9-39.

used to provide the energy direct. Within the Kohn-Sham formalism, the attraction between the electrons and the nuclei, the Coulomb part of the electron-electron repulsion and the kinetic energy of non-interaction electrons are calculated exactly. Only the non-classical part of the electron-electron repulsion (the exchange energy) plus a small part of the kinetic energy are described by the approximate functionals. In this formalism the usual expression for the DFT energy is:

$$E_{\text{DFT}}[\rho] = T_{\text{ni}}[\rho] + V_{\text{ne}}[\rho] + V_{\text{ee}}[\rho] + E_{\text{xc}}[\rho]$$

Here T_{ni} symbolizes the exact kinetic energy of a non-interacting system, V_{ne} is the potential energy generated by the interaction between nuclei and electrons, V_{ee} is the potential energy generated by the interaction between electrons (the Coulomb energy) and E_{xc} includes exchange and correlation energies as well as other contributions (such as a small correction to the kinetic energy) not accounted for in previous terms. The challenge in DFT is to design a functional for E_{xc} . The usual approach is to handle the large exchange part and the small correlation part separately. These exchange-and-correlation functional will be discussed in section 2.1.6.

The greatest advantage of DFT compared to *ab initio* calculations is the low computational cost, especially for large systems. On the other hand, it is not possible to carry out a systematic improvement by taking more electron configurations into account, which could be done for *ab initio* methods. The only way to improve DFT results is to use better functionals.

2.1.4 Amsterdam Density Functional (ADF).¹¹

ADF¹² is a Fortran programme. It performs calculations on atoms and molecules in either gas phase or in solution. ADF can be used for the study of diverse fields such as molecular spectroscopy, organic and inorganic chemistry, crystallography and pharmacology. A separate programme in the ADF package (BAND) is available for the study of periodic systems such as crystals, surfaces, and polymers. The underlying theory is the Kohn-Sham formalism, as described in section 2.1.3. This implies a one-electron picture of the many-electron systems, but yields in principle the exact electron density (and related properties) and the total energy.

¹¹ *ADF User's Guide*, Release 2007.01, Scientific Computing & Modelling NV, Amsterdam, **2007**, p10.

¹² G. Te Velde, F.M Bickelhaupt, E.J. Baerends, C.F. Guerra, S.J.A. Van Gisbergen, J.G. Snijders, T. Ziegler, *J. Comput. Chem.* **2001** (22) 931-967.

2.1.5 Gaussian03.¹³

Gaussian03 is one of a series of electronic structure programmes. Starting from the basic laws of quantum mechanics (section 2.1.2), Gaussian predicts the energies, molecular structures and vibrational frequencies of molecular systems, along with numerous molecular properties derived from these basic computation types. It can be used to study molecules and reactions under a wide range of conditions, including both stable species and compounds which are difficult or impossible to observe experimentally such as short-lived intermediates and transition structures.

2.1.6 Exchange-and-correlation (XC) Functional.^{8,14}

The Density Functional, also called the exchange-and-correlation (XC) functional, may be divided into four different subgroups:

- **Local Density Approximation:** LDA implies that the XC functional in each point in space depends only on the (spin) density at that same point.
- **Generalized Gradient Approximation:** GGA is an addition to the LDA part, by including terms that depend on derivatives of the density.
- **Hybrid functionals:** A hybrid GGA stands for some combination of a standard GGA with a part of Hartree Fock exchange.
- **Meta functionals:** A meta-GGA has a GGA part, but also depends on the kinetic energy density. A meta-hybrid has a GGA part, a part of Hartree-Fock exchange and a part that depends on the kinetic energy density.

¹³ Gaussian 03, Revision C.02, M.J. Frisch, G.W. Trucks, H.B. Schlegel, G.E. Scuseria, M.A. Robb, J.R. Cheeseman, J.A. Montgomery Jr., T. Vreven, K.N. Kudin, J.C. Burant, J.M. Millam, S.S. Iyengar, J. Tomasi, V. Barone, B. Mennucci, M. Cossi, G. Scalmani, N. Rega, G.A. Petersson, H. Nakatsuji, M. Hada, M. Ehara, K. Toyota, R. Fukuda, J. Hasegawa, M. Ishida, T. Nakajima, Y. Honda, O. Kitao, H. Nakai, M. Klene, X. Li, J.E. Knox, H.P. Hratchian, J.B. Cross, V. Bakken, C. Adamo, J. Jaramillo, R. Gomperts, R.E. Stratmann, O. Yazyev, A.J. Austin, R. Cammi, C. Pomelli, J.W. Ochterski, P.Y. Ayala, K. Morokuma, G.A. Voth, P. Salvador, J.J. Dannenberg, V.G. Zakrzewski, S. Dapprich, A.D. Daniels, M.C. Strain, O. Farkas, D.K. Malick, A.D. Rabuck, K. Raghavachari, J.B. Foresman, J.V. Ortiz, Q. Cui, A.G. Baboul, S. Clifford, J. Cioslowski, B.B. Stefanov, G. Liu, A. Liashenko, P. Piskorz, I. Komaromi, R.L. Martin, D.J. Fox, T. Keith, M.A. Al-Laham, C. Peng, A. Nanayakkara, M. Challacombe, P.M.W. Gill, B. Johnson, W. Chen, M.W. Wong, C. Gonzalez, J.A. Pople, Gaussian, Inc., Wallingford CT, **2004**.

¹⁴ *ADF User's Guide*, Release 2007.01, Scientific Computing & Modelling NV, Amsterdam, **2007**, p66-69.

The applicable GGA functionals in this study can be divided into three groups with either exchange correction, correlations correction or both corrections. They are listed below.

For the exchange part, the options are:

- **Becke:** the gradient correction proposed in 1988 by Becke.¹⁵
- **PW91x:** the exchange correction proposed in 1991 by Perdew-Wang.¹⁶
- **PBEx:** the exchange correction proposed in 1996 by Perdew-Burke-Ernzerhof.¹⁷
- **OPTX:** the OPTX exchange correction proposed in 2001 by Handy-Cohen.¹⁸

For the correlation part, the options are:

- **Perdew:** the correlation term presented in 1986 by Perdew.¹⁹
- **PBEc:** the correlation term presented in 1996 by Perdew-Burke-Ernzerhof.¹⁷
- **PW91c:** the correlation correction of Perdew-Wang (1991).¹⁶
- **LYP:** the Lee-Yang-Parr 1988 correlation correction.²⁰

Some GGA options define the exchange and correlation parts in one stroke. These are:

- **BP86:** this is equivalent to Becke + Perdew together.
- **PW91:** this is equivalent to pw91x + pw91c together.
- **PBE:** this is equivalent to PBEx + PBEc together.
- **BLYP:** this is equivalent to Becke (exchange) + LYP (correlation).
- **OLYP:** this is equivalent to OPTX (exchange) + LYP (correlation).
- **OPBE:** this is equivalent to OPTX (exchange) + PBEc (correlation).²¹

¹⁵ A.D. Becke, *Phys. Rev.* **1988** (A38) 3098-3100.

¹⁶ J.P. Perdew, J.A. Chevary, S.H. Vosko, K.A. Jackson, M.R. Pederson, D.J. Singh, C. Fiolhais, *Phys. Rev. B* **1992** (46) 6671-6687. Erratum: J.P. Perdew, J.A. Chevary, S.H. Vosko, K.A. Jackson, M.R. Pederson, D.J. Singh, C. Fiolhais, *Phys. Rev. B* **1993** (48) 4978.

¹⁷ J.P. Perdew, K. Burke, M. Ernzerhof, *Phys. Rev. Lett.* **1996** (77) 3865-3868; Erratum: J.P. Perdew, K. Burke, M. Ernzerhof, *Phys. Rev. Lett.* **1997** (78) 1396.

¹⁸ N.C. Handy, A.J. Cohen, *Mol. Phys.* **2001** (99) 403-412.

¹⁹ J.P. Perdew, *Phys. Rev.* **1986** (B33) 8822-8824; Erratum: J.P. Perdew, *Phys. Rev.* **1986** (B34) 7406.

²⁰ (a) C. Lee, W. Yang, R.G. Parr, *Phys. Rev. B* **1988** (37) 785-789. (b) B.G. Johnson, P.M.W. Gill, J.A. Pople, *J. Chem. Phys.* **1993** (98) 5612-5626. (c) T.V. Russo, R.L. Martin, P.J. Hay, *J. Chem. Phys.* **1994** (101) 7729-7737.

²¹ M. Swart, A.W. Ehlers, K. Lammertsma, *Mol. Phys.* **2004** (102) 2467-2474.

The applicable hybrid functionals in this study can be described as follows:

- **B3LYP:** ADF uses VWN5 in the B3LYP functional (20% Hartree-Fock exchange) by Stephens-Devlin-Chablowski-Frisch.²²
- **B3LYP*:** a modified B3LYP functional (15% Hartree-Fock exchange) by Reiher-Salomon-Hess.²³

The applicable meta functionals in this study can be described as follows:

- **TPPS:** A meta-GGA functional by Tao-Perdew-Staroverov-Scuseria.²⁴
- **TPPSh:** A meta-hybrid functional (10% HF exchange) by Tao-Perdew-Staroverov-Scuseria.²⁴

2.1.7 Database.^{25,26}

The basis functions used by ADF (see section 2.1.4) are commonly known as Slater Type Orbitals (STOs). This is different from most other DFT programmes, which usually employ Gaussian Type Orbitals (GTOs), for which many standard basis sets are available in the literature. The advantage of the STOs is that fewer of them are needed than with GTOs to get a reasonable description of the molecule. A disadvantage is that not much work has been done to develop balanced STO basis sets. In a recent study by Mireia Güell and co-workers,²⁷ STOs and GTO basis sets were evaluated systematically by comparing the spin-state energies of iron complexes. They found that STO basis sets give consistent and rapidly converging results, while the convergence (with respect to basis set size) is much slower for the GTO basis sets.

A basis set can roughly be characterized by two factors: its size (single-, double-, triple-zeta; with or without polarization) and by the level of frozen core approximation. The STO basis sets provided by ADF are SZ, DZ, DZP, TZP, and TZ2P. The increasing numbers point to an

²² P.J. Stephens, F.J. Devlin, C.F. Chabalowski, M.J. Frisch, *J. Phys. Chem.* **1994** (98) 11623-11627.

²³ M. Reiher, O. Salomon, B.A. Hess, *Theor. Chem. Acc.* **2001** (107) 48-55.

²⁴ (a) J. Tao, J.P. Perdew, V.N. Staroverov and G.E. Scuseria, *Phys. Rev. Lett.* **2003** (91) 146401-146404. (b) V.N. Staroverov, G.E. Scuseria, J. Tao and J.P. Perdew, *J. Chem. Phys.* **2003** (119) 12129-12137.

²⁵ *ADF User's Guide*, Release 2007.01, Scientific Computing & Modelling NV, Amsterdam, **2007**, p13-15, 77.

²⁶ J. Hill, L. Subramanian, A. Maiti, *Molecular Modeling Techniques in Material Sciences*, CRC Press, Boca Raton, **2005**, p258-259.

²⁷ M. Güell, J.M. Luis, M. Solà, M. Swart, *J. Phys. Chem. A* **2008** (112) 6384-6391.

increase in size and quality. It is not possible to give a formally correct short general classification for each basis set directory. However, generally speaking we can say that SZ is a single-zeta basis set, DZ is a double zeta basis set, DZP is a double zeta polarized basis, TZP is a core double zeta, valence triple zeta, polarized basis set, and finally TZ2P is a core double zeta, valence triple zeta, doubly polarized basis.

For all-electron calculations and for calculations of heavy elements (Actinides), it is necessary to include relativistic effect. ZORA refers to the Zero Order Regular Approximation. This formalism requires special basis sets, primarily to include much steeper core-like functions. The above basis sets are then classified as ZORA/SZ to ZORA/TZ2P. The ZORA/QZ4P basis set for example can be loosely described as core triple zeta, valence quadruple zeta, with four sets of polarization functions. The TZ2P+ basis sets for the transition metals Sc to Zn are nearly identical to TZ2P except for a better description of the *d*-space (4 *d*-functions instead of 3). The ZORA/TZ2P+ basis sets for the lanthanides La to Yb are nearly identical to TZ2P except for a better description of the *f*-space (4 *f*-functions instead of 3). AUG stands for augmented. These are augmented standard basis sets with some diffuse STOs added, especially meant for time-dependent-DFT (TDDFT) calculations. They are named ASZ, ADZ, ADZP, ATZP, and ATZ2P, which means augmented SZ, augmented DZ, augmented DZP, augmented TZP, and augmented TZ2P, respectively.

Some common GTO basis sets available for other DFT programmes (for example Gaussian03) are: 3-21G, 6-31G, 6-31G*, 6-311G, 6-311+G**, VDZP, VTZ2D2P, Roos_ANO-aug-dz, cc-pVTZ and cc-pVQZ. The increasing numbers point to an increase in size and quality. The notation of the series of Pople basis sets (first five mentioned above) is typically *x*-*yz*G. In this case, *x* represents the number of primitive Gaussians, consisting of each core atomic orbital basis function. The *y* and *z* indicate that the valence orbitals are composed of two basis functions each, the first one composed of a linear combination of *y* primitive Gaussian functions, the other composed of a linear combination of *z* primitive Gaussian functions. In addition to these basis sets, polarization functions are denoted by an asterisk (*). Two asterisks (**) indicate that polarization functions are also added to light atoms (H and He). Another common addition is the addition of diffuse functions, denoted by a plus sign (+). Two plus signs (++) indicate that diffuse functions are also added to light atoms. The more demanding GTO basis sets were developed by Ahlrichs (VDZP, VTZ2D2P) and Dunning (cc-pVTZ, cc-pVQZ).

2.2 Fundamental Concepts.

2.2.1 Basic Point Group Theory.^{28,29,30,31}

The study of symmetry in molecules is an adaptation of the mathematical group theory. The symmetry of a molecule can be described by listing all the symmetry elements of the molecule and this allows one to classify the molecule. The symmetry of a molecule can be described by 5 types of symmetry elements.

- **Identity (E).**

The identity operation is the operation of doing nothing - every molecule has this element. Although this element seems a bit insignificant, it is necessary to include the identity in the description of a molecule's symmetry in order to be able to apply the theory of groups. It is called unity (German: Einheit) because it is analogous to multiplying by one.

- **Rotational axis (C_n).**

The rotational axis is an operation where the molecule is rotated $360^\circ/n$ around an axis, resulting in a molecule indistinguishable from the original. This is also called an n -fold rotational axis and abbreviated C_n . A molecule can have more than one rotational axis. The axis with the highest n is called the principal axis.

- **Plane of symmetry (σ).**

The plane of symmetry is a plane of reflection through which an exact mirror image of the original molecule is given and is abbreviated σ . Three types of planes are possible. The first is a symmetry plane parallel to the principal axis and is called vertical (σ_v). The second is perpendicular to the principal axis and is called horizontal (σ_h). The third is if a vertical symmetry plane that additionally bisects the angle between two 2-fold rotation axes perpendicular to the principal axis and is called dihedral (σ_d).

²⁸ P.H. Walton, *Beginning Group Theory for Chemistry*, Oxford University Press, Oxford, **1998**, p4-75, 137-143.

²⁹ A. Vincent, *Molecular symmetry and group theory*, Second Edition, John Wiley & Sons, England, **2001**, p1-64.

³⁰ *ADF User's Guide*, Release 2007.01, Scientific Computing & Modelling NV, Amsterdam, **2007**, p249-250.

³¹ W.K. Nicholson, *Linear algebra with applications*, Third Edition, PWS Publishing Company, Boston, **1995**, p33-96.

- **Inversion centre (*i*).**

This operation generates inversion through the centre and is abbreviated *i*. A molecule has a centre of symmetry when, for any atom in the molecule, an identical atom exists diametrically opposite this centre and an equal distance from it. It is not necessary that an atom should be at the centre.

- **Rotation-reflection axis (S_n).**

The rotation-reflection axis is an axis around which a rotation of $360^\circ/n$ takes place, followed by a reflection in a plane perpendicular to it and leaves the molecule unchanged. This is also called an *n*-fold improper rotation axis and is abbreviated S_n (*n* necessarily even).

The 5 symmetry elements are associated with 5 mathematical symmetry operations. By using these 5 symmetry elements, one can classify a molecule by assigning to it a single point group symbol. A point group is a set of symmetry operations forming a mathematical group, for which at least one point remains fixed under all operations of the group. Various methods can be used for the assignment of the point group symbol, of which a flow chart is most common. Computer software (for example Chemcraft³²) can also be used to automatically assign a point group symbol to a molecule. There are numerous point groups of which only 22 are most common in chemistry. Table 2.3 contains a list of these 22 common point groups.

Thus, the point group of a molecule is shorthand for a collection of symmetry operations which can be carried out on the molecule. The symmetry operations are mathematical representations that are one of two types: reducible or irreducible. The reducible representations can be seen as combinations of irreducible representations, whereas the irreducible representations cannot be further reduced. In chemistry, one is only interested in the irreducible representations since they can be used to describe the functions which are solutions to the Schrödinger equation (section 2.1.2). This is the mathematical connection between the symmetry of a molecule and the energy of a molecule. Luckily the irreducible representations for all the point groups have been calculated beforehand and are summarized in a table called a character table. The word character is used since the numbers are characteristic of the matrices from which they are derived. Each set of irreducible representation can be represented by a shorthand symbol which is called the Mulliken symbol. There is a set of mathematical rules which can be used for the assignment of

³² G.A. Zhurko, D.A. Zhurko, *CHEMCRAFT*, Version 1.6 (Build 304), 2009.

Mulliken symbols, but for chemists these derivations are not of interest. It is thus only important to understand the character tables. The character tables also capture important information about the orbitals which form a base for the irreducible representations. This information is conventionally listed on the right hand side of the character table. The C_{2v} character table is given in Table 2.2 as an example. Other character tables can be found in references [28] and [29].

Table 2.2: The C_{2v} character table.

C_{2v}	E	C_2	$\sigma_v(xz)$	$\sigma_v'(yz)$		
A_1	1	1	1	1	z	x^2, y^2, z^2
A_2	1	1	-1	-1	R_z	xy
B_1	1	-1	1	-1	x, R_y	xz
B_2	1	-1	-1	1	y, R_x	yz

The above character table can be described as follows:

Point group symbol: C_{2v}

Symmetry operations: $E, C_2, \sigma_v(xz), \sigma_v'(yz)$

Mulliken symbols: A_1, A_2, B_1, B_2

Irreducible representations: 1, -1

Common bases for representations: $R_x, R_y, R_z, x^2, y^2, x, y, z, xy, xz, yz, z^2$

SURVEY OF LITERATURE AND FUNDAMENTAL ASPECTS

Table 2.3: A selection of some common point groups.

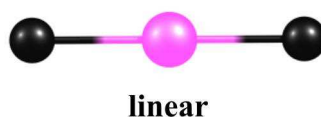
Point group	Symmetry elements	Simple description	Mulliken symbol
C_1	E	no symmetry	A
C_i	E, i	inversion centre	$A_g A_u$
C_s	E, σ_h	planar	$A' A''$
$C_{\infty v}$	$E, 2C_{\infty}, \sigma_v$	linear	$\sigma \pi \delta \phi$
$D_{\infty h}$	$E, 2C_{\infty}, \infty\sigma_i, i, 2S_{\infty}, \infty C_2$	linear with inversion centre	$\sigma_g \sigma_u \pi_g \pi_u \delta_g \delta_u \phi_g \phi_u$
C_2	E, C_2	"open book geometry"	A B
C_{2h}	E, C_2, i, σ_h	planar with inversion centre	$A_g A_u B_g B_u$
C_{2v}	$E, C_2, \sigma_v(xz), \sigma_v'(yz)$	angular or see-saw	$A_1 A_2 B_1 B_2$
C_{3v}	$E, 2C_2, 3\sigma_v$	trigonal pyramidal	$A_1 A_2 E$
C_{4v}	$E, 2C_4, C_2, 2\sigma_v, 2\sigma_d$	square pyramidal	$A_1 A_2 B_1 B_2 E$
D_3	$E, C_3(z), 3C_2$	triple helix, chiral	$A_1 A_2 E$
D_{2h}	$E, C_2(z), C_2(y), C_2(x), i, \sigma(xy), \sigma(xz), \sigma(yz)$	planar with inversion centre	$A_g A_u B_{1g} B_{1u} B_{2g} B_{2u} B_{3g} B_{3u}$
D_{3h}	$E, 2C_3, 3C_2, \sigma_h, 3\sigma_v, 2S_3$	trigonal planar or trigonal bipyramidal	$A_1' A_1'' A_2' A_2'' E' E''$
D_{4h}	$E, 2C_4, C_2, 2C_2', 2C_2, i, 2S_4, \sigma_h, 2\sigma_v, 2\sigma_d$	square planar	$A_{1g} A_{1u} A_{2g} A_{2u} B_{1g} B_{1u} B_{2g} B_{2u} E_g E_u$
D_{5h}	$E, 2C_5, 2C_5^2, 5C_2, \sigma_h, 5\sigma_v, 2S_5, 2S_5^3$	pentagonal	$A_1' A_1'' A_2' A_2'' E_1' E_1'' E_2' E_2''$
D_{6h}	$E, 2C_6, 2C_3, C_2, 3C_2', 3C_2, i, 3S_3, 2S_6^3, \sigma_h, 3\sigma_d, 3\sigma_v$	hexagonal	$A_{1g} A_{1u} A_{2g} A_{2u} B_{1g} B_{1u} B_{2g} B_{2u} E_{1g} E_{1u} E_{2g} E_{2u}$
D_{2d}	$E, 2S_4, C_2, 2C_2, 2C_2', 2\sigma_d$	90° twist	$A_1 A_2 B_1 B_2 E$
D_{3d}	$E, 2C_3, 3C_2, i, 2S_6, 3\sigma_d$	60° twist	$A_{1g} A_{1u} A_{2g} A_{2u} E_g E_u$
D_{4d}	$2S_8, 2C_4, 2S_8^3, C_2, 4C_2', 4\sigma_d$	45° twist	$A_1 A_2 B_1 B_2 E_1 E_2 E_3$
D_{5d}	$E, 2C_5, 2C_5^2, 5C_2, i, 3S_{10}^3, 2S_{10}, 5\sigma_d$	36° twist	$A_{1g} A_{1u} A_{2g} A_{2u} E_{1g} E_{1u} E_{2g} E_{2u}$
T_d	$E, 8C_3, 3C_2, 6S_4, 6\sigma_d$	tetrahedral	$A_1 A_2 E T_1 T_2$
O_h	$E, 8C_3, 6C_2, 6C_4, 3C_2, i, 6S_4, 8S_6, 3\sigma_h, 6\sigma_d$	octahedral or cubic	$A_{1g} A_{1u} A_{2g} A_{2u} E_g E_u T_{1g} T_{1u} T_{2g} T_{2u}$

2.2.2 Transition Metal Coordination.^{33,34}

A transition metal is defined³⁵ as an element whose atom has an incomplete d -sub-shell or which can give rise to cations with an incomplete d -sub-shell. Whereas a transition metal compound is a structure consisting of a central transition metal atom, coordinated to one or more ligands. These compounds may be brightly coloured and some are paramagnetic, due to the partially filled d -shells. The variety of transition metal compounds originate from the diversity of available oxidation states (for the transition metal) and their ability to form complexes with a wide range of ligands. This results in a wide range of coordination numbers and geometries. The total number of other atoms directly linked to the central element is termed the coordination number³⁶ and this can vary from 2 to as many as 16, of which 6 is the most common.

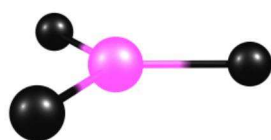
- **Coordination number 2 (ML_2).**

This coordination number is relatively rare for transition metals, since the two ligands will have to be oriented 180° apart. The coordination geometry is linear ($D_{\infty h}$).

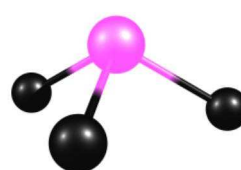


- **Coordination number 3 (ML_3).**

The most important 3-coordinate arrangements are trigonal planar (D_{3h}) and trigonal pyramidal (C_{3v}) in which the three ligands are oriented 120° apart.



trigonal planar



trigonal pyramidal

³³ F.A. Cotton, G. Wilkinson, P.L. Gaus, *Basic inorganic chemistry*, Third Edition, John Wiley & Sons, New York, 1995, p166-170, 503.

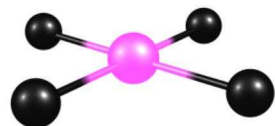
³⁴ F. Mathey, A. Sevin, *Molecular Chemistry of the Transition Elements - an introductory course*, John Wiley & Sons, England, 1996, p19-28.

³⁵ *Compendium of Chemical Terminology*, Internet Edition (<http://goldbook.iupac.org>), International Union of Pure and Applied Chemistry (IUPAC), "transition element".

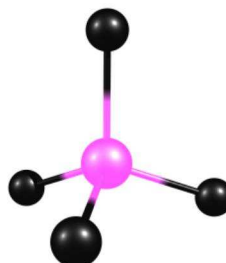
³⁶ *Compendium of Chemical Terminology*, Internet Edition (<http://goldbook.iupac.org>), International Union of Pure and Applied Chemistry (IUPAC), "coordination number".

- **Coordination number 4 (ML₄).**

This is a very important coordination number. The best known 4-coordinate arrangements are square planar (D_{4h}) and tetrahedral (T_d). The tetrahedral arrangement is the more common while the square planar arrangement is found almost exclusively with metal ions having a d^8 electronic configuration.



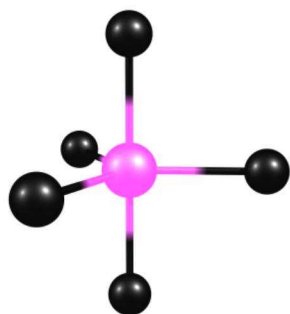
square planar



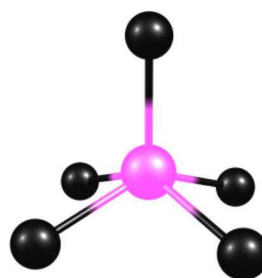
tetrahedral

- **Coordination number 5 (ML₅).**

This coordination number is less common than four or six, but is still very important. The most important 5-coordinate arrangements are trigonal bipyramidal (D_{3h}) and square pyramidal (C_{4v}). For the trigonal bipyramidal, a substitution of one of the axial ligands typically would lower the symmetry to C_{3v} whereas a substitution of one of the equatorial ligands would lower the symmetry to C_{2v} . It is interesting to note that these trigonal bipyramidal and square pyramidal geometries usually differ little in energy and thus the one may become converted into the other by small changes in bond angles.



trigonal bipyramidal

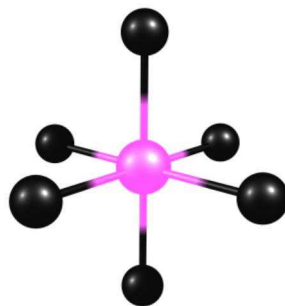


square pyramidal

- **Coordination number 6 (ML₆).**

This coordination number is most important of them all, since nearly all cations form 6-coordinated complexes. The octahedron is often distorted, even in cases where all ligands are chemically the same. There are three principal forms of distortion of an octahedron. The tetragonal distortion (symmetrical distortion along one C_4 -axis) gives a D_{4h} symmetry, the

rhombic distortion (unsymmetrical distortion along one C_4 -axis) gives a D_{2h} symmetry and the trigonal distortion gives a D_{3d} symmetry.



octahedral

2.2.3 Crystal Field Theory (CFT).^{37,38,39}

There are different approaches to explain the bonding in transition metal complexes. One very familiar approach is the crystal field theory (CFT). CFT is an electrostatic model that uses the negative charge on the non-bonding ligand electrons to create an electric field around the positively charged metal centre. CFT focuses on the energy changes (splitting) of the five degenerate atomic d -orbitals (Figure 2.1) on the metal centre, when surrounded by the point charges from the ligands. For alkali metal ions containing a symmetric sphere of charge, calculations of energies are generally quite successful. However, for transition metal cations that contain varying numbers of d -electrons in orbitals that are not spherically symmetric, the situation is quite different. Despite above, CFT still provides a remarkably good qualitative explanation of many of the transition metal properties. The most common type of metal complex is octahedral, although tetrahedral and other complex geometries can also be described by CFT.

This splitting is affected by the following factors:

- The nature of the metal ion.
- The metal's oxidation state - a higher oxidation state leads to a larger splitting.
- The arrangement of the ligands around the metal ion.

³⁷ F.A. Cotton, G. Wilkinson, P.L. Gaus, *Basic inorganic chemistry*, Third Edition, John Wiley & Sons, New York, **1995**, p504-544.

³⁸ C.E. Housecroft, A.G. Sharpe, *Inorganic Chemistry*, Second Edition, Pearson Prentice Hall, Upper Saddle River, **2005**, p556-570.

³⁹ G.E. Rodgers, *Introduction to coordination, solid state and descriptive inorganic chemistry*, McGraw-Hill, New York, **1994**, p54-88.

- The nature of the ligands surrounding the metal ion - the stronger the effect of the ligands, the greater the difference between the high and low energy 3d groups.

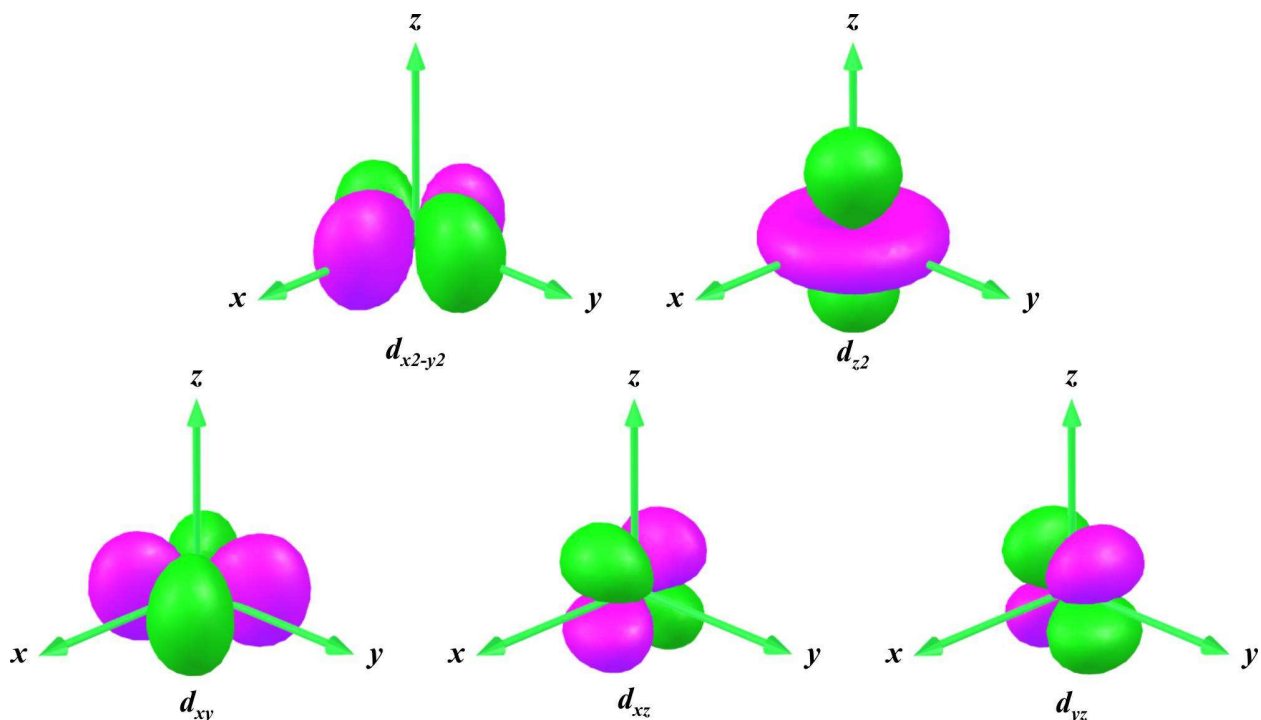


Figure 2.1: The five atomic d -orbitals on the Cartesian axis. There are two atomic d -orbitals that point direct along the Cartesian axis: d_{z^2} (which points along the z -axis) and $d_{x^2-y^2}$ (which has lobes on both the x - and y -axes). The other three atomic d -orbitals (d_{xy} , d_{xz} and d_{yz}), have lobes in between the Cartesian axis. A 45° rotation of d_{xy} along the z -axis results in $d_{x^2-y^2}$ and a 90° rotation of d_{xz} along the z -axis results in and d_{yz} .

Octahedral crystal field.

Consider a first row metal cation surrounded by six identical ligands, placed on the Cartesian axis at the vertices of an octahedron. As mentioned before, each ligand is treated as a negative point charge and there is an electrostatic attraction between the metal ion and ligands. However, there is also a repulsive interaction between the electrons in the atomic d -orbitals (Figure 2.1) and the ligand point charges, due to the repulsion between similar charges. As the distance between the ligands and the metal ion decreases, the electrons from the ligands will be closer to the $d_{x^2-y^2}$ and d_{z^2} atomic orbitals and further away from the d_{xy} , d_{xz} and d_{yz} atomic orbitals. Thus, the d -electrons closer to the ligands will have a higher energy than those further away, which results in the atomic d -orbitals splitting in energy. This means that the $d_{x^2-y^2}$ and d_{z^2} atomic orbitals are destabilized while the d_{xy} , d_{xz} and d_{yz} atomic orbitals are stabilized. From the O_h character table (section 2.2.1), it can be deduced that the $d_{x^2-y^2}$ and d_{z^2} atomic orbitals have an e_g

symmetry and the d_{xy} , d_{xz} and d_{yz} atomic orbitals possess a t_{2g} symmetry. The energy separation between them is called Δ_{oct} . To maintain an energy equilibrium, the e_g level lies $3/5\Delta_{\text{oct}}$ above and the t_{2g} level lies $2/5\Delta_{\text{oct}}$ below the energy of the unsplit atomic d -orbitals. This pattern of splitting, in which the algebraic sum of all energy shifts of all atomic orbitals is zero, is said to "preserve the centre of gravity" of the set of levels and is called the crystal field stabilization energy (CFSE). The splitting of energy is illustrated in Figure 2.5. The magnitude of Δ_{oct} is determined by the strength of the crystal field. Factors governing the magnitude are the identity and oxidation state of the metal ion and the nature of the ligands.

High-spin (HS) and low-spin (LS).

Let us have a look at the effects of different numbers of electrons occupying the atomic d -orbitals in an octahedral crystal field. For a d^1 system, only one state is possible, which is t_{2g}^1 . For a d^4 system, two arrangements are available: the four electrons may occupy the t_{2g} set with the configuration t_{2g}^4 (large Δ_{oct} , Figure 2.2 left) or may singly occupy four atomic d -orbitals with the configuration $t_{2g}^3 e_g^1$ (small Δ_{oct} , Figure 2.2 right). This corresponds to LS (Figure 2.2 left) and HS (Figure 2.2 right) respectively. The distinction between the LS and HS configurations is governed by the size of the pairing energy (E_p) *versus* the crystal field splitting energy (Δ). For the LS configuration, the next question arises - where is the paired electron? Is it $d_{xy}^2 d_{xz}^1 d_{yz}^1$, $d_{xy}^1 d_{xz}^2 d_{yz}^1$ or $d_{xy}^1 d_{xz}^1 d_{yz}^2$? The preferred configuration is that with the lowest energy and depends on where it is energetically preferable to place the fourth electron. Thus for a d^5 system, ten different arrangements (3 LSs, 6 intermediate-spins and 1 HS) are possible (Figure 2.3). These different arrangements are called alternative spin states and will be used in this study.

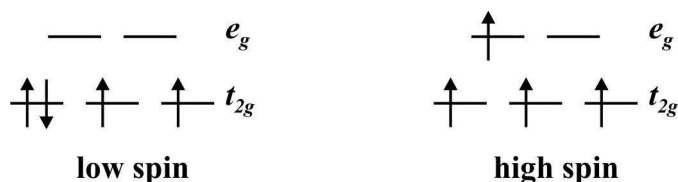


Figure 2.2: Illustration of a LS and HS d^4 system in an octahedral environment.

SURVEY OF LITERATURE AND FUNDAMENTAL ASPECTS

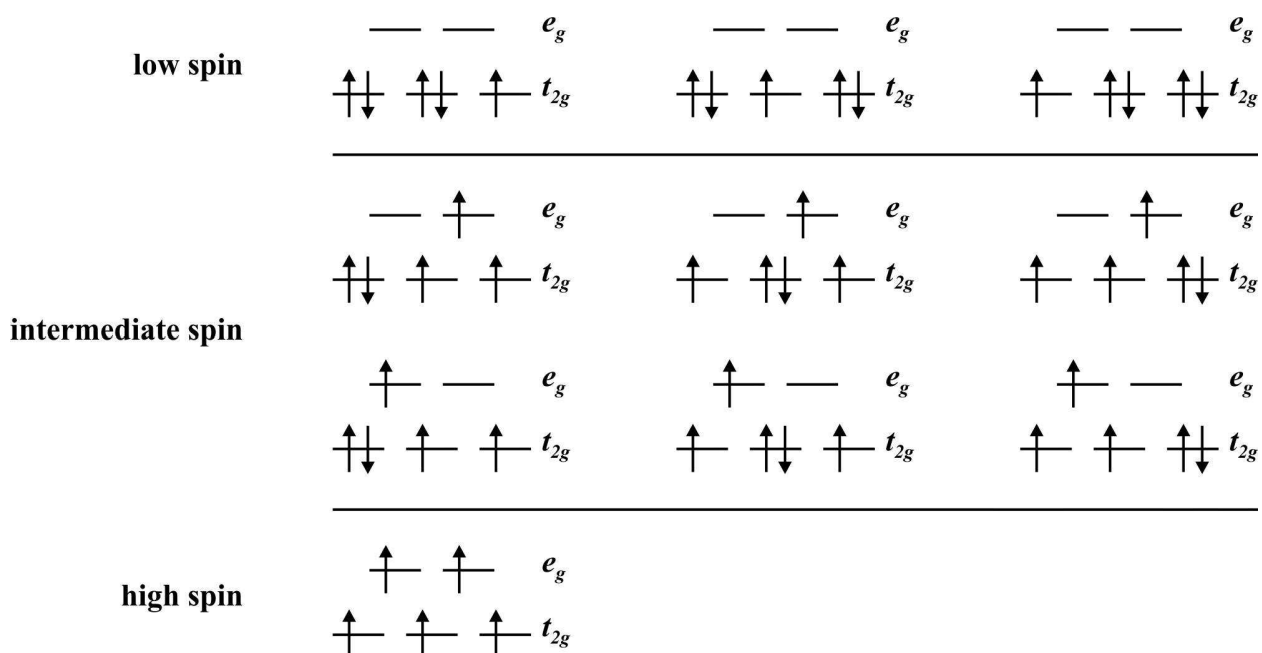


Figure 2.3: Illustration of alternative spin states (LS, intermediate spin and HS) of a d^5 system in an octahedral environment.

Jahn-Teller distortions.

Octahedral complexes of d^9 and high-spin d^4 ions are often distorted in such a way that the axial metal-ligand bonds (along the z -axis) are of different lengths from the remaining four equatorial metal-ligand bonds (x - and y -axes). This is illustrated in Figure 2.4. For a high-spin d^4 ion, one of the e_g atomic orbitals contains one electron while the other is vacant. If the singly occupied orbital is in the d_{z^2} atomic orbital, most of the electron density in this orbital will be concentrated between the cation and the two ligands on the z -axis. Thus, there will be a greater electrostatic repulsion associated with these ligands than with the other four and the complex suffers elongation (Figure 2.4 left). On the other hand, if the singly occupied orbital is in the $d_{x^2-y^2}$ atomic orbital, it would lead to elongation along the x - and y -axes (Figure 2.4 right). A similar argument applies for a d^9 system where the two atomic orbitals in the e_g set are singly and doubly occupied respectively. Distortions of this kind are called Jahn-Teller distortions.

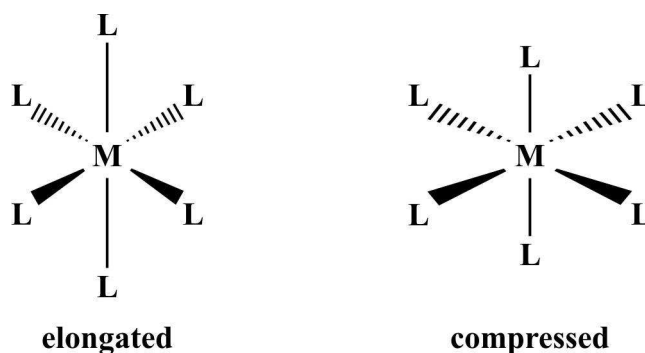


Figure 2.4: Jahn-Teller distortions along the z -axis. The Jahn-Teller theorem states that any non-linear molecular system in a degenerate electronic state will be unstable and will undergo distortion to form a system of lower symmetry and lower energy, thereby removing the degeneracy.

Tetrahedral crystal field.

Tetrahedral complexes are the second most common type. Here four ligands form a tetrahedron (T_d) around the transition metal ion. This time the negative charges lie between the Cartesian axis and electrons in the d_{xy} , d_{yz} and d_{xz} atomic orbitals are repelled more than those in the $d_{x^2-y^2}$ and d_{z^2} atomic orbitals. Since none of the orbitals points direct at the negative charge, the separation of the two sets of orbitals is smaller than in an octahedral ligand field. The energy difference between the two groups is Δ_{tet} with the $d_{x^2-y^2}$ and d_{z^2} atomic orbitals (e_g) lower in energy than the d_{xy} , d_{xz} and d_{yz} atomic orbitals (t_{2g}) - the opposite way around to the octahedral case (Figure 2.5). The Δ_{tet} is significantly less than the Δ_{oct} , for the reason mentioned above and also since the tetrahedron has fewer ligands which logically exert a weaker ligand field. Essentially, most tetrahedral complexes are high-spin, since less energy is needed for a t_2 to e transition.

Other crystal fields.

Figure 2.5 shows the crystal field splittings for a variety of coordination geometries with the relative splittings of the atomic d -orbitals. By using these splitting diagrams, it is possible to rationalize the magnetic properties of a given complex. However, CFT only applies to simple complexes.

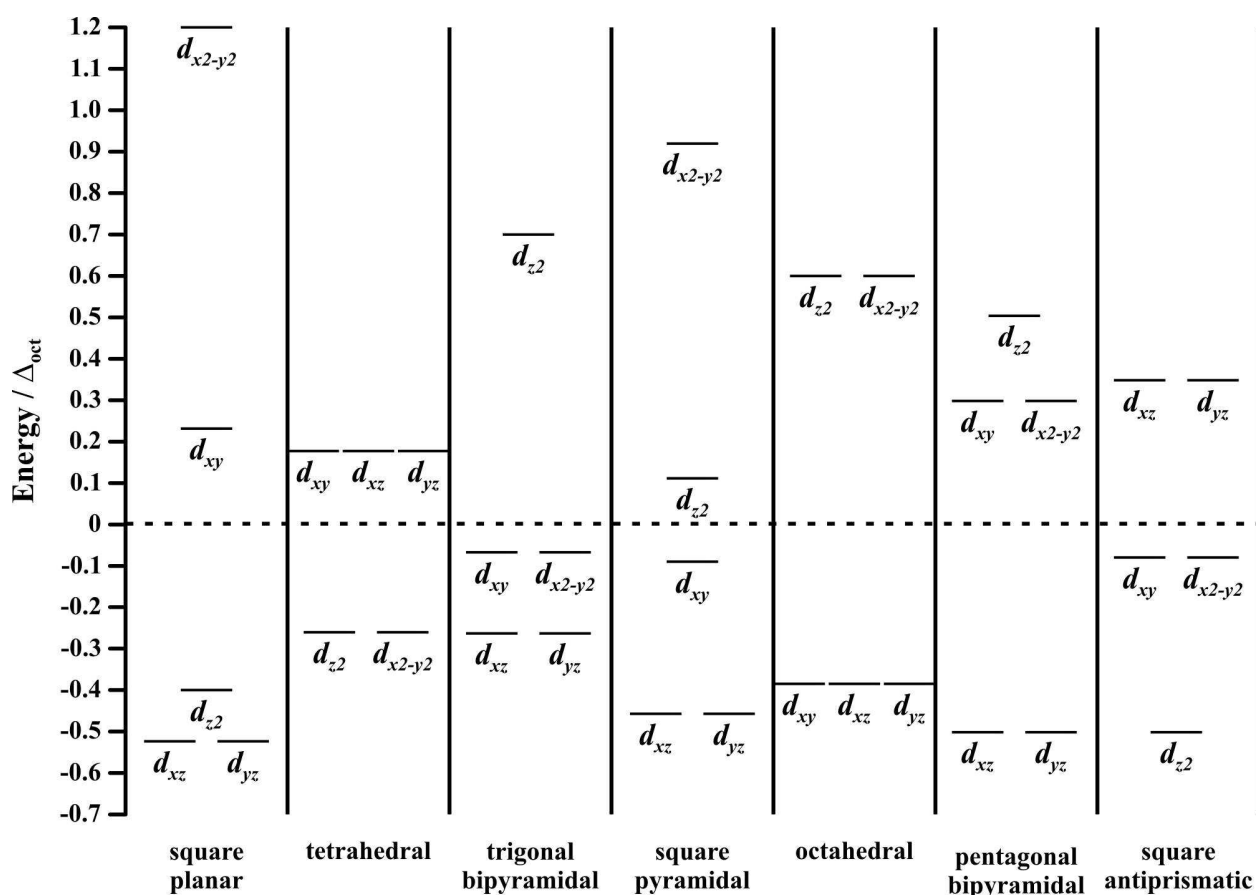


Figure 2.5: The crystal field splitting diagrams for some common fields. Splittings are given with respect to Δ_{oct} .

2.2.4 Molecular Orbital (MO) Theory.^{37,38}

Another approach to explain the bonding in transition metal complexes is the molecular orbital (MO) theory. In MO theory, electrons are not assigned to individual bonds, but are treated as moving under the influence of the nuclei in the whole molecule. The probable position of the electrons can be described by an MO wave function which describes the different MOs of a molecule. MOs can be arranged in energy levels that account for the stability of various molecules.

Consider an octahedral ML_6 complex where the ligands have only σ -orbitals (no π -orbitals) directed toward the metal ion. The six σ -orbitals are designated σ_x and σ_{-x} (along the x -axis), σ_y and σ_{-y} (along the y -axis) and σ_z and σ_{-z} (along the z -axis). These six orbitals combine to make six distinct linear combinations called ligand group orbitals (LGOs). Each LGO has a symmetry that is correctly oriented to overlap with one of the s -, p - or d -orbitals of the metal. An example is given in Figure 2.6. This method is called the linear combination of atomic orbitals approximation and is used in computational chemistry.

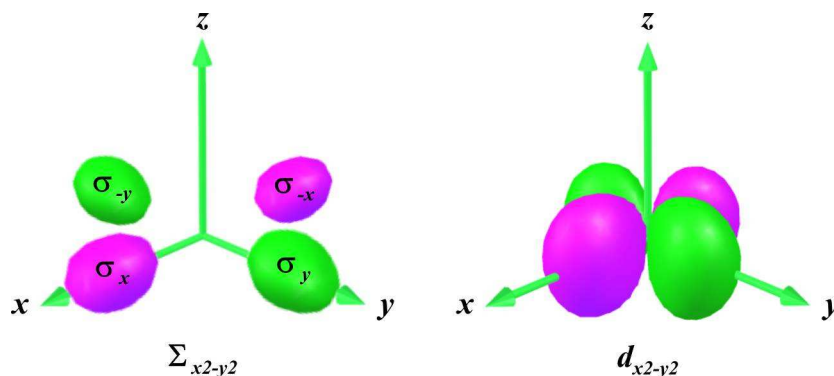


Figure 2.6: As an example, four LGOs (left) with the correct symmetry to enable it to overlap with the metal $d_{x^2-y^2}$ atomic orbital (right). Since they are on the x - and y -axes, they are designated as σ_x , σ_x , σ_y and σ_y .

Each such overlap between one of the six LGOs and a metal orbital results in the formation of a bonding MO and an antibonding MO. If this orbital is of a type in which the electron in the orbital has a higher probability of being between nuclei than elsewhere, the orbital will be a bonding orbital and will tend to hold the nuclei together. If the electrons tend to be present in a molecular orbital in which they spend more time elsewhere than between the nuclei, the orbital will function as an antibonding orbital and will actually weaken the bond. Figure 2.7 gives an energy-level diagram that shows the formation of these bonding and antibonding MOs.

MO theory can further be generalized by including π -orbitals. One must differentiate between two types of ligands: π -donor and π -acceptor ligands. A π -donor ligand donates electrons to the metal centre in an interaction that involves a filled ligand orbital and an empty metal orbital, whereas a π -acceptor ligand accepts electrons from the metal centre in an interaction that involves a filled metal orbital and an empty ligand orbital (Figure 2.8). The ligand group π -orbitals are filled and lie above (but relatively close to) the ligand group σ -orbitals. The π -orbitals can overlap with the d_{xy} , d_{yz} and d_{xz} atomic orbitals of the metal and this leads to bonding (t_{2g}) and antibonding (t_{2g}^*) MOs. The positions of these sets of t_{2g} and t_{2g}^* orbitals in the MO energy-level diagram are variable depending on the nature of the ligand π -orbitals.

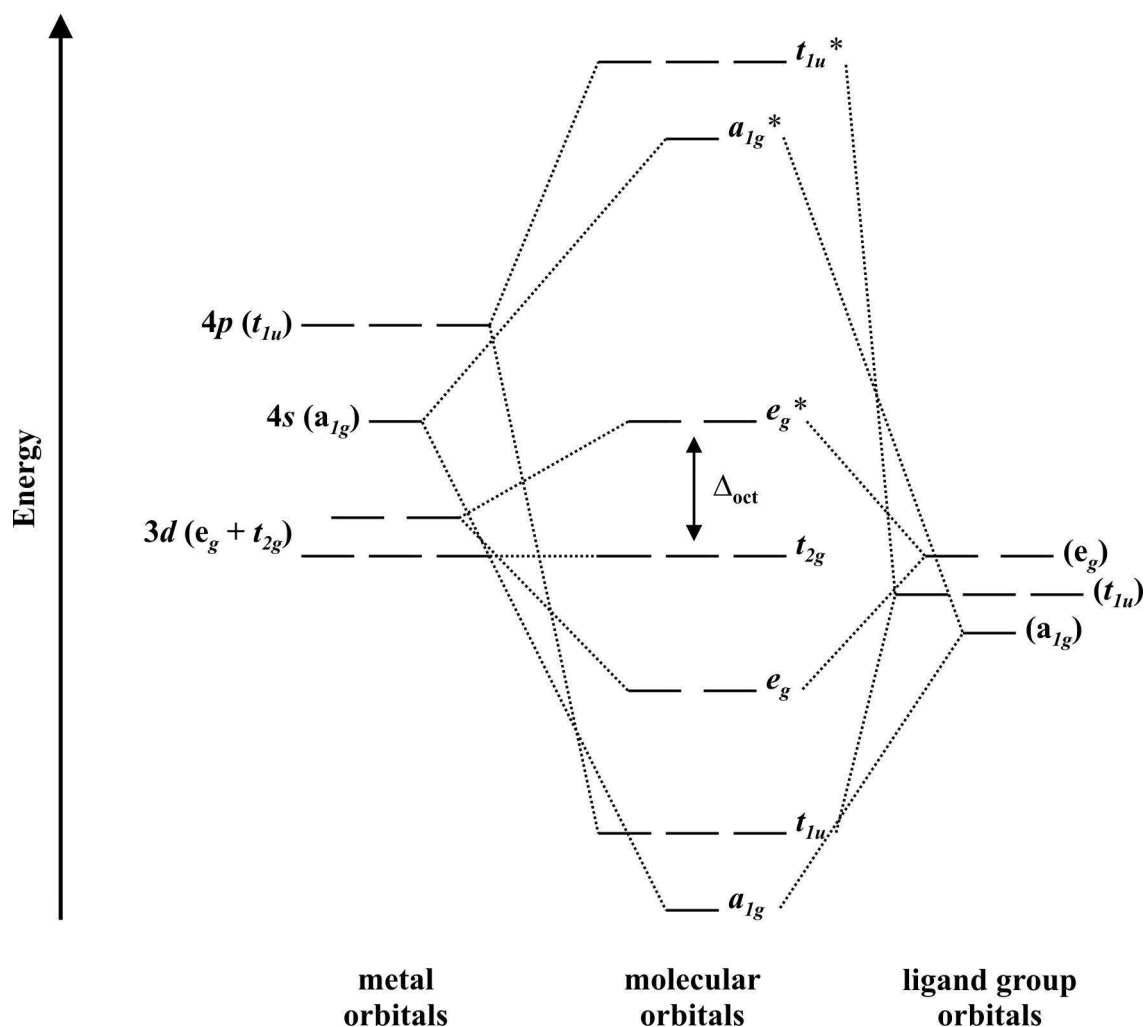


Figure 2.7: An approximate MO diagram for the formation of ML_6 complexes (where M is a first row metal) using the LGO approach. The bonding only involves M-L σ -interactions (no π -orbitals).

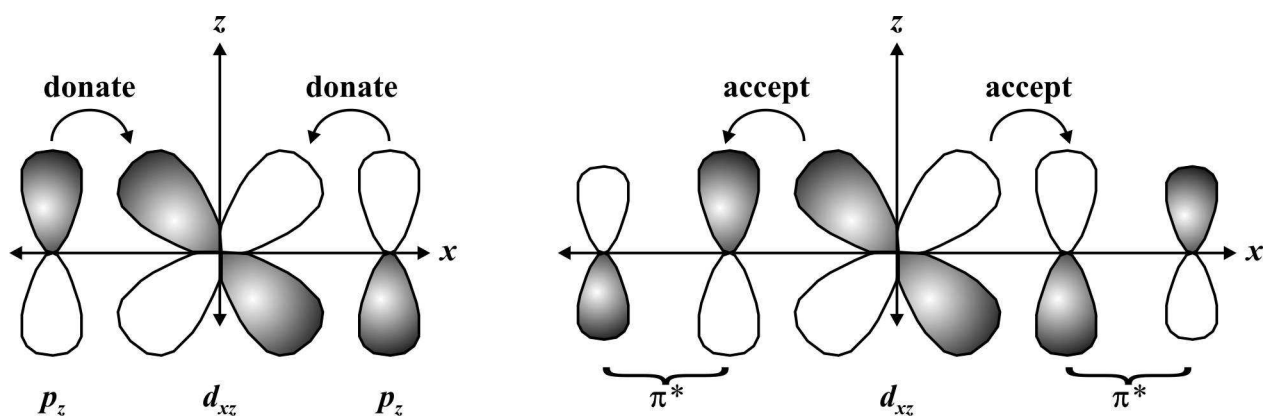


Figure 2.8: π -Bond formation in a linear L-M-L unit in which the metal and ligand donor atoms lie on the x -axis: between the metal d_{xz} and the ligand p_z orbitals as for a π -donor ligand, for example L = Γ (left); and between the metal d_{xz} and the ligand π^* -orbitals as for a π -acceptor ligand, for example L = CO (right).

The following important differences between octahedral ML_6 complexes containing σ -donor, π -donor and π -acceptor ligands exist:

- Δ_{oct} decrease in going from a σ -complex to one containing π -donor ligands.
- For a complex with π -donor ligands, increased π -donation stabilizes the t_{2g} level and destabilizes the t_{2g}^* , thus decreasing Δ_{oct} .
- Δ_{oct} values are relatively large for complexes containing π -acceptor ligands and such complexes are likely to be LS.
- For a complex with π -acceptor ligands, increased π -acceptance stabilizes the t_{2g} level, thus increasing Δ_{oct} .

2.2.5 Ligand Field Theory (LFT).^{37,38}

Ligand field theory (LFT) is an extension of CFT that assigns certain parameters as variables rather than taking them as equal to the values found for free ions, thereby taking into account the potential covalent character of the metal-ligand bond.⁴⁰ In other words, LFT (like CFT) is confined to the role of atomic d -orbitals, but (unlike CFT) the LFT approach is not a purely electrostatic model. It is a freely parameterized model and uses Δ_{oct} along with the Racah parameters, which are obtained from electronic spectroscopic data. LFT is more powerful than either CFT or MO theory, but unfortunately it is also more abstract.

2.2.6 Spin Crossover (SCO).^{41,42}

The choice between a low-spin (LS) and a high-spin (HS) configurations for d^4 to d^7 complexes is not always unique and a spin crossover (SCO) sometimes occurs. The electronic ground state of these SCO complexes may be reversibly interchanged under external stimuli such as temperature, pressure, magnetic field or light irradiation. This type of molecular magnetism is one of the most spectacular examples of molecular bistability driven by external constraints leading to molecular switches or memory.

⁴⁰ *Compendium of Chemical Terminology*, Internet Edition (<http://goldbook.iupac.org>), International Union of Pure and Applied Chemistry (IUPAC), "ligand field".

⁴¹ C.E. Housecroft, A.G. Sharpe, *Inorganic Chemistry*, Second Edition, Pearson Prentice Hall, Upper Saddle River, 2005, p584.

⁴² P. Gamez, J.S. Costa, M. Quesada, G. Aromí, *Dalton Trans.* 2009, 7845-7853.

As mentioned in section 2.2.3, the atomic d -orbitals of an octahedral complex split into the t_{2g} and e_g sets with an energy separation of Δ_{oct} and therefore the complexes can either exist in LS or HS states. As an example, Figure 2.9 illustrates the possible spin states for iron(II) and iron(III) complexes. This spin state is influenced by the nature of the ligand field surrounding the metal centre. In weak fields, HS is the ground state (corresponding to the highest possible spin multiplicity) and the d -electrons are distributed over the t_{2g} and e_g sets. Strong fields again stabilize the LS state with minimum multiplicity. In this case (Figure 2.9), the t_{2g} set is completely occupied before electrons are added to the e_g set. The energy gap between these orbitals (Δ_{oct}) varies subject to the ligands used to generate the metal coordination compounds. If the appropriate energy gap is achieved by the application of an external stimulus, the d -electron(s) transfers from the t_{2g} set to the e_g set and the compound passes from one configuration to the other. This phenomenon is called spin crossover.

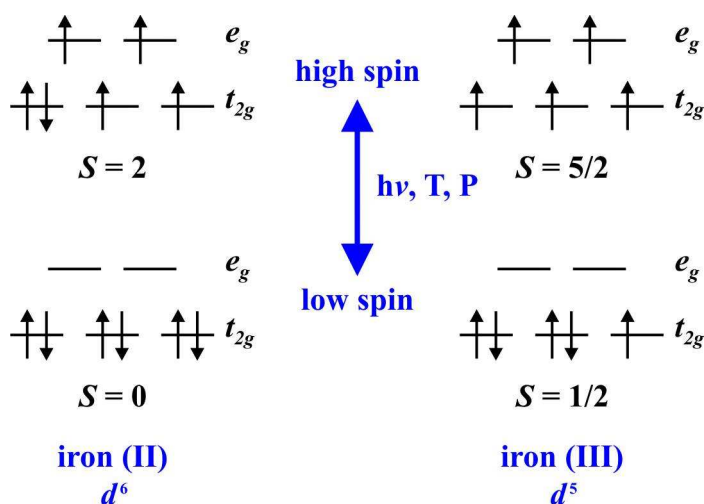


Figure 2.9: Schematic representation of the two possible spin states for iron(II) and iron(III) coordination compounds in an octahedral environment.

2.2.7 Potential Energy Surface (PES).⁴³

Introduction.

The potential energy surface (PES)⁴⁴ is a geometric hypersurface on which the potential energy of a set of reactants is plotted as they interact, as a function of the coordinates representing the molecular geometries of the system. Thus, the PES is the connection between molecular structure and energetics. The hypersurface name comes from the fact that the total energy of an atom's arrangement can be represented as a curve (coordinate has only one parameter) or multidimensional surface (coordinate has more than one parameter). The best way to visualize a two-dimensional PES, where the coordinate has two parameters x and y and is plotted *versus* the potential energy, is to think of a topographic map (Figure 2.10). The PES is generally used within the Born-Oppenheimer approximation to model chemical reactions and interactions in simple chemical systems.

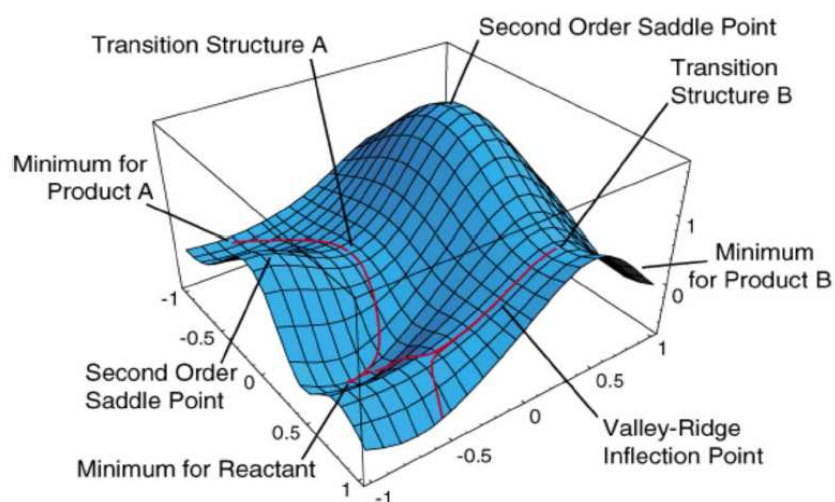


Figure 2.10: As example, the two-dimensional PES of a simple reaction: reactant \rightarrow [transition state A] \rightarrow product A or reactant \rightarrow [transition state B] \rightarrow product B. This PES provides important information about the mechanism of the reaction.⁴⁵

⁴³ (a) W.J. Hehre, *A guide to molecular mechanics and quantum chemical calculations*, Wavefunction, Irvine, **2003**, p1-15. (b) E Lewars, *Computational Chemistry, Introduction to the theory and Applications of Molecular and Quantum Mechanics*, Kluwer Academic Publishers, Boston, **2003**, p9-29. (c) C.J. Cramer, *Essentials of Computational chemistry - theories and models*, Second Edition, Wiley, Chichester, **2004**, p19-27.

⁴⁴ *Compendium of Chemical Terminology*, Internet Edition (<http://goldbook.iupac.org>), International Union of Pure and Applied Chemistry (IUPAC), "potential-energy (reaction) surface".

⁴⁵ www.chem.wayne.edu.

Simple Example: Cyclohexane.

Let us look at the two-dimensional PES for the ring inversion in cyclohexane, as an elementary example (Figure 2.11). This PES contains three distinct energy minima - two of lower energy identified as "chair" and one of higher energy identified as "boat". According to the PES, the interconversion process occurs in two steps, with the boat structure as an intermediate. The two transition states (the states corresponding to the highest energy along this reaction coordinate) leading to this intermediate, adopt structures in which five of the ring carbons lie almost in one plane. The interconversion of the chair cyclohexane into the boat intermediate *via* the transition state, can be viewed as a restricted rotation about one for the ring bonds. Correspondingly, the interconversion of the boat intermediate into the other chair form can be viewed as rotation around the opposite ring bond. Overall, two independent "bond rotations", pausing at the high (but stable) energy boat intermediate, effect conversion of one chair structure into another equivalent chair. This is an example of motions which all molecules may undergo and the energy can be given as a function of reaction coordinate. Diagrams like these provide important information about reactions, *e.g.* structures, stability, reactivity and selectivity.

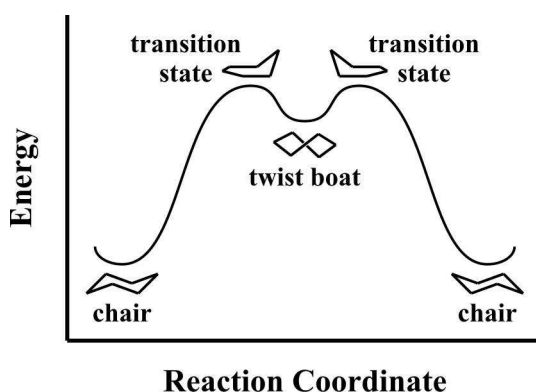


Figure 2.11: The PES for the ring inversion in cyclohexane.

Thermodynamics and Kinetics.

The relative stability of reactants and products is indicated on the PES by their relative heights and is an indication of the thermodynamics of the reaction. The energy of the products in an exothermic reaction is lower than that of the reactants (Figure 2.12 left). The opposite is true for an endothermic reaction, where the energy of the products is higher than that of the reactants (Figure 2.12 right). According to thermodynamics, the amount of products in an exothermic reaction will be greater than the number of reactants, at infinite time. The actual ratio of products to reactants can be calculated by the Boltzmann equation:

$$\frac{[\text{products}]}{[\text{reactants}]} = \exp[-(E_{\text{products}} - E_{\text{reactants}}) / k T] \quad (\text{Equation 2.1})$$

where E is the energy of the products and reactants respectively, k is the Boltzmann constant and T is the temperature (K). Where two or more different products may form in a reaction, thermodynamics tells us that the products with the lowest energy will form in the greatest abundance at infinite time, independent of the pathway. This product would be referred to as the thermodynamic product.

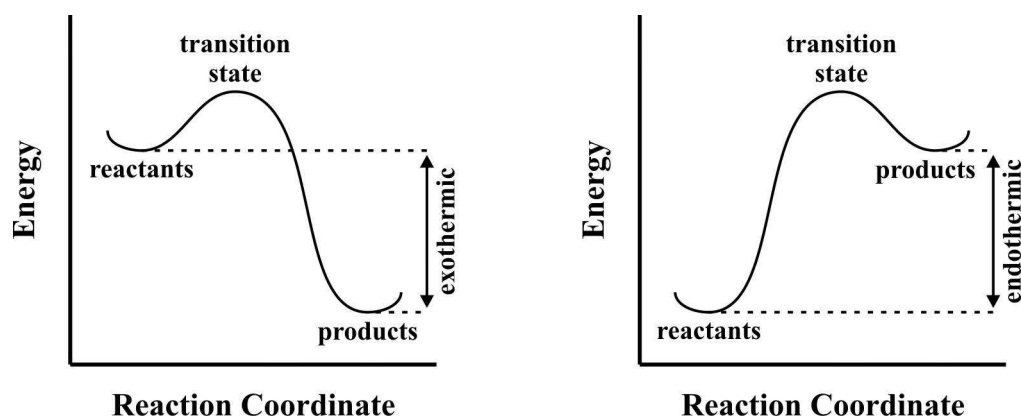


Figure 2.12: The PES for a simple exothermic (left) and endothermic (right) reaction.

The rate at which the reaction occurs depends on the activation energy. This is represented by the difference in energy between the transition state and the reactants. The rate constant can be calculated by the Arrhenius equation:

$$k = A \exp[-(E_{\text{transition state}} - E_{\text{reactants}}) / R T] \quad (\text{Equation 2.2})$$

where k is the rate constant, A is the pre-exponential constant (or pre-exponential factor), E is the energy of the transition state and reactants respectively, R is the gas constant and T is the temperature (K). The difference between the transition state energy and the reactants energy is commonly referred to as the activation energy or the energy barrier. Where two or more different products may form in a reaction, kinetics tells us that the product with the lowest energy barrier will form the fastest, independent of the lowest energy product. This product would be referred to as the kinetic product.

Thus, there are two different and independent mechanisms controlling product distributions - thermodynamic and kinetic (Figure 2.13). This is why some chemical reactions yield one distribution of products under one set of conditions and an entirely different distribution of products under a different set of conditions.

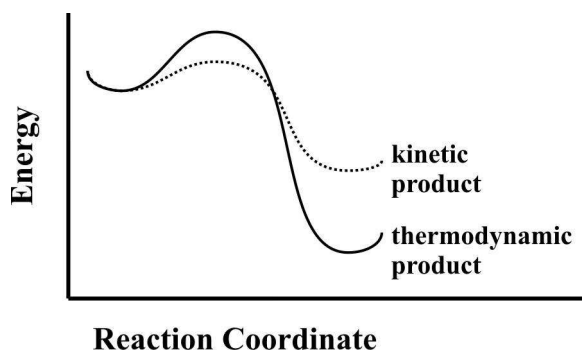


Figure 2.13: A PES illustrating the thermodynamic and kinetic mechanisms controlling product distributions.

Reaction Mechanism.

In practice, chemical reactions generally do not occur in a single step, but rather involve several distinct steps and one or more intermediates. The overall sequence of the steps is called the reaction mechanism and can be represented by a PES (Figure 2.14). The step with the highest energy barrier in the PES will be the rate-limiting step. In terms of thermodynamics, one only has to focus on the relative energy between the reactants and products. However, to get a better understanding of the whole reaction mechanism, it is of great importance to look at the kinetics of the reaction and thus obtaining information about the transition states.

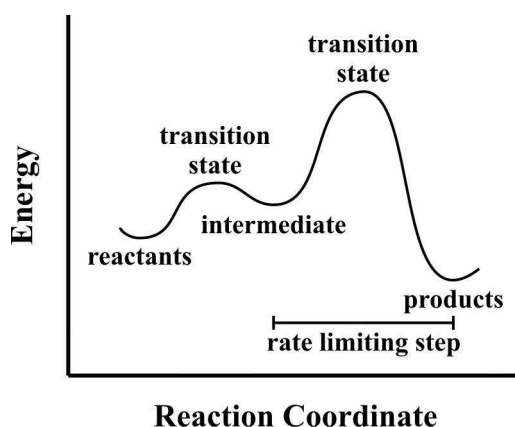


Figure 2.14: A PES of a simple reaction mechanism, involving one reaction intermediate.

2.3 Electrochemistry.

2.3.1 Introduction.

Electroanalytical methods in chemistry are a class of techniques which study an analyte by measuring the potential and/or current in an electrochemical cell containing the analyte. These methods can be assigned to several categories depending on which aspects of the cell are controlled and which are measured. The three main categories are:

- **Voltammetry:** The cell's current is measured while actively altering the cell's potential.
- **Potentiometry:** The difference in electrode potentials is measured.
- **Coulometry:** The cell's current is measured over time.

Some of the most sensitive and informative analytical techniques in the chemist's arsenal can be described by electrochemistry. Methods such as cyclic voltammetry (CV), stripping voltammetry, differential pulse polarography and chronoamperometry are not only capable of assaying trace concentrations of an electroactive analyte, but also supply useful information concerning its chemical and physical properties. Quantities such as oxidation potentials, diffusion coefficients, electron transfer rates and electron transfer numbers are readily obtained using electroanalytical methods, whereas it would be more difficult to obtain using other techniques. Electroanalytical methods can be combined with spectroscopic techniques *in situ* to provide information concerning molecular structures and reaction mechanisms of transient electroactive species. Cyclic voltammetry (CV) is one of the simplest and most popular electroanalytical methods.⁴⁶ The effectiveness of this method lies in its ability to probe redox behaviour of electro-active species over a wide potential range in a relatively short time.

⁴⁶ P.T. Kissinger, W.R. Heineman, *J. Chem. Educ.* **1983** (60) 702-706.

2.3.2 Cyclic Voltammetry (CV).^{46,47,48,49,50}

Basic CV experiment.

Cyclic voltammetry involves the measurement of the resulting current between a working electrode and an auxiliary electrode, when the potential of the working electrode is oscillated in an unstirred solution. The potential of the small, static working electrode is controlled relatively to a reference electrode. Numerous reference electrodes are available, most commonly used is the saturated calomel electrode (SCE) or a silver/silver chloride electrode (Ag/AgCl). The controlled potential can be viewed as an excitation signal. This excitation signal causes the potential of the working electrode to sweep back and forth between the two designated switching potentials. The experiment starts at an initial potential (E_i) proceeding to a predetermined limit switching potential ($E_{\lambda 1}$), where the direction of the scan is reversed. This signal is a linear potential scanning with a triangular waveform (Figure 2.15). Although the potential scan is frequently terminated at the end of the first cycle, it can be continued for any number of cycles (as indicated by the broken line) - hence the terminology cyclic voltammetry. The scanning rate is reflected by the slope and varies from microvolts to volts, but is usually between 50 to 1000 $\text{mV}\cdot\text{s}^{-1}$.

⁴⁷ D.H. Evans, K.M. O'Connell, R.A. Peterson, M.J. Kelly, *J. Chem. Educ.* **1983** (60) 290-293.

⁴⁸ D.A. Skoog, D.M. West, F.J. Holler, *Fundamentals of Analytical Chemistry*, Seventh Edition, Saunders College Publishers, Philadelphia, **1996**, p460-496.

⁴⁹ P.T. Kissinger, W.R. Heineman, *Laboratory techniques in electroanalytical Chemistry*, Marcel Dekker, Inc., New York, **1984**, p84-94, 469-485.

⁵⁰ A.J. Bard, L.R. Faulkner, *Electrochemical Methods: Fundamentals and Applications*, Wiley, New York, **1980**, p213-248.

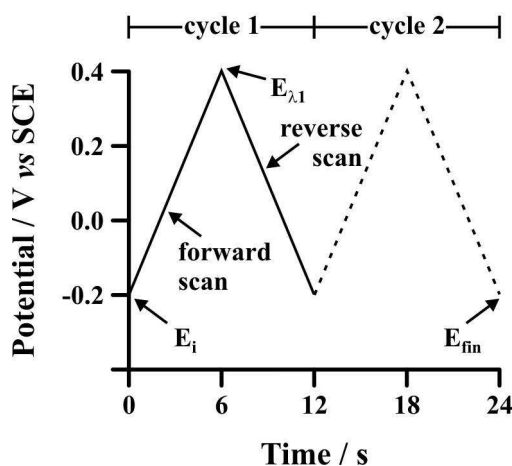


Figure 2.15: Typical potential-time excitation signal for cyclic voltammetry - a triangular potential waveform with switching potentials at -0.2 and 0.4 V *versus* SCE.

The resulting voltammogram is given in Figure 2.16. The voltammogram is a display of the current response (vertical axis) *versus* the applied potential (horizontal axis). Since the potential varies linearly with time, the horizontal axis can also be thought of as a time axis. The differences between the successive scans are important in obtaining and understanding information about the reaction mechanisms.

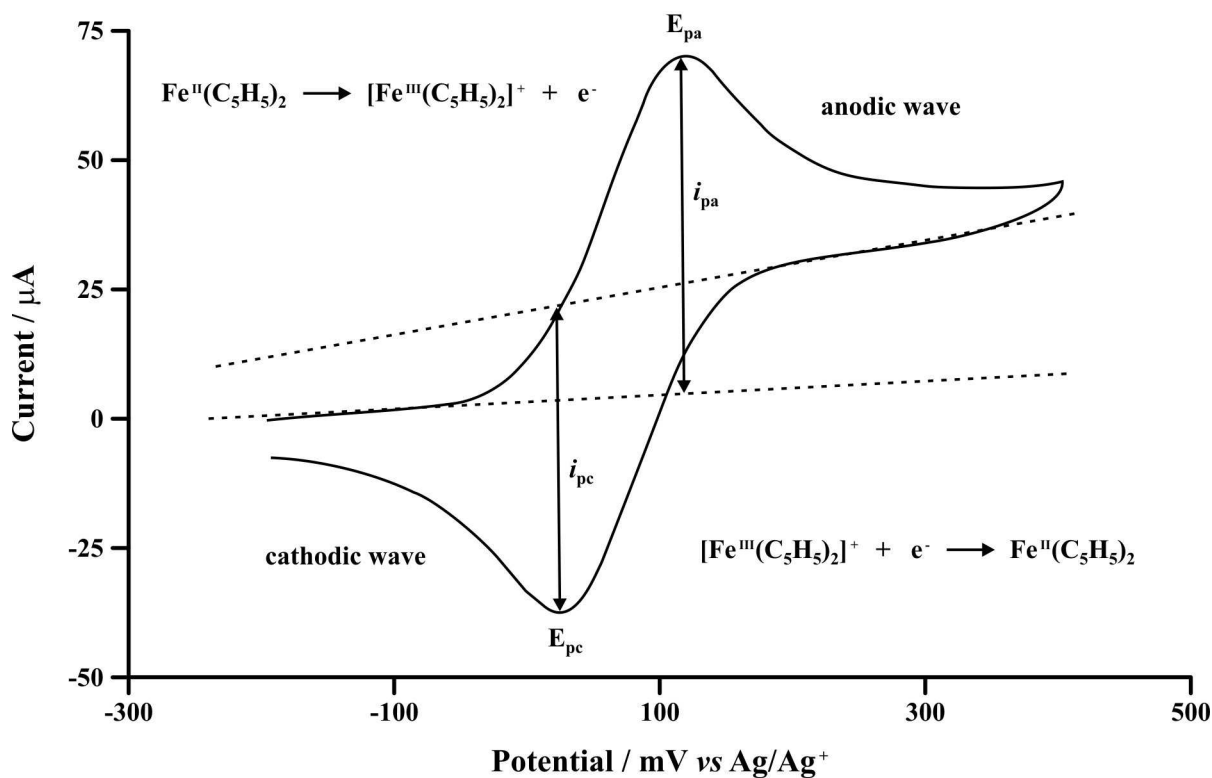


Figure 2.16: A voltammogram of 3.0 mmol.dm⁻³ Fc (ferrocene = [Fe(C₅H₅)₂]) measured in 0.1 mol.dm⁻³ tetrabutylammonium hexafluorophosphate/acetonitrile at a scan rate of 100 mV.s⁻¹ with a glassy carbon working electrode (25°C).

Important parameters of CV.

The most important parameters of cyclic voltammetry are the peak anodic (E_{pa}) and cathodic (E_{pc}) potentials and the magnitudes of the peak anodic (i_{pa}) and cathodic (i_{pc}) current (indicated in Figure 2.16). One method of measuring the peak currents (i_{pa} and i_{pc}) involves the extrapolation of a baseline as shown in Figure 2.16. The establishment of a correct baseline is essential for the accurate measurement of the peak currents. With this information, the following important parameters can be calculated:

Current ratio	$\frac{i_{pa}}{i_{pc}}$	(Equation 2.3)
---------------	-------------------------	-----------------------

Difference in peak potentials	$\Delta E_p = E_{pa} - E_{pc}$	(Equation 2.4)
-------------------------------	--------------------------------	-----------------------

Formal reduction potential	$E^{0'} = \frac{E_{pa} + E_{pc}}{2}$	(Equation 2.5)
----------------------------	--------------------------------------	-----------------------

One should distinguish between two important processes in electrochemistry: electrochemical processes (defined in terms of the difference in peak potentials) and chemical processes (measured in terms of current ratios). For a redox couple to be electrochemically reversible, the difference in peak potentials (ΔE_p) should theoretically be 59 mV at 25°C for a one electron transfer process. ΔE_p should also be independent of the scan rate. The difference in peak potentials increases above 59 mV due to slow electron transfer kinetics at the electrode surface as well as high solvent resistance over potentials. Under the experimental conditions of this study, a ΔE_p up to 90 mV is considered electrochemically reversible. For the redox couple to be chemically reversible the i_{pa} and i_{pc} values should be identical, in other words, the current ratio should be one. This indicates that the electron transfer process is not followed by a chemical reaction.

The peak current for a chemically reversible system is described by the Randles-Sevcik equation for the forward sweep of the first cycle:

Randles-Sevcik equation	$i_p = (2.687 \times 10^5) n^{\frac{3}{2}} D^{\frac{1}{2}} v^{\frac{1}{2}} A C$	(Equation 2.6)
-------------------------	---	-----------------------

where i_p is the peak current (A), the constant 2.687 has a unit ($C \cdot mol^{-1} \cdot V^{-1/2}$), n is the electron stoichiometry, D is the diffusion coefficient ($cm^2 \cdot s^{-1}$), v is the scan rate ($V \cdot s^{-1}$), A is the electrode area (cm^2) and C is the concentration ($mol \cdot cm^{-3}$). Accordingly plots of i_{pa} and i_{pc} versus $v^{1/2}$ should be linear with intercepts at the origin.

The redox couple is electrochemically quasi-reversible or irreversible when both the oxidation and reduction processes take place, but there is a slow electron exchange between the electrode and the redox species in solution. The difference in peak potentials of $90 \text{ mV} \leq \Delta E_p \leq 150 \text{ mV}$ indicates quasi-reversible behaviour, while $\Delta E_p > 150 \text{ mV}$ is treated as electrochemically irreversible. A complete chemically irreversible system is one where only oxidation or reduction occurs. The electrochemically and chemically reversibility/irreversibility are demonstrated in Figure 2.17.

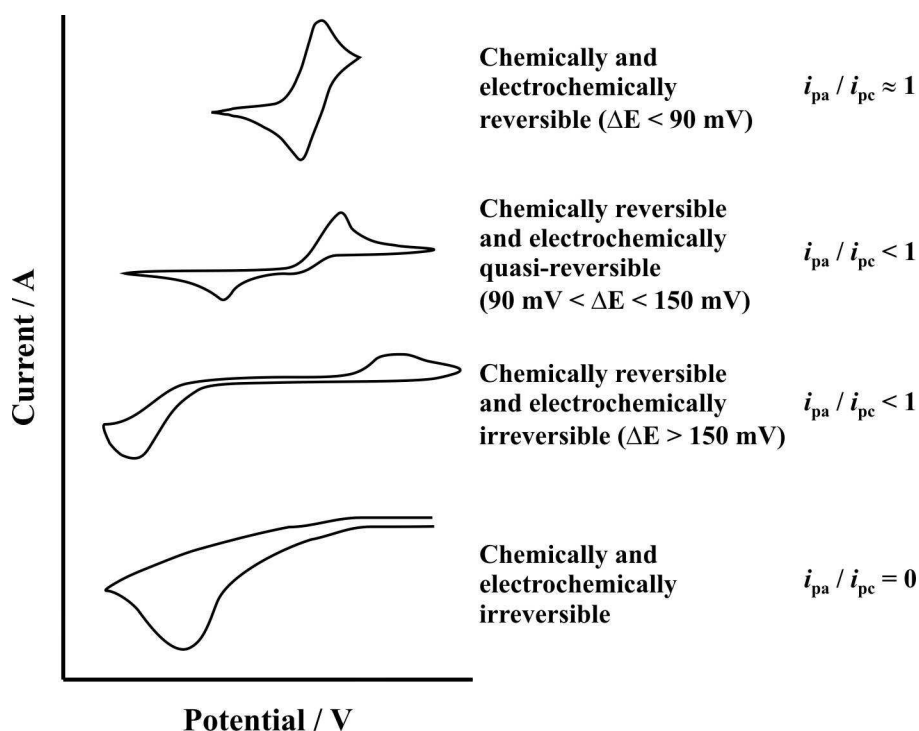


Figure 2.17: A schematic representation of the cyclic voltammograms expected for electrochemically reversible, quasi-reversible and irreversible systems.

Solvent system.

A suitable medium is needed for electrochemical phenomena to occur. The term "solvent system" is used to describe the medium consisting of both a solvent and a supporting electrolyte. Important properties that an ideal solvent system should possess are:

- **Electrochemical and chemical inertness:** The solvent system should not undergo any electrochemical reactions over a wide range of potentials and it should not react with the electroactive species or with intermediates or products of the electrode reaction under investigation.

- **High electrical conductivity:** In order to support the passage of an electrical current, the solvent system should contain a solvent with a low electrical resistance (large dielectric constant, $\epsilon \geq 10$) and a recommendable supporting electrolyte, to increase the conductivity of the medium.
- **Good solvent power:** The electroactive substances under investigation must be soluble at least to the extent of $1 \times 10^{-4} \text{ dm}^{-3}$ and the electrolyte concentration must be at least 10 times, but preferably 100 times, that of the electrochemical species under investigation.

There is not one good solvent system suitable for all experiments. However, a commonly used system for both inorganic salts and organic compounds is CH_3CN (acetonitrile) with tetrabutylammonium hexafluorophosphate (TBAPF_6 , $[\text{NBu}_4][\text{PF}_6]$) as the supporting electrolyte. The $\text{CH}_3\text{CN}/\text{TBAPF}_6$ system exhibits a wide potential range with positive and negative decomposition potentials of +3.5 V and -2.9 V respectively *versus* SCE.⁴⁹ One disadvantage is that CH_3CN is rather nucleophilic and can act as a coordinating solvent. DCM or THF can be used when a strictly non-coordinating solvent is required.

New supporting electrolytes and the use of non-traditional solvents have increased options in electrochemical studies. The use of the non-coordinating (but very expensive) supporting electrolyte tetrabutylammonium tetrakis(pentafluorophenyl)borate ($[\text{NBu}_4][\text{B}(\text{C}_6\text{F}_5)_4]$) improves electrochemical results compared to results obtained when using the weak coordinating electrolyte TBAPF_6 .⁵¹ It was shown that with the use of this new electrolyte, electrochemistry could be conducted in solvents of low dielectric strength and reversible electrochemistry could be obtained for compounds that are normally irreversible.⁵² It was also shown that the peak separation between two very close oxidation peaks could be better analysed with the use of this electrolyte.⁵³

Reference electrode.

Prior to the 1980's, nearly all experimental papers specified potentials of a reference electrode *versus* normal hydrogen electrode (NHE) or saturated calomel electrode (SCE). However, IUPAC has since recommend that all electrochemical data be reported *versus* an internal

⁵¹ L. Pospisil, B.T. King, J. Michl, *Electrochim. Acta* **1998** (44) 103-108.

⁵² R.J. le Suer, W.E. Geiger, *Angew. Chem., Int. Ed.* **2000** (39) 248-250.

standard.^{54,55} In organic media, Fc/Fc⁺ couple (Fc = ferrocene) is a convenient internal standard (Fc/Fc⁺ exhibits $E^0 = 400 \text{ mV versus NHE}$).⁵⁶ NHE and SCE are used for measurements in aqueous solutions. However, in many instances electrochemical measurements in water are impossible due to insolubility or instability. With non-aqueous solvents, an experimental reference electrode such as Ag/Ag⁺ (0.01 mol.dm⁻³ AgNO₃ in CH₃CN) or Ag/AgCl may be used.

2.3.3 Spectroelectrochemistry (SEC).^{57,58,59}

Spectroelectrochemistry (SEC) combines the two quite different techniques, electrochemistry and spectroscopy, to study the redox chemistry of inorganic, organic and biological molecules. Oxidation states are changed electrochemically (in a specially designed electrochemical cell) by addition or removal of electrons at an electrode. The products of the redox transformation or the following chemical reactions are then simultaneously monitored *in situ* by spectroscopic techniques. Frequently used spectroscopic techniques are ultraviolet (UV, 200-350 nm), visible (Vis, 350-700 nm), near-infrared (NIR, 700-1000 nm) and infrared (IR). Fluorescence, Raman, Resonance Raman, electronic spin resonance (ESR) and nuclear magnetic resonance (NMR) spectroscopy can also be used. SEC is a convenient way for obtaining spectra and reduction potentials and for observing subsequent chemical reactions of electrogenerated species.

Optically transparent electrochemical cells (OTE cells).

An optically transparent electrode, which enables light to be passed through its surface and the adjacent solution, is most commonly used for performing transmission spectroelectrochemical experiments. Various OTE cell designs are available depending on the spectroscopic apparatus used in the experiment. The optically transparent electrode can be:

⁵³ W.J. Moore, *Physical Chemistry*, Fourth Edition, Longman Group Limited, London, **1972**, p333-334.

⁵⁴ R.R. Gagné, C.A. Koval, G.C. Lisensky, *Inorg. Chem.* **1980** (19) 2854-2855.

⁵⁵ G. Gritzner, J. Kúta, *Pure & Appl Chem* **1984** (56) 461-466.

⁵⁶ H.M. Koepp, H. Wendt, H. Strehlow, *Z. Elektrochem.* **1964**, (64) 483-491.

⁵⁷ W. Plieth, G.S. Wilson, C. Gutiérrez De La Fe, *Pure & Appl. Chem.* **1998** (70) 1395-1414.

⁵⁸ P.T. Kissinger, W.R. Heineman, *Laboratory techniques in electroanalytical Chemistry*, Marcel Dekker, Inc., New York, **1984**, p63-64, 283-289.

⁵⁹ A.J. Bard, L.R. Faulkner, *Electrochemical Methods: Fundamentals and Applications*, Wiley, New York, **1980**, p577-583.

- A thin metal film on a transparent substrate. The thickness must not exceed 100 nm for the film to remain transparent, since this can result in a high electrical resistance.
- A glass plate with a thin film of an optically transparent, conducting material. For example, indiumdoped tin oxide (ITO).
- A gold minigrad between transparent substrates.
- A thicker, free-standing metal mesh.

Ideally, when using OTE cells, the reactant (dissolved in bulk solution) should not absorb radiation in the wavelength window of the product. If it does, detection of the product may be difficult if the beam travels through a significant thickness of reactant solution. This is reduced (if not eliminated) with optically transparent thin layer electrochemical cells (OTTLE cells).

Optically transparent thin layer electrochemical cells (OTTLE cells).

The optically transparent thin layer electrodes consist of a metal (Au, Ag, Ni) micromesh containing small (10-30 μm) holes, which couples good optical transmission (over 50%) with good electrical conductivity. Such a minigrad is usually sandwiched between two microscopic slides, which form a thin-layer cell. The OTTLE is placed in the spectrophotometer so that the optical beam is passed through the transparent electrode and solution. The working volume of such a cell is typically 30-100 μl . The OTTLE cell used in this study is displayed in Figure 2.18.

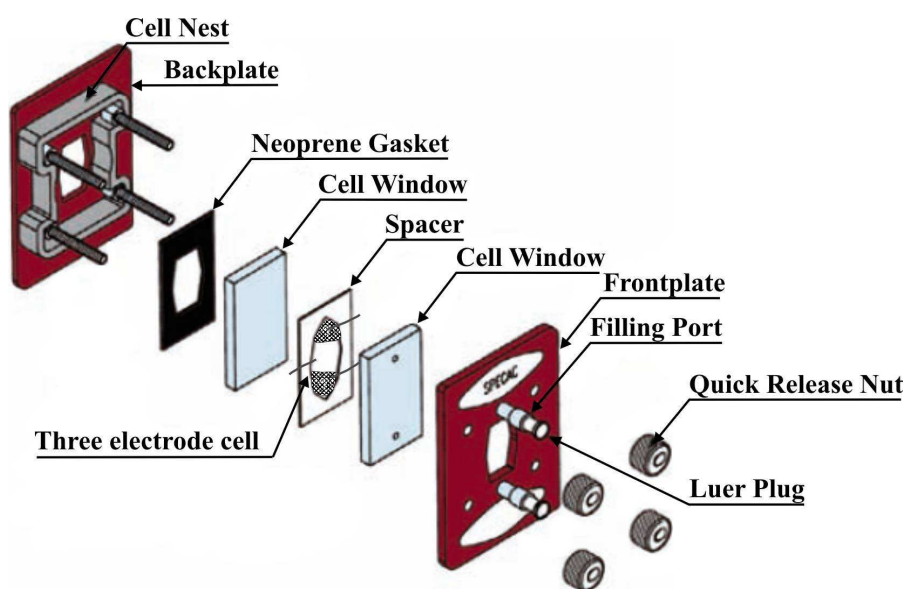


Figure 2.18: The general-purpose OTTLE cell used in this study. The three electrode cell consists out of a Pt minigrad as working electrode, a Ag/Ag⁺ wire as reverence electrode and a Pt wire as auxiliary electrode.⁶⁰

⁶⁰ www.specac.com, Omni-Cell™ System - Data Sheet.

2.4 Rhodium complexes.

2.4.1 Square planar Rh(I) and octahedral Rh(III) chemistry.

2.4.1.1 General properties.^{61,62,63}

The chemistry of rhodium(I) is almost entirely one involving π -bonding ligands such as CO, PR_3 , RNC, alkenes, cyclopentadienyls and aryls. In a complex, rhodium forms square planar, tetrahedral, octahedral and five-coordinate species. The latter two are commonly produced by addition of neutral ligands to the first two. The criteria for relative stability of five- and four-coordinate species are by no means fully established. Substitution reactions of square species, which are often rapid, proceed by an associative pathway involving five-coordinate intermediates. Most of the square planar complexes undergo oxidative addition reactions and these lead to octahedral rhodium(III) complexes with π -bonding ligands. These Rh(I)-Rh(III) oxidation changes are important in catalytic cycles.

The rhodium(I) complexes are usually prepared by reduction of similar rhodium(III) complexes or of halide species such as $\text{Rh}^{\text{III}}\text{Cl}_3 \cdot 3\text{H}_2\text{O}$ in the presence of a complexing ligand. Hundreds of complexes are known and only a few representative examples synthesized from $\text{Rh}^{\text{III}}\text{Cl}_3 \cdot 3\text{H}_2\text{O}$ are shown in Figure 2.19.

⁶¹ F.A. Cotton, G. Wilkinson, C.A. Murillo, M. Bochmann, *Advanced inorganic chemistry*, Sixth edition, John Wiley & Sons, New York, **1999**, p1041-1042.

⁶² Y.S. Varshavsky, T.G. Cherkosova, N.A. Buzina, L.S. Bresler, *J. Organomet. Chem.* **1994** (464) 239-245.

⁶³ J. Conradie, T.S. Cameron, M.A.S. Aquino, G.J. Lambrecht, J.C. Swarts, *Inorg. Chim. Acta* **2005** (358) 2530-2542.

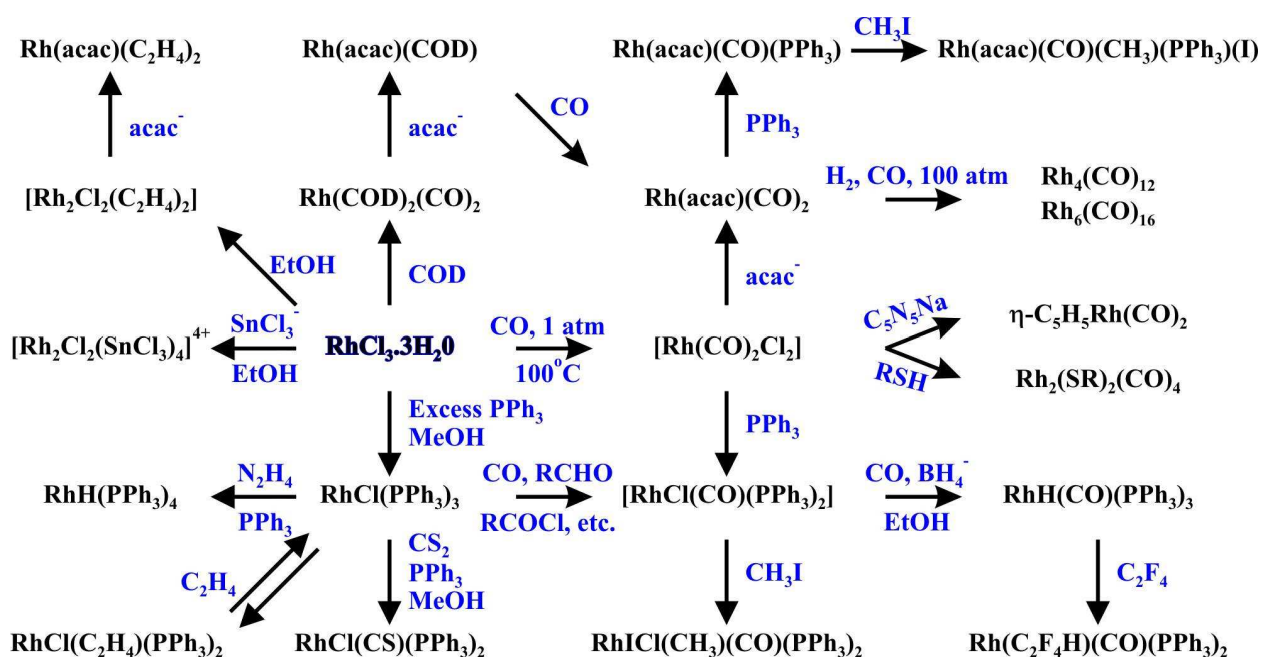


Figure 2.19: Preparations and reactions of rhodium(I) and rhodium(III) compounds from $\text{Rh}^{\text{III}}\text{Cl}_3\cdot\text{H}_2\text{O}$.

2.4.1.2 Carbonyl (CO) bonding to a metal.^{64,65,66}

The fact that refractory metals, with high heats of atomization ($\sim 400 \text{ kJ}\cdot\text{mol}^{-1}$), and an inert molecule like CO are capable of uniting to form stable, molecular compounds is quite surprising, especially when the CO molecules retain their individuality. Moreover, the Lewis basicity of CO is negligible. The explanation lies in the multiple nature of the M-CO bond. The bonding is best explained by a molecular orbital diagram as illustrated in Figure 2.20.

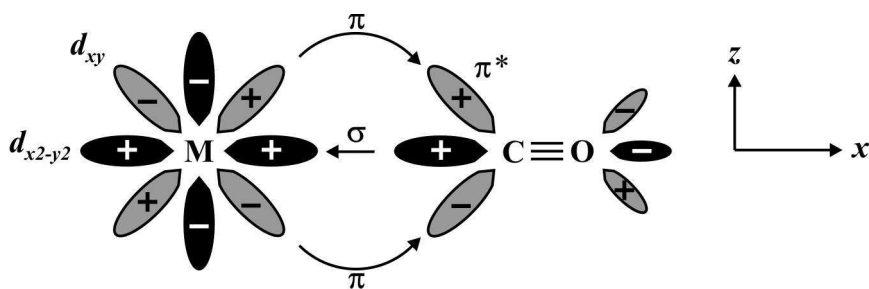


Figure 2.20: The formation of the metal←CO σ -bond using a lone electron pair on the carbon and the formation of the metal→CO π -backbond. Other orbitals on the CO ligand are omitted for clarity.

⁶⁴ F.A. Cotton, G. Wilkinson, P.L. Gaus, *Basic Inorganic Chemistry*, Third edition, John Wiley & Sons, New York, 1995, p649-650.

⁶⁵ A. Roodt, G.J.J. Steyn, *Recent Rs. Devel. Inorganic Chem.* **2000** (2) 1-23.

⁶⁶ S. Franks, F.R. Hartley, J.R. Chipperfield, *Inorg. Chem.* **1981** (20) 3238-3242.

Firstly, there is a dative overlap of the filled carbon σ -orbital. The lone pair electrons of the carbon are donated to the empty metal $d_{x^2-y^2}$ -orbital to form a σ -bond. Secondly, there is a dative overlap of the filled d_{π} -orbital of the metal with an empty antibonding p_{π} -orbital of the CO to form a π -bond. This bonding mechanism is synergic, since the drift of metal electrons into the CO orbitals will tend to make the CO as a whole negative and, hence, will increase its electron donating property via the σ -orbital of the carbon. Also, the drift of electrons to the metal in the σ -bond tends to make the CO positive, thus enhancing the acceptor strength of the π^* -orbitals. Therefore, the effects of σ -bond formation strengthen the π -bonding and vice versa.

The main lines of physical evidence showing the multiple nature of the M-CO bonds are bond lengths and vibrational spectra. According to the preceding description of the bonding, as the extent of back-donation from M to CO increases, the M-C bond becomes stronger and the C \equiv O bond becomes weaker which results in a lower CO-stretching frequency (ν_{CO}). Therefore the multiple bonding should be evidenced by shorter M-C and longer C-O bonds as compared with M-C single bonds and C \equiv O triple bonds respectively and the ν_{CO} will decrease as illustrated in Figure 2.21. Although C-O bond lengths are rather insensitive to bond order, for M-C bonds in selected compounds there is an appreciable shortening consistent with the π -bonding concept.



Figure 2.21: Tighter bonded C-O bonds (left) have a higher CO-stretching frequency (ν_{CO}) than weaker bonded C-O bonds (right).

Infrared spectra have been widely used in the study of metal carbonyls since the CO-stretching frequency (ν_{CO}) gives a very strong sharp band that is well separated from other vibrational modes of any other ligands also present. Where the free CO molecule has a $\nu_{\text{CO}} = 2143 \text{ cm}^{-1}$, it has a lower ν_{CO} when bonded to a rhodium(I) complex. Although the oxidative addition of CH_3I to rhodium(I) complexes will be discussed in section 2.4.1.4, Figure 2.22 and Figure 2.23 illustrate and explain the CO-stretching frequency (ν_{CO}) shifts during the reaction.

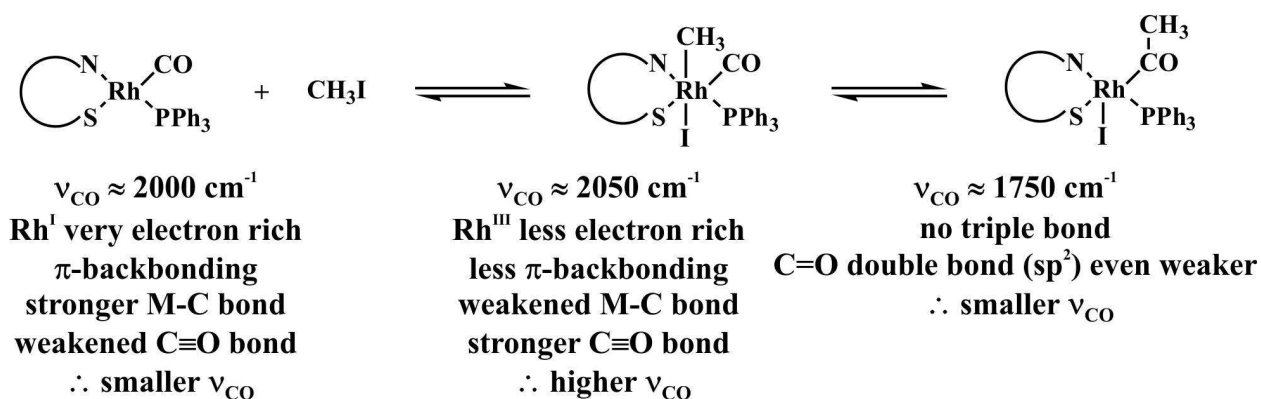


Figure 2.22: CO-stretching frequency (ν_{CO}) shifts during oxidative addition reaction of CH_3I to a $[\text{Rh}(\text{L},\text{L}')\text{-BID}(\text{CO})(\text{PPh}_3)]$ complex, where L,L'-BID is a monocharged bidentate ligand with donor atoms L and L' equal to N and S.

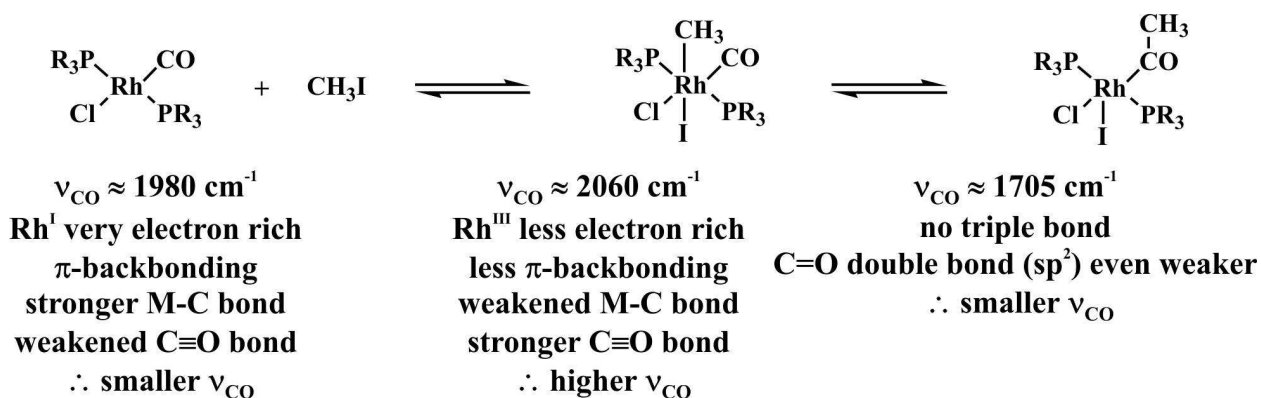


Figure 2.23: CO-stretching frequency (ν_{CO}) shifts during oxidative addition reaction of CH_3I to *trans*- $[\text{RhCl}(\text{CO})(\text{PR}_3)_2]$ where PR_3 = triarylphosphine.

2.4.1.3 Trivalent phosphine (PX_3) bonding to a metal.^{67,68,69,70,71}

PX_3 compounds can be π -acceptor ligands when X is fairly electronegative (Ph, OR) or very electronegative (Cl, F). Tertiary phosphines and phosphates are much better Lewis bases than CO and can form many complexes where π acidity plays little or no role. This is observed with

⁶⁷ F.A. Cotton, G. Wilkinson, C.A. Murillo, M. Bochmann, *Advanced Inorganic Chemistry*, Sixth edition, John Wiley & Sons, New York, **1999**, p642.

⁶⁸ A. Pidcock, In: C.A. McAuliffe (Editor), *Transition Metal Complexes of Phosphorus, Arsenic and Antimony Ligands*, Macmillan, London, **1973**, Part 1.

⁶⁹ J. Emsly, D. Hall, *The Chemistry of Phosphorus*, Harper and Row Publishers, **1976**, Chapter 5.

⁷⁰ C.A. McAuliffe, W. Levason, *Phosphine, Arsine and Stibine Complexes of the Transition Elements*, Elsevier Scientific Publishing Company, Amsterdam, **1979**, Chapter 3.

⁷¹ D.S. Marynick, *J. Am. Chem. Soc.* **1984** (106) 4064-4065.

the phosphine complexes of the early transition metals and with metal atoms of any kind in their higher oxidation states where the M-P distances show no evidence of significant π -bonding. In almost any CO-containing molecule, one or more CO groups can be replaced with a PX_3 or a similar ligand. While the occurrence of π -bonding from M to P is a generally acknowledged fact, the explanation for it entails controversy. The widely credited explanation is the figure that is shown in Figure 2.24, in which phosphorus specifically employs a pair of its d -orbitals to accept metal electrons.

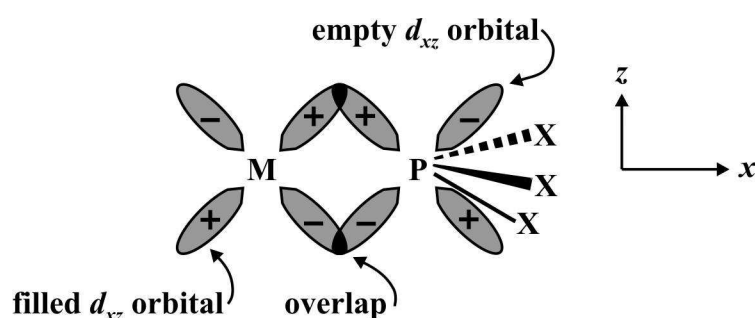


Figure 2.24: The backbonding from a filled metal d -orbital to an empty phosphorus $3d$ -orbital in the PX_3 ligand taking the internuclear axis as the x -axis. An exactly similar overlap occurs in the xy -plane between the d_{xy} -orbitals.

Of course, not all M-P bond properties can be explained by the π -bond model in Figure 2.24. According to Pidcock⁶⁸ there are clearly two extremes: firstly, complexes containing the metal in oxidation states greater than +2 contain predominantly pure σ -bonds with phosphine ligands and secondly, those in low oxidation states, especially with such ligands as PF_3 , PCl_3 and $P(OPh)_3$ form bonds with phosphines which contain a σ - as well as a π -component. It has been proposed by Marynick⁷¹ (on the basis of quantum mechanical calculations) that phosphorus p -orbitals and the P-X σ^* -orbitals may play a major role in accepting metal d_π electrons, even to the complete exclusion of the phosphorus d_π -orbitals. Experimental evidence for or against such ideas is lacking. Figure 2.25 shows the probability that a π -bond will form between phosphorus and the appropriate ligand.

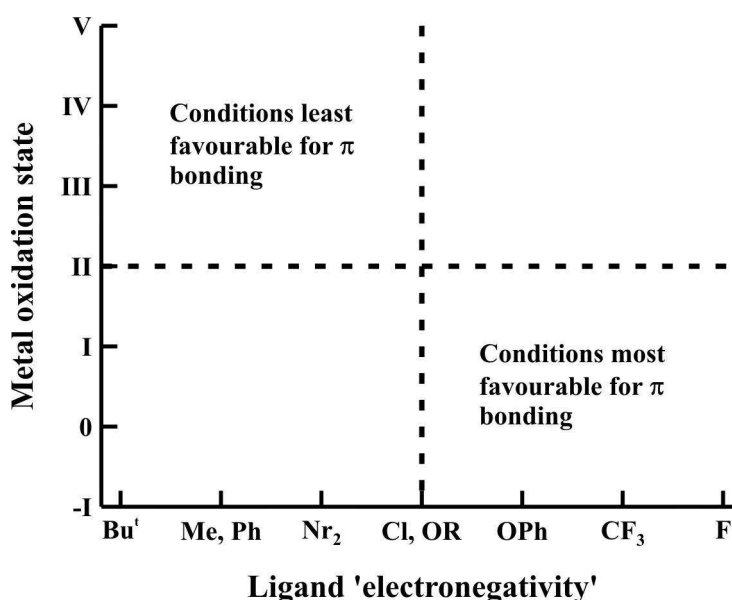


Figure 2.25: Dependence of π -bonding on oxidation state of metal and 'electronegativity' of the phosphorus ligands, based on tetracoordinate phosphorus.

2.4.1.4 General oxidative addition in rhodium complexes.

Introduction.^{72,73,74,75,76,77}

The process of oxidative addition in transition metal chemistry is used to describe the addition of neutral molecules (X-Y) to transition metal complexes having no more than 16 valence electrons. Oxidative addition is demonstrated in Figure 2.26, where the forward reaction is oxidative addition and the reverse reaction is reductive elimination.

⁷² F. Mathey, A. Sevin, *Molecular Chemistry of the Transition Elements - an introductory course*, John Wiley & Sons, England, **1996**, p28-50.

⁷³ F.A. Cotton, G. Wilkinson, P.L. Gaus, *Basic Inorganic Chemistry*, Third edition, John Wiley & Sons, New York, **1995**, p704-708.

⁷⁴ K.F. Purcell, J.C. Kotz, *Inorganic Chemistry*, W.B. Saunders Company, Philadelphia, **1977**, p938-948.

⁷⁵ J.P. Collman, L.S. Hegeudus, *Principles and Applications of Organotransition Metal Chemistry*, University Science Books, Mill Valley, California, **1980**, p176-258.

⁷⁶ J.P. Birk, J. Halpern, A.L. Pichard, *J. Am. Chem. Soc.* **1968** (90) 4491-4492.

⁷⁷ R. Ugo, *Coord. Chem. Rev.* **1968** (3) 319-344.

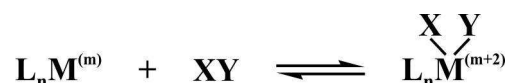


Figure 2.26: Oxidative addition of the neutral molecule XY to the transition metal complex $\text{L}_n\text{M}^{(m)}$ with n = number of ligands (L) bonded to the metal (M) and m = the oxidation state of M before oxidative addition.

These terms merely describe a reaction and have no mechanistic implications. The mechanisms can be extremely complicated and vary with the nature of the metal-ligand system and the molecule that is oxidatively added.

For an oxidative addition reaction to proceed, there must be:

- non-bonding electron density on the metal,
- two vacant coordination sites on the complex L_nM to allow the formation of two new bonds to X and Y and
- the oxidation state of the central metal atom has to be two units lower than the most stable oxidation state of the metal.

Whether the equilibrium in Figure 2.26 lies on the reduced-metal or the oxidized-metal side, depends most critically on:

- the nature of the metal,
- the nature of the ligands L in the complex,
- the nature of the added molecule XY and of the bonds M-X and M-Y so formed and
- the medium in which the reaction is conducted.

For transition metals, the most common oxidative addition reactions involve complexes of the metals with d^8 and d^{10} electron configurations, for example Rh(I), Ir(I) and Pt(II). In general, the oxidative addition to unsaturated square planar, 16 electron, d^8 complexes gives saturated six-coordinate, 18 electron, d^6 complexes (Figure 2.27 (a)). Coordinatively saturated five-coordinate, 18 electron, d^8 complexes must lose one of the original ligands in the oxidative addition of two new ligands to give a saturated six-coordinate, 18 electron, d^6 complex as the final product (Figure 2.27 (b)). Coordinatively saturated d^8 compounds are typically less reactive and usually add only the stronger oxidizing addenda XY. Frequently d^{10} complexes are coordinatively unsaturated, being only three or four-coordinate, so addition occurs readily (example in Figure 2.27 (c)).

SURVEY OF LITERATURE AND FUNDAMENTAL ASPECTS

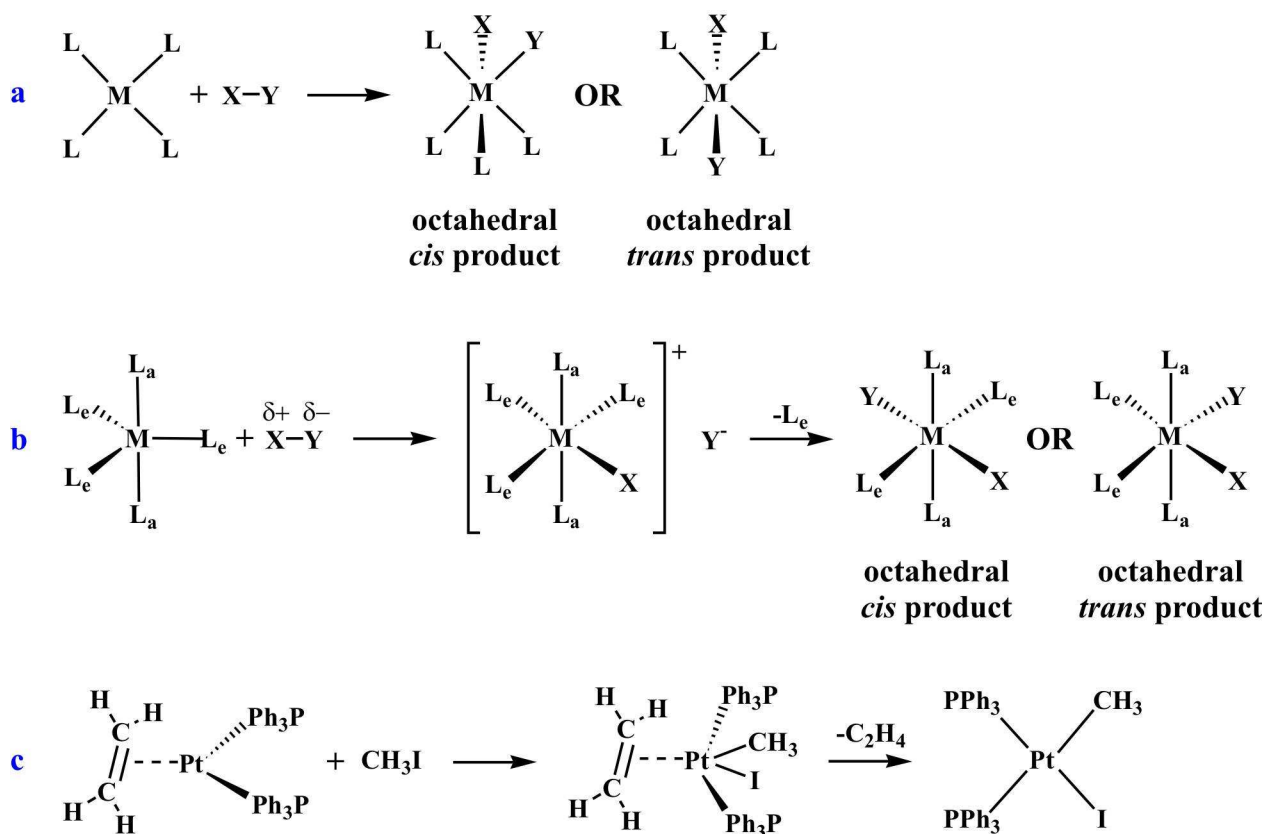


Figure 2.27: Oxidative addition to d^8 and d^{10} complexes. (a) Oxidative addition to unsaturated square planar d^8 complex ML_4 with metal M and ligands L. (b) Oxidative addition to saturated trigonal bipyramidal d^8 complex (L_a = an axial ligand, L_e = an equatorial ligand). (c) Oxidative addition to coordinatively unsaturated d^{10} complex.

As explained in section 2.2.7, the final product of an oxidative addition reaction will be the isomer or mixture of isomers that is thermodynamically the most stable under the reaction conditions. The nature of the ligands, solvent, temperature, pressure, and the like, will have a decisive influence on this. The mechanism of oxidative addition determines the initial oxidative addition product. The nature of the final product, however, does not necessarily give a guide to the initial product or the mechanism of the addition, since isomerization of the initial product may occur.

Mechanism of oxidative addition reactions.^{72,73,75,78,79,80,81}

Although it is still widely speculated what the intimate mechanism of oxidative addition is, two general types can be defined: that of one- and that of two-electron oxidative addition. These two types differ from one another due to the fact that the intermediate of the one-electron mechanism is paramagnetic and the two-electron mechanism involves a paired electron process. The one-electron mechanism can be described as a free-radical mechanism while the two-electron mechanism is dependent on the polarity of the proposed transition state and can be divided into three subcategories. These main mechanisms are listed below:

- a. the free-radical mechanism,
- b.i. the three-centred concerted mechanism,
- b.ii. the S_N2 mechanism and
- b.iii. the ionic mechanism.

Pearson⁸¹ has pointed out that reactions proceeding with reasonably low activation energies involve an electron flow between orbitals with the same symmetry properties. For oxidative addition, electrons must flow from a filled metal orbital into an antibonding X-Y orbital. This allows the X-Y bond to be broken and new bonds to the metal to be formed. The X-Y antibonding orbital must overlap in phase with a filled metal orbital, as illustrated in Figure 2.28.

⁷⁸ J.K. Kochi, *Organometallic Mechanism and Catalysis*, Academic Press, London, **1978**.

⁷⁹ R.J. Cross, *Chem. Soc. Rev.* **1985** (14) 197-223.

⁸⁰ R.S. Dickson, *Organometallic Chemistry of Rhodium and Iridium*, Academic Press, London, **1983**, p70-79.

⁸¹ R.G. Pearson, *Symmetry Rules for Chemical Reactions*, Wiley, New York, **1976**, p405-413.

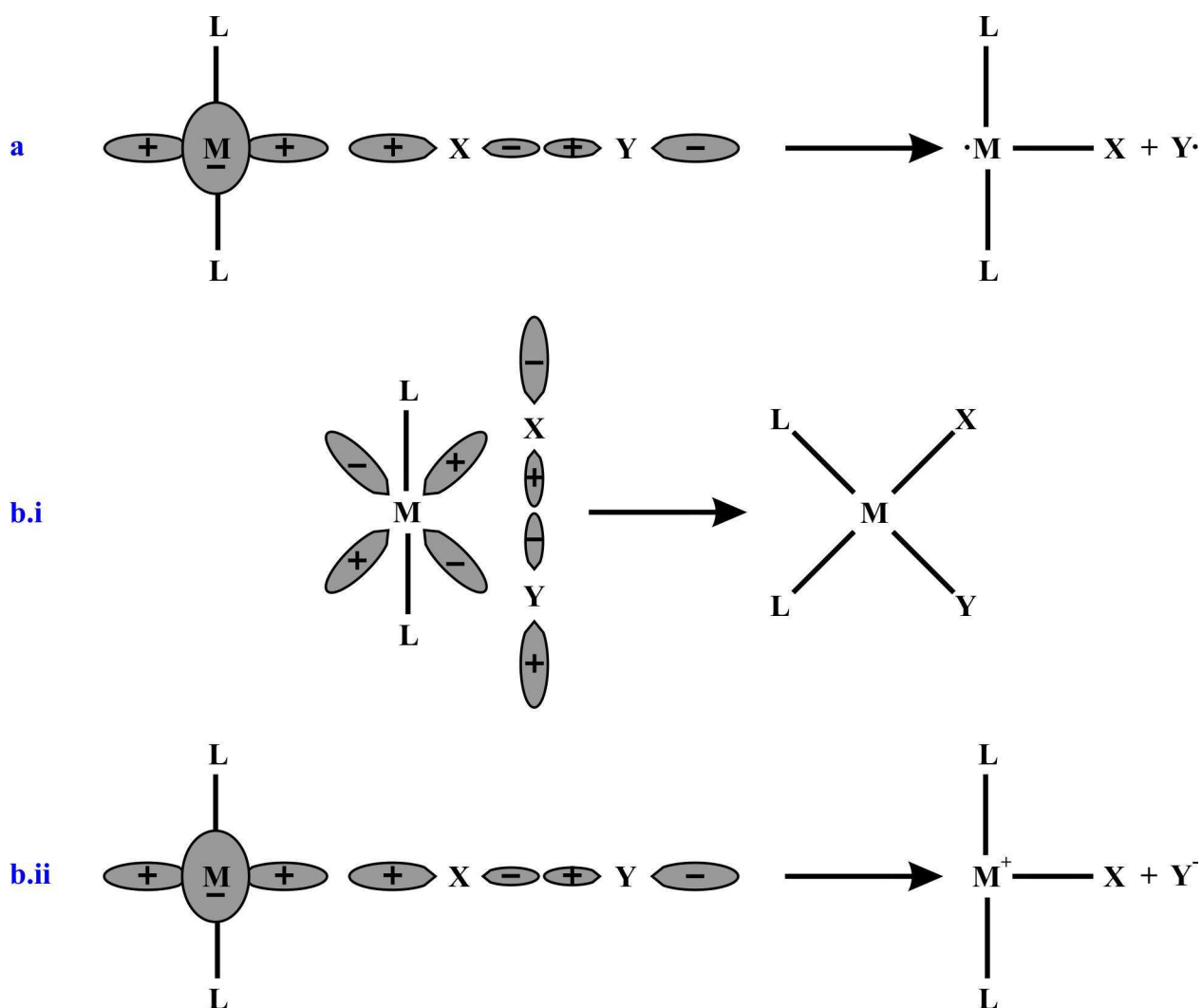


Figure 2.28: Symmetry-allowed overlap of orbitals for electron transfer in oxidative addition to 16 electron ML_4 complexes. Two ligands are above and below the plane of the page. **(a)** The free-radical mechanism. **(b.i.)** The three-centred concerted mechanism. **(b.ii.)** the S_N2 mechanism.

a. The free-radical mechanism.^{72,81,82,83,84}

The free-radical mechanisms, as illustrated in Figure 2.29, are generally observed when the participating complex is a strong reducing agent and are favoured by the increasing stability of the radical $[L_nM-X]^\cdot$ (see Figure 2.28). In certain cases, radical-chain processes are observed. They are often initiated by O_2 or peroxides and can be blocked by inhibitors such as bulky phenols.

⁸² J.A. Labinger, A.V. Kramer, J.A. Osborn, *J. Am. Chem. Soc.* **1973** (95) 7908-7909.

⁸³ M.F. Lappert, P.W. Ledner, *J. Chem. Soc., Chem. Commun.* **1973** 948-949.

⁸⁴ J.K. Stille, R.W. Fries, *J. Am. Chem. Soc.* **1974** (96) 1514-1518.

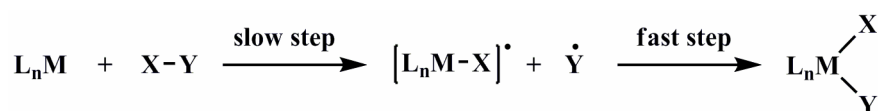


Figure 2.29: The free-radical mechanism for oxidative addition.

Free-radical mechanisms are found for organic bromides and iodides reacting with Ir(I) and Pt(0) complexes. Rh and Pd are less likely to give free-radical reactions. Evidence shows that *trans* addition products and racemates of optically active alkyl groups are formed. Although the *trans* products are the most probable products, rearrangements lead to *cis* products and therefore cannot be ruled out. Non-polar solvents (or the absence of solvents) favour a free-radical mechanism.

b.i. The three-centred concerted mechanism.^{72,80}

The three-centred concerted mechanism follows the scheme, as illustrated in Figure 2.30.

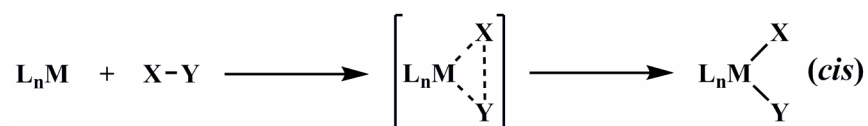


Figure 2.30: The three-centred concerted mechanism for oxidative addition.

Here, filled d_{xz} - and d_{xy} -orbitals on the metal interact with antibonding orbitals of the substrate X-Y (Figure 2.28 (b.i)) to produce a cyclic transition state. The product formed by this route will have a *cis*-arrangement. As would be expected for a concerted process, the kinetics is of second order. As with the free-radical mechanism, non-polar solvents (or the absence of solvents) favour a three-centred concerted mechanism.

b.ii. The S_N2 mechanism.^{72,80}

In the S_N2 mechanism, the metal complex plays the role of a nucleophile to produce a polar intermediate, as illustrated in Figure 2.31.

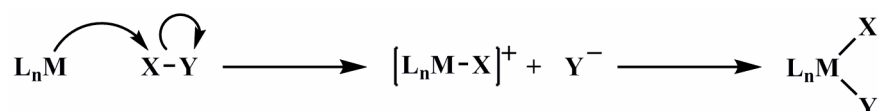


Figure 2.31: The S_N2 mechanism for oxidative addition.

As with the three-centred concerted mechanism, the kinetics is of second order and the activation entropy (ΔS^\ddagger) is negative. However, unlike the three-centred concerted mechanism, the product can have either *cis* or *trans* geometry and the reaction is accelerated by polar solvents. The S_N2 mechanism seems particularly appropriate to oxidative addition reactions with alkyl and acyl halides.

b.iii. The ionic mechanism.⁷²

Ionic mechanisms generally require the presence of a strongly dissociated protic acid H-X as a reagent. This means that a polar solvent is necessary. Two cases have been recognized, as illustrated in Figure 2.32.

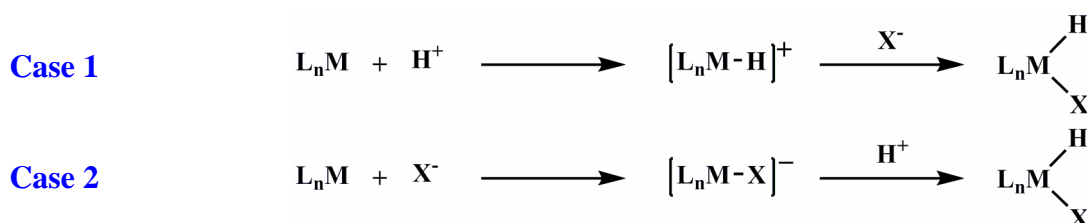


Figure 2.32: The two variants of the ionic mechanism.

In the more common one (Case 1 in Figure 2.32), the complex is sufficiently basic to protonate, after which the anion bonds to give the final product. The opposite case, in which the halide ion attacks first, followed by protonation of the intermediate, is rare. The first route is favoured by basic ligands and a low oxidation state, the second by electron acceptor ligands and a positive charge on the metal.

2.4.1.5 General carbonyl insertion and methyl migration in rhodium complexes.

Introduction.^{72,85,86,87}

An insertion reaction can be defined as the incorporation of an unsaturated two-electron ligand (A=B) into an M-X σ -bond (X being a one-electron ligand) of a transition metal complex L_nM-X . Of the various classifications of insertion reactions, two are considered here:

⁸⁵ J.P. Collman, L.S. Hegedus, *Principles and Applications of Organotransition Metal Chemistry*, University Science Books, Mill Valley, California, **1980**, p259-298.

⁸⁶ K. Noack, F. Calderazzo, *J. Organomet. Chem.* **1967** (10) 101-104.

⁸⁷ Y. Yamamoto, H. Yamazaki, *J. Organomet. Chem.* **1970** (24) 717-724.

(i) Insertion types (1,1) and (1,2) etc. depending on how the addition between M and X to A=B takes place. Each proceeds through two distinct steps. The first involves incorporating A=B as a ligand into the metal coordination sphere (L_nM-X must have no more than 16 electrons because the reaction requires a vacant coordination site.) The second step, often called migratory-insertion, incorporates A=B into the M-X bond. See Figure 2.33.

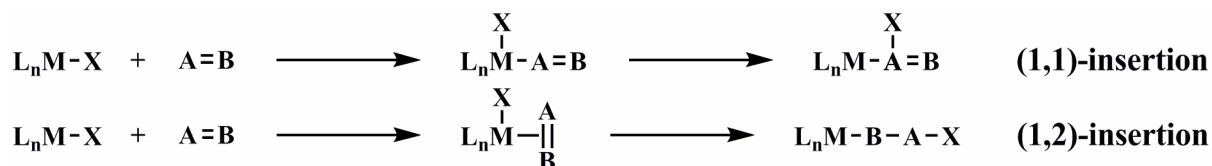


Figure 2.33: (1,1) and (1,2) insertion reactions of an unsaturated two-electron ligand (A=B) into a M-X σ -bond (X being a one-electron ligand).

The metal's oxidation state remains unchanged in both the (1,1)- and (1,2)-insertion reactions. The migration of X to A=B (or A=B to X) requires that these ligands adopt a *cis* geometry within the metal sphere. During the migratory-insertion, the number of electrons and the metal coordination number decrease by two units and one unit respectively. The addition of a two-electron ligand is often required to stabilize the complex that is produced. Carbon monoxide (CO) is the ligand that most commonly undergoes (1,1) insertions. Alkenes and alkynes invariably give (1,2) insertions.

(ii) The insertion processes can also be classified as intramolecular “migratory insertions” or as intermolecular “nucleophilic additions”. The intramolecular “migratory insertions” take place by the combination of X and A=B, while both are coordinated to the metal (the second step of both insertion reactions of Figure 2.33). See Figure 2.34 for examples of intra- and intermolecular insertion reactions. The reaction $CH_3Mn(CO)_5 + {}^{13}CO \rightarrow CH_3COMn(CO)_4({}^{13}CO)$ is considered as an intramolecular “migratory insertion” since the carbonyl insertion took place at a CO group already coordinated to $CH_3Mn(CO)_5$ and not at the ${}^{13}CO$ group.

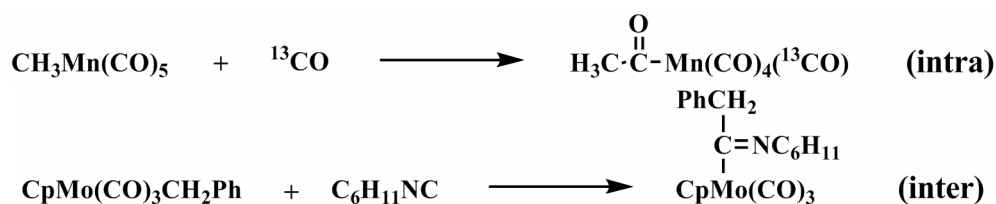


Figure 2.34: Example of an intra- and an intermolecular insertion reaction.

Mechanism of insertion of CO.^{88,89}

Generally speaking, a carbonyl insertion reaction is regarded as known when any one of the following stoichiometric reactions has been fully characterized:

- | | |
|---------------------------------------|--|
| a. $R-M + CO \rightarrow RCO-M$ | CO insertion into the metal-carbon σ -bond of a metal complex which may or may not contain carbonyl groups. |
| b. $R-M(CO) \rightarrow RCO-M$ | Conversion of a coordinated CO group into an acyl (or aroyl) group. |
| c. $R-M(CO) + L \rightarrow RCO-M(L)$ | CO insertion into a metal carbonyl complex promoted by a Lewis base L. |

(L = two-electron ligand, R is an alkyl or related σ -bonded group.)

Carbonyl insertion reactions for square planar complexes may be represented as in Figure 2.35, where $[MR(CO)]$ is a reactant or an intermediate, R is an alkyl or related σ -bonded group, L stands for any ligand including CO and M represents a metal together with its ancillary ligands.

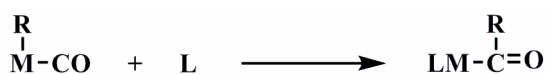


Figure 2.35: Carbonyl (CO) insertion reactions for square planar complexes.

The insertion reaction is best considered as an intramolecular alkyl migration to a coordinated carbon monoxide ligand in a *cis*-position and the migration probably proceeds through a three-centred transition state as illustrated in Figure 2.36.

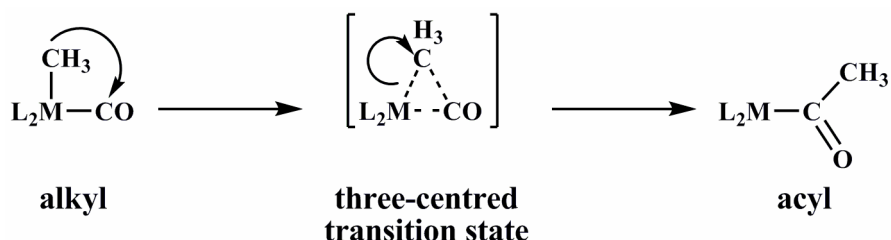


Figure 2.36: Three-centred transition state proposed for carbonyl insertion reaction.

⁸⁸ F. Calderazzo, *Angew. Chem. Int. Ed. Engl.* **1977** (16) 299-311.

⁸⁹ F.A. Cotton, G. Wilkinson, C.A. Murillo, M. Bochmann, *Advanced Inorganic Chemistry*, Sixth edition, John Wiley & Sons, New York, **1999**, p1208-1212.

2.4.2 The Monsanto Process: $[\text{Rh}(\text{CO})_2\text{I}_2]^- + \text{CH}_3\text{I}$.

90,91,92,93,94,95,96,97,98,99,100,101,102

Introduction.

In 1966, the Monsanto Company initiated the development of a rhodium-catalysed process for the carbonylation of methanol to acetic acid. This process was named the Monsanto process and was commercialised in 1970. Over the years the Monsanto process was the dominant industrial process used in the production of millions of tons of acetic acid. Therefore this process has been studied in detail - both experimentally^{90,92,93,100,101,102} and theoretically.^{91,94,95,96,97,98,99} The typical commercial operating conditions for the Monsanto process are a 30-60 atm pressure and a 150-200°C temperature. These are much milder conditions than the cobalt-catalysed process (600 atm, 230°C) which used to be used in the production of acetic acid (commercialised in 1960 by BASF).¹⁰³

Maitlis *et al.*⁹⁰ have shown that the Monsanto process can be analyzed as a cyclic series of separate reactions, as illustrated in Figure 2.37. Analyzing the process in this way gives one

⁹⁰ P.M. Maitlis, A. Haynes, G.J. Sunley, M.J. Howard, *J. Chem. Soc., Dalton Trans.* **1996** 2187-2196.

⁹¹ T.R. Griffin, D.B. Cook, A. Haynes, J.M. Pearson, D. Monti, G.E. Morris, *J. Am. Chem. Soc.* **1996** (118) 3029-3030.

⁹² A. Haynes, B.E. Mann, G.E. Morris, P.M. Maitlis, *J. Am. Chem. Soc.* **1993** (115) 4093-4100.

⁹³ A. Haynes, B.E. Mann, D.J. Gulliver, G.E. Morris, P.M. Maitlis, *J. Am. Chem. Soc.* **1991** (113) 8567-8569.

⁹⁴ M. Feliz, Z. Freixa, P.W.N.M. van Leeuwen, C. Bo, *Organometallics* **2005** (24) 5718-5723.

⁹⁵ E.A. Ivanova, V.A. Nasluzov, A.I. Rubaylo, N. Rösch, *Chemistry for Sustainable Development* **2003** (11) 101-107.

⁹⁶ E.A. Ivanova, P. Gisdakis, V.A. Nasluzov, A.I. Rubailo, N. Rösch, *Organometallics* **2001** (20) 1161-1174.

⁹⁷ T. Kinnunen, K. Laasonen, *J. Mol. Struct. (Theochem)* **2001** (542) 273-288.

⁹⁸ M. Cheong, T. Ziegler, *Organometallics* **2005** (24) 3053-3058.

⁹⁹ M. Cheong, R. Schmid, T. Ziegler, *Organometallics* **2000** (19) 1973-1982.

¹⁰⁰ D. Forster, *J. Am. Chem. Soc.* **1976** (98) 846-848.

¹⁰¹ C.E. Hickey, P.M. Maitlis, *J. Chem. Soc., Chem. Commun.* **1984** 1609-1611.

¹⁰² D. Forster, *Adv. Organomet. Chem.* **1979** (17) 255-267.

¹⁰³ R.T. Eby, T.C. Singleton, In: B.E. Leach (Editor), *Applied Industrial Catalysis*, Academic Press, New York, **1983**, Vol. 1, p275-296.

useful information about each step in the cycle. The catalytic cycle (Figure 2.37) of the Monsanto process is made up of six separate reactions steps. The first step (reaction of methanol with HI to give CH_3I) and the last step (the reaction of CH_3COI with water to give acetic acid and regenerate HI) are purely organic. The anion $[\text{Rh}(\text{CO})_2\text{I}_2]^-$ (**a**) was found to be the initial catalytically active species. The interaction of (**a**) with the substrate CH_3I results in the formation of the six-coordinated alkyl complex $[\text{Rh}(\text{CO})_2\text{I}_2\text{CH}_3\text{I}]^-$ (**b**). The alkyl complex is kinetically unstable and the methyl group migrates to the carbonyl group, which results in the formation of the five-coordinated acyl complex $[\text{Rh}(\text{CO})(\text{COCH}_3)\text{I}_3]^-$ (**c**). This acyl complex is then carbonylated to form the six-coordinated $[\text{Rh}(\text{CO})_2(\text{COCH}_3)\text{I}_3]^-$ (**d**), that reductively eliminates CH_3COI and regenerates $[\text{Rh}(\text{CO})_2\text{I}_2]$ (**a**), which starts the whole cycle all over again.

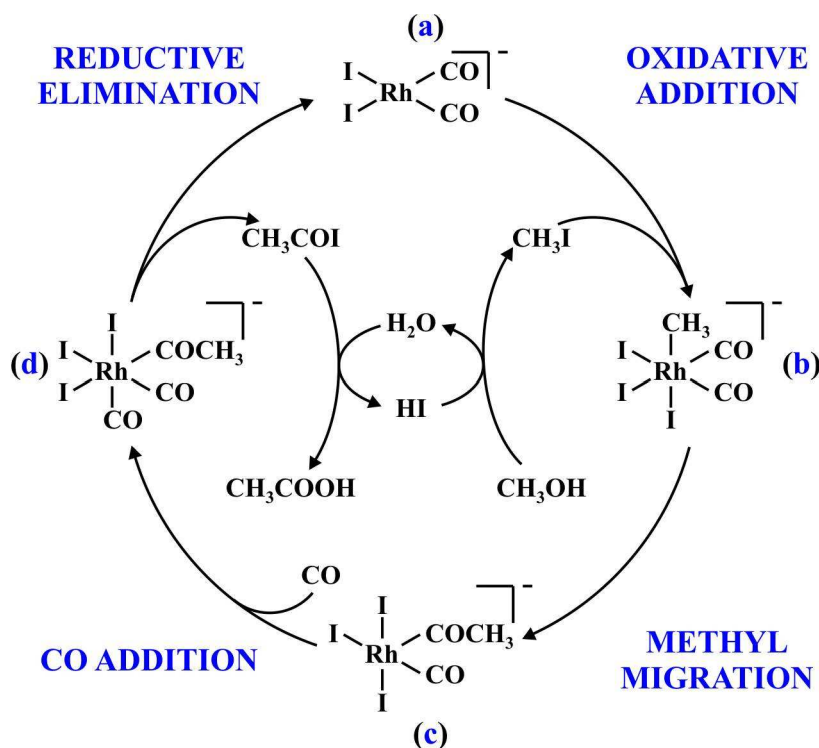


Figure 2.37: The Monsanto process: the catalytic cycle of the carbonylation of methanol to acetic acid.

Detailed kinetic studies have been performed, using spectrophotometric (IR)^{90,92,93,100} and spectroscopic (¹³C NMR)^{90,92,93} techniques. The reaction rate is first order in both [(**a**)] and [CH_3I] and is independent of CO pressure. Initially, (**b**) was not detected. This intermediate was first detected by Haynes *et al.*^{92,93} in neat CH_3I solvent using FTIR and FTNMR techniques. The efficiency of the Monsanto process is largely due to the rapid conversion of (**b**) into (**c**), leading to a low standing concentration of (**b**) and minimizing side reactions such as methane formation.

Computational studies of the kinetics and conformers have also been performed. The main programmes used were Gaussian^{91,95,96,97} and ADF.^{94,98,99} Functionals like BPE,⁹⁴ BP86,^{94,95,96,98,99} and B3LYP^{94,97} were used along with various basis sets. Calculations were performed in gas phase,^{95,96,97,99} as well as in solution (methanol,^{94,98} DCM^{94,95,96} and CH₃I⁹⁹). Although the results differ between methods (especially the effect of the different solvents on the kinetic data), the general findings and conclusions were the same.

During the Monsanto process, different isomers of each complex in the reaction cycle are possible. The isomers have been investigated both experimentally (IR, ¹³C NMR and crystal structure determination) and computationally. All the possible isomers of (a) - (d) are given in Figure 2.38.

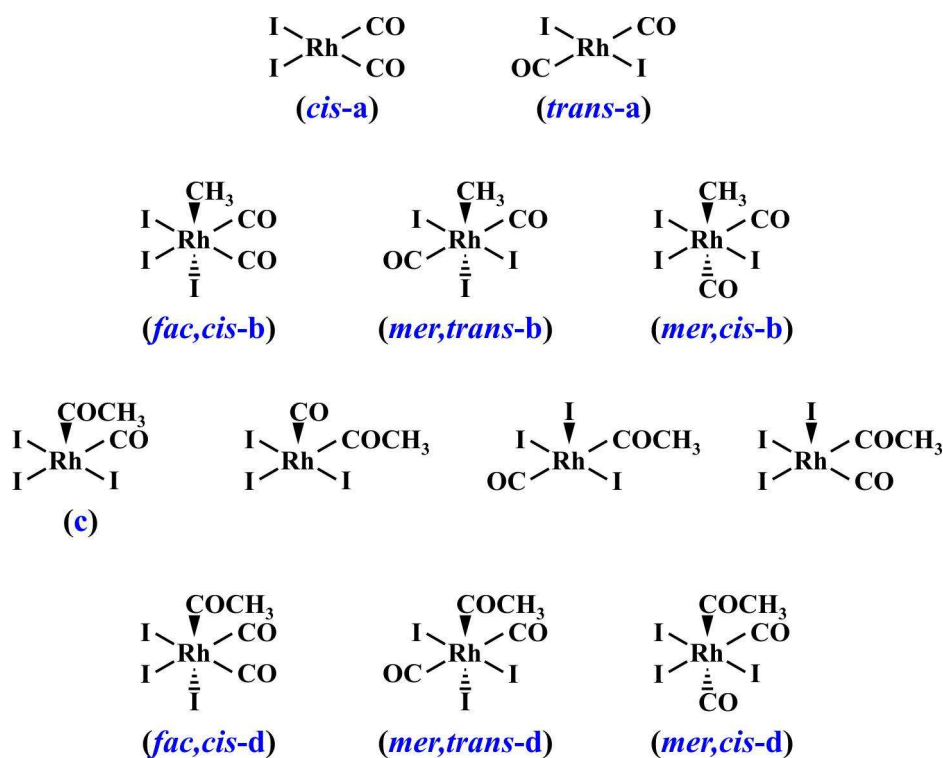
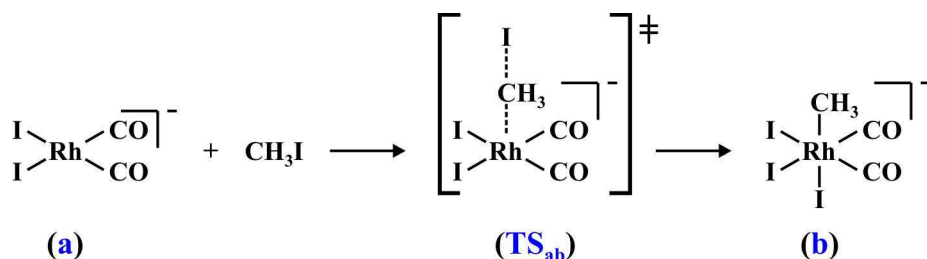


Figure 2.38: Various isomers possible for complexes (a) - (d) in the Monsanto process.

Oxidative addition.



The first reaction in the catalytic cycle is the oxidative addition of CH_3I to the active catalyst **(a)**. This is the rate-determining step in the cycle and obeys second-order kinetics (first order in **[(a)]** and $[\text{CH}_3\text{I}]$). Experimental studies^{90,100,101} indicate that the oxidative addition occurs through a two-step $\text{S}_{\text{N}}2$ mechanism, which is consistent with various computational studies.^{91,94,95,96,97,98} The first step of the $\text{S}_{\text{N}}2$ mechanism is the nucleophilic substitution of iodide by the metal complex (TS_{ab}), presumed to proceed with inversion of configuration at the carbon of the methyl group. The second step is the subsequent coordination of iodide, which completes the addition to give a six-coordinated alkyl **(b)** complex. In this CH_3I addition, the oxidation state of the metal centre changes from I to III.

For the initial complex **(a)**, two isomers are possible: *cis* and *trans* (Figure 2.38). Various computational studies^{95,96,98,99} indicate that the *cis*-**(a)** isomer is more stable than the corresponding *trans*-**(a)** isomer by 34-38 $\text{kJ}\cdot\text{mol}^{-1}$. This is in agreement with IR and ^{13}C NMR experimental data^{93,102} in which the initial catalytically active complex has been characterized as the *cis*-**(a)** isomer.

Three types of transition states between **(a)** and **(b)** were considered computationally: two resulting from *trans* addition ("linear/back" and "bent") and one resulting from *cis* addition ("front").^{94,95,96} The linear/back transition state structure corresponds to an $\text{S}_{\text{N}}2$ mechanism, characterized by a linear $\text{Rh}-\text{C}_{\text{methyl}}-\text{I}$ arrangement and by an $\text{I}-\text{C}_{\text{methyl}}-\text{H}$ angle close to 90° . The methyl hydrogen atoms are located in the equatorial plane of the five-coordinated carbon atom, resulting in a trigonal bipyramidal arrangement. The bent and front transition state structures correspond to a side-on approach of the $\text{C}_{\text{methyl}}-\text{I}$ bond to the rhodium atom. The bent transition state structure leads to the same product as the linear/back transition state structure - a neutral five-coordinated rhodium complex and a free iodide ion. Both the mechanisms of the linear/back and the bent transition state structures are therefore described as $\text{S}_{\text{N}}2$ processes. The front transition state structure corresponds to a concerted three-centred oxidative addition mechanism,

in which the Rh-I and Rh-C_{methyl} bonds form simultaneously as I-C_{methyl} bond breaks, resulting in the *cis* addition of the methyl iodide. The linear/back addition of CH₃I to *cis*-(**a**) was preferred 125-128 kJ.mol⁻¹ above the bent and front additions of CH₃I to the same isomer.⁹⁴ This clearly discards the possibility of the bent and front mechanisms and suggests that the linear/back mechanism is the only possible transition state (TS_{ab}) for the oxidative addition of CH₃I to the Monsanto catalyst. The calculated⁹⁷ ΔG (Gibbs free energy) values for the reaction *cis*-(**a**) → (TS_{ab}) are in agreement with the experimental^{90,92,101} values.

As for the intermediate (**b**), three isomers are possible: *fac,cis*, *mer,trans* and *mer,cis* (Figure 2.38). Computational studies^{96,97,99} could not point out the most stable isomer with a clear cut of energy. Selected calculated relative energies of the three possible isomers of (**b**) are given in Table 2.4.

Table 2.4: The calculated relative energy (kJ.mol⁻¹) of the three possible isomers of (**b**) in the Monsanto cycle.

	reference [96] ⁱ	reference [97] ⁱⁱ	reference [99] ⁱⁱⁱ
<i>fac,cis</i>	9 (6)	16 (15)	0 (0)
<i>mer,trans</i>	0 (0)	0 (0)	1 (2)
<i>mer,cis</i>	11 (8)	17 (18)	4 (5)

ⁱ Solvent DCM, standard basis set. Parenthesis: Solvent DCM, extended basis set.

ⁱⁱ Gas phase, including ZPE corrections. Parenthesis: Gas phase, excluding ZPE corrections.

ⁱⁱⁱ Gas phase. Parenthesis: Solvent CH₃I.

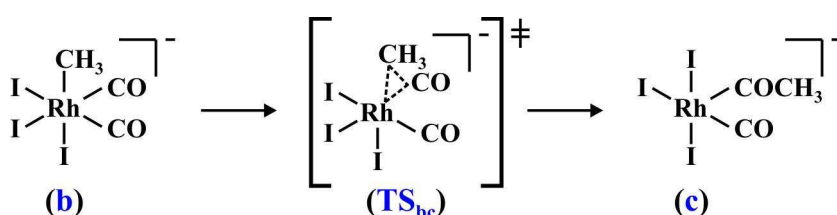
From the above table it can be seen that all the isomers of (**b**) exhibit relatively similar energies (within 18 kJ.mol⁻¹). According to references [96] and [97], the *mer,trans*-(**b**) isomer is found to be the most stable, while reference [99] indicates that the *fac,cis*-(**b**) and *mer,trans*-(**b**) isomers are practically equi-energetic. All results agree that the *mer,cis*-(**b**) isomer is the least stable. The higher relative energy of the *fac,cis*-(**b**) isomer *versus* the *mer,trans*-(**b**) isomer (as found by references [96] and [97]) can be explained by the molecular orbitals at the reaction site. The main interaction in the σ-type bonding in the Rh-C_{methyl} bond is due the interaction between the metal *d*_{z2}-orbital and the C_{methyl}-I σ-orbital. In (**a**), the *d*_{z2}-orbital is orthogonal to the plane formed by the ligands. For the *mer,trans*-(**b**) isomer, the CH₃ group is located linearly on top of the metal and the orbitals have a good overlap. For the *fac,cis*-(**b**) isomer however, the CH₃ group is not located linearly on top of the metal. The CH₃ group and the axial-iodide tilt respectively towards the planar-iodides and the carbonyl groups. This is due to the repulsion of the axial-iodide by the planar-iodides and results in the elongation of the Rh-I_{axial} bond in the

fac,cis-(b) isomer. This weakens the Rh-I_{axial} bond and destabilizes the *fac,cis*-(b) isomer, as demonstrated by the relative energies.

The *fac,cis*-(b) and *mer,trans*-(b) isomers are the oxidative addition products of *trans* addition of CH₃I to *cis*-(a) and *trans*-(a) respectively. Though, the higher energy of *trans*-(a) prevents the reaction of *trans*-(a) → *mer,trans*-(b) from occurring. Thus, the formation of *fac,cis*-(b) after the addition of CH₃I to *cis*-(a) is preferred. Since the (b) isomers exhibit relatively similar energies (within 18 kJ.mol⁻¹), it is proposed that intermediate (b) possesses the geometry of *fac,cis*-(b).

An experimental study⁹⁰ revealed that according to IR data a *cis*-dicarbonyl rhodium species was present (two carbonyl bands with similar intensities), while the ¹³C NMR data showed that the two carbonyl ligands were equivalent (one doublet in the rhodium carbonyl region). Therefore, taking both the IR and the ¹³C NMR results into account, the *fac,cis*-(b) isomer is intermediate (b). This is in agreement with that which was proposed by the theoretical study.

Methyl migration.



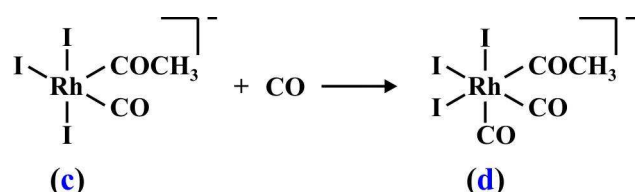
The second reaction in the Monsanto process is the 1,1-insertion that goes *via* an intramolecular methyl migration to the carbonyl ligand (TS_{bc}). The six-coordinated alkyl (b) complex automatically converts into a five-coordinated acyl (c) complex. There are four isomers of complex (c) possible with different groups in the apical position: one with COCH₃, one with CO and two with iodide (Figure 2.38). The acyl (c) complex with the COCH₃ group in the apical position was found to be 37-81 kJ.mol⁻¹ lower in energy than the other three isomers.⁹⁹ All computational results^{95,96,97,99} are in agreement that this isomer is the most stable isomer for complex (c). This is also the only complex in the Monsanto process of which a crystal structure was obtained. The COCH₃ group of the crystal structure is also in the apical position.^{104,105}

¹⁰⁴ G.W. Adams, J.J. Daly, D. Forster, *J. Organomet. Chem.* **1974** (71) C17-C19.

¹⁰⁵ H. Adams, N.A. Bailey, B.E. Mann, C.P. Manuel, C.M. Spencer, A.G. Kent, *J. Chem. Soc., Dalton Trans.* **1988** 489-496.

The transition states between **(b)** and **(c)** were considered computationally and the activation parameters were calculated. The 1,1-insertion in *fac,cis*-**(b)** was preferred. The calculated^{95,96,97,99} ΔG (Gibbs free energy) values for the reaction *fac,cis*-**(b)** \rightarrow (**TS**_{bc}) are in agreement with the experimental⁹² values.

Carbonyl addition.



Upon heating, complex **(c)** regenerates complex **(a)**,⁹⁰ therefore indicating the reversibility of both the oxidative addition and the methyl migration processes. The decomposition of complex **(c)** produces CH_3I instead of CH_3COI , therefore it is important to trap complex **(c)** by the addition of CO .

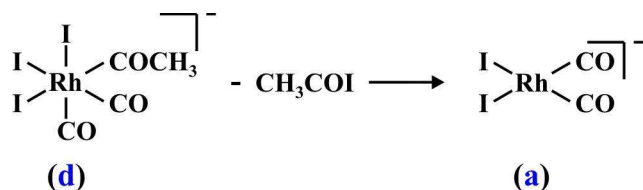
The intake of CO by complex **(c)** results in the six-coordinated octahedral **(d)** complex. Three isomers for complex **(d)** are possible: *fac,cis*, *mer,trans* and *mer,cis* (Figure 2.38). As for complex **(b)**, the *mer,cis*-**(d)** isomer was found^{95,96} to be the least stable (Table 2.5). The *mer,trans*-**(d)** and *fac,cis*-**(d)** isomers were found to be almost equi-energetic, with the *fac,cis*-**(d)** isomer 5-7 $\text{kJ}\cdot\text{mol}^{-1}$ more than the *mer,trans*-**(d)** isomer. The slight preference in energy of the *mer,trans*-**(d)** isomer above the *fac,cis*-**(d)** isomer can be explained by the more favourable orientation of the sterically asymmetric CH_3CO ligand.⁹⁶ To distinguish between the isomers *mer,trans*-**(d)** and *fac,cis*-**(d)** as the preferred structure of complex **(d)**, one has to look at the next step, **(d)** \rightarrow **(a)**.

Table 2.5: The relative energy ($\text{kJ}\cdot\text{mol}^{-1}$) of the three possible isomers of **(d)**.

	reference [96] ⁱ
<i>fac,cis</i>	7 (5)
<i>mer,trans</i>	0 (0)
<i>mer,cis</i>	26 (25)

ⁱ Solvent DCM, standard basis set. Parenthesis: Solvent DCM, extended basis set.

Reductive elimination.



This final organometallic step in the catalytic cycle has received less attention. The last elementary step of the catalytic cycle is the reductive elimination of CH_3COI from the octahedral complex (d). Different routes of (d) \rightarrow (a) have been considered computationally and the route of *fac,cis*-(d) \rightarrow *cis*-(a) was found to be the preferable route.⁹⁵ Therefore it is suggested that isomer (d) possesses the structure of *fac,cis*-(d).

Free energy profile.

The free energy profile of the mechanism of the reaction $[\text{Rh}(\text{CO})_2\text{I}_2]^- + \text{CH}_3\text{I}$ (the Monsanto process) is given in Table 2.6. From these data it is evident that the (a) \rightarrow (TS_{ab}) oxidative addition step has the highest free energy barrier (calculated 135-189 $\text{kJ}\cdot\text{mol}^{-1}$, experimental 100 $\text{kJ}\cdot\text{mol}^{-1}$) and is therefore the rate-determining step of the overall reaction. The barriers for the (b) \rightarrow (TS_{bc}) migratory insertion and the (d) \rightarrow (TS_{da}) reductive elimination steps are much more modest (calculated 45-77 $\text{kJ}\cdot\text{mol}^{-1}$ and 75 $\text{kJ}\cdot\text{mol}^{-1}$, respectively). The calculated and experimental free energies are in the same range.

Table 2.6: The Gibbs free energy ($\text{kJ}\cdot\text{mol}^{-1}$) of the reaction $[\text{Rh}(\text{CO})_2\text{I}_2]^- + \text{CH}_3\text{I}$. Complexes are labelled according to Figure 2.37, with TS = transition state.

	reference [90] ⁱ	reference [95] ⁱⁱ	reference [96] ⁱⁱⁱ	reference [99] ^{iv}
(a)	0	0 (0)	0	-
(TS _{ab})	100	135 (189)	135	-
(b)	14	42 (24)	42	0
(TS _{bc})	95	89 (69)	116	72 (77)
(c)	-6	11 (-6)	11	-
(d)	-	2 (-21)	2	-
(TS _{da})	-	77 (54)	77	-

ⁱ Experimental at 35 °C in CH_2Cl_2 - CH_3I .

ⁱⁱ Solvent DCM. Parenthesis: Gas phase.

ⁱⁱⁱ Solvent DCM, extended basis set.

^{iv} Solvent CH_3I . Parenthesis: Gas phase.

2.4.3 [Rh(β -diketonato)(CO)(PPh₃)] + CH₃I.

62,106,107,108,109,110,111,112,113,114

Introduction.

Rhodium complex compounds are one of the most widely spread industrial homogeneous catalysts for organic raw material processing. The most classic example is the Monsanto process, where methanol is converted into acetic acid with the aid of a rhodium catalyst (section 2.4.2). The oxidative addition of methyl iodide to rhodium(I) carbonyl compounds has significant implications in catalysis, especially when followed by methyl migration to give the acyl derivatives. The high catalytic reactivity of rhodium complexes is in many respects due to the nature of the ligands attached to the rhodium. Therefore, in order to achieve a better understanding of the ways of purposeful alteration of the reactivity of such systems, in detail studies of the reaction mechanism are of great importance.

The Monsanto process has been studied in detail, both experimentally and theoretically. In contrast, the same reaction promoted from [Rh(L,L'-BID)(CO)(PPh₃)] complexes (where L,L'-BID is a monoanionic bidentate ligand with donor atoms L and L' or β -diketonato ligands, Figure 2.39) has mostly been studied experimentally (Table 2.7 and Table 2.8). On the basis of extensive kinetic studies of these reactions, reaction schemes have been proposed for the oxidative addition of methyl iodide to [Rh(L,L'-BID)(CO)(PPh₃)] complexes. These schemes are summarized in Figure 2.40.

¹⁰⁶ J. Conradie, J.C. Swarts, *Organometallics* **2009** (28) 1018-1026.

¹⁰⁷ M.M. Conradie, J. Conradie, *S. Afr. J. Chem.* **2008** (61) 102-111.

¹⁰⁸ N.F. Stuurman, J. Conradie, *J. Organomet. Chem.* **2009** (694) 259-268.

¹⁰⁹ M.M. Conradie, J. Conradie, *Inorg. Chim. Acta* **2009** (362) 519-530.

¹¹⁰ M.M. Conradie, J. Conradie, *Inorg. Chim. Acta* **2008** (361) 208-218.

¹¹¹ M.M. Conradie, J. Conradie, *Inorg. Chim. Acta* **2008** (361) 2285-2295.

¹¹² J. Conradie, G.J. Lamprecht, A. Roodt, J.C. Swarts, *Polyhedron* **2007** (26) 5075-5087.

¹¹³ S.S. Basson, J.G. Leipoldt, A. Roodt, J.A. Venter, T.J. van der Walt, *Inorg. Chim. Acta* **1986** (119) 35-38.

¹¹⁴ S.S. Basson, J.G. Leipoldt, J.T. Nel, *Inorg. Chim. Acta* **1984** (84) 167-172.

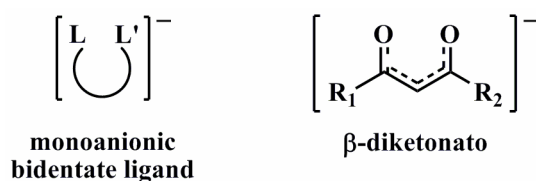


Figure 2.39: The L,L'-BID ligand is a monoanionic bidentate ligand with donor atoms L and L'. They are easily complexed to metals like rhodium. An example of an L,L'-BID ligand is a β -diketone ($\text{R}_1\text{COCH}_2\text{COR}_2$) with donor atoms O and O. When β -diketones are complexed to a metal like rhodium, they are deprotonated ($\text{R}_1\text{COCHCOR}_2$)⁻ and noted as β -diketonato. Complexes like these are used in this study.

[Rh^I(L,L'-BID)(CO)(PPh₃)] isomers + CH₃I

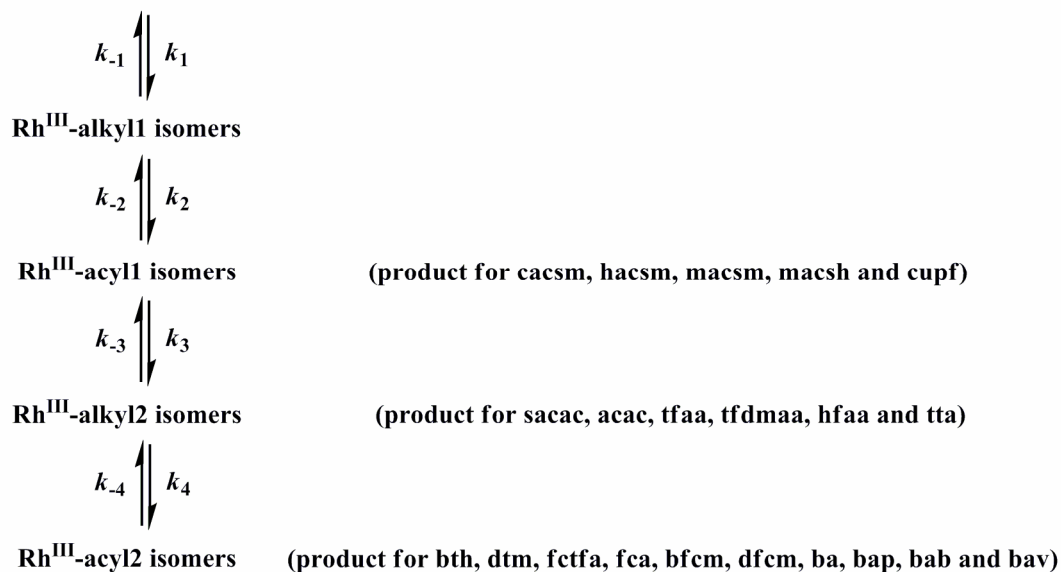


Figure 2.40: The general reaction scheme for the oxidative addition of methyl iodide to $[\text{Rh}(\text{L,L}'\text{-BID})(\text{CO})(\text{PPh}_3)]$ complexes (L,L'-BID is a monoanionic bidentate ligand with donor atoms L and L' or β -diketonato ligands, as defined in Table 2.7 and Table 2.8).

The notations "Rh^{III}-alkyl1" and "Rh^{III}-acyl1" in the above figure refer respectively to the first alkylated $[\text{Rh}^{\text{III}}(\text{L,L}'\text{-BID})(\text{CH}_3)(\text{CO})(\text{PPh}_3)(\text{I})]$ and acylated $[\text{Rh}^{\text{III}}(\text{L,L}'\text{-BID})(\text{COCH}_3)(\text{PPh}_3)(\text{I})]$ complexes that are formed. When the last number in the notations change to "2", such as in "Rh^{III}-alkyl2" and "Rh^{III}-acyl2", it shows that after the first alkylated or acylated species had formed, it converted to a second, different but more stable, alkylated or acylated structural isomer. Examples of kinetic and structural studies done on $[\text{Rh}(\text{L,L}'\text{-BID})(\text{CO})(\text{PPh}_3)]$ complexes are summarized in Table 2.7 and Table 2.8.

CHAPTER 2

Table 2.7: Summary of the kinetic and crystal structures of selected [Rh(L,L'-BID)(CO)(PPh₃)] complexes. Atom assignment is as in Figure 2.39.

L,L'-BID		L	L'	Rh kinetic study	Rh crystal structure	
					Rh(I)	Rh(III)
Hcasm	methyl(2-cyclohexylamino-1-cyclopentene-1-dithiocarboxylate)	N	S	[65]	[65]	-
Hhacsm	methyl(2-amino-1-cyclopentene-1-dithiocarboxylate)	N	S	[65]	[115]	-
Hmacsm	methyl(2-methylamino-1-cyclopentene-1-dithiocarboxylate)	N	S	[65]	[116]	-
Hmacsh	2-methylamino-1-cyclopentene-1-dithiocarboxylate	N	S	[65]	-	-
Hstsc	salicylaldehydethiosemicarbazose	N	S	[65]	[65]	[65]
Hcupf	cupferron	O	O	[117]	-	[117]
Hdmavk	dimethylaminovinylketone	O	N	-	[118]	[118][119]
Hsacac	thioacetylacetone	O	S	[120] [121]	[122]	-
Hmnt	maleonitriledithiolate	S	S	-	-	[123]
Na[S ₂ PPh ₂]	Na[S ₂ PPh ₂]	S	S	-	-	[124]

Table 2.8: Summary of the kinetic and crystal structures of selected [Rh(β -diketonato)(CO)(PPh₃)] complexes. Atom assignment is as in Figure 2.39.

β -diketonone ⁱ R ₁ COCH ₂ COR ₂		R ₁	R ₂	L	L'	Rh kinetic study	Rh crystal structure	
							Rh(I)	Rh(III)
Hacac	acetylacetone	CH ₃	CH ₃	O	O	[62] [113] [114]	[125]	-
Htfaa	trifluoroacetylacetone	CF ₃	CH ₃	O	O	[114]	-	-
Htfdmaa	trifluorodimethylacetylacetone	CH(CH ₃) ₂	CF ₃	O	O	[114]	[126]	-
Hptf	pivaloyltrifluoroacetone	C(CH ₃) ₃	CF ₃	O	O	-	[127]	-
Hhfaa	hexafluoroacetylacetone	CF ₃	CF ₃	O	O	[114]	-	-
Htfhd	trifluorohexanedione	CH ₂ CH ₃	CF ₃	O	O	-	[128]	-
Hdbm	dibenzoylmethane	Ph	Ph	O	O	-	[129]	-
Htta	thenoyltrifluoroacetone	CF ₃	C ₄ H ₃ S	O	O	[110]	[130]	-
Hbth	benzoylthenoylacetylacetone	Ph	C ₄ H ₃ S	O	O	[111]	-	-
Hdtm	dithenoylmethane	C ₄ H ₃ S	C ₄ H ₃ S	O	O	[111]	-	-
Hfctfa	ferrocenoyltrifluoroacetone	Fc	CF ₃	O	O	[112] [106]	[131]	[112]
Hfca	ferrocenoylacetylacetone	Fc	CH ₃	O	O	[106]	-	-
Hbfc	benzoylferrocenoylmethane	Fc	Ph	O	O	[106]	-	-
Hdfcm	diferrocenoylmethane	Fc	Fc	O	O	[106]	-	-
Hba	benzoylacetylacetone	CH ₃	Ph	O	O	[108]	[132]	-
Hbap	propanylacetylacetone	CH ₂ CH ₃	Ph	O	O	[108]	-	-
Hbab	buterylacetylacetone	(CH ₂) ₂ CH ₃	Ph	O	O	[108]	-	-
Hbav	valerylacetylacetone	(CH ₂) ₃ CH ₃	Ph	O	O	[108]	-	-

ⁱ β -diketonone is a type of L,L'-BID ligand, with L,L' = O,O.

¹¹⁵ G.J.J. Steyn, A. Roodt, I. Poletaeva, Y.S. Varshavsky, *J. Organomet. Chem.* **1997** (536/7) 197-205.

¹¹⁶ G.J.J. Steyn, A. Roodt, J.G. Leipoldt, *Inorg. Chem.* **1992** (31) 3477-3481.

¹¹⁷ S.S. Basson, J.G. Leipoldt, A. Roodt, J.A. Venter, *Inorg. Chim. Acta* **1987** (128) 31-37.

¹¹⁸ L.J. Damoense, W. Purcell, A. Roodt, J.G. Leipoldt, *Rhodium Ex.* **1994** (5) 10-13.

¹¹⁹ L.J. Damoense, W. Purcell, A. Roodt, *Rhodium Ex.* **1995** (14) 4-9.

¹²⁰ J.G. Leipoldt, S.S. Basson, L.J. Botha, *Inorg. Chim. Acta* **1990** (168) 215-220.

¹²¹ J.A. Venter, J.G. Leipoldt, R. van Eldik, *Inorg. Chem.* **1991** (30) 2207-2209.

¹²² L.J. Botha, S.S. Basson, J.G. Leipoldt, *Inorg. Chim. Acta* **1987** (126) 25-28.

¹²³ C.H. Cheng, B.D. Spivack, R. Eisenberg, *J. Am. Chem. Soc.* **1977** (99) 3003-3011.

¹²⁴ J.A. Cabeza, V. Riera, M.A. Villa-Garcia, L. Ouahab, S. Triki, *J. Organomet. Chem.* **1992** (441) 323-331.

¹²⁵ J.G. Leipoldt, S.S. Basson, L.D.C. Bok, T.I.A. Gerber, *Inorg. Chim. Acta* **1987** (26) L35-L37.

¹²⁶ J.G. Leipoldt, S.S. Basson, J.T. Nel, *Inorg. Chim. Acta* **1983** (74) 85-88.

Stereochemistry of the reaction.

The proposed reaction scheme, with specific stereochemistry, for the oxidative addition of methyl iodide to $[\text{Rh}(\beta\text{-diketonato})(\text{CO})(\text{PPh}_3)]$ complexes is given in Figure 2.41. The stereochemistry of the rhodium(I) and rhodium(III) complexes stems from information obtained from single crystal X-ray crystallography, NMR and DFT computational studies on related complexes that generally react in the same way as the monocarbonylphosphine rhodium complexes. The research that concluded the stereochemistry of each rhodium complex is explained below.

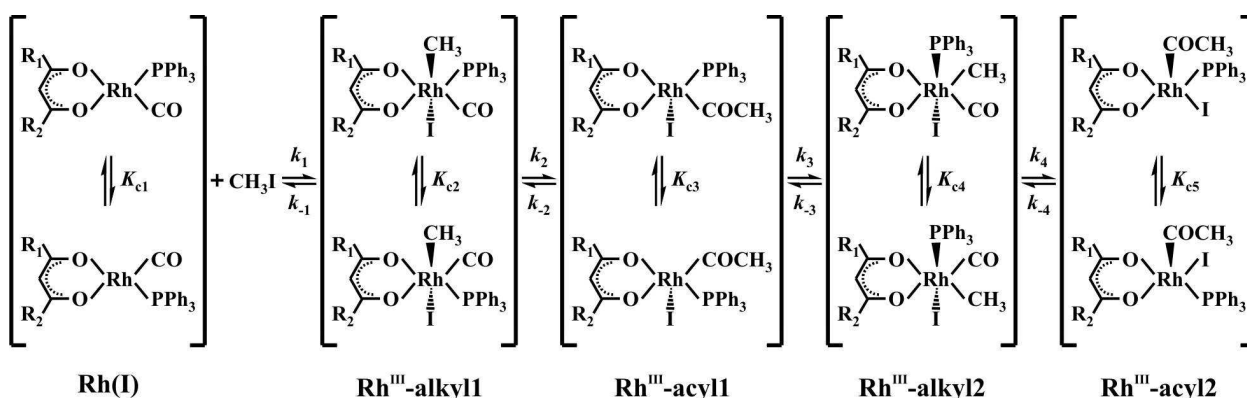


Figure 2.41: The proposed reaction scheme for the oxidative addition of methyl iodide to $[\text{Rh}(\beta\text{-diketonato})(\text{CO})(\text{PPh}_3)]$ complexes and the following carbonyl insertion reactions, showing specific stereochemistry.

For the $[\text{Rh}(\text{L,L}'\text{-BID})(\text{CO})(\text{PPh}_3)]$ complexes (where L,L'-BID = N,S-BID = cacs,macs,macsm and macsh) both the *cis* and *trans* addition of methyl iodide is proposed, with the acyl (containing the COCH_3 group in the apical position) as the final product.⁶⁵

¹²⁷ J.G. Leipoldt, S.S. Basson, J.H. Potgieter, *Inorg. Chim. Acta* **1986** (117) L3-L5.

¹²⁸ E.C. Steynberg, G.J. Lamprecht, J.G. Leipoldt, *Inorg. Chim. Acta* **1987** (133) 33-37.

¹²⁹ D. Lamprecht, G.J. Lamprecht, J.M. Botha, K. Umakoshi, Y. Sasaki, *Acta Crystallogr., Sect. C: Cryst. Struct. Commun.* **1997** (53) 1403-1405.

¹³⁰ J.G. Leipoldt, L.D.C. Bok, J.S. van Vollenhoven, A.I. Pieterse, *J. Inorg. Nucl. Chem.* **1978** (40) 61-63.

¹³¹ G.J. Lamprecht, J.C. Swarts, J. Conradie, J.G. Leipoldt, *Acta Crystallogr., Sect. C: Cryst. Struct. Commun.* **1993** (49) 82-84.

- **Rhodium(I) isomers.**

The rhodium(I) isomers have a square planar arrangement, formed by the β -diketonato ligand and the CO and PPh₃ groups. The geometry of the rhodium(I) isomers was solved by single crystal X-ray crystallographic structures of [Rh(β -diketonato)(CO)(PPh₃)] complexes (Table 2.8). All these crystals contained one independent molecule in the asymmetric unit, except for β -diketonato dbm and ba which had two molecules in the asymmetric unit. For the asymmetric β -diketonato ligands, two isomers were characterized on the NMR^{62,106,108,110,111,112} The DFT calculations^{107,109} are in agreement with the experimental results.

- **Rh^{III}-alkyl1 isomers.**

The Rh^{III}-alkyl1 isomers have an octahedral arrangement, with the CO and PPh₃ groups in the plane of the β -diketonato ligand and the I and CH₃ group in the apical position. This proposed geometry of the Rh^{III}-alkyl1 isomers is in agreement with the geometries of [Rh(β -diketonato)(CH₃)(CO)(PPh₃)(I)]-alkyl1 (where β -diketonato = tta, bth and dtm) which were obtained by solution-NMR techniques and DFT calculations.^{109,111} The Rh^{III}-alkyl1 isomers result from *trans* addition of CH₃I to rhodium(I), *i.e.* with the CH₃ group and the iodide above and below the square planar plane of the rhodium(I) reactant. The *trans* addition of CH₃I was also preferred by the Monsanto catalyst (section 2.4.2).

- **Rh^{III}-acyl1 isomers.**

It is proposed that the Rh^{III}-acyl1 isomers have a square pyramidal arrangement, with the COCH₃ and PPh₃ groups in the plane of the β -diketonato ligand and the I in the apical position. This would be the geometry after methyl migration from Rh^{III}-alkyl1. Only a possible geometry of the Rh^{III}-acyl1 isomers can be proposed, since no corresponding structure or geometry for any related β -diketonato complex has to date been determined by any technique.

- **Rh^{III}-alkyl2 isomers.**

The Rh^{III}-alkyl2 isomers have an octahedral arrangement, with the CO and CH₃ groups in the plane of the β -diketonato ligand and the I and PPh group in the apical position. The structure of one of the Rh^{III}-alkyl2 isomers of [Rh(fctfa)(CH₃)(CO)(PPh₃)(I)]-alkyl2 was crystallographically characterized.¹¹² The spectroscopic and spectrophotometric properties of [Rh(fctfa)(CH₃)(CO)(PPh₃)(I)]-alkyl2 and [Rh(β -diketonato)(CH₃)(CO)(PPh₃)(I)]-alkyl2 (where

¹³² W. Purcell, S.S. Basson, J.G. Leipoldt, A. Roodt, H. Preston, *Inorg. Chim. Acta* **1995** (234) 153-156.

β -diketonato = bap, bab and bav) are in agreement with each other. This geometry is also in agreement with solution-NMR techniques and DFT calculations on $[\text{Rh}(\beta\text{-diketonato})(\text{CH}_3)(\text{CO})(\text{PPh}_3)(\text{I})\text{-alkyl}]_2$ (where β -diketonato = tta, bth and dtm).^{109,110,111}

• **Rh^{III}-acyl₂ isomers.**

It is proposed by DFT calculations^{107,109} that the Rh^{III}-acyl₂ isomers have a square pyramidal arrangement, with the I and PPh₃ group in the plane of the β -diketonato ligand and the COCH₃ group in the apical position. No $[\text{Rh}(\beta\text{-diketonato})(\text{COCH}_3)(\text{PPh}_3)(\text{I})\text{-acyl}]_2$ has crystallographically been characterized, but the crystal structures of related $[\text{Rh}(\text{L,L}'\text{-BID})(\text{COCH}_3)(\text{PPh}_3)(\text{I})\text{-acyl}]$ products (Table 2.7) are in agreement with the proposed structure where the COCH₃ group is in the apical position, indicating that this geometry is thermodynamically preferred.

2.4.4 $[\text{Rh}(\text{acac})(\text{P}(\text{OPh})_3)_2] + \text{CH}_3\text{I}$.^{133,134,135}

Introduction.

The reaction between methyl iodide and $[\text{Rh}(\text{L,L}'\text{-BID})(\text{P}(\text{OPh})_3)_2]$ is very similar to the reaction between methyl iodide and $[\text{Rh}(\text{CO})_2\text{I}_2]^-$ (Monsanto catalyst, section 2.4.2) and methyl iodide and $[\text{Rh}(\text{L,L}'\text{-BID})(\text{CO})(\text{PPh}_3)]$ complexes (section 2.4.3). In all three the cases, a neutral alkyl halide is added to a square planar rhodium(I) complex. The main difference between the reaction with $[\text{Rh}(\text{L,L}'\text{-BID})(\text{P}(\text{OPh})_3)_2]$ and the other two types of complexes is that this complex contains no carbonyl group bonded to the rhodium centre. Therefore, no methyl migration is possible after the oxidative addition of the alkyl halide. Another difference is the electronic and steric effect on the rate of the reaction of the bulky triphenylphosphite ligands. The oxidative addition reaction between CH₃I and $[\text{Rh}(\text{L,L}'\text{-BID})(\text{P}(\text{OPh})_3)_2]$ complexes (Table 2.9) has only been studied experimentally.

¹³³ G.J. van Zyl, G.J. Lamprecht, J.G. Leipoldt, T.W. Swaddle, *Inorg. Chim. Acta* **1988** (143) 223-227.

¹³⁴ J.G. Leipoldt, E.C. Steynberg, R. van Eldik, R. *Inorg. Chem.* **1987** (26) 3068-3070.

¹³⁵ G.J. van Zyl, G.J. Lamprecht, J.G. Leipoldt, *Inorg. Chim. Acta* **1987** (129) 35-37.

Table 2.9: Summary of the kinetic and crystal structures of selected $[\text{Rh}(\text{L},\text{L}'\text{-BID})(\text{P}(\text{OPh})_3)_2]$ complexes. Atom assignment is as in Figure 2.39.

L,L'-BID				L	L'	Rh kinetic study	Rh crystal structure	
							Rh(I)	Rh(III)
Hbpha	benzoylphenylhydroxylamine			O	O	[136]	-	[137]
β -diketone ⁱ $\text{R}_1\text{COCH}_2\text{COR}_2$		R ₁	R ₂	L	L'	Rh kinetic study	Rh crystal structure	
							Rh(I)	Rh(III)
Hacac	acetylacetonone	CH ₃	CH ₃	O	O	[133] [134]	[138]	-
Htfaa	trifluoroacetylacetonone	CF ₃	CH ₃	O	O	[133] [134]	[139]	[140] ⁱⁱ
Hhfaa	hexafluoroacetylacetonone	CF ₃	CF ₃	O	O	[133]	-	-
Hdbm	dibenzoylmethane	Ph	Ph	O	O	[133]	-	-
Hba	benzoylacetonone	CH ₃	Ph	O	O	[133]	-	-
Htfba	trifluorobenzoylacetonone	CF ₃	Ph	O	O	[133]	[141]	-

ⁱ β -diketone is a type of L,L'-BID ligand, with L,L' = O,O.

ⁱⁱ Rhodium(III) product of the reaction: $[\text{Rh}(\text{tfaa})(\text{P}(\text{OPh})_3)_2] + \text{I}_2$ [135].

General reaction.¹³³

On the basis of kinetic studies of this reaction, a simplified reaction scheme has been proposed for the oxidative addition of methyl iodide to $[\text{Rh}(\beta\text{-diketonato})(\text{P}(\text{OPh})_3)_2]$ complexes (Figure 2.42). Experimentally determined large negative values of the volume (ΔV^\ddagger) and the entropy (ΔS^\ddagger) of activation for the oxidative addition reaction of methyl iodide to a series of $[\text{Rh}(\beta\text{-diketonato})(\text{P}(\text{OPh})_3)_2]$ complexes indicated a mechanism which occurs *via* a polar transition state which is consistent with the $\text{S}_{\text{N}}2$ mechanism.

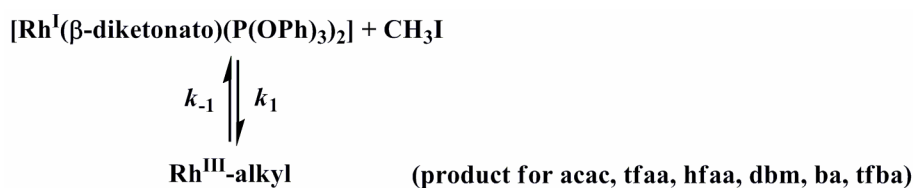


Figure 2.42: The general reaction scheme for the oxidative addition of methyl iodide to $[\text{Rh}(\beta\text{-diketonato})(\text{P}(\text{OPh})_3)_2]$ complexes (β -diketonato ligands defined in Table 2.9).

¹³⁶ G.J. Lamprecht, J.H. Beetge, *S. Afr. J. Chem.* **1987** (40) 131-133.

¹³⁷ G.J. Lamprecht, G.J. Van Zyl, J.G. Leipoldt, *Inorg. Chim. Acta* **1989** (164) 69-72.

¹³⁸ J.G. Leipoldt, G.J. Lamprecht, G.J. Van Zyl, *Inorg. Chim. Acta* **1985** (96) L31-L34.

¹³⁹ G.J. Van Zyl, G.J. Lamprecht, J.G. Leipoldt, *Inorg. Chim. Acta* **1985** (102) L1-L4.

¹⁴⁰ G.J. Van Zyl, G.J. Lamprecht, J.G. Leipoldt, *Inorg. Chim. Acta* **1986** (122) 75-79.

¹⁴¹ G.J. Lamprecht, J.G. Leipoldt, G.J. Van Zyl, *Inorg. Chim. Acta* **1985** (97) 31-35.

- **Rhodium(I).**

The rhodium(I) complex has a square planar arrangement, formed by the β -diketonato ligand and the two P(OPh)_3 groups. The geometry of rhodium(I) was solved by single crystal X-ray crystallographic structures of three $[\text{Rh}(\beta\text{-diketonato})(\text{P(OPh)}_3)_2]$ complexes (Table 2.9). All these crystals contained two molecules in the asymmetric unit, except for β -diketonato tfba which had only one molecule in the asymmetric unit. The two molecules in the asymmetric unit are enantiomers (mirror images) and have virtually the same bond distances and angles around the rhodium centre. Since the P(OPh)_3 groups bonded to the rhodium centre are chemically symmetrical, only one isomer is possible.

- **Rh^{III}-alkyl.**

On the grounds of ^1H NMR data,¹³³ the structure of the product of the oxidative addition, $[\text{Rh}(\beta\text{-diketonato})(\text{P(OPh)}_3)_2(\text{CH}_3)(\text{I})]$, is proposed to adopt an octahedral arrangement with the two P(OPh)_3 groups in the plane of the β -diketonato ligand and the I and CH_3 group in the apical position. This Rh^{III}-alkyl product results from *trans* addition of CH_3I to rhodium(I). *Trans* addition was also preferred by $[\text{Rh}(\text{CO})_2\text{I}_2]^-$ (Monsanto catalyst, section 2.4.2) and $[\text{Rh}(\beta\text{-diketonato})(\text{CO})(\text{PPh}_3)]$ complexes (section 2.4.3). No $[\text{Rh}(\beta\text{-diketonato})(\text{P(OPh)}_3)_2(\text{CH}_3)(\text{I})]$ -alkyl has crystallographically been characterized, but the crystal structures of related products, $[\text{Rh}(\text{bpha})(\text{P(OPh)}_3)_2(\text{CH}_3)(\text{I})]$ and $[\text{Rh}(\text{tfaa})(\text{P(OPh)}_3)_2(\text{I})_2]$ (Table 2.9) are in agreement with the proposed structure where the added ligands are above and below the square planar plane, also indicating that this geometry is thermodynamically preferred.

2.5 Iron complexes.

2.5.1 [Fe(β -diketonato)₃].

Introduction.¹⁴²

Metal atoms, especially transition metals, are present at the active catalytic centre in almost a third of all known enzymes. Iron and zinc are especially important and occur in relatively high concentration in the human body (5.4 and 2.4 g per 70 kg, respectively) of which most of this is involved in the enzyme function.¹⁴³ These metals are involved in a number of processes, including binding of substrates to orient them properly for subsequent reaction, mediating oxidation/reduction and electron transport reactions through reversible changes in the metal oxidation state and electrostatically stabilizing negative charges.

Tris(β -diketonato) metal(III) complexes are particularly accessible species for studying bonding, ligand coordination and Jahn-Teller distortion in organometallic systems. These 6-coordinated metal(III) complexes have approximately an octahedral arrangement. Tris(β -diketonato) iron(III) complexes are often used in iron-catalyzed cross-coupling reactions (Figure 2.43).^{144,145,146} Organometallic reagents (R'-MX) act as a nucleophile and attack the electrophilic carbon atom of an organic compound (R-X') to yield a carbon-carbon bond. The iron-catalyzed cross-coupling reactions need only a short reaction time (typically 5 to 30 min) and are performed at low temperatures (typically -20 to 0 °C). Similar nickel- or palladium-catalyzed cross-coupling reactions need much longer reaction time (typically 2 to 40 hours) and are performed at elevated temperatures (typically 40 to 90 °C).¹⁴⁷ Furthermore, [Fe(β -diketonato)₃] catalysts are 100 times

¹⁴² I. Diaz-Acosta, J. Baker, J.F. Hinton, P. Pulay, *Spectrochimica Acta Part A* **2003** (59) 363-377.

¹⁴³ H. Douglas, *Bioorganic Chemistry*, Third Edition, Springer, New York, **1996**.

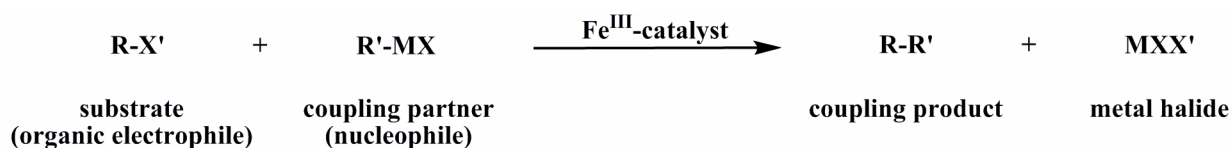
¹⁴⁴ J.K. Kochi, *J. Organomet. Chem.* **2002** (653) 11-19.

¹⁴⁵ (a) B.D. Sherry, A. Fürstner, *Acc. Chem. Res.* **2008** (41) 1500–1511. (b) A. Fürstner, A. Leitner, M. Méndez, H. Krause. *J. Am. Chem. Soc.* **2002** (124) 13856-13863. (c) B. Scheiper, M. Bonnekessel, H. Krause, A. Fürstner, *J. Org.Chem.* **2004** (69) 3943-3949.

¹⁴⁶ G. Cahiez, H. Avedissian, *Synthesis* **1998** 1199-1205.

¹⁴⁷ F. Diederich, P.J. Stang, *Metal-catalyzed Cross-coupling Reactions*, Wiley-VCH: Weinheim, Germany, **1998**.

cheaper than [Pd(β -diketonato)₂] catalysts, are environment friendly and can easily be stored for long periods under normal laboratory conditions.



R = alkyl, aryl, vinyl, allyl, alkynyl, benzyl, acyl

R' = alkyl, aryl, vinyl, allyl, alkynyl, benzyl

X, X' = I, Br, Cl

M = Mg, Zn, Cu, Sn, Si, B

Figure 2.43: General iron-catalyzed cross-coupling reaction.

Synthesis.^{148,149,150,151}

Tris(β -diketonato) iron(III) complexes are being synthesized for almost more than a century.¹⁵² In general, three methods are used to synthesize [Fe(β -diketonato)₃] complexes (Figure 2.44). The first method involves the addition of an ethanol solution of the neutralized β -diketone ligand to an aqueous solution of the iron nitrate or sulphate, buffered with sodium acetate. The product precipitates to drive the reaction to completion. The second method involves the dissolution of the β -diketone in aqueous ammonia (if the ligand is water soluble) or a mixture of aqueous ammonia and ethanol. Aqueous ammonia removes the methane proton from the β -diketone and forms the ammonium salt. The ammonium salt is then reacted with the iron nitrate or sulphate. The precipitation of the product drives the reaction to completion. In the third method, the ligand is added directly to a suspension of the iron chloride in ethanol. In this method, the reaction is driven by the evaporation of the gaseous hydrogen chloride and the addition of a base is unnecessary.

¹⁴⁸ E.W. Berg, J.T. Truemper, *J. Phys. Chem.* **1960** (64) 487-490.

¹⁴⁹ S. Misumi, M. Aihara, Y. Nonaka, *Bull. Chem. Soc. Jpn* **1970** (43) 774-778.

¹⁵⁰ M.L. Morris, R.W. Moshier, R.E. Sievers, *Inorg. Chem.* **1963** (2) 411-412.

¹⁵¹ W.O. McSharry, M. Cefola, J. White, *Inorg. Chim. Acta* **1980** (38) 161-165.

¹⁵² G.T. Morgan. H.W. Moss, *J. Chem. Soc.* **1914** (105) 189-201.

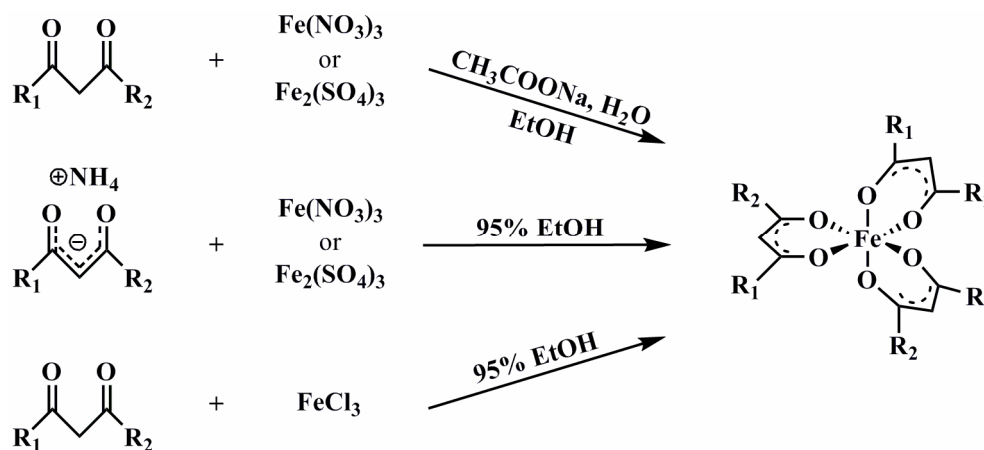


Figure 2.44: Methods commonly used to synthesize $[\text{Fe}(\beta\text{-diketonato})_3]$ complexes.

Structural properties.

The first tris(β -diketonato) iron(III) complex to be characterized by X-ray crystallography was $[\text{Fe}(\text{acac})_3]$ in 1956.¹⁵³ Since then only a few more crystal structures of $[\text{Fe}(\beta\text{-diketonato})_3]$ complexes were solved. A summary of these structures are given in Table 2.10. The $[\text{Fe}(\beta\text{-diketonato})_3]$ complexes have an octahedral arrangement of the oxygen atoms around the iron(III) centre. For unsymmetrical β -diketonato ligands of the $[\text{Fe}(\beta\text{-diketonato})_3]$ complex, two isomers are possible: a facial isomer (*fac*), where the three ligands are symmetrically arranged, and a meridional isomer (*mer*) (Figure 2.45). Although the *fac* isomer is more common in the crystal structures, the *mer* isomer was also found.^{154,155} For $[\text{Fe}(\text{tfaa})_3]$, both the *mer* isomer and the *fac* isomer crystal structures were found in separate studies.^{154,156} The Fe-O bond lengths of the structures are between 1.95-2.00 Å and the inner angles of O-Fe-O are between 85-89°. These parameters are more or less constant for the different R groups on the β -diketonato backbone.

¹⁵³ R.B. Roof Jr., *Acta Crystallogr.* **1956** (9) 781-786.

¹⁵⁴ I.A. Baidina, P.A. Stabnikov, I.K. Igumenov, S.V. Borisov, *Koord. Khim. (Russ.) (Coord. Chem.)* **1986** (12) 404-408.

¹⁵⁵ H. Soling, *Acta Chem. Scand. A* **1976** (30) 163-170.

¹⁵⁶ I.A. Baidina, P.A. Stabnikov, I.K. Igumenov, S.V. Borisov, *Koord. Khim. (Russ.) (Coord. Chem.)* **1986** (12) 258-265.

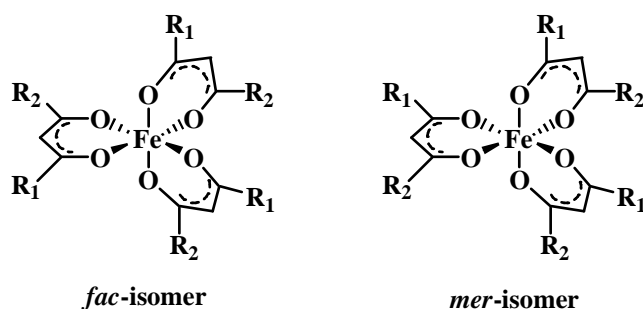


Figure 2.45: The facial (*fac*) and meridional (*mer*) isomers of $[\text{Fe}(\beta\text{-diketonato})_3]$ complexes with unsymmetrical β -diketonato ligands.

Table 2.10: Summary of structural information of selected $[\text{Fe}(\beta\text{-diketonato})_3]$ complexes. Groups R_1 and R_2 assignment is as in Figure 2.45.

	β -diketone $R_1\text{COCH}_2\text{COR}_2$	R_1	R_2	Isomer	Fe-O / Å (average)	O-Fe-O / ° (average)	Ref
Hacac	acetylacetone	CH_3	CH_3	-	1.99(1) 2.012 1.99(1) 1.99(1) 1.95(2)	87.4(6) 87.1 87.0(3) 87.4(2) 89(1)	[157] [157] ⁱ [158] [159] [153]
Hba	benzoylacetone	CH_3	Ph	<i>fac</i>	- ⁱⁱ	- ⁱⁱ	[156]
Htba	tert-butyl acetoacetate	CH_3	$\text{OC}(\text{CH}_3)_3$	<i>fac</i>	2.00(5)	87.5(6)	[160]
Htfaa	trifluoroacetylacetone	CH_3	CF_3	<i>fac</i> <i>mer</i>	- ⁱⁱ 1.99(3)	- ⁱⁱ 87.2(9)	[154] [156]
Hhfaa	hexafluoroacetylacetone	CF_3	CF_3	-	2.00(2)	87.0(6)	[161]
Htta	thenoyltrifluoroacetone	CF_3	$\text{C}_4\text{H}_5\text{S}$	<i>mer</i>	1.99(2)	87(1)	[155]
Hptf	pivaloyltrifluoroacetone	CF_3	$\text{C}(\text{CH}_3)_3$	<i>fac</i>	1.99(3)	86.4(3)	[162]
Hdbm	dibenzoylmethane	Ph	Ph	-	1.99(3) 1.99(2)	86(1) 86.4(9)	[156] [163]
Hdpm	dipivaloylmethane	$\text{C}(\text{CH}_3)_3$	$\text{C}(\text{CH}_3)_3$	-	2.00(2)	84.8(1)	[164]

ⁱ Computational study.

ⁱⁱ No structural parameters available.

UV/vis absorption.¹⁶⁵

Tris(β -diketonato) iron(III) complexes are high-spin d^5 systems for which absorption spectra of ligand field bands are not to be expected. The intensive absorption bands in the wavelength range 250-700 nm, observed for solutions of $[\text{Fe}(\beta\text{-diketonato})_3]$ complexes in the

¹⁵⁷ I. Diaz-Acosta, J. Baker, W. Cordes, P. Pulay, *J. Phys. Chem. A* **2001** (105) 238-244.

¹⁵⁸ J. Iball, C.H. Morgan, *Acta Cryst.* **1967** (23) 239-244.

¹⁵⁹ M.-L. Hu, Z.-M. Jin, Q. Miao, L.-P. Fang, *Z. Kristallogr. - New Cryst. Struct.* **2001** (216) 597-598.

¹⁶⁰ U.K. Urs, K. Shalini, S.A. Shivashankarb, T.N. Guru Row, *Acta Cryst.* **2000** (C56) e448-e449.

¹⁶¹ C.E. Pfluger, P.S. Haradem, *Inorg. Chim. Acta* **1983** (69) 141-146.

¹⁶² I.A. Baidina, N.V. Kurat'eva, P.A. Stabnikov, S.A. Gromilov, *J. Struct. Chem.* **2007** (48) 494-499.

¹⁶³ B. Kaitner, B. Kamenar, *Cryst. Struct. Commun.* **1980** (9) 487-492.

¹⁶⁴ I.A. Baidina, P.A. Stabnikov, V.I. Alekseev, I.K. Igumenov, S.V. Borisov, *J. Struct. Chem.* **1986** (27) 427-434.

¹⁶⁵ G. Gumbel, H. Elias, *Inorg. Chim. Acta* **2003** (342) 97-106.

non-coordinating solvent DCM (Table 2.11), are based on ligand excitation and charge transfer of both the metal to ligand and ligand to metal types.^{166,167} Modification of the alkyl groups according to the series [Fe(acac)₃] → [Fe(dibm)₃] → [Fe(dpm)₃] has practically no effect on the absorption spectra, characterized by absorption bands at approximately 270, 350 and 440 nm. The introduction of phenyl groups, as in [Fe(ba)₃] and [Fe(dbm)₃], however, causes a small red shift of these three characteristic bands. UV/vis data for selected [Fe(β-diketonato)₃] complexes are summarized in Table 2.11.

Table 2.11: UV/vis absorption data (between 250 and 500 nm) for selected [Fe(β-diketonato)₃] complexes in the solvent DCM at 298 K. Groups R₁ and R₂ assignment is as in Figure 2.45.

β-diketone R ₁ COCH ₂ COR ₂		R ₁	R ₂	λ _{max} / nm	Ref
Hacac	acetylacetonone	CH ₃	CH ₃	274, 354, 438	[165]
Hdibm	didimethylacetylacetonone	CH(CH ₃) ₂	CH(CH ₃) ₂	270, 356, 438	[165]
Hdpm	dipivaloylmethane	C(CH ₃) ₃	C(CH ₃) ₃	270, 358, 434	[165]
Hba	benzoylacetonone	CH ₃	Ph	302, 386, 452	[165]
Hdbm	dibenzoylmethane	Ph	Ph	314, 408, 471	[165]
Htta	thenoyltrifluoroacetonone	CF ₃	C ₄ H ₃ S	338, 388, 434	[165]

Cyclic Voltammetry (CV).

Cyclic voltammetry (CV) involves the measurement of the resulting current between a working electrode and an auxiliary electrode, when the potential of the working electrode is oscillated in an unstirred solution (section 2.3.2). Endo *et al.*¹⁶⁸ found that [Fe(dbm)₃] showed electrochemically reversible behaviour (ΔE_p = 60 mV), whereas those of the other [Fe(β-diketonato)₃] complexes in his study showed electrochemically irreversible behaviour (ΔE_p between 130 and 500 mV). See Figure 2.46 for examples of the cyclic voltammograms. The data are summarized in Table 2.12.

The [Fe(β-diketonato)₃] complexes are of the high-spin (*S* = 5/2) type. In the reduced form it is also high-spin (*S* = 2). The overall electrochemical reaction is: [Fe^{III}(β-diketonato)₃] + e⁻ ⇌ [Fe^{II}(β-diketonato)₃]⁻. The different redox potentials for the series of complexes in Table 2.12 are due to the different electronic densities at the metal centre due to the different substituents on the β-diketonato ligands.

¹⁶⁶ R.L. Lintvedt, L.K. Kernitzky, *Inorg. Chem.* **1970** (9) 491-494.

¹⁶⁷ N.T. Moxon, J.H. Moffett, A.K. Gregson, *J. Inorg. Nucl. Chem.* **1981** (43) 2695-2702.

¹⁶⁸ K. Endo, M. Furukawa, H. Yamatera, H. Sano, *Bull. Chem. Soc. Jpn.* **1980** (53) 407-410.

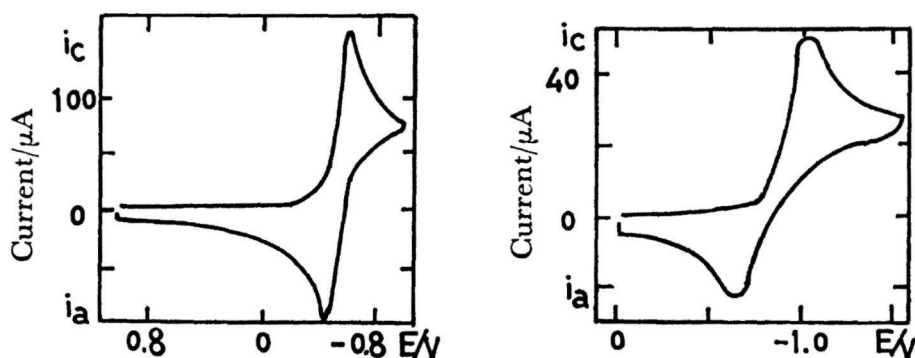


Figure 2.46: Cyclic voltammograms for 5 mM of [Fe(ba)₃] (left, electrochemically reversible) and 5 mM of [Fe(dpm)₃] (right, electrochemically irreversible) with 0.1 M TBAP as supporting electrolyte. The scan rate is 100 mV/s and the potential is measured against a saturated Ag/AgCl electrode.¹⁶⁸

Table 2.12: Summary CV data of selected [Fe(β -diketonato)₃] complexes. Groups R₁ and R₂ assignment is as in Figure 2.45.

[Fe(β -diketonato) ₃]	β -diketone	R ₁	R ₂	E _{pc} / V	E _{pa} / V	ΔE_p / mV	E ^{0'} / V	Ref
[Fe(dpm) ₃]	dipivaloylmethane	C(CH ₃) ₃	C(CH ₃) ₃	-1.16	-0.66	500	-0.91	[168] ⁱ
[Fe(acac) ₃]	acetylacetone	CH ₃	CH ₃	-0.68	-0.55	130	-0.62	[168] ⁱ
				-0.65	-0.59	60	-0.62	[169] ⁱⁱ
[Fe(ba) ₃]	benzoylacetone	CH ₃	Ph	-0.61	-0.47	140	-0.54	[168] ⁱ
[Fe(dbm) ₃]	dibenzoylmethane	Ph	Ph	-0.55	-0.49	60	-0.52	[168] ⁱⁱⁱ
[Fe(tfaa) ₃]	trifluoroacetylacetone	CF ₃	CH ₃	0.00	0.19	190	0.10	[168] ⁱ
[Fe(tfba) ₃]	trifluorobenzoylacetone	CF ₃	Ph	0.07	0.21	140	0.14	[168] ⁱ
[Fe(tta) ₃]	thenoyltrifluoroacetone	CF ₃	C ₄ H ₅ S	0.06	0.19	130	0.13	[168] ⁱ
[Fe(hfaa) ₃]	hexafluoroacetylacetone	CF ₃	CF ₃	0.50	0.72	220	0.61	[168] ⁱ

ⁱ Solvent DMF, supporting electrolyte TBAP (tetrabutylammonium perchlorate), versus Ag/AgCl (saturated), scan rate 100 mV/s.

ⁱⁱ Solvent DME, supporting electrolyte TEAP (tetraethylammonium perchlorate), versus SCE, scan rate 1000 mV/s.

ⁱⁱⁱ Solvent DMF, supporting electrolyte TBAP (tetrabutylammonium perchlorate), versus Ag/AgCl (saturated), scan rate 500 mV/s.

2.5.2 [Fe(salen)(CH₃)₂(COCH₃)₂(py)₂].

Introduction.^{170,171,172}

The spin crossover behaviour (section 2.2.6) in iron complexes has been studied extensively to understand the mechanisms and various factors influencing the phenomenon. The design of new molecular compounds exhibiting spin crossover (SCO) is one of growing importance in the research of functional materials, especially for applications in display devices,¹⁷³ threshold

¹⁶⁹ S. Misumi, M. Aihara, Y. Nonaka, *Bull. Chem. Soc. Jpn.* **1970** (43) 774-778.

¹⁷⁰ M.M. Bhadbhade, D. Srinivas, *Polyhedron* **1998** (17) 2699-2711.

¹⁷¹ J.-Q. Tao, Z.-G. Gu, T.-W. Wang, Q.-F. Yang, J.-L. Zuo, X.-Z. You, *Inorg. Chim. Acta* **2007** (360) 4125-4132.

¹⁷² X. Zhang, Y. Fu, X. Chen, C. Yang, J. Qin, M. Inokuchi, *J. Incl. Phenom Macrocycl. Chem.* **2007** (59) 217-222.

¹⁷³ O. Kahn, C.J. Martinez, *Science* **1998** (279) 44-48.

indicators and biomedical imaging.¹⁷⁴ The implications of SCO in metalloproteins (*e.g.* myoglobin, haemoglobin and cytochromes) are also explored. Factors like substitution, axial ligands, counterions and solvent of crystallization influence the nature of spin state crossover.¹⁷⁵ Variable temperature X-ray structural studies have revealed that the electron transfer rate is coupled to intermolecular solid state effects and the onset of dynamic motions of a solvent molecule in the lattice. The dynamic disorders in the lattice lead to rapid spin interconversion rates and reversible abrupt transition while static order leads to slow rates and gradual SCO behaviour.¹⁷⁶

SCO is most commonly observed for iron(II) complexes with the nitrogen donor atoms and represents a transition between the high-spin state ($S = 2$) to the low-spin state ($S = 0$), which can be induced by a variation of temperature, pressure or by light irradiation.¹⁷⁷ SCO in salen type complexes was observed initially by Nishida *et al.*¹⁷⁸ and later Kennedy *et al.*¹⁷⁹ have reported a detailed study of the influence of uncoordinated anion on the spin state interconversion dynamics.

In this study, we turn our attention to the salen type complex $[\text{Fe}(\text{salen})(\text{CH}_3)_2(\text{COCH}_3)_2(\text{py})_2]$, where py is axial pyridine ligands (Figure 2.47). This complex was first investigated by Jäger *et al.*¹⁸⁰ Recently, Weber *et al.*¹⁸¹ performed a solution NMR study of this iron(II) SCO complex.

¹⁷⁴ R.N. Muller, L. Vander Elst, S. Laurent, *J. Am. Chem. Soc.* **2003** (125) 8405-8407.

¹⁷⁵ H. Toftlund, *Coord. Chem. Rev.* **1989** (94) 67-108.

¹⁷⁶ M.D. Timken, C.E. Strouse, S.M. Soltis, S.A. Daverio, D.N. Hendrickson, A.M. Abdel-Mawgoud, S.R. Wilson, *J. Am. Chem. Soc.* **1986** (108) 395-402.

¹⁷⁷ (a) S. Bonhommeau, G. Molnár, A. Galet, A. Zwick, J.A. Real, J.J. McGarvey, A. Bousseksou, *Angew. Chem., Int. Ed.* **2005** (44) 4069-4073. (b) P. Gütllich, Y. Garcia, H.A. Goodwin, *Chem. Soc. Rev.* **2000** (29) 419-427.

¹⁷⁸ Y. Nishida, S. Oshi, S. Kida, *Chem. Lett.* **1975** 79-80.

¹⁷⁹ B.J. Kennedy, A.C. McGrath, K.S. Murray, B.W. Skelton, A.H. White, *Inorg. Chem.* **1987** (26) 483-495.

¹⁸⁰ E.G. Jäger, In: L. Fabbrizzi, A. Poggi (Editors), *Chemistry at the Beginning of the Third Millennium*, Springer-Verlag: Heidelberg, Germany, **2000** 103-138.

¹⁸¹ B. Weber, F.A. Walker, *Inorg. Chem.* **2007** (46) 6794-6803.

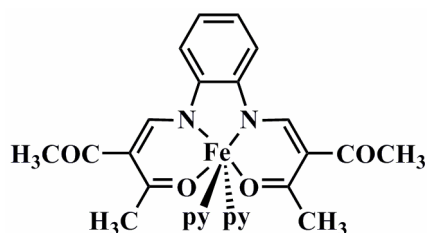


Figure 2.47: The salen type complex $[\text{Fe}(\text{salen})(\text{CH}_3)_2(\text{COCH}_3)_2(\text{py})_2]$ (where py = pyridine) used in this study.

Solution NMR study.¹⁸¹

In the work of Weber *et al.*¹⁸¹ they introduce a method for analyzing the spin transitions of iron(II) complexes in solution. Iron(II) is the most important metal centre for SCO complexes. Most of the investigations on spin-transition complexes are focused on solid-state properties. However, whereas packing effects are sometimes useful and lead to the desired properties, there are several other cases where experiments in solution give more detailed answers to open questions. In solution, packing effects are switched off and a better comparison/study of the effect of different substituents or the influence of the bridging ligand on the “communication” between the linked iron centres is possible. Such investigations are important for the understanding of cooperative interactions in the solid state and therefore for designed syntheses of new spin-transition compounds.

The magnetic susceptibility of $[\text{Fe}(\text{salen})(\text{CH}_3)_2(\text{COCH}_3)_2(\text{py})_2]$ was measured in a pyridine- d_5 /toluene- d_8 mixture (50/50, v/v) with the toluene- CD_2H residual methyl proton signal as a reference on a Varian Unity-300 spectrometer. Magnetic susceptibility is the degree of magnetization of a material in response to an applied magnetic field. Figure 2.48 shows the plots of the effective magnetic moment per mole of compound (μ_{eff}) as a function of temperature for $[\text{Fe}(\text{salen})(\text{CH}_3)_2(\text{COCH}_3)_2(\text{py})_2]$. For comparison purposes, the results from solid-state susceptibility measurements are given as well (solid triangles in Figure 2.48). At room temperature, the complex is in the high-spin (HS) state, with μ_{eff} equals to $5.10 \mu_{\text{B}}$. Deviations from the theoretically expected values are due to difficulties in obtaining an accurately weighed amount of the air-sensitive iron(II) compound. As the temperature is lowered, the magnetic moment decreases. Significant differences can be found between the behaviour in solution and that in the solid state. In comparison, a powder sample of $[\text{Fe}(\text{salen})(\text{CH}_3)_2(\text{COCH}_3)_2(\text{py})_2]$ shows an abrupt spin transition, whereas the transition curve in solution is gradual, as expected for a mononuclear complex. The critical temperature $T_{1/2}$ (with HS mole fraction $\gamma_{\text{HS}} = 0.5$) is 210 K for the pyridine/toluene solution of $[\text{Fe}(\text{salen})(\text{CH}_3)_2(\text{COCH}_3)_2(\text{py})_2]$. A significantly

lower critical temperature is found for the abrupt spin transition of the powder sample of $[\text{Fe}(\text{salen})(\text{CH}_3)_2(\text{COCH}_3)_2(\text{py})_2]$ (177 K). The packing of the molecules in the crystal therefore influences the thermodynamic parameters of the spin transition.

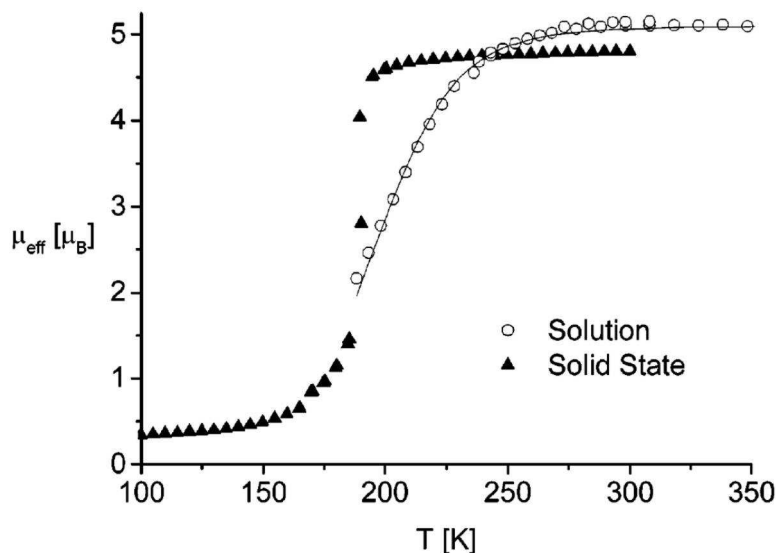


Figure 2.48: Plot of the effective magnetic moment per mole of compound (μ_{eff}) versus temperature (T). Magnetic property of $[\text{Fe}(\text{salen})(\text{CH}_3)_2(\text{COCH}_3)_2(\text{py})_2]$, determined in solution (open circles) and in the solid state (solid triangles).¹⁸¹

2.5.3 [Fe(porphyrin)(Ar)].

Introduction.¹⁸²

Porphyrin type molecules (porphyrinoids) consist of a large class of macrocyclic molecules with a carbon and nitrogen skeleton. Porphyrinoids are called “the colours of life”, since many porphyrinoids have intense colours and play an important role in nature. They owe their bright colours to intense absorptions in the near ultraviolet and visible regions. The word porphyrin is actually derived from the Greek word for purple, porphura. Two well-known porphyrinoids are the heme cofactor in blood and chlorophyll in plants. The heme cofactor in blood is an iron-containing porphyrin, where it serves as an O_2 and a CO_2 carrier. The heme cofactor also gives the red colour to blood. Chlorophyll is a magnesium chlorin (a reduced porphyrin, Figure 2.50) and is a vital component in photosynthesis as a light-harvesting pigment and is also

¹⁸² L.R. Milgrom, *The colours of life*; Oxford University Press, Oxford, 1997.

responsible for the green colour of leaves and grass. The main function of porphyrinoids is to bind to metal atoms that act as centres for significant biochemical events.

The porphyrin skeleton consists of four pyrrole units, linked together by four methine bridges. This 22 π -electron system has a [18]annulene substructure and like typical aromatic compounds, unsubstituted porphyrins are planar. The porphyrin structure is given in Figure 2.49 and Figure 2.50 illustrates selected general porphyrinoids.

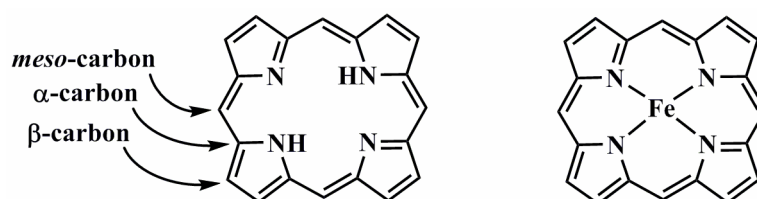


Figure 2.49: Structure of the free base porphyrin (left) and unsubstituted iron porphyrin (right). Key carbons are indicated with arrows.

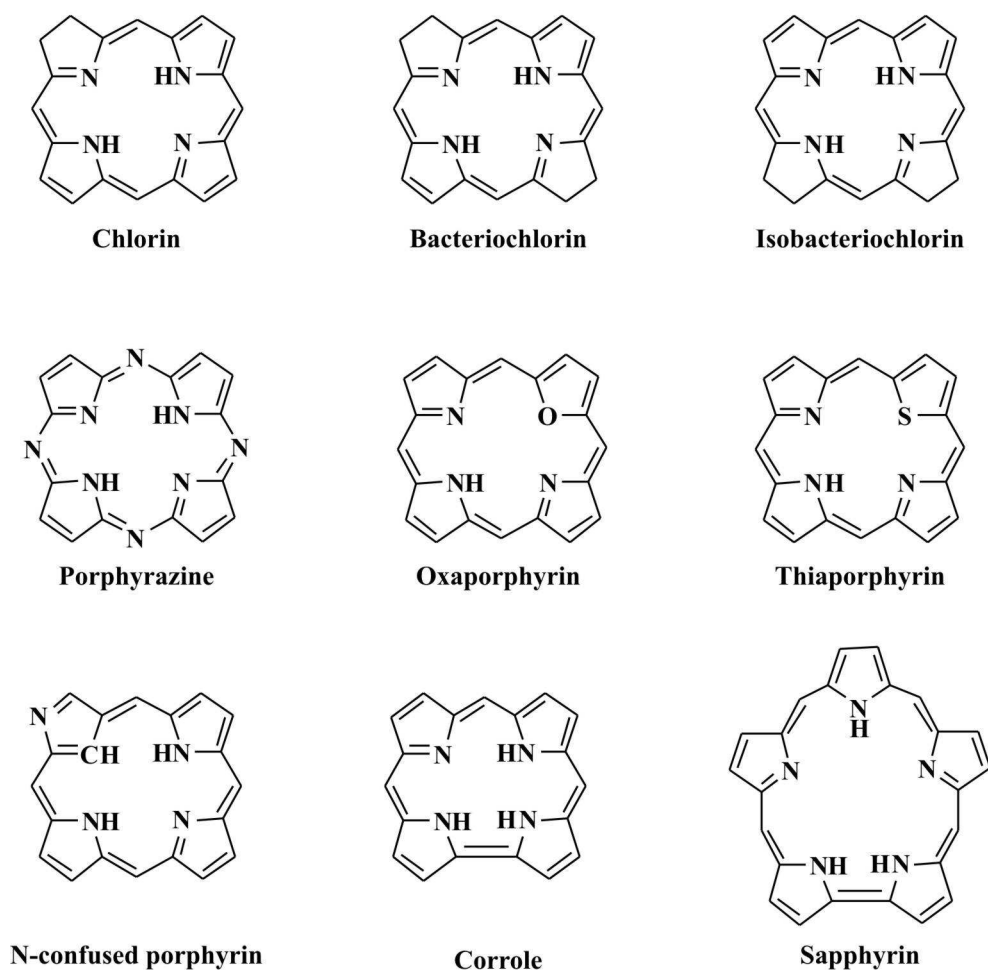


Figure 2.50: Selected general porphyrinoids.

Non-planar deformations of porphyrins.

Many biological porphyrin cofactors are observed to be non-planar. This is suspected to play an important role in biological functions of these compounds.^{183,184} Non-planar distortion of substituted porphyrins may be caused by peripheral steric crowding, electronic interactions involving axial ligands, crystal packing effects, the size of the central ion and specific metal-ligand orbital interactions. The four common non-planar deformations of porphyrins are the ruffled (D_{2d}), saddled (D_{2d}), waved (C_{2h}) and domed (C_{4v})-conformations. They all result in a lowering of the ideal D_{4h} symmetry of a planar porphyrin (the symmetry is given in parentheses). The different out-of-plane deformations are illustrated in Figure 2.51.

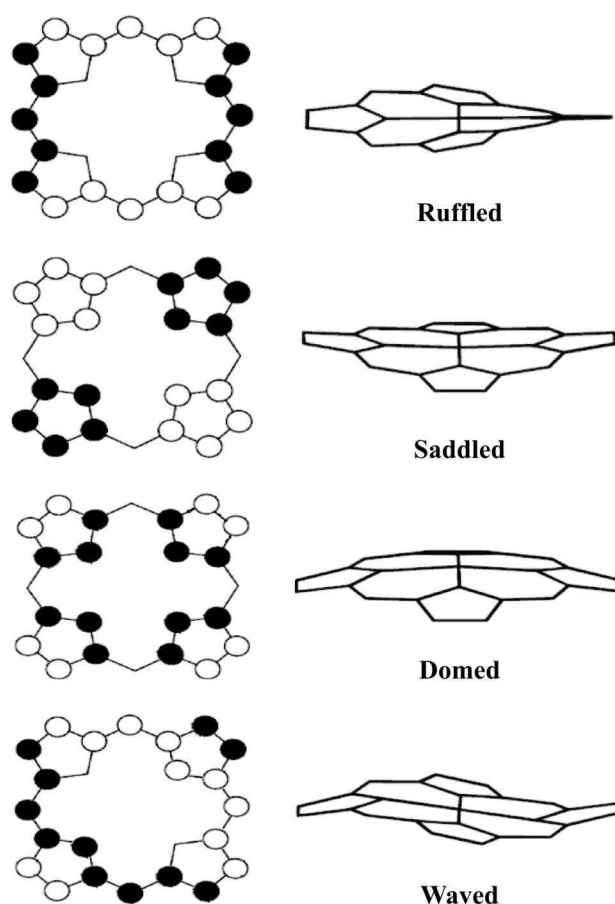


Figure 2.51: A schematic illustration of the four most common non-planar deformations in porphyrins. Filled circles represent displacement above the mean porphyrin plane and open circles represent displacement below.¹⁸²

In the ruffled conformation, the *meso*-carbons are alternately above and below the mean porphyrin plane. A small central ion is the primary driving force for this out-of-plane

¹⁸³ W.R. Scheidt, Y. Lee, *J. Struct. Bond.* **1987** (64) 1-70.

¹⁸⁴ J.A. Shelnutt, Z.Z. Song, J.G. Ma, S.L. Jia, W. Jentzen, C. Medforth, *J. Chem. Soc. Rev.* **1998** (27) 31-41.

deformation. Ruffling is often observed together with a metal-pyrrole nitrogen (M-N_p) bond length less than 2.0 Å.¹⁸⁵ Additional factors causing the porphyrin macrocycle to ruffle are steric interactions and electronic effects due to axial ligands and peripheral substituents. The C_α-N-N-C_α torsion angle is often used to describe the degree of ruffling.

In the saddled out-of-plane deformation geometry, the pyrrole rings are alternately tilted above and below the mean porphyrin plane. The *meso*-carbons lie in the mean porphyrin plane. The principal driving forces for this are short M-N_p bonds and peripheral substituents.

In the domed conformation, the metal ion, the pyrrole nitrogens and the α-carbons are above the mean plane and the β-carbons below the mean plane. This conformation is often observed when the central metal ion is large and requires large M-N_p bonds. Steric interactions with large axial ligands and other porphyrins in sandwich systems are other driving forces.

Waved porphyrins are quite rare. In this conformation, two opposing pyrrole rings are tilted above and below the mean porphyrin plane.

Interaction between the metal *d*-orbitals and the porphyrin HOMOs may affect the ground state in metalloporphyrins, as mentioned. In planar metalloporphyrins, the metal *d*-orbitals and the porphyrin HOMOs are orthogonal and an overlap between them is not allowed. Once the porphyrin undergoes non-planar distortion, like ruffling and saddling, certain orbital overlaps become symmetry-allowed (Table 2.13). For instance, ruffling makes the metal(*d*_{xy})-porphyrin(*a*_{2u}) orbital interaction symmetry-allowed, where the *d*_{xy}-orbital is the *t*_{2g}-type *d*-orbital in the porphyrin plane.¹⁸⁶ Saddling turns on the metal(*d*_{x²-y²})-porphyrin(*a*_{2u}) orbital interaction, where the *d*_{x²-y²}-orbital is the *e*_g-type *d*-orbital in the porphyrin plane.¹⁸⁷ Doming results in metal(*d*_{z²})-porphyrin(*a*_{2u}) orbital interaction.

¹⁸⁵ J.L. Hoard, *Science* **1971** (174) 1295-1302.

¹⁸⁶ R.-J. Cheng, Y.-K. Wang, P.-Y. Chen, Y.-P. Han, C.-C. Chang, *Chem. Com.* **2005**, 1312-1314.

¹⁸⁷ R.-J. Cheng, P.-Y. Chen, *Chem. Eur. J.* **1999** (5) 1708-1715.

Table 2.13: Correlation between the standard D_{4h} irreducible representations and the irreducible representations of some relevant lower-order point groups of macrocyclic ligands. For the D_{2d} configuration, there are two possible orientations of the ligand HOMOs.¹⁸⁸ Possible overlaps are marked in bold for the given conformation.

Orbital	Point group					
	D_{4h} planar	D_{2d} ruffled	D_{2d} saddled	C_{4v} domed	D_{2h} waved	Cs
d_{xy}	b_{2g}	b_2	b_1	b_2	b_{2g}	a'
d_{xz}	e_g	e	e	E	b_{3g}	a''
d_{yz}	e_g	e	e	E	b_{2g}	a''
$d_{x^2-y^2}$	b_{1g}	b_1	b_2	b_1	a_u	a'
d^2	a_{1g}	a_1	a_1	a_1	a_g	a'
Ligand HOMOs	D_{4h} planar	D_{2d} ruffled	D_{2d} saddled	C_{4v} domed	D_{2h} waved	Cs
a_{1u}	a_{1u}	b_1	b_1	a_2	a_u	a''
a_{2u}	a_{2u}	b_2	b_2	a_1	b_{1u}	a''

Electronic structure of porphyrins: The four-orbital model.

Porphyrins have a very characteristic UV/vis spectrum, with strong absorption in the near ultraviolet region (Soret band) and weaker absorption in the visible region (Q-band) (Figure 2.52). The four-orbital model, developed by Gouterman, gives a theoretical explanation of the UV-spectra.^{189,190} According to this model, the two highest occupied molecular orbitals (HOMOs) and two of the lowest unoccupied molecular orbitals (LUMOs) of a typical metalloporphyrin are near degenerate. The model also assumes that these four molecular orbitals (MOs) are energetically well separated from the other MOs. Gouterman's four-orbital model is still considered as a cornerstone in modern porphyrin chemistry and is highly supported by modern theoretical calculations.¹⁹¹

¹⁸⁸ T. Vangberg, A. Ghosh, *J. Am. Chem. Soc.* **1999** (121) 12154-12160.

¹⁸⁹ M. Gouterman, *J. Mol. Spectrosc.* **1961** (6) 138-163.

¹⁹⁰ M. Gouterman, In: D. Dolphin (Editor), *The Porphyrins*, Academic Press, New York, **1978**, Vol 3, p1-165.

¹⁹¹ A. Ghosh, T. Vangberg, *Theor. Chem. Acc.* **1997** (97) 143-149.

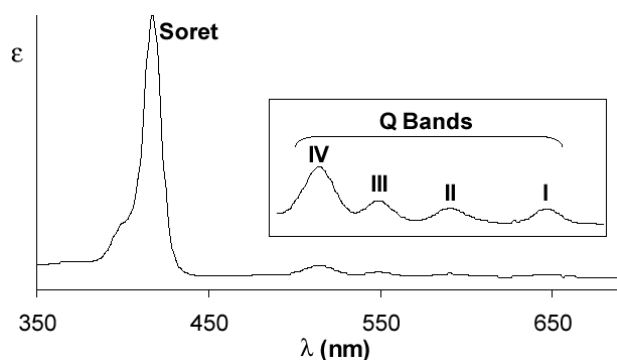


Figure 2.52: The electronic absorption spectra of a free-base *meso*-tetraphenylporphyrin, as an example of the characteristic UV/vis spectrum of porphyrins. The insert shows a magnified Q band region.¹⁹⁰

One-electron transition between the two HOMOs and LUMOs results in two pairs of degenerate (π, π^*) excited states, which account for the Soret band and Q-band absorption seen in the UV/vis spectrum. The four-orbital model is validated by the gas-phase ultraviolet photoelectron spectrum.¹⁹² The ultraviolet photoelectron spectrum shows that the two lowest ionization potentials are close to each other and well separated from all other ionization potentials. DFT(PW91) calculations on the ionization potentials of free base porphyrins reproduced the experimental ionization potentials accurately.¹⁹¹

The four-orbital model may be used to predict the energy of the two HOMOs relative to each other. Figure 2.53 sketches the four frontier orbitals of a metalloporphyrin according to the four-orbital model. Due to different amplitudes at the *meso*-positions, it is clear that electron donating or electron withdrawing peripheral substituents at the *meso*-positions affect the a_{1u} and the a_{2u} HOMOs differently. With large amplitudes on the *meso*-carbons, the a_{2u} HOMO will be stabilized by electron withdrawing *meso*-substituents and destabilized electron donating *meso*-substituents. The a_{1u} HOMO has no amplitude at the *meso*-positions and is not expected to be strongly affected by *meso*-substituents. On the other hand, substituents in β -position should primarily affect the a_{1u} HOMO.^{193,194}

¹⁹² P. Dupuis, R. Roberg, C. Sandorfy, *Chem. Phys. Lett.* **1980** (75) 434-437.

¹⁹³ A. Ghosh, In: K.M. Kadish, K.M. Smith, R. Guilard (Editors), *The Porphyrin Handbook*, Academic, San Diego, **2000**, Vol. 7, Chapter 47, p1-38.

¹⁹⁴ E. Steene, T. Wondimagegn, A. Ghosh, *J. Phys. Chem. B* **2001** (105) 11406-11413.

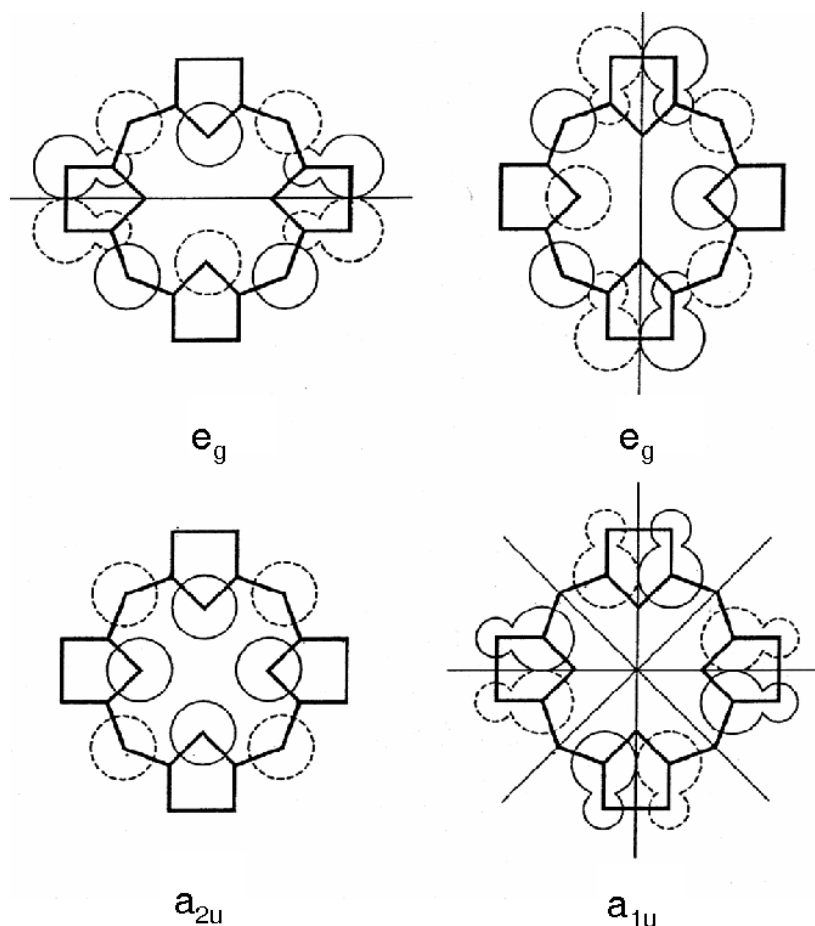


Figure 2.53: Schematic visualization of the porphyrin HOMO (below) and LUMO (above).¹⁹⁰

Iron porphyrins.

Most of the chemistry of iron is that of iron(II) and iron(III), but iron complexes with the iron in higher oxidation states are also known in a small number of compounds. High valent iron complexes have been detected or proposed as reactive intermediates for various iron enzymes and a number of synthetic models of these enzymes have also been proposed. These models have been studied in detail and a key point of interest in these studies is whether these species are oxidized in a metal- or ligand-centred fashion.

Peroxidase compound I intermediates of heme proteins are formally Fe(V) compounds, but the iron centre itself generally cannot sustain a +5 oxidation state. Hence, these intermediates are usually described as Fe(IV)-oxo porphyrin radicals.¹⁹⁵ For both compound I and II intermediates and their models, a common feature appears to be that two unpaired electrons are localized on

¹⁹⁵ J. Turner, A. Gold, R. Weiss, D. Mandon, A.X. Trautwein, *J. Porphyrins Phtalocyanines* **2001** (5) 357-364.

the ferryl group, distributed approximately 1:1 between the iron and the oxygen atoms.^{196,197} A recent theoretical finding¹⁹⁸ is that the radical in Compound I may not be exclusively localized on the porphyrin, but is partially delocalized on the axial ligand for relatively strong basic anionic axial ligands such as imidazolate and thiolate. The active site structure of peroxidase has a hydrogen bond between the proximal histidine ligand and a conserved aspartate group. This hydrogen bond has been proposed to impart an imidazolate character to the histidine ligand.¹⁹⁹

To model these effects, Deeth²⁰⁰ and Green²⁰¹ independently reported DFT calculations on both $[\text{Fe}(\text{porphyrin})(\text{O})(\text{ImH})]^+$ and $[\text{Fe}(\text{porphyrin})(\text{O})(\text{Im})]^0$ (ImH = Imidazole, Im⁻ = Imidazolate). The former compound appeared to be a normal fully developed porphyrin radical^{196,200,201} whereas more than half of the radical spin appeared to be delocalized onto the imidazolate ligand in the latter compound.^{200,201} Deeth²⁰⁰ also showed that porphyrin ruffling can result in a redistribution of the unpaired electron density of $[\text{Fe}(\text{porphyrin})(\text{O})(\text{ImH})]^+$, while Vangberg and Ghosh¹⁸⁸ subsequently showed that this redistribution probably results from a metal(d_{xy})-porphyrin(a_{2u}) orbital interaction that becomes symmetry allowed in a ruffled porphyrin (both orbitals transform as b_2 in a D_{2d} ruffled porphyrin as shown in Table 2.13).

The radical character of the axial thiolate ligand in a chloroperoxidase compound I (CPO-I) has been supported by a variety of DFT calculations,^{202,203,204} although a resonance Raman study by Hosten *et al.*²⁰⁵ favours an a_{1u} type radical formulation for CPO-I. With respect to the nature and strength of the spin coupling between the radical and the $S = 1$ ferryl group, the different calculations diverge and both doublet and quartet states have been obtained as ground states for CPO-I models. CPO-I is unique among Compound I intermediates in having an experimentally

¹⁹⁶ H. Kuramochi, L. Noodleman, D.A. Case, *J. Am. Chem. Soc.* **1997** (119) 11442-11451.

¹⁹⁷ A. Ghosh, J. Almlöf, L. Que Jr., *J. Phys. Chem.* **1994** (98) 5576-5579.

¹⁹⁸ J. Antony, M. Grodzicki, A.X. Trautwein, *J. Phys. Chem. A*, **1997** (101) 2692-2701.

¹⁹⁹ M. Gajhede, D.J. Schuller, A. Henriksen, A.T. Smith, T. Poulos, *Nat. Struct. Biol.* **1997** (4) 1032-1038.

²⁰⁰ R.J. Deeth, *J. Am. Chem. Soc.* **1999** (121) 6074-6075.

²⁰¹ M.T. Green, *J. Am. Chem. Soc.* **2000** (122) 9495-9499.

²⁰² M. Filatov, N. Harris, S. Shaik, *J. Chem. Soc. Perkins trans.* **1999** (2) 399-410.

²⁰³ D.L. Harris, G. Loew, *J. Am. Chem. Soc.* **1998** (120) 8941-8948.

²⁰⁴ M.T. Green, *J. Am. Chem. Soc.* **1999** (121) 7939-7940.

²⁰⁵ C.M. Hosten, A.M. Sullivan, V. Palaniappan, M.M. Fitzgerald, J. Turner, *J. Biol. Chem.* **1994** (269) 13966-13978.

detected doublet ground state,^{206,207} unlike other compound I species which are quartet.²⁰⁸ For the model complex $[\text{Fe}(\text{porphyrin})(\text{O})(\text{SMe})]^0$ (SMe = methylthiolate) DFT (B3LYP) calculations by Green²⁰⁴ do reproduce this observation, ascribing the doublet state to an anti-ferromagnetic coupling involving an $\text{Fe}(d_\pi)$ - $\text{S}(p_\pi)$ orbital overlap.

An Fe(V)-oxo perferryl porphyrin intermediate was reported by Murakami *et al.*,²⁰⁹ who reported that it can most likely be described as a $[\text{Fe}^{\text{V}}(\text{porphyrin})(\text{O})(\text{OMe})]^0$ (OMe = methoxide) complex. DFT (PW91/TZP) calculations indicated that much of the radical spin of $[\text{Fe}(\text{porphyrin})(\text{O})(\text{OMe})]^0$ ($S = 3/2$) was localized on the methoxy oxygen and thus the iron centre cannot be regarded as true Fe(V).²⁰⁸ The optimized Fe-O bond distance was found to be 1.68 Å, nearly identical to a distance of 1.69 Å in the optimized geometry of the Compound II analogue $[\text{Fe}(\text{porphyrin})(\text{O})(\text{OMe})]^-$ ($S = 1$), indicating that the electronic character of the ferryl group may be similar in the two compounds.

Results from DFT (PW91/TZP) calculations on peroxidase Compound II model compounds $[\text{Fe}^{\text{IV}}(\text{porphyrin})(\text{O})]$ (C_{4v} , $S = 1$) and $[\text{Fe}^{\text{IV}}(\text{porphyrin})(\text{NH})]$ (C_{4v} , $S = 1$) reported by Dey and Ghosh²¹⁰ yielded optimized Fe-O and Fe-N_{imido} distances of 1.634 Å and 1.698 Å, respectively. The optimized Fe-N_{por} bond distances were reported to be 2.009 Å, the C_α-C_{meso} bond distance 1.387 Å and the C_α-C_{meso}-C_α bond angle 125.6° for the $[\text{Fe}^{\text{IV}}(\text{porphyrin})(\text{O})]$ complex. In both compounds the unpaired electron spins are completely localized on the central Fe-oxo/imido units, the individual spin populations being 1.199 for the Fe in $[\text{Fe}^{\text{IV}}(\text{porphyrin})(\text{O})]$ and 0.775 in $[\text{Fe}^{\text{IV}}(\text{porphyrin})(\text{NH})]$, 0.826 for the O in $[\text{Fe}^{\text{IV}}(\text{porphyrin})(\text{O})]$ and 1.289 for the N_{imido} in $[\text{Fe}^{\text{IV}}(\text{porphyrin})(\text{NH})]$.²¹⁰ In $[\text{Fe}^{\text{IV}}(\text{porphyrin})(\text{py})]$, where the additional pyridine is an axial ligand, the optimized Fe-O distance is reported to be 1.652 Å and the corresponding M-N_{py} bond length 2.250 Å. There is an expansion of the Fe-O bond length relative to the $[\text{Fe}^{\text{IV}}(\text{porphyrin})(\text{O})]$ complex. As in $[\text{Fe}^{\text{IV}}(\text{porphyrin})(\text{O})]$, the unpaired electron density is

²⁰⁶ R. Rutter, M. Valentine, M.P. Hendrich, L.P. Hager, P.G. Debrunner, *Biochemistry* **1983** (22) 4769-4744.

²⁰⁷ R. Rutter, L.P. Hager, H. Dhonau, M.P. Hendrich, M. Valentine, P.G. Debrunner, *Biochemistry* **1984** (23) 6809-6816.

²⁰⁸ A. Ghosh, E. Steene, *J. Biol. Inorg. Chem.* **2001** (6) 739-752.

²⁰⁹ T. Murakami, K. Yamaguchi, Y. Watanabe, I. Morishima, *Bull. Chem. Soc. Jpn.* **1998** (71) 1343-1353.

²¹⁰ A. Dey, A. Ghosh, *J. Am. Chem. Soc.* **2002** (124) 3206-3207.

completely localized on the ferryl group with the Fe and O spin populations being 1.136 and 0.911 respectively.²⁰⁸

The only examples known to the author of true Fe(V) porphyrins where the *d*-electron occupancy can be described as $d_{xy}^1 d_{xz}^1 d_{yz}^1$, are the Fe(V) nitrido porphyrin complexes [Fe^V(OEP)(N)] first isolated by Wagner and Nakamoto.^{211,212} Resonance Raman spectral investigations revealed a band that was assigned to an Fe(V)N_{nitrido} stretch on the basis of isotope substitution experiments. To further investigate these complexes, Dey and Ghosh²¹⁰ have carried out some DFT (PW91/TZP) calculations giving an optimized Fe-N_{nitrido} bond distance of 1.722 Å, which is significantly longer than the optimized Fe-O bond distance in [Fe^{IV}(porphyrin)(O)] mentioned earlier. For [Fe^V(OEP)(N)], the optimized Fe-N_{Por} bond distances were reported to be 2.008 Å, the C_α-C_{meso} bond distances were 1.378 Å and the C_α-C_{meso}-C_α bond angles were 125.6°. ²¹⁰ This may be interpreted in the following manner: Although the Fe-N_{nitrido} stretching frequency of [Fe^V(OEP)(N)] is higher than the Fe-O stretching frequency of [Fe^{IV}(OEP)(O)],²¹³ the former vibration corresponds to a lower force constant. Dey and Ghosh²¹⁰ found the three unpaired electron spins of [Fe^V(OEP)(N)] to be entirely localized on the Fe-N_{nitrido} unit and the Fe and the N_{nitrido} spin populations were 1.579 and 1.550, respectively.

²¹¹ W.D. Wagner, K. Nakamoto, *J. Am. Chem. Soc.* **1988** (110) 4044-4045.

²¹² W.D. Wagner, K. Nakamoto, *J. Am. Chem. Soc.* **1989** (111) 1590-1598.

²¹³ L.M. Proniewicz, K. Bajdor, K. Nakamoto, *J. Phys. Chem.* **1986** (90) 1760-1766.

3

Results and discussion

3.1 Rhodium complexes.

3.1.1 Introduction.

Ever since the formulation of the transition state (TS) theory¹ more than a half a century ago, great effort has been devoted to developing models for characterizing transition states. The reason for this effort is evident; it is the transition state that governs the height of the reaction barrier, so any general insight into the nature of the transition state is likely to provide a greater understanding of those factors that govern chemical reactivity.

The transition state of a reaction step is considered to be the highest energy point on the minimum two-dimensional potential energy surface (PES), hence, the reaction path. Reactions are considered to occur *via* the path of the lowest energy from reactants to products. The transition state is the point of highest energy on this path. As such it represents a saddle point on the free energy surface. On the free energy multidimensional surface, it is an energy minimum with respect to every other variable, except the reaction path.

The mechanism of a reaction is a stepwise description of how reactants are converted to products. Of course, some reactions occur in a single step. Such reactions are termed "concerted". More generally, reactions are found to occur in a stepwise fashion. These reactions may consist of 2, 3 or many more steps. In any stepwise reaction, intermediates must be formed. By definition an intermediate is any of the species encountered on the reaction path between the reactants and products which represent a free energy minimum. For examples of the mechanism of oxidative addition reactions, see section 2.4.1.4 (Chapter 2).

¹ (a) H. Eyring, *J. Chem. Phys.* **1935** (3) 107-115. (b) E. Wigner, *Trans. Faraday SOC.* **1938** (34) 29-41. (c) S.C. Tucker, D.G. Truhlar, In: J. Bertran, I.G. Csizmadia (Editors), *New Theoretical Concepts for Understanding Organic Reactions*, NATO ASI Series; Kluwer Academic Publishers: Dordrecht, **1988**, Volume C267, p291. (d) J.T. Hynes, *Annu. Rev. Phys. Chem.* **1985** (36) 573-597.

The rhodium studies in this chapter focus on the oxidative addition reaction of methyl iodide to square planar rhodium(I) complexes. Two types of rhodium complexes were investigated: monocarbonyltriphenylphosphine rhodium complexes $[\text{Rh}(\beta\text{-diketonato})(\text{CO})(\text{PPh}_3)]$ (sections 3.1.2 and 3.1.3) and triphenylphosphite rhodium complexes $[\text{Rh}(\beta\text{-diketonato})(\text{P}(\text{OPh})_3)_2]$ (section 3.1.4) (where $\beta\text{-diketonato}$ is a monoanionic bidentate ligand with two oxygen donor atoms $(\text{R}_1\text{COCHCOR}_2)^-$).

The reaction, $[\text{Rh}(\beta\text{-diketonato})(\text{CO})(\text{PPh}_3)] + \text{CH}_3\text{I}$, consists of many steps with numerous transition states, intermediate products and reaction products. As representative example, $[\text{Rh}(\text{acac})(\text{CO})(\text{PPh}_3)]$ (Hacac = acetylacetonate) was used to study the complete reaction (section 3.1.2). This study consists of an experimental part and a DFT computational part that complement each other. In the experimental part, the reaction products were identified and the stereochemistry of these products was determined. Only the reactant $[\text{Rh}(\text{acac})(\text{CO})(\text{PPh}_3)]^2$ has been solved by solid state X-ray crystallography and to date the stereochemistry of all the reaction products is unknown. The experimental study was done by conducting an *in situ* NMR study of the reaction $[\text{Rh}(\text{acac})(\text{CO})(\text{PPh}_3)] + \text{CH}_3\text{I}$ (section 3.1.2.1). Having the reaction products identified with specific stereochemistry, the multistep reaction mechanism was investigated by means of an in depth DFT computational study (section 3.1.2.3). Finally, the oxidative addition reaction was generalized by investigating the first part of this multistep reaction mechanism for a selected series of $[\text{Rh}(\beta\text{-diketonato})(\text{CO})(\text{PPh}_3)]$ complexes (section 3.1.3).

The main difference between the reaction of methyl iodide with $[\text{Rh}(\beta\text{-diketonato})(\text{CO})(\text{PPh}_3)]$ complexes and with $[\text{Rh}(\beta\text{-diketonato})(\text{P}(\text{OPh})_3)_2]$ complexes, is that the latter complex contains no carbonyl group bonded to the rhodium centre. The consequence of this is that the reaction $[\text{Rh}(\beta\text{-diketonato})(\text{P}(\text{OPh})_3)_2] + \text{CH}_3\text{I}$ is a three step reaction mechanism with only one transition state, one intermediate product and one reaction product. As representative example, $[\text{Rh}(\text{acac})(\text{P}(\text{OPh})_3)_2]$ was used in the DFT computational study of the reaction mechanism of this oxidative addition reaction (section 3.1.4). Due to the computational requirement of optimizing such a big molecular system, simplified models of $[\text{Rh}(\text{acac})(\text{P}(\text{OPh})_3)_2]$ were also

² J.G. Leipoldt, S.S. Basson, L.D.C. Bok, T.I.A. Gerber, *Inorg. Chim. Acta* **1987** (26) L35-L37.

investigated to see whether these models gave the same information regarding the oxidative addition reaction, whilst saving on computing resources.

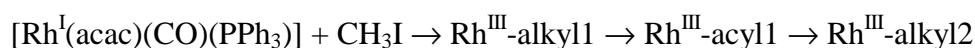
The crystal structure of a dicarbonyl square planar $[\text{Rh}(\beta\text{-diketonato})(\text{CO})_2]$ complex, a precursor for the synthesis of $[\text{Rh}(\beta\text{-diketonato})(\text{CO})(\text{PPh}_3)]$ and $[\text{Rh}(\beta\text{-diketonato})(\text{P}(\text{OPh})_3)_2]$ complexes, is presented (section 3.1.5) at the end of this rhodium study.

Herewith, the results of the dicarbonyl, monocarbonyltriphenylphosphine and triphenylphosphite rhodium studies.

3.1.2 $[\text{Rh}(\text{acac})(\text{CO})(\text{PPh}_3)] + \text{CH}_3\text{I}$.

3.1.2.1 Introduction.

The first experimental study of the oxidative addition of methyl iodide to $[\text{Rh}(\beta\text{-diketonato})(\text{CO})(\text{PPh}_3)]$ complexes was reported by Basson *et al.*³ for $\beta\text{-diketonato} = \text{acac}$, tfdma , tfaa and hfaa . According to this and follow-up studies,^{4,5} the oxidative addition of methyl iodide to $[\text{Rh}(\text{acac})(\text{CO})(\text{PPh}_3)]$ occurs according to the following reaction scheme:



The notations "Rh^{III}-alkyl1" and "Rh^{III}-acyl1" above refer respectively to the first alkylated $[\text{Rh}^{\text{III}}(\text{acac})(\text{CH}_3)(\text{CO})(\text{PPh}_3)(\text{I})]$ and acylated $[\text{Rh}^{\text{III}}(\text{acac})(\text{COCH}_3)(\text{PPh}_3)(\text{I})]$ complexes that are formed. When the last number in the notation changes to '2', as in "Rh^{III}-alkyl2", it shows that after the first alkylated complex had formed, it converted to a second, different but more stable, alkylated structural isomer.

Since then, many similar studies have been conducted on a series of $[\text{Rh}(\beta\text{-diketonato})(\text{CO})(\text{PPh}_3)]$ complexes, some of which showed another reaction step and the formation of a second acylated structural isomer, Rh^{III}-acyl2.^{6,7,8,9} The inclusion of Rh^{III}-acyl2 in

³ S.S. Basson, J.G. Leipoldt, J.T. Nel, *Inorg. Chim. Acta* **1984** (84) 167-172.

⁴ S.S. Basson, J.G. Leipoldt, A. Roodt, J.A. Venter, T.J. van der Walt, *Inorg. Chim. Acta* **1986** (119) 35-38.

⁵ Y.S. Varshavsky, T.G. Cherkosova, N.A. Buzina, L.S. Bresler, *J. Organomet. Chem.* **1994** (464) 239-245.

⁶ J. Conradie, G.J. Lamprecht, A. Roodt, J.C. Swarts, *Polyhedron* **2007** (26) 5075-5087.

⁷ J. Conradie, J.C. Swarts, *Organometallics* **2009** (28) 1018-1026.

RESULTS AND DISCUSSION

the reaction scheme leads to the reaction scheme below, with proposed stereochemistry, based on reaction studies of $[\text{Rh}(\beta\text{-diketonato})(\text{CO})(\text{PPh}_3)]$ complexes (section 2.4.3, Chapter 2).

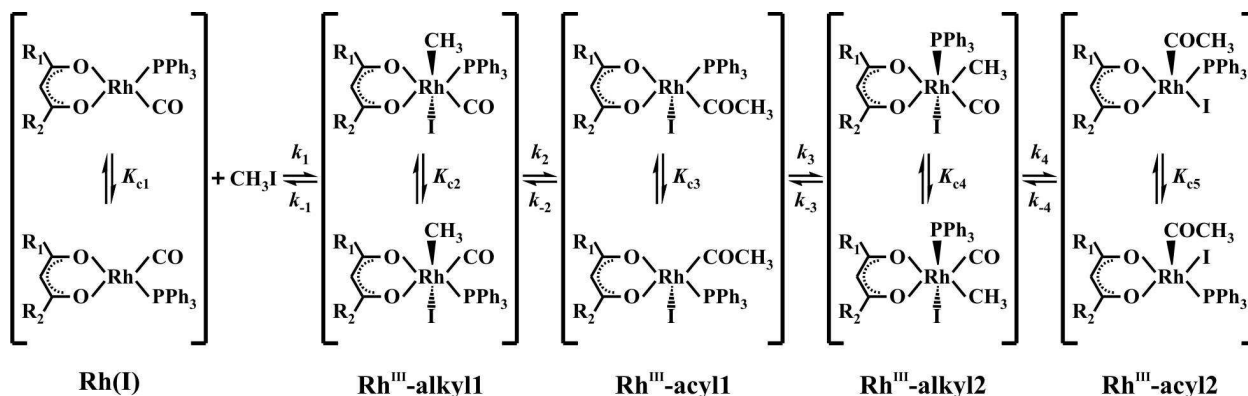


Figure 3.1: The proposed reaction scheme of the reaction of methyl iodide with $[\text{Rh}(\beta\text{-diketonato})(\text{CO})(\text{PPh}_3)]$, showing specific stereochemistry.

It is of interest to see whether the reaction $[\text{Rh}(\text{acac})(\text{CO})(\text{PPh}_3)] + \text{CH}_3\text{I}$ also gives the $\text{Rh}^{\text{III}}\text{-acyl2}$ product and whether the stereochemistry of Figure 3.1 also applies to this reaction. Since the acac ligand bonded to the rhodium centre is symmetrical, only one isomer in each reaction step has to be considered and the reaction scheme in Figure 3.1 can be simplified to the reaction scheme in Figure 3.2. With ^1H NMR spectroscopy, the $\text{Rh}^{\text{III}}\text{-alkyl}$ complexes of the $[\text{Rh}^{\text{III}}(\text{acac})(\text{CH}_3)(\text{CO})(\text{PPh}_3)(\text{I})]$ type and the $\text{Rh}^{\text{III}}\text{-acyl}$ complexes of the $[\text{Rh}^{\text{III}}(\text{acac})(\text{COCH}_3)(\text{PPh}_3)(\text{I})]$ type can be identified by the resonance signals of the methyl groups at $\sim 2.0\text{-}1.3$ ppm and ~ 3 ppm respectively.^{5,6,7,8,9,10} Additionally, ^1H NOESY spectroscopy provides valuable information of the stereochemistry of the reaction products, when no crystals suitable for X-ray analysis have been obtained.

⁸ M.M. Conradie, J. Conradie, *Inorg. Chim. Acta* **2008** (361) 2285-2295.

⁹ N.F. Stuurman, J. Conradie, *J. Organomet. Chem.* **2009** (694) 259-268.

¹⁰ M.M. Conradie, J. Conradie, *Inorg. Chim. Acta* **2008** (361) 208-218.



Figure 3.2: The proposed reaction scheme of the reaction of methyl iodide with [Rh(acac)(CO)(PPh₃)], showing specific stereochemistry. The colour code in this figure will be used throughout this section.

3.1.2.2 Reaction products - NMR study.

Representative ¹H NMR spectra of a sample, recorded *in situ* during the reaction [Rh(acac)(CO)(PPh₃) + CH₃I], are presented in Figure 3.3 and selected spectral parameters are summarized in Table 3.1 (the region of phenyl protons of the triphenylphosphine ligand (PPh₃) is excluded). The two spectra shown were recorded at 10 minutes and 18 hours respectively after the reaction has been initiated. Different rhodium complexes (colour coded according to Table 3.1 and Figure 3.2) can be distinguished on the spectra.

Table 3.1: ¹H NMR spectral parameters of the reaction of methyl iodide with [Rh(acac)(CO)(PPh₃)]. The colour code in this table will be used throughout this section.

Compound	$\delta^1\text{H} / \text{ppm}$					Coupling constants / Hz ⁱⁱⁱ
	CH (acac)	CH ₃ (acac) ⁱ	CH ₃ (acac) ⁱⁱ	CH ₃ (Rh-CH ₃)	CH ₃ (Rh-COCH ₃)	
Rh(I)	5.449	2.108	1.623	-	-	-
Rh ^{III} -alkyl1	5.496	2.089	1.959	1.387	-	² J = 2, ³ J = 2
Rh ^{III} -acyl1	5.471	2.230	1.662	-	2.966	-
Rh ^{III} -alkyl2	4.898	1.743	1.735	1.676	-	² J = 2, ³ J = 4
Rh ^{III} -acyl2	5.523	2.223	1.651	-	2.904	-

ⁱ The CH₃ side groups of the acac ligand nearest to the O *trans* to the PPh₃ group.

ⁱⁱ The CH₃ side groups of the acac ligand nearest to the O *cis* to the PPh₃ group.

ⁱⁱⁱ ²J(H-C-Rh) and ³J(H-C-Rh-P) coupling of the methyl protons of the alkyl complexes.

RESULTS AND DISCUSSION

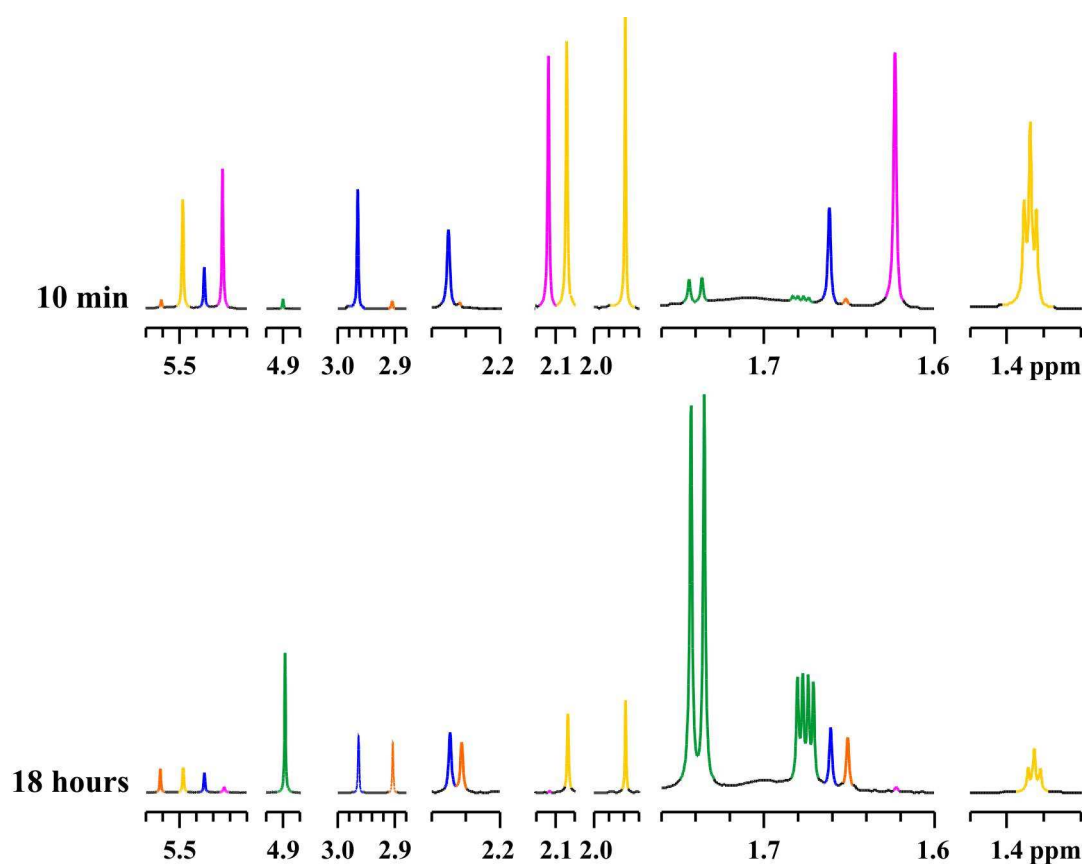


Figure 3.3: ^1H NMR spectra of the reaction of methyl iodide with $[\text{Rh}(\text{acac})(\text{CO})(\text{PPh}_3)]$. The two spectra were recorded at 10 minutes and 18 hours respectively after the reaction had been initiated. The peaks are colour coded according to the Rh(I) and Rh(III) complexes in Table 3.1 and Figure 3.2.

The signals in the ^1H NMR spectra of the reaction $[\text{Rh}(\text{acac})(\text{CO})(\text{PPh}_3)] + \text{CH}_3\text{I}$ (Figure 3.3) were assigned to the applicable Rh(III) complexes by monitoring the relative increase and decrease of the peaks as the reaction proceeds and by comparing it with the data obtained by Varshavsky *et al.*⁵ The group of low field signals represents the methine region (5.6-4.8 ppm) of the methine (CH) protons of the acac ligand. The methine signals of Rh(I), Rh^{III}-alkyl1, Rh^{III}-acyl1 and Rh^{III}-acyl2 are located at ~5.5 ppm, whereas the methine signal of Rh^{III}-alkyl2 is shifted to a higher field (4.90 ppm). This shift of the methine proton is due to shielding caused by the phenyl rings, as was described in a previous oxidation addition study of $[\text{Rh}(\text{fctfa})(\text{CO})(\text{PPh}_3)]$.¹¹ In the crystal structure⁶ of $[\text{Rh}(\text{fctfa})(\text{CH}_3)(\text{CO})(\text{PPh}_3)(\text{I})]$ -alkyl2, the PPh_3 group and the iodide are above and below the plane formed by the fctfa ligand and the other two groups bonded to the rhodium centre. The positioning of the PPh_3 group above the plane as in $[\text{Rh}(\text{fctfa})(\text{CH}_3)(\text{CO})(\text{PPh}_3)(\text{I})]$ -alkyl2, implies that as the PPh_3 group rotates, a Ph group will

¹¹ M.M. Conradie, J. Conradie, *S. Afr. J. Chem.* **2008** (61) 102-111.

be rotating direct above the methine proton of the β -diketonato ligand. The ring current inside the phenyl ring shields the methine proton direct below it to a higher field.¹² Therefore, the observed higher field shift of the methine proton of the acac ligand in $[\text{Rh}(\text{acac})(\text{CH}_3)(\text{CO})(\text{PPh}_3)(\text{I})]\text{-alkyl2}$ is consistent with the PPh_3 group being positioned above the plane. By the same reasoning, it is expected that the PPh_3 group of $[\text{Rh}(\text{acac})(\text{COCH}_3)(\text{PPh}_3)(\text{I})]\text{-alkyl1}$ should be positioned in the square planar plane formed by the acac ligand, since the methine signal at ~ 5.5 ppm is not shifted to a higher field. These results are in agreement with the stereochemistry of the complexes proposed in Figure 3.2.

The remaining resonances, namely a number of peaks in the methyl region (3.0-1.3 ppm), correspond to various protons of the methyl (CH_3) groups. Three types of methyl groups are present: the CH_3 side groups of the acac ligand, the CH_3 groups bonded direct to the rhodium atom (as in alkyl complexes) and the CH_3 groups bonded to a carbonyl group (as in acyl complexes). The Rh(I) and Rh(III) complexes present in the reaction mixture have different stereochemistry around the rhodium centre. The chemical environment, of the two CH_3 side groups of the symmetrical acac ligand bonded to the rhodium centre, is therefore different for each complex. One should therefore expect to observe five pairs of acac methyl peaks as the reaction progresses: one pair from the Rh(I) complex and four pairs from the Rh(III) complexes. The pairs of acac methyl peaks are as follow: 2.11 & 1.62 ppm for Rh(I), 2.09 & 1.96 ppm for $\text{Rh}^{\text{III}}\text{-alkyl1}$, 2.23 & 1.66 ppm for $\text{Rh}^{\text{III}}\text{-acyl1}$, 1.74 & 1.73 ppm for $\text{Rh}^{\text{III}}\text{-alkyl2}$ and 2.22 & 1.65 ppm for $\text{Rh}^{\text{III}}\text{-acyl2}$. A shift of ~ 0.5 ppm exists between the acac methyl pairs of Rh(I), $\text{Rh}^{\text{III}}\text{-acyl1}$ and $\text{Rh}^{\text{III}}\text{-acyl2}$. The shift of the $\text{Rh}^{\text{III}}\text{-alkyl1}$ methyl pairs is smaller (~ 0.1 ppm), but is still significant. The $\text{Rh}^{\text{III}}\text{-alkyl2}$ methyl pairs have a very small shift of 0.008 ppm. According to this data, all the rhodium complexes except $\text{Rh}^{\text{III}}\text{-alkyl2}$ must have the PPh_3 group oriented in the plane of the acac ligand (Figure 3.2). In this way, the acac methyl group *cis* to the PPh_3 group is shielded through space, causing the signal of this group to move to a higher field compared to the acac methyl group *trans* to the PPh_3 group. For $\text{Rh}^{\text{III}}\text{-alkyl2}$, the PPh_3 group is oriented in the apical position (Figure 3.2). This results in the shielding of both the acac methyl groups of $\text{Rh}^{\text{III}}\text{-alkyl2}$ (as is also the case with this complex's methine peak) causing both signals to move with almost an equal shift to a higher field.

¹² J. Clayden, N. Greeves, S. Warren, P. Wothers, *Organic Chemistry*, Oxford University Press, Oxford, UK, 2001, p251.

RESULTS AND DISCUSSION

Remaining are the last two types of methyl groups: the CH₃ groups bonded direct to the rhodium atom (as in alkyl complexes) and the CH₃ groups bonded to a carbonyl group (as in acyl complexes).

The COCH₃ methyl groups are expected as singlets in the region of ~3 ppm, whereas the Rh-CH₃ methyl groups are expected as doublets of doublets in the region of 2.0-1.3 ppm.^{5,6,7,8,9,10} The doublets of doublets are expected as a result of the spin-spin coupling of the protons with rhodium (spin = 1/2; ²J; ¹H-¹³C-¹⁰³Rh) and phosphorous (spin = 1/2; ³J; ¹H-¹³C-¹⁰³Rh-³¹P).¹³ The singlets at 2.97 and 2.90 ppm represent the COCH₃ methyl groups of Rh^{III}-acyl1 and Rh^{III}-acyl2 respectively. The doublets of doublets at 1.39 and 1.68 ppm represent the Rh-CH₃ methyl groups of Rh^{III}-alkyl1 and Rh^{III}-alkyl2 respectively. It is interesting to note that the coupling constants to rhodium are similar in both Rh^{III}-alkyl1 and Rh^{III}-alkyl2 (2 Hz), but the values of the coupling constants to phosphorous are noticeably different (2 and 4 Hz respectively). It was suggested by Varshavsky *et al.*⁵ that the difference in coupling is due to the difference in the relative positions of the methyl and the phosphine ligands of Rh^{III}-alkyl1 and Rh^{III}-alkyl2. This is in agreement with the stereochemistry of the complexes proposed in Figure 3.2.

To further investigate the stereochemistry, 1D ¹H NOESYs were recorded *in situ* during the reaction, to establish the relative dispositions of the ligands in Rh^{III}-alkyl1 and Rh^{III}-alkyl2 (Figure 3.4 and Figure 3.5 respectively). Irradiation of the Rh-CH₃ resonance of Rh^{III}-alkyl1 (at *ca* 1.4 ppm), resulted in an NOE coupling with the PPh₃ groups, the methine proton and the CH₃ side groups of the acac ligand (Figure 3.4). This result is only possible if the CH₃ group, bonded to the rhodium centre of Rh^{III}-alkyl1, is above the square planar plane, with the PPh₃ group adjacent to the CH₃ group. The NOE coupling with the methine proton rules out the possibility of the CH₃ group being in the square planar plane. From the 1D ¹H NOESY spectra it is not possible to establish whether the CO group or the I is adjacent to the CH₃ group, since these groups do not contain any protons. These results are in agreement with the stereochemistry of the Rh^{III}-alkyl1 complex proposed in Figure 3.2.

¹³ C.A. Reilly, H. Thyret, *J. Am. Chem. Soc.* **1967** (89) 5144-5149.

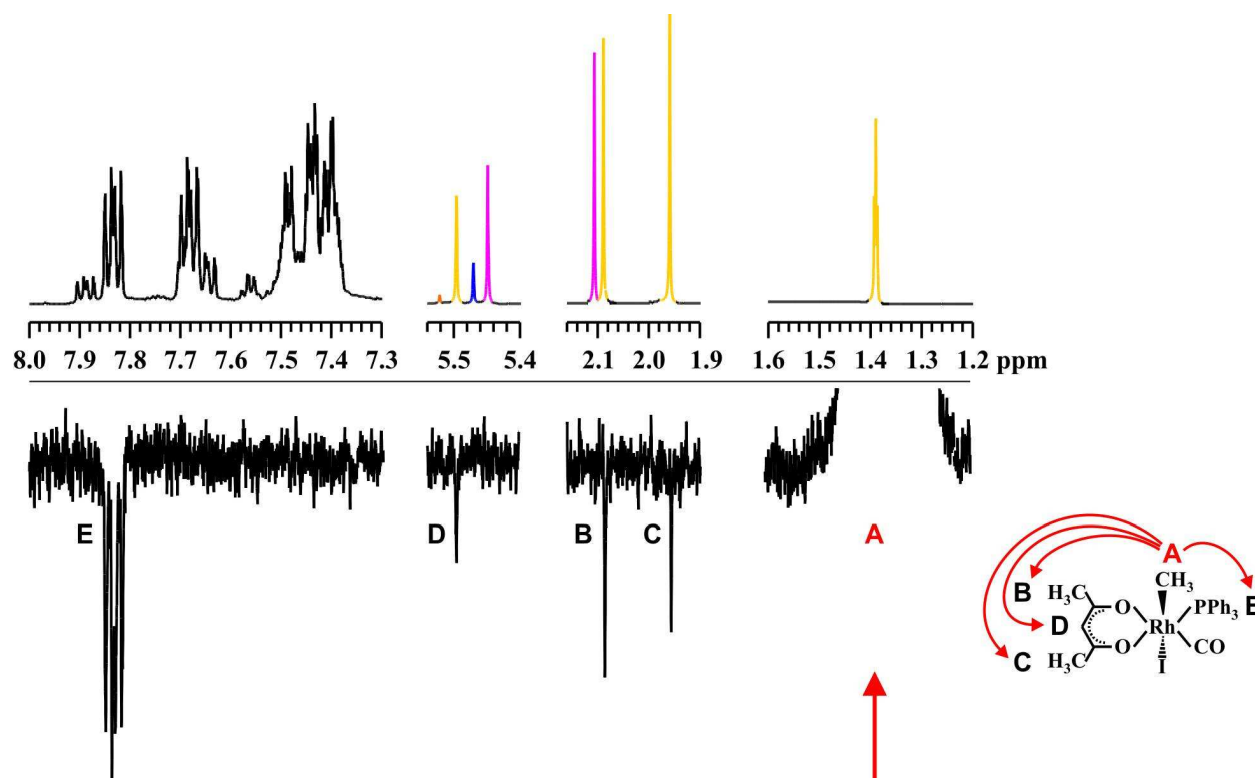


Figure 3.4: ^1H NMR (top) and 1D ^1H NOESY (bottom) of $[\text{Rh}^{\text{III}}(\text{acac})(\text{CO})(\text{PPh}_3)(\text{Me})(\text{I})]\text{-alkyl1}$, pulsing on the Rh-CH_3 resonance at *ca* 1.4 ppm. Coupling is as illustrated.

Insight into the stereochemistry of $\text{Rh}^{\text{III}}\text{-acyl1}$, by means of 1D ^1H NOESY spectroscopy, is not possible. Firstly, the conversion of $\text{Rh}^{\text{III}}\text{-acyl1}$ to $\text{Rh}^{\text{III}}\text{-alkyl2}$ is very rapid and it is not practical to perform a NOESY on the timescale of the NMR. Secondly, only the signal of COCH_3 (2.97 ppm) and the one CH_3 side group of the acac ligand (2.23 ppm) is sufficiently isolated from the other signals in order to be irradiated independently. Irradiation of these two peaks will result in no usable data, since only a positive NOE coupling may be used and the absence of a coupling is regarded as not a positive result. To confirm the stereochemistry of the rhodium complexes by means of 1D ^1H NOESY spectroscopy, a group containing protons is needed in the apical position. Since the suggested structure of $\text{Rh}^{\text{III}}\text{-acyl1}$ does not contain such a group, no reliable insight into the stereochemistry of $\text{Rh}^{\text{III}}\text{-acyl1}$ can be obtained by means of 1D ^1H NOESY spectroscopy.

Irradiation of the PPh_3 resonance of $\text{Rh}^{\text{III}}\text{-alkyl2}$ (at *ca* 7.8-7.4 ppm), resulted in an NOE coupling with the Rh-CH_3 groups, the methine proton and the CH_3 side groups of the acac ligand (Figure 3.5). This result is only possible if the PPh_3 group is above the square planar plane, with the CH_3 group adjacent to the PPh_3 group. The NOE coupling with the methine proton rules out

RESULTS AND DISCUSSION

the possibility of the PPh₃ group being in the square planar plane. From the 1D ¹H NOESY spectra it is not possible to establish whether the CO group or the I is adjacent to the PPh₃ group, since these groups do not contain any protons. These results are in agreement with the proposed reaction scheme in Figure 3.2. Irradiation of the Rh-CH₃ resonance of Rh^{III}-alkyl₂ (at *ca* 1.68 ppm) resulted in a NOE coupling with the PPh₃ groups. This result is consistent with the Rh-CH₃ group being adjacent to the PPh₃ group. Irradiation of the methine proton resonance of Rh^{III}-alkyl₂ (at *ca* 4.9 ppm) resulted in a NOE coupling with the PPh₃ groups and the CH₃ side groups of the acac ligand. This result is only possible if the PPh₃ group is above the square planar plane. The combination of the last two results therefore indicated that the Rh-CH₃ group is in the square planar plane. These results are in agreement with the stereochemistry of the Rh^{III}-alkyl₂ complex proposed in Figure 3.2.

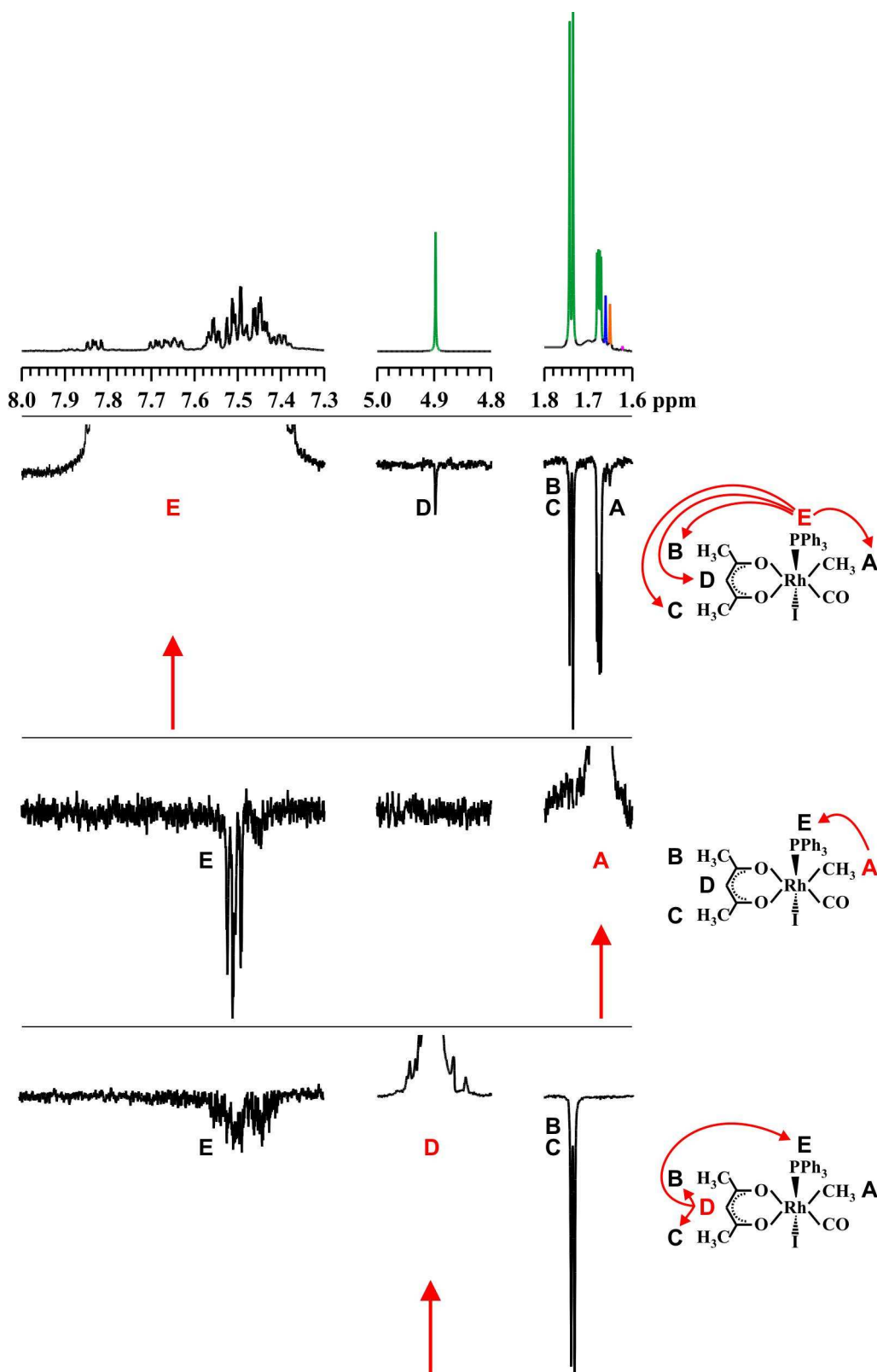


Figure 3.5: ^1H NMR (top) and three 1D ^1H NOESYs (bottom) of $[\text{Rh}^{\text{III}}(\text{acac})(\text{CO})(\text{PPh}_3)(\text{Me})(\text{I})]$ -alkyl₂, pulsing on the resonances as indicated. Coupling is as illustrated.

In conclusion, all ^1H NMR and 1D ^1H NOESY data presented here are in agreement with the stereochemistry of the reaction $[\text{Rh}(\text{acac})(\text{CO})(\text{PPh}_3)] + \text{CH}_3\text{I}$, proposed in Figure 3.2. This scheme was proposed on the basis of information obtained from the methyl iodide reaction with similar $[\text{Rh}(\beta\text{-diketonato})(\text{CO})(\text{PPh}_3)]$ complexes (section 2.4.3, Chapter 2). To summarize the findings of this NMR study:

- Methyl iodide is oxidatively added to the square planar Rh(I) complex to form an octahedral Rh^{III} -alkyl1 complex with the CH_3 group in the apical position and the PPh_3 group in the plane of the acac ligand. The relative positions of the I and the CO group can not be determined by 1D ^1H NOESY spectroscopy.
- Migration of the CH_3 group to the CO group results in a square pyramidal Rh^{III} -acyl1 complex with the PPh_3 groups in the plane of the acac ligand. No further reliable insight into the stereochemistry of Rh^{III} -acyl1 can be obtained by means of 1D ^1H NOESY spectroscopy.
- The next product observed in this reaction is an octahedral Rh^{III} -alkyl2 complex with the CH_3 group in the plane of the acac ligand and the PPh_3 group in the apical position. The relative positions of the I and the CO group can not be determined by 1D ^1H NOESY spectroscopy.
- The final product observed on the NMR is a square pyramidal Rh^{III} -acyl2 complex with the PPh_3 group in the plane of the acac ligand.

Although all these findings are in agreement with the stereochemistry proposed in Figure 3.2, some uncertainties still remain about the relative position of the I, the CO and the COCH_3 groups in these Rh(III) reaction products. Therefore, before a study of the mechanism of the multistep reaction $[\text{Rh}(\text{acac})(\text{CO})(\text{PPh}_3)] + \text{CH}_3\text{I}$ can be performed, more research on the stereochemistry of the reaction products is needed. This was addressed by a DFT computational study of the relative stability of the possible reaction products, as presented in the first part of section 3.1.2.3.

3.1.2.3 Reaction products and mechanism - DFT computational study.

DFT calculations were carried out on the reaction $[\text{Rh}(\text{acac})(\text{CO})(\text{PPh}_3)] + \text{CH}_3\text{I}$, using the PW91 functional and the TZP basis set. The solvent used in all the calculations is methanol ($\epsilon_0 = 32.6$). This DFT computational method was tested and found reliable for $[\text{Rh}(\beta\text{-diketonato})(\text{CO})(\text{PPh}_3)]$ complexes in a previous study.¹⁴ For the details of the methods and equations used, see section 4.5.2.1 (Chapter 4). The reactants, $[\text{Rh}(\text{acac})(\text{CO})(\text{PPh}_3)]$ and CH_3I , are taken as the energy zero

¹⁴ M.M. Conradie, J. Conradie, *Inorg. Chim. Acta* **2009** (362) 519-530.

level for all energies and thermodynamic parameters stated. Energies (E) refer to the total bonding energies (E_{TBE}) in $\text{kJ}\cdot\text{mol}^{-1}$.

Reaction products.

Theoretically, the different arrangements of the groups bonded to the rhodium(III) centre after the oxidative addition of CH_3I give rise to a possibility of twelve different octahedral Rh^{III} -alkyl isomers and six different square pyramidal Rh^{III} -acyl isomers. Since the enantiomers (six Rh^{III} -alkyl and three Rh^{III} -acyl mirror images) display the same computational and chemical properties, they can be excluded. This leaves one with the possibility of six Rh^{III} -alkyl isomers and three Rh^{III} -acyl isomers, as illustrated in Figure 3.6. The possibility of Rh^{III} -acyl isomers with a trigonal bipyramidal arrangement was also inspected, but resulted in such high relative energies that they were omitted from this study. The relative energies (ΔE) of all the possible Rh^{III} -alkyl and Rh^{III} -acyl reaction products are given in Figure 3.6.

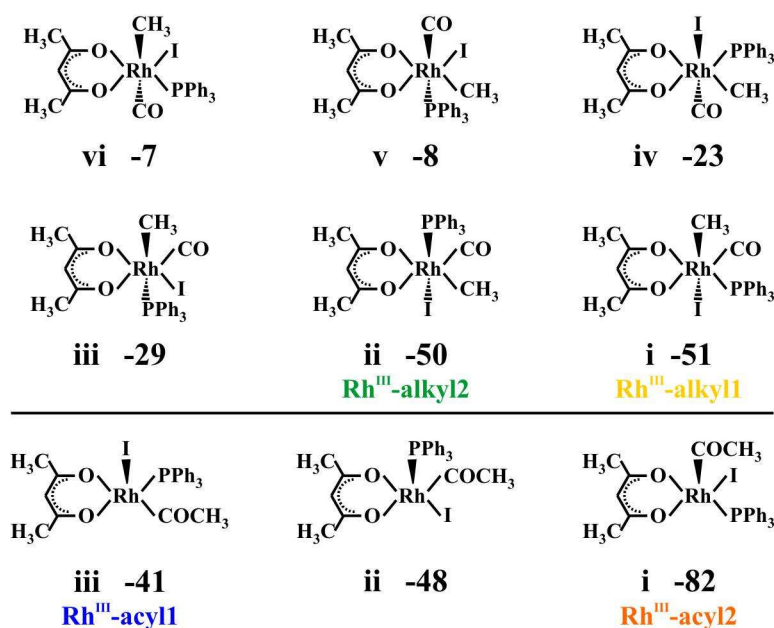


Figure 3.6: The theoretically possible Rh^{III} -alkyl and Rh^{III} -acyl reaction products in the reaction of methyl iodide with $[\text{Rh}(\text{acac})(\text{CO})(\text{PPh}_3)]$, excluding enantiomers. The energy ($\text{kJ}\cdot\text{mol}^{-1}$) of each complex is given relative to the reactants.

When comparing the relative energies of the possible Rh^{III} -alkyl complexes in Figure 3.6 with each other, the lowest energy alkyl isomers are alkyl-i and alkyl-ii. They are more than $21 \text{ kJ}\cdot\text{mol}^{-1}$ stable than the other possible Rh^{III} -alkyl complexes and would therefore be the most probable products in the reaction. Methyl iodide will be added either *cis* or *trans* to the square

RESULTS AND DISCUSSION

planar Rh(I) complex. Alkyl-ii is the lowest *cis* addition product, whilst alkyl-i is the lowest *trans* addition product. To distinguish whether *cis* or *trans* addition occurs, one has to consider the relative activation energies (ΔE^\ddagger) of the *cis* and *trans* transition states. The *trans* addition of methyl iodide in a linear/back manner was found to be more than 114 kJ.mol⁻¹ lower in energy than a *trans* addition in a bent manner or a *cis* addition in a front manner (Figure 3.7). These transition states will be discussed shortly. Alkyl-i would therefore be the preferred product of the oxidative addition reaction, which is Rh^{III}-alkyl1 in Figure 3.2. The geometry of alkyl-i is consistent with the NMR results of the Rh^{III}-alkyl1 complex of this study (section 3.1.2.1). According to the NMR study, the Rh^{III}-alkyl1 complex has a geometry with the CH₃ group in the apical position and the PPh₃ group in the plane of the acac ligand. But the NMR study could not distinguish between the relative position of the I and the CO group in this Rh^{III}-alkyl1 complex. According to the computational data, Rh^{III}-alkyl1 has a geometry with the CO group in the plane of the acac ligand and the I in the apical position (Figure 3.6).

The activation energy (ΔE^\ddagger) of alkyl-ii to be formed direct from the *cis* addition of methyl iodide to rhodium(I) is too high (138 kJ.mol⁻¹). Since alkyl-i and alkyl-ii are equi-energetic, it is possible that alkyl-ii would form after rearrangement of the groups around the rhodium centre of alkyl-i (Rh^{III}-alkyl1). The geometry of alkyl-ii is consistent with the NMR results of the Rh^{III}-alkyl2 complex of this study (section 3.1.2.1). According to the NMR study, the Rh^{III}-alkyl2 complex has a geometry with the CH₃ group in the plane of the acac ligand and the PPh₃ group in the apical position. Based on the calculated relative stability of all the possible alkyl products (Figure 3.6), alkyl-ii would therefore be Rh^{III}-alkyl2. In the next section, a detailed DFT computational study of the reaction mechanism leading to Rh^{III}-alkyl2 from Rh^{III}-alkyl1 will be presented for additional proof of the proposed geometry of Rh^{III}-alkyl2.

The most stable product of the different rhodium(III) complexes in Figure 3.6, with a clear cut of energy, is Acyl-i. Acyl-i would therefore be the final and most stable product to be formed in the reaction, which is Rh^{III}-acyl2 in Figure 3.2. The geometry of Acyl-i is also consistent with the NMR results where it was found that the Rh^{III}-acyl2 complex has a geometry with the PPh₃ group in the plane of the acac ligand. This leaves us with either Acyl-ii or Acyl-iii as Rh^{III}-acyl1. When comparing the relative energies of these Rh^{III}-acyl isomers, one can not distinguish between them on the grounds of their relative energies, since they only differ by 7 kJ.mol⁻¹.

Though, NMR results indicate that the PPh_3 group of Rh^{III} -acyl1 should be in the plane of the acac ligand. This rules out Acyl-ii and leaves only Acyl-iii as Rh^{III} -acyl1.

The stereochemistry of the reaction products of the reaction $[\text{Rh}(\text{acac})(\text{CO})(\text{PPh}_3)] + \text{CH}_3\text{I}$ can now fully be predicted on the grounds of the computational and the experimental (NMR) results. The geometries of Rh^{III} -alkyl1, Rh^{III} -alkyl2, Rh^{III} -acyl1 and Rh^{III} -acyl2 are as indicated by the labels in Figure 3.6. Though, a reaction product can only be formed if the activation energy (ΔE^\ddagger) is low enough for the reaction to occur. Therefore, a full DFT computational study of the transition states, the intermediate products and the reaction products is necessary to confirm the proposed stereochemistry of the different reaction products of the reaction $[\text{Rh}(\text{acac})(\text{CO})(\text{PPh}_3)] + \text{CH}_3\text{I}$. This step by step reaction mechanism is presented next.

Mechanism of the first reaction: $\text{Rh}(\text{I}) + \text{CH}_3\text{I} \rightarrow \text{Rh}^{\text{III}}$ -alkyl1.

The first step in the reaction is the oxidative addition of methyl iodide to the rhodium(I) complex. Three types of transition state structures (Figure 3.7) have been reported on the oxidative addition of methyl iodide to square planar rhodium(I) complexes (especially the Monsanto catalyst $[\text{Rh}(\text{CO})_2\text{I}_2]^-$, section 2.4.2, Chapter 2). Two types of TS structures result from *trans* addition ("linear/back" and "bent") and one type of TS structure results from *cis* addition ("front"). The linear/back transition state structure corresponds to an $\text{S}_{\text{N}}2$ mechanism, characterized by a linear $\text{Rh}-\text{C}_{\text{CH}_3}-\text{I}$ arrangement and by an $\text{Rh}-\text{C}_{\text{CH}_3}-\text{H}$ angle close to 90° . The methyl hydrogen atoms are located in the equatorial plane of the five-coordinated carbon atom, resulting in a trigonal bipyramidal arrangement. The bent and front transition state structures correspond to a side-on approach of the $\text{C}_{\text{CH}_3}-\text{I}$ bond to the rhodium atom. The bent transition state structure leads to the same intermediate product as the linear/back transition state structure - a cationic five-coordinated rhodium complex and a free iodide ion. The front transition state structure corresponds to a concerted three-centred oxidative addition mechanism, in which the $\text{Rh}-\text{I}$ and $\text{Rh}-\text{C}_{\text{CH}_3}$ bonds are formed simultaneously as $\text{I}-\text{C}_{\text{CH}_3}$ bond breaks, resulting in the *cis* addition of the methyl iodide.

RESULTS AND DISCUSSION

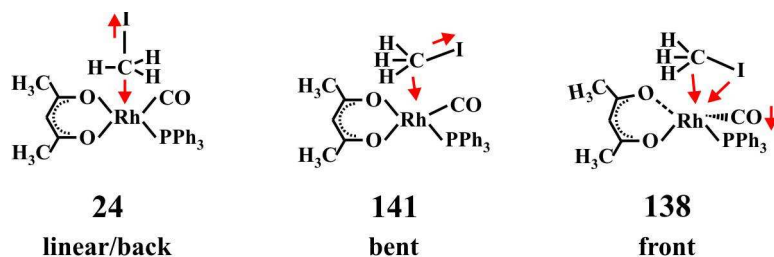


Figure 3.7: Schematic illustration of a "linear/back", "bent" and "front" transition states of the reaction $[\text{Rh}(\text{acac})(\text{CO})(\text{PPh}_3)] + \text{CH}_3\text{I}$. The movement of the applicable atoms in the transition state is indicated with the red arrows. The activation energies (ΔE^\ddagger) of the transition states are as indicated ($\text{kJ}\cdot\text{mol}^{-1}$).

All three the types of transition states were calculated for the oxidative addition reaction of methyl iodide to $[\text{Rh}(\text{acac})(\text{CO})(\text{PPh}_3)]$. The linear/back transition state is favoured with an activation barrier (ΔE^\ddagger) of $24 \text{ kJ}\cdot\text{mol}^{-1}$, which is $114 \text{ kJ}\cdot\text{mol}^{-1}$ less than the other two transition states. The activation energies and the thermodynamic data of the three types of transition states are given in Table 3.2. The experimental Gibbs free energy (ΔG^\ddagger) of the oxidative addition reaction, $[\text{Rh}(\beta\text{-diketonato})(\text{CO})(\text{PPh}_3)] + \text{CH}_3\text{I}$, is in the order of $75\text{-}90 \text{ kJ}\cdot\text{mol}^{-1}$.^{7,8,9,10} The calculated Gibbs free energy of only the linear/back transition state ($71 \text{ kJ}\cdot\text{mol}^{-1}$) is in agreement with related experimental values. It is therefore clear that the oxidative addition of methyl iodide to $[\text{Rh}(\text{acac})(\text{CO})(\text{PPh}_3)]$ occurs *via* a linear/back type of *trans* addition to form a cationic five-coordinated intermediate product (IM_{ab}) with a free iodide, as illustrated in Figure 3.8. The free iodide drifts away in the solvent system and can react with any neighbouring five-coordinated product. The coordination of an iodide to the cationic five-coordinated intermediate product proceeds with barrierless energy to an alkyl product with the geometry of Rh^{III} -alkyl1 (b) in Figure 3.6. The energy needed to rearrange the ligands of the cationic five-coordinated rhodium intermediate before the coordination of iodide, is too high for the rearrangement to occur (105 and $130 \text{ kJ}\cdot\text{mol}^{-1}$ *versus* the barrierless coordination of the iodide). The thermodynamic data of the reactants, the transition state (TS_{ab}), the cationic five-coordinated intermediate product (IM_{ab}) and the reaction product Rh^{III} -alkyl1 (b) are given in Table 3.3. The optimized structures with selected geometrical parameters are given in Figure 3.13 (reactants and reaction product), Figure 3.14 (intermediate product) and Figure 3.15 (transition state). The $\text{C}_{\text{CH}_3}\text{-I}$ bond length in the free methyl iodide is 2.18 \AA . This $\text{C}_{\text{CH}_3}\text{-I}$ bond length increases up to 2.61 \AA in the transition state (TS_{ab}) (Figure 3.8). At this point, the CH_3 group is 2.50 \AA away from the rhodium centre and the methyl hydrogen atoms are located in an equatorial plane with a $\text{Rh-C}_{\text{CH}_3}\text{-H}$ angle close to 90° . The CH_3 group continues to move closer to the rhodium centre. The $\text{C}_{\text{CH}_3}\text{-Rh}$ distance changes from 2.50 \AA to 2.08 \AA to 2.11 \AA as the reaction progresses

(TS_{ab}) → (IM_{ab}) → (b). In the step (IM_{ab}) → (b), the I also coordinates to the rhodium centre with a final Rh-I bond length of 2.96 Å.

Table 3.2: The PW91/TZP/methanol calculated relative activation energies and the thermodynamic data of the three types of transition states of the oxidative addition reaction [Rh(acac)(CO)(PPh₃)] + CH₃I. All energy values are given compared to the reactants.

	ΔE^\ddagger / kJ.mol ⁻¹	ΔH^\ddagger_{298K} / kJ.mol ⁻¹ <i>i</i>	ΔG^\ddagger_{298K} / kJ.mol ⁻¹ <i>ii</i>	ΔS^\ddagger_{298K} / J.K ⁻¹ .mol ⁻¹ <i>iii</i>
linear/back	24	27	71	-147
bent	141	139	184	-150
front	138	131	181	-167

i Enthalpy, calculated by equation 4.2 (section 4.5.2.1, Chapter 4).

ii Gibbs free energy, calculated by equation 4.3 (section 4.5.2.1, Chapter 4).

iii Entropy, calculated from the temperature dependent partition function in ADF at 298.15 K.

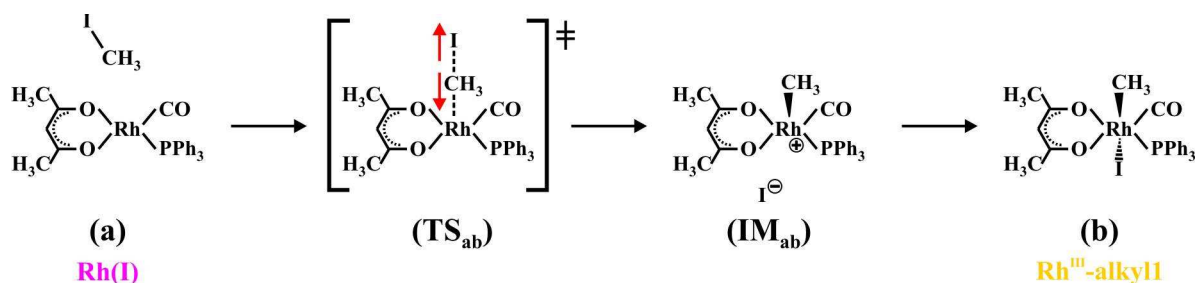


Figure 3.8: Reaction mechanism of the oxidative addition of methyl iodide to the square planar rhodium(I) complex [Rh(acac)(CO)(PPh₃)]. The movement of the applicable atoms in the transition state is indicated with the red arrows.

Mechanism of the second reaction: Rh^{III}-alkyl1 → Rh^{III}-acyl1.

The second reaction in the current study is the intramolecular migration of the CH₃ group to the CO group (Figure 3.9) in the six-coordinated Rh^{III}-alkyl1 (b) to form the five-coordinated Rh^{III}-acyl1 (c). The optimized structures with selected geometrical parameters are given in Figure 3.13 (reaction products), Figure 3.14 (intermediate product) and Figure 3.15 (transition state). The relative energies (ΔE) are given in Table 3.3. The axial CH₃ group in Rh^{III}-alkyl1 (b) has a Rh-C_{CH₃} bond length of 2.11 Å. This bond length increases up to 2.31 Å as the CH₃ group moves out of the axial position towards the CO group. At the point of the transition state (TS_{bc}), the CH₃ group is 1.91 Å away from the CO group which is slightly lifted out of the planar plane formed by the acac ligand. During the (b) → (TS_{bc}) step the Rh-C_{co}-O angle changed from 175° to 166° and the C_{CH₃}-Rh-CO angle changed from 89° to 53°. The transition state (TS_{bc}) has an activation barrier of 70 kJ.mol⁻¹. The CH₃ group continues to move further away from the rhodium centre and results in an intermediate product (IM_{bc}) which is 39 kJ.mol⁻¹ lower in energy than the transition state (TS_{bc}). At this point, the CH₃ group formed a 1.53 Å bond with the CO group and is 2.72 Å away from the centre rhodium with a C_{CH₃}-Rh-CO angle of 101°. Internal rotation by ~180° of the COCH₃ group in the intermediate product (IM_{bc}) leads to the Rh^{III}-alkyl1 (c) reaction product which is 21 kJ.mol⁻¹ lower in energy than the intermediate product (IM_{bc}). The C_{CH₃}-Rh-CO and Rh-C_{co}-O angles of the Rh^{III}-alkyl1 (c) reaction product are 21° and 104° respectively and the C_{CH₃}-C_{CO} bond length is 1.50 Å. The COCH₃ and PPh₃ groups lie in the plane formed by the acac ligand and the I is in the apical position.

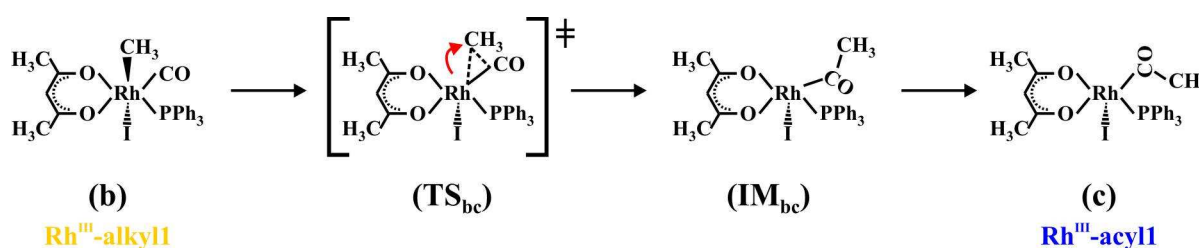


Figure 3.9: Reaction mechanism of the interconversion of Rh^{III}-alkyl1 to Rh^{III}-acyl1. The movement of the applicable atoms in the transition state is indicated with the red arrows.

Mechanism of the third reaction: Rh^{III}-acyl1 → Rh^{III}-alkyl2.

The third reaction in the current study is the interconversion of Rh^{III}-acyl1 (c) to Rh^{III}-alkyl2 (d) (Figure 3.10) which occurs in four distinctive steps. The optimized structures with selected geometrical parameters are given in Figure 3.13 (reaction products), Figure 3.14 (intermediate product) and Figure 3.15 (transition states). The relative energies (ΔE) are given in Table 3.3. The PPh₃ group in Rh^{III}-acyl1 (c) is in the plane formed by the acac ligand with a PPh₃-Rh-I angle of 94°. The interconversion is initiated by the movement of the PPh₃ group towards the apical position. At the point of the transition state (TS_{cd1}), the PPh₃-Rh-I angle has increased to 141°. The frequency animation of the transition state (TS_{cd1}) shows a strong movement of the PPh₃ group towards the apical position as well as strong movement of the O_{acac} atom (*trans* to the PPh₃ group) towards the PPh₃ group to rapidly decrease the O_{acac}-Rh-PPh₃ angle as the PPh₃-Rh-I angle increases. The PPh₃ group continues to move towards the apical position and results in an intermediate product (IM_{cd}) which is 90 kJ.mol⁻¹ lower in energy than the transition state (TS_{cd1}). The PPh₃ group is now in the apical position with the O_{acac}-Rh-PPh₃ and PPh₃-Rh-I angles 90° and 173° respectively. The Rh-O_{acac} bond length of the O_{acac} atom (*trans* to the COCH₃ group) slightly increased from 2.23 Å to 2.24 Å during the (TS_{cd1}) → (IM_{cd}) step. The COCH₃ group has rotated by ~90° and lies now flat in the planar plane formed by the acac. The reaction proceeds with a second transition state (TS_{cd2}) by the migration of the CH₃ group from the CO group towards the rhodium centre. The C_{CH₃}-C_{CO} distance increases from 1.53 Å to 1.87 Å to 2.84 Å as the reaction progresses (IM_{cd}) → (TS_{cd2}) → (d). The activation barrier of the methyl migration transition state (TS_{cd2}) is 27 kJ.mol⁻¹ and the reaction product Rh^{III}-alkyl2 (d) is 76 kJ.mol⁻¹ lower in energy than the transition state (TS_{cd2}). The reaction product Rh^{III}-alkyl2 (d) has an octahedral arrangement with the CO and CH₃ groups in the plane formed by the acac ligand and the I and PPh₃ group in the apical positions. Rh^{III}-alkyl2 was the main product of the NMR study (Figure 3.3).

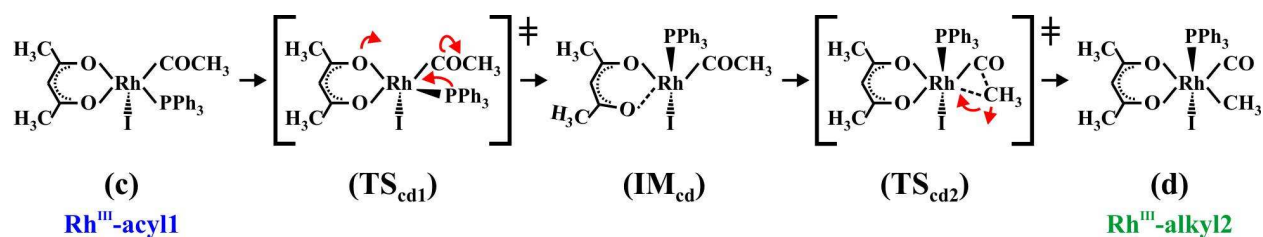


Figure 3.10: Reaction mechanism for the interconversion of Rh^{III}-acyl1 to Rh^{III}-alkyl2. The movement of the applicable atoms in the transition state is indicated with the red arrows.

Mechanism of the fourth reaction: Rh^{III}-alkyl2 → Rh^{III}-acyl2.

The final reaction in the current study is the interconversion of Rh^{III}-alkyl2 (d) to Rh^{III}-acyl2 (e) (Figure 3.11) which occurs in four distinctive steps. The optimized structures with selected geometrical parameters are given in Figure 3.13 (reaction products), Figure 3.14 (intermediate product) and Figure 3.15 (transition states). The relative energies (ΔE) are given in Table 3.3. The first two steps are the same as the backward reaction of Rh^{III}-alkyl2 (d) through the transition state (TS_{cd2}) to the intermediate product (IM_{cd}). This means, (TS_{de1}) = (TS_{cd2}) and (IM_{de}) = (IM_{cd}). The activation barrier of this backward methyl migration transition state (TS_{de1}) is 76 kJ.mol⁻¹ and the intermediate product (IM_{de}) is 27 kJ.mol⁻¹ lower in energy than the transition state (TS_{de1}). The backward equilibrium was experimentally observed in [Rh(fctfa)(CO)(PPh₃)]⁷ (Hfctfa = ferrocenyltrifluoroacetone) and the Monsanto catalyst.¹⁵ After Rh^{III}-alkyl2 (d) has interconverted back to (IM_{de}) = (IM_{cd}), the reaction proceeds through transition state (TS_{de2}) to the final reaction product Rh^{III}-acyl2 (e). The transition state (TS_{de2}) for the forward reaction to Rh^{III}-acyl2 (e) is favoured by 76 kJ.mol⁻¹ above the transition state (TS_{cd1}) for the backward reaction to Rh^{III}-acyl1 (c). The activation barrier of the transition state (TS_{de2}) is 14 kJ.mol⁻¹ and the reaction product Rh^{III}-acyl2 (e) is 95 kJ.mol⁻¹ lower in energy than the transition state (TS_{de2}). The Rh-O_{acac} bond length of the O_{acac} atom (*trans* to the COCH₃ group) in the intermediate product (IM_{de}) changes from 2.24 Å to 2.25 Å to 2.07 Å as the reaction progresses (IM_{de}) → (TS_{de2}) → (e). The acac ligand of the transition state (TS_{de2}) detaches itself from the rhodium centre on the side *trans* to the COCH₃ group. This is necessary, since the acac ring flips during the transition state (TS_{de2}) as the I and PPh₃ group move closer to each other. The P_{PPh₃}-Rh-I angles change from 173° to 140° to 93° as the reaction progresses (IM_{de}) → (TS_{de2}) → (e). The acac ligand is again fully bonded in the reaction product Rh^{III}-acyl2 (e).

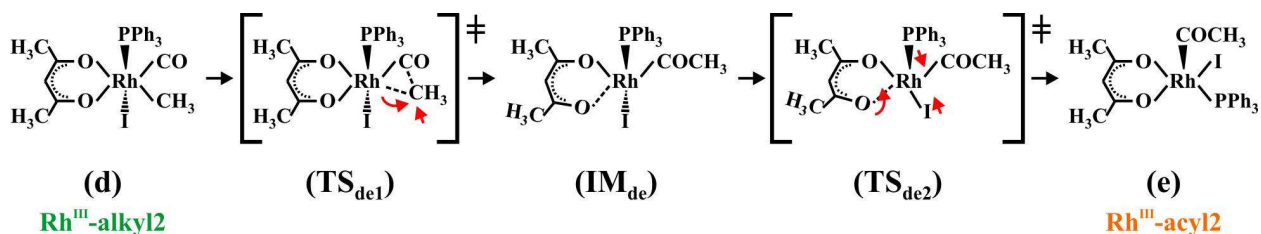


Figure 3.11: Reaction mechanism for the interconversion of Rh^{III}-alkyl2 to Rh^{III}-acyl2. The movement of the applicable atoms in the transition state is indicated with the red arrows.

¹⁵ P.M. Maitlis, A. Haynes, G.J. Sunley, M.J. Howard, *J. Chem. Soc., Dalton Trans.* **1996** 2187-2196.

Free energy profile.

The free energy profile of the mechanism of the multistep reaction $[\text{Rh}(\text{acac})(\text{CO})(\text{PPh}_3)] + \text{CH}_3\text{I}$ is given in Figure 3.12 and the thermodynamic data are summarized in Table 3.3. It is therefore evident that the $\text{Rh}^{\text{III}}\text{-acyl1 (c)} \rightarrow (\text{TS}_{\text{cd1}})$ methyl migration reaction has the highest free energy barrier ($\Delta G^\ddagger = 119 \text{ kJ}\cdot\text{mol}^{-1}$) and is therefore the rate-determining step of the overall reaction. This value is in agreement with the experimental value of $\sim 96 \text{ kJ}\cdot\text{mol}^{-1}$ of the $\text{Rh}^{\text{III}}\text{-acyl1} \rightarrow \text{Rh}^{\text{III}}\text{-alkyl2}$ conversion of $[\text{Rh}^{\text{III}}(\beta\text{-diketonato})(\text{COCH}_3)(\text{PPh}_3)(\text{I})\text{-acyl1}]$ (with $\beta\text{-diketonato} = \text{fctfa, fca, dfcm}$ and bfcm).^{6,7} The transition states (TS_{ab}), (TS_{bc}) and (TS_{de1}) have all similar free energy barriers of $65\text{-}74 \text{ kJ}\cdot\text{mol}^{-1}$. The final reaction product $\text{Rh}^{\text{III}}\text{-acyl2 (e)}$ has an overall negative free energy value of $-20 \text{ kJ}\cdot\text{mol}^{-1}$, indicating that the multistep reaction $[\text{Rh}(\text{acac})(\text{CO})(\text{PPh}_3)] + \text{CH}_3\text{I} \rightarrow \text{Rh}^{\text{III}}\text{-acyl2 (e)}$ will be spontaneous.

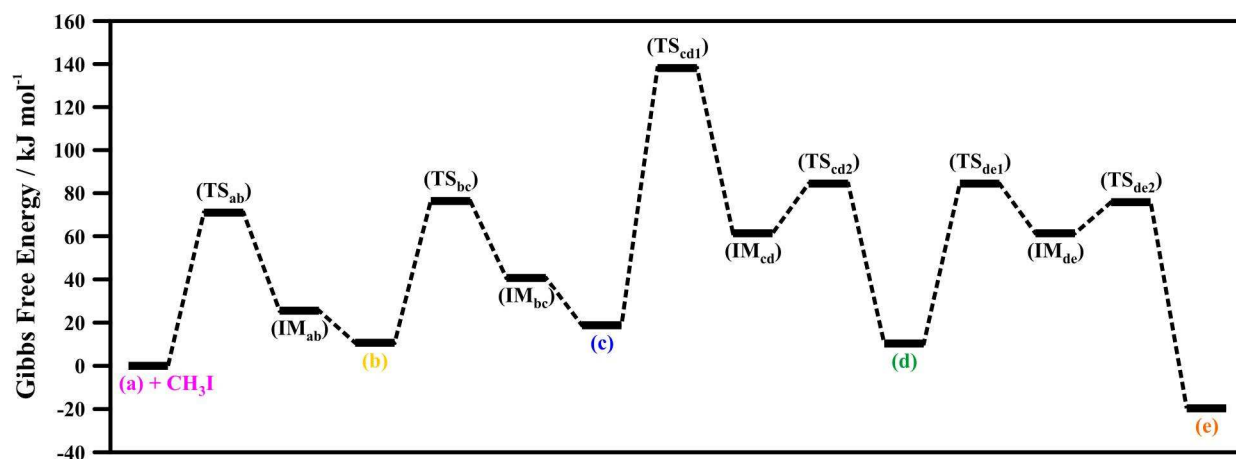


Figure 3.12: The Gibbs free energy of the reactants, transition states, intermediate products and reaction products during the multistep reaction $[\text{Rh}(\text{acac})(\text{CO})(\text{PPh}_3)] + \text{CH}_3\text{I}$.

Conclusions.

The linear/back transition state of the oxidative addition of CH_3I to the square planar $[\text{Rh}(\text{acac})(\text{CO})(\text{PPh}_3)]$ complex corresponds to an $\text{S}_{\text{N}}2$ nucleophilic attack by the rhodium metal centre on the methyl iodide. Bent and front types of transition states exist as well, but lie at a much higher energy level. The multistep reaction $[\text{Rh}(\text{acac})(\text{CO})(\text{PPh}_3)] + \text{CH}_3\text{I}$ consists of fourteen distinctive steps of which the $\text{Rh}^{\text{III}}\text{-acyl1 (c)} \rightarrow (\text{TS}_{\text{cd1}})$ step is the rate-determining step. The stereochemistry of the reaction products during the reaction is as proposed in Figure 3.2.

RESULTS AND DISCUSSION

Tables and graphs.

Table 3.3: The PW91/TZP/methanol calculated relative energies and the thermodynamic data of the transition states, the intermediate products and the reaction products during the reaction $[\text{Rh}(\text{acac})(\text{CO})(\text{PPh}_3)] + \text{CH}_3\text{I}$. All energy values are given compared to the reactants. Complexes are labelled according to Figures 3.7-3.10, with TS = transition state and IM = intermediate product.

	ΔE / $\text{kJ}\cdot\text{mol}^{-1}$	$\Delta H^{298\text{K}}$ / $\text{kJ}\cdot\text{mol}^{-1}$ ⁱ	$\Delta G^{298\text{K}}$ / $\text{kJ}\cdot\text{mol}^{-1}$ ⁱⁱ	$\Delta S^{298\text{K}}$ / $\text{J}\cdot\text{K}^{-1}\cdot\text{mol}^{-1}$ ⁱⁱⁱ
(a) Rh(I)	0	0	0	0
(TS _{ab})	24	27	71	-147
(IM _{ab})	13	-25	26	-168
(b) Rh^{III}-alkyl1	-51	-39	11	-166
(TS _{bc})	19	23	76	-179
(IM _{bc})	-20	-11	41	-175
(c) Rh^{III}-acyl1	-41	-27	19	-154
(TS _{cd1})	89	91	138	-157
(IM _{cd})	-1	5	61	-189
(TS _{cd2})	26	32	84	-177
(d) Rh^{III}-alkyl2	-50	-38	10	-163
(TS _{de1}) = (TS _{cd2})	26	32	84	-177
(IM _{de}) = (IM _{cd})	-1	5	61	-189
(TS _{de2})	13	25	76	-169
(c) Rh^{III}-acyl2	-82	-66	-20	-157

ⁱ Enthalpy, calculated by equation 4.2 (section 4.5.2.1, Chapter 4).

ⁱⁱ Gibbs free energy, calculated by equation 4.3 (section 4.5.2.1, Chapter 4).

ⁱⁱⁱ Entropy, calculated from the temperature dependent partition function in ADF at 298.15 K.

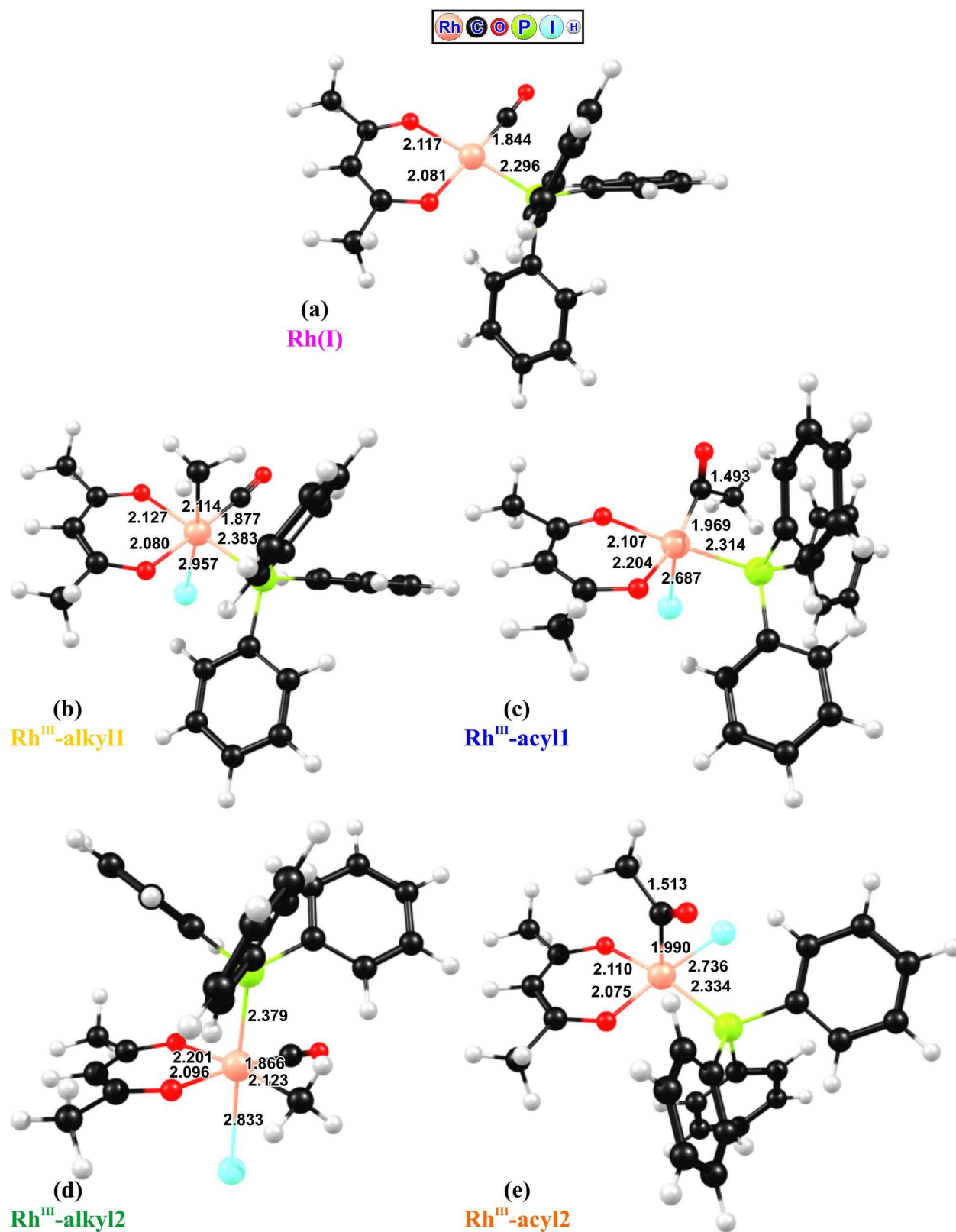


Figure 3.13: Optimized structures of the reactants and reaction products during the reaction $[\text{Rh}(\text{acac})(\text{CO})(\text{PPh}_3)] + \text{CH}_3\text{I}$. Distances are given in (Å). The colour code of the atoms is as indicated.

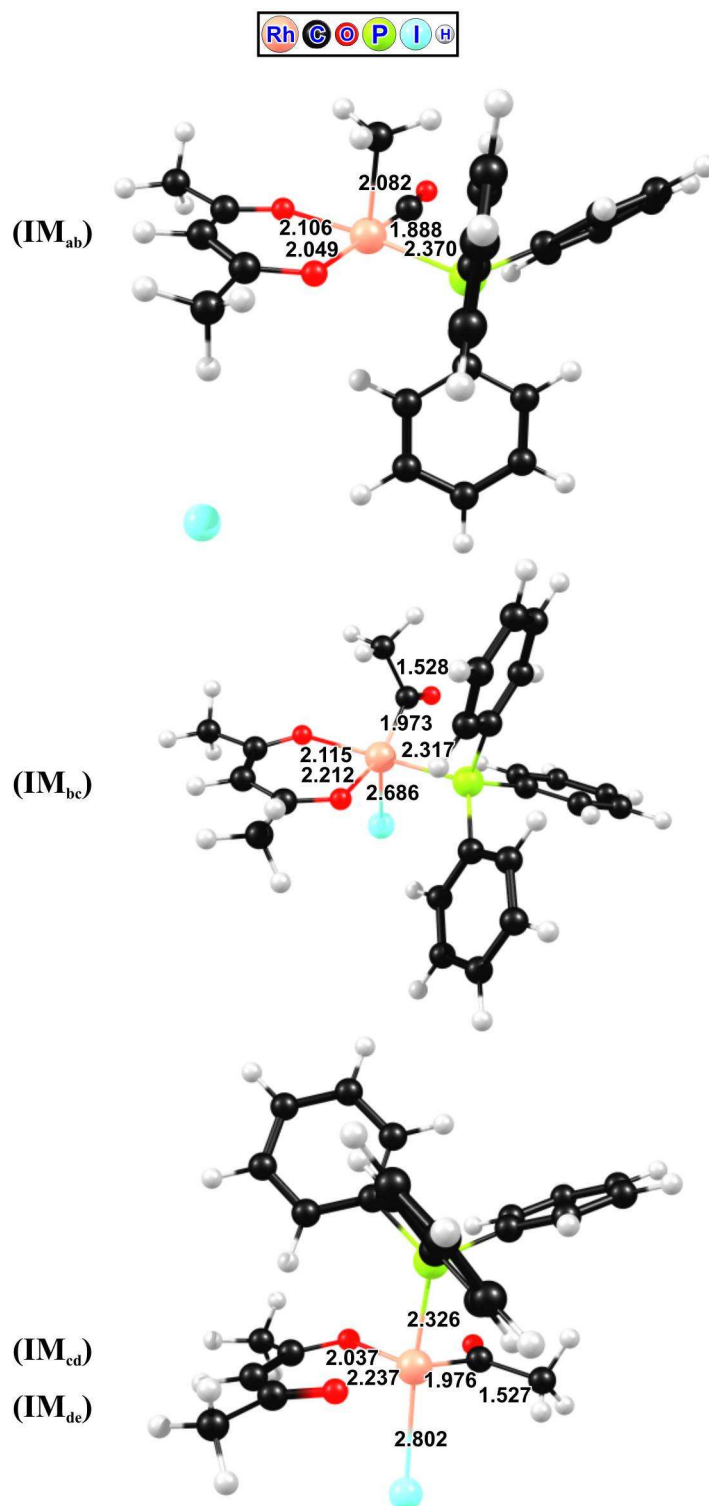


Figure 3.14: Optimized structures of the intermediate products during the reaction [Rh(acac)(CO)(PPh₃)] + CH₃I. Distances are given in (Å). The colour code of the atoms is as indicated.

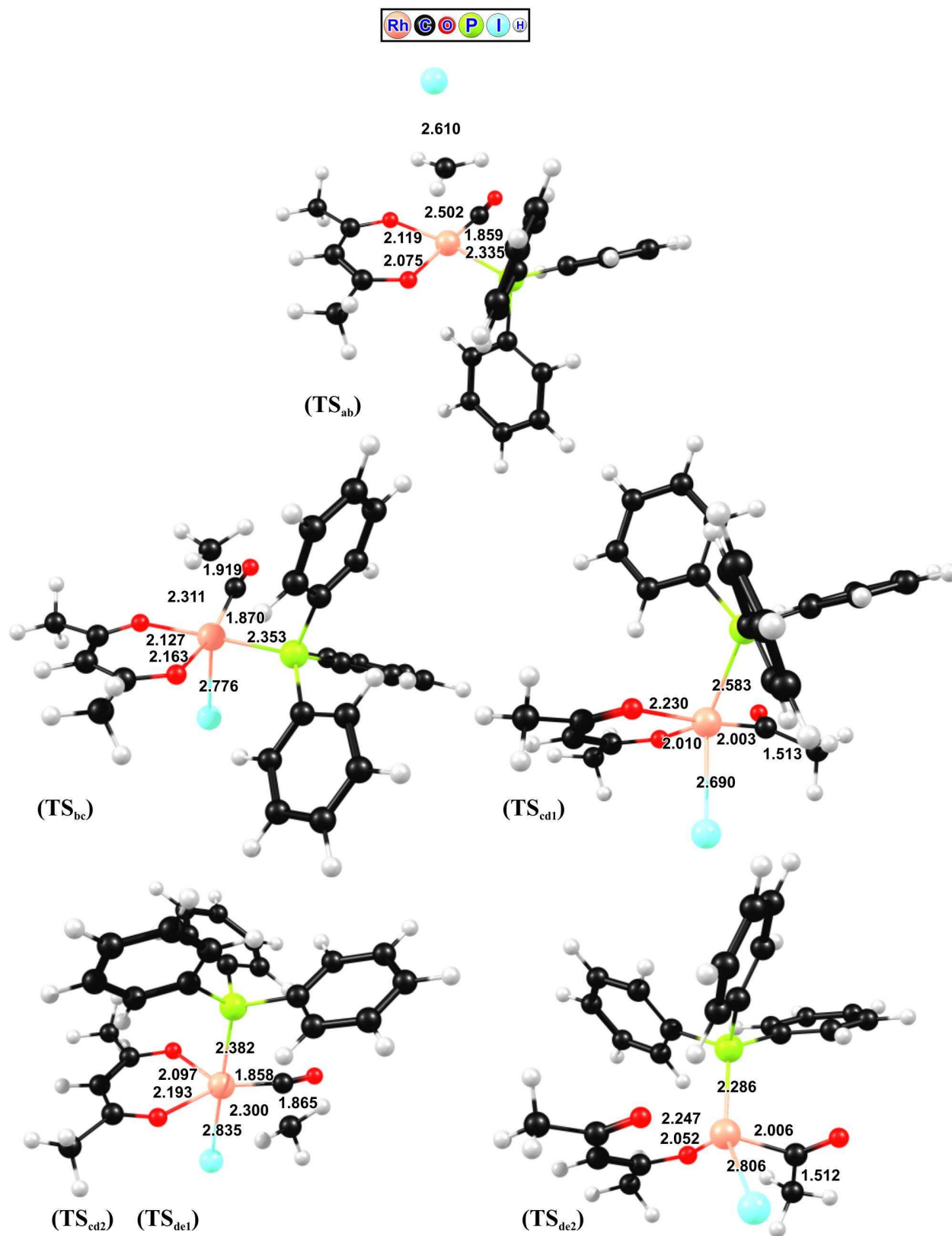


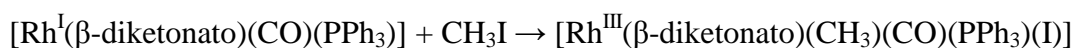
Figure 3.15: Optimized structures of the transition states during the reaction [Rh(acac)(CO)(PPh₃)] + CH₃I. Distances are given in (Å). The colour code of the atoms is as indicated.

3.1.3 [Rh(β -diketonato)(CO)(PPh₃)] + CH₃I.

3.1.3.1 Introduction.

Chemistry, like many other sciences finds itself in, is a competitive world. Competition determines the outcome of catalysts, in other words, whether a given catalyzed reaction is successful in generating a desired product in good yield, the product is obtained as a mixture or in very low yield. In general, the outcome of any competition is determined by the relative activation energies of each competing mechanism. If the reactants are the same for each of the competing processes, the situation simplifies further: the results of the competition are determined by the relative free energies of the transition states of each mechanism. Hence, it is the transition states which actually compete!

Rhodium catalysts are widely used in syntheses, of which the Monsanto catalyst¹⁵ is the best known example. The first (and rate determining) step in this carbonylation reaction is the oxidative addition of methyl iodide to the active catalyst (section 2.4.2, Chapter 2). To further investigate the first step of the oxidative addition of methyl iodide to the monocarbonyltriphenylphosphine rhodium catalysts, a DFT computational study was conducted for a series of [Rh(β -diketonato)(CO)(PPh₃)] complexes to explore the influence of the different side groups of the β -diketonato ligand on the activation energy (ΔE^\ddagger) of the transition states of each complex. The reaction under investigation is:



where β -diketonato = tta, bth, dtm and acac (Htta thenoyltrifluoroacetone, Hbth = benzoylthenoylacetone, Hdtm = dithenoylmethane and Hacac = acetylacetone), as illustrated in Figure 3.16. The solvent used in all the calculations is chloroform ($\epsilon_0 = 4.8$). The PW91/TZP computational method was tested and found reliable for [Rh(β -diketonato)(CO)(PPh₃)] complexes in a previous study.¹⁴ For further details of the methods and equations used, see section 4.5.2.1 (Chapter 4). The reactants, [Rh(β -diketonato)(CO)(PPh₃)] and CH₃I, are taken as the energy zero level for all energies and thermodynamic parameters stated. Energies (E) refer to the total bonding energies (E_{TBE}) in kJ.mol⁻¹.

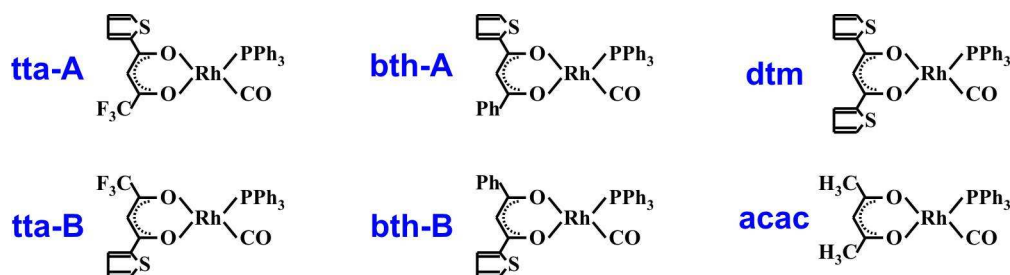


Figure 3.16: Schematic illustration of the $[\text{Rh}(\beta\text{-diketonato})(\text{CO})(\text{PPh}_3)]$ complexes of this study, where Htta = thenoyltrifluoroacetone, Hbth = benzoylthenoylacetone, Hdtm = dithenoylmethane and Hacac = acetylacetone. The labels "A" and "B" refer to the two stereo isomers of tta and bth.

The reaction of methyl iodide with the thenoyl ($\text{C}_4\text{H}_3\text{S}$) containing $[\text{Rh}(\beta\text{-diketonato})(\text{CO})(\text{PPh}_3)]$ complexes ($\beta\text{-diketonato} = \text{tta}, \text{bth}$ and dtm , Figure 3.16) proceeds through the same reaction sequence as with the reaction between methyl iodide and $[\text{Rh}(\text{acac})(\text{CO})(\text{PPh}_3)]$ (Figure 3.1 and Figure 3.2).^{8,10,14} Experimental^{8,10,14} and DFT computational¹⁴ studies are in agreement that the oxidative addition product, $[\text{Rh}(\text{RCOCHCO}(\text{C}_4\text{H}_3\text{S}))(\text{COCH}_3)(\text{PPh}_3)(\text{I})\text{-alkyl}]$ (where $\text{R} = \text{CF}_3, \text{Ph}$ and $\text{C}_4\text{H}_3\text{S}$), has an octahedral arrangement with the CO and PPh_3 groups in the plane of the $\beta\text{-diketonato}$ ligand and the I and CH_3 group in the apical position (section 2.4.3, Chapter 2). This is the product of *trans* addition of CH_3I to rhodium(I), as was also found for $[\text{Rh}(\text{acac})(\text{CO})(\text{PPh}_3)]$ (section 3.1.2) and the Monsanto catalyst.¹⁵ One main difference between the complexes of the current study and $[\text{Rh}(\text{acac})(\text{CO})(\text{PPh}_3)]$, is the introduction of two stereo isomers of $[\text{Rh}(\text{tta})(\text{CO})(\text{PPh}_3)]$ and $[\text{Rh}(\text{bth})(\text{CO})(\text{PPh}_3)]$ due to the unsymmetrical $\beta\text{-diketonato}$ backbone (Figure 3.16). The transition states of the oxidative addition of methyl iodide to both the stereo isomers therefore have to be considered. $[\text{Rh}(\text{dtm})(\text{CO})(\text{PPh}_3)]$, like $[\text{Rh}(\text{acac})(\text{CO})(\text{PPh}_3)]$, has a symmetrical $\beta\text{-diketonato}$ backbone and therefore only has one isomer in each step. This study focuses only on the first step of the oxidative addition reaction of methyl iodide to the rhodium(I) complex, in order to compare the thermodynamic parameters of these $[\text{Rh}(\text{RCOCHCO}(\text{C}_4\text{H}_3\text{S}))(\text{CO})(\text{PPh}_3)]$ complexes with that of $[\text{Rh}(\text{acac})(\text{CO})(\text{PPh}_3)]$ and the Monsanto catalyst. The first three steps of the oxidative addition reaction $[\text{Rh}(\text{RCOCHCO}(\text{C}_4\text{H}_3\text{S}))(\text{CO})(\text{PPh}_3)] + \text{CH}_3\text{I}$ is illustrated in Figure 3.17.

RESULTS AND DISCUSSION

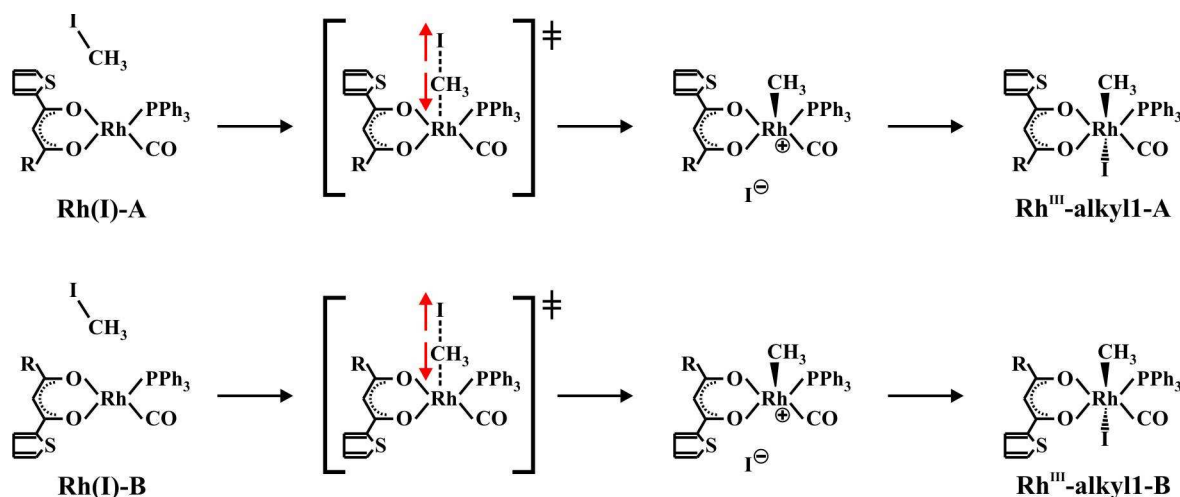


Figure 3.17: The first three steps of the oxidative addition reaction of methyl iodide with $[\text{Rh}(\beta\text{-diketonato})(\text{CO})(\text{PPh}_3)]$ ($\beta\text{-diketonato} = \text{tta, bth and dtm}$), showing specific stereochemistry and both stereo isomers.

3.1.3.2 Geometries of the transition states (TS).

The linear/back transition states of the reaction in Figure 3.17 were determined by DFT computational calculations. Table 3.4 summarizes the main geometric parameters of the calculated transition states of the oxidative addition reaction of methyl iodide to $[\text{Rh}(\beta\text{-diketonato})(\text{CO})(\text{PPh}_3)]$ ($\beta\text{-diketonato} = \text{tta, bth, dtm and acac}$) as well as to $[\text{Rh}(\text{CO})_2\text{I}_2]^-$ (the Monsanto catalyst). The transition state (TS) structures exhibit similar characteristics. For the TS $[\text{Rh}(\beta\text{-diketonato})(\text{CH}_3)(\text{CO})(\text{PPh}_3)]^+$ complexes, the $\text{Rh}-\text{C}_{\text{methyl}}$ bond lengths (2.39-2.45 Å) are slightly shorter than the $\text{I}-\text{C}_{\text{methyl}}$ bond lengths (2.61-2.72 Å). As for the TS $[\text{Rh}(\text{CO})_2(\text{CH}_3)\text{I}_2]$, the $\text{Rh}-\text{C}_{\text{methyl}}$ and the $\text{I}-\text{C}_{\text{methyl}}$ bond lengths were found to be of equal length (2.6 Å).¹⁶ The $\text{Rh}-\text{C}_{\text{methyl}}-\text{I}$ angles are the same for all the complexes (174-176°). The angle at which the CH_3I molecule enters the environment of the Rh centre, represented by the $\text{C}_{\text{methine}}-\text{Rh}-\text{C}_{\text{methyl}}-\text{I}$ torsion angle, is unique for each complex. In all the $[\text{Rh}(\beta\text{-diketonato})(\text{CO})(\text{PPh}_3)]$ complexes, the angle at which the CH_3I molecule approaches the rhodium centre is tilted slightly away from the PPh_3 group (Figure 3.21).

3.1.3.3 Molecular orbitals (MO) of the transition states (TS).

Rhodium(I) is a $d_{xz}^2 d_{yz}^2 d_{xy}^2 d_{z^2}^2 d_{x^2-y^2}^0$ complex of which the HOMO (highest occupied molecular orbital) exhibits mainly a d_{z^2} character. The main contribution to the $\text{Rh}-\text{C}_{\text{CH}_3}$ bond in

¹⁶ M. Feliz, Z. Freixa, P.W.N.M. van Leeuwen, C. Bo, *Organometallics* **2005** (24) 5718-5723.

the TS comes from the overlap of the d_{z^2} HOMO of the rhodium atom with the p_z LUMO (lowest unoccupied molecular orbital) of the methyl carbon. Since the molecular orbitals of the TS $[\text{Rh}(\beta\text{-diketonato})(\text{CH}_3)(\text{CO})(\text{PPh}_3)]^+$ ($\beta\text{-diketonato} = \text{tta}, \text{bth}, \text{dtm}$ and acac) look similar, the HOMO and LUMO visualizations of $[\text{Rh}(\text{tta})(\text{CH}_3)(\text{CO})(\text{PPh}_3)]^+-\text{A}$ are given in Figure 3.18 as representative example.

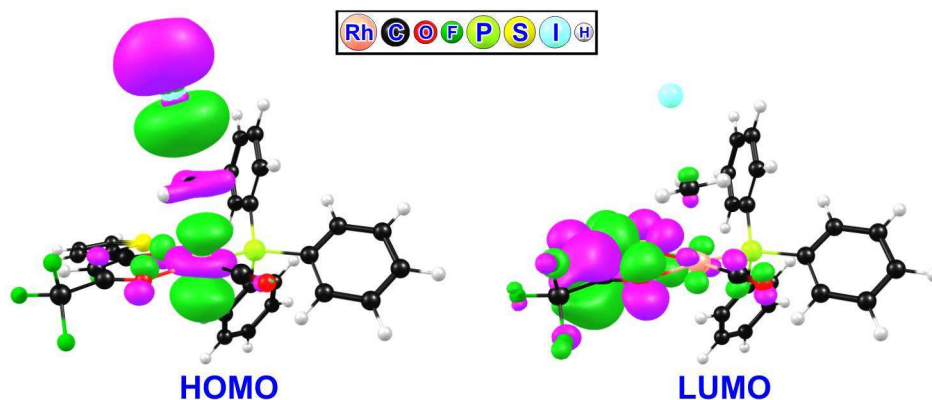


Figure 3.18: HOMO (highest occupied molecular orbital) and LUMO (lowest unoccupied molecular orbital) visualization of the transition state of $[\text{Rh}(\text{tta})(\text{CO})(\text{CH}_3)(\text{PPh}_3)(\text{I})]^{z-\text{A}}$, as a representative example of $[\text{Rh}(\beta\text{-diketonato})(\text{CO})(\text{CH}_3)(\text{PPh}_3)(\text{I})]^{z}$ ($\beta\text{-diketonato} = \text{tta}, \text{bth}, \text{dtm}$ and acac). Note the d_{z^2} -orbital at the rhodium centre of the HOMO diagram and the p_z -orbital at the methyl group of the LUMO diagram. The colour code of the atoms is as indicated.

3.1.3.4 Energy profile of the reaction.

The calculated relative energies (ΔE) of the reactants, TS structures and products are visualized in Figure 3.19 and the activation energies (ΔE^\ddagger) are tabulated in Table 3.4. The energy profile of the $[\text{Rh}(\beta\text{-diketonato})(\text{CO})(\text{PPh}_3)]$ complexes in this study is similar. The activation energies of the transition states vary between 27-33 $\text{kJ}\cdot\text{mol}^{-1}$ and the formation of the alkyl-products is 39-48 $\text{kJ}\cdot\text{mol}^{-1}$ lower in energy relative to the reactants. The relative energies of the reactants, transition states and the reaction product of the different isomers (A and B) of tta and bth are within 1 $\text{kJ}\cdot\text{mol}^{-1}$ of each other. $[\text{Rh}(\text{tta})(\text{CO})(\text{PPh}_3)]$ has the highest activation barrier (33 $\text{kJ}\cdot\text{mol}^{-1}$) followed by $[\text{Rh}(\text{bth})(\text{CO})(\text{PPh}_3)]$ (28-29 $\text{kJ}\cdot\text{mol}^{-1}$), $[\text{Rh}(\text{acac})(\text{CO})(\text{PPh}_3)]$ (27 $\text{kJ}\cdot\text{mol}^{-1}$) and $[\text{Rh}(\text{dtm})(\text{CO})(\text{PPh}_3)]$ (25 $\text{kJ}\cdot\text{mol}^{-1}$).

RESULTS AND DISCUSSION

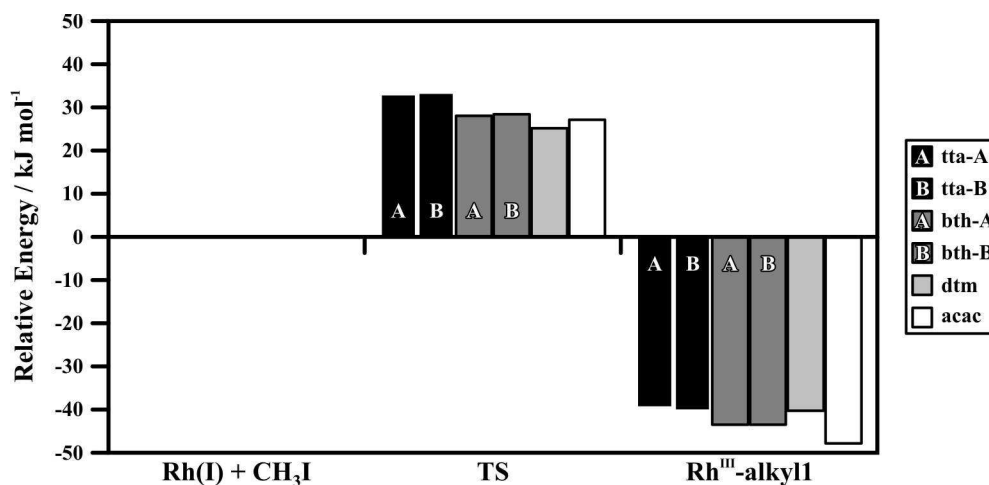


Figure 3.19: PW91/TZP/chloroform calculated relative energies (ΔE) of the reactants, the transition states and the alkyl reaction products of the oxidative addition reaction of methyl iodide to $[\text{Rh}(\beta\text{-diketonato})(\text{CO})(\text{PPh}_3)]$ ($\beta\text{-diketonato}$ = tta, bth, dtm and acac). The labels "A" and "B" refer to the two stereo isomers of tta and bth, as illustrated in Figure 3.16. The energy of the reactants is taken as zero.

Whereas the rate of the reaction is theoretically expressed by the activation barrier, experimentally it is expressed by the kinetic rate constant (k_1) (Table 3.4). The larger the value of k_1 , the faster the reaction. The linear equation ($y = mx + c$) defining the relationship between the theoretical and experimental expression is: $k_1 = (2.93 \times 10^{-3}) \Delta E^\ddagger + 0.106$ (Figure 3.20). The largest ΔE^\ddagger for tta is in agreement with the fact that the k_1 of this reaction is the slowest. The trend for the $[\text{Rh}(\beta\text{-diketonato})(\text{CO})(\text{PPh}_3)]$ complexes in this study are as follow:

$$\begin{array}{ccc}
 \begin{array}{l} \text{larger } k_1 \\ \text{smaller } \Delta E^\ddagger \\ \text{faster oxidative addition reaction} \end{array} & \text{dtm - acac - bth - tta} & \begin{array}{l} \text{smaller } k_1 \\ \text{larger } \Delta E^\ddagger \\ \text{slower oxidative addition reaction} \end{array}
 \end{array}$$

The kinetic rate constant of the Monsanto catalyst¹⁵ ($0.000068 \text{ mol}^{-1} \cdot \text{dm}^3 \cdot \text{s}^{-1}$) is not of the order of the kinetic rate constants of the $[\text{Rh}(\beta\text{-diketonato})(\text{CO})(\text{PPh}_3)]$ ($\beta\text{-diketonato}$ = tta, bth, dtm and acac) complexes (Table 3.4), although the ΔE^\ddagger energies are similar. The linear relationship expressed in Figure 3.20 is therefore only applicable to $[\text{Rh}(\beta\text{-diketonato})(\text{CO})(\text{PPh}_3)]$ complexes.

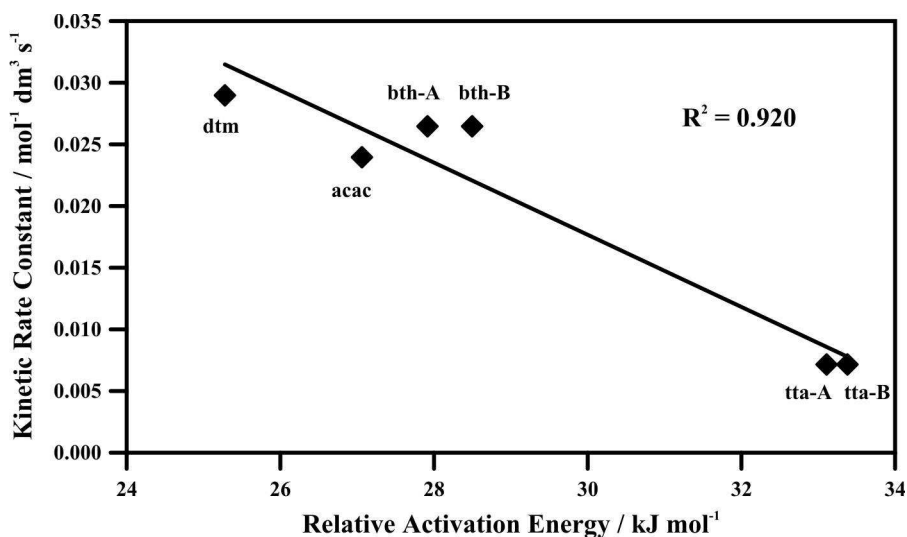


Figure 3.20: A plot of the activation energies (ΔE^\ddagger) versus the kinetic rate constants (k_1) of the reaction $[\text{Rh}(\beta\text{-diketonato})(\text{CO})(\text{PPh}_3)]$ ($\beta\text{-diketonato} = \text{tta, bth and dtm}$) + CH_3I . The labels "A" and "B" refer to the two stereo isomers of tta and bth, as illustrated in Figure 3.16.

3.1.3.5 Thermodynamic data.

The thermodynamic data are summarized in Table 3.5. The calculated enthalpy of activation (ΔH^\ddagger) is between 26-39 $\text{kJ}\cdot\text{mol}^{-1}$ for the $[\text{Rh}(\beta\text{-diketonato})(\text{CO})(\text{PPh}_3)]$ complexes in this study. The large negative entropy of activation (ΔS^\ddagger) ($< -131 \text{ J}\cdot\text{K}^{-1}\cdot\text{mol}^{-1}$) is consistent with an associative mechanism. The experimental Gibbs free energy (ΔG^\ddagger) of the oxidative addition reaction, $[\text{Rh}(\beta\text{-diketonato})(\text{CO})(\text{PPh}_3)] + \text{CH}_3\text{I}$, is in the order of 75-90 $\text{kJ}\cdot\text{mol}^{-1}$.^{7,8,9,10} The calculated Gibbs free energy of 72-84 $\text{kJ}\cdot\text{mol}^{-1}$ is in a high agreement with this. The thermodynamic data of the Monsanto catalyst are similar to that of the $[\text{Rh}(\beta\text{-diketonato})(\text{CO})(\text{PPh}_3)]$ complexes in this study.

3.1.3.6 Conclusions.

The oxidative addition of CH_3I to the square planar $[\text{Rh}(\beta\text{-diketonato})(\text{CO})(\text{PPh}_3)]$ ($\beta\text{-diketonato} = \text{tta, bth, dtm and acac}$) complexes corresponds to an $\text{S}_{\text{N}}2$ nucleophilic attack by the rhodium metal centre on the methyl iodide. The transition states of the complexes in this study all exhibit similar geometrical and thermodynamical data. The experimental kinetic rate constants (k_1) and the theoretical activation energies (ΔE^\ddagger) exhibit a linear relationship. This linear relationship of the $[\text{Rh}(\beta\text{-diketonato})(\text{CO})(\text{PPh}_3)]$ complexes does not apply to the Monsanto catalyst. Though, the activation energies (ΔE^\ddagger) of the $[\text{Rh}(\beta\text{-diketonato})(\text{CO})(\text{PPh}_3)]$ complexes in this study are similar to that of the Monsanto catalyst. It is therefore recommended

RESULTS AND DISCUSSION

to further investigate the catalytic properties of $[\text{Rh}(\beta\text{-diketonato})(\text{CO})(\text{PPh}_3)]$ complexes as promising rhodium based catalysts.

3.1.3.7 Tables and graphs.

Table 3.4: The PW91/TZP/chloroform calculated selected geometrical parameters, TS imaginary frequencies and activation energies (ΔE^\ddagger) of the transition states of the oxidative addition reaction of methyl iodide to $[\text{Rh}(\beta\text{-diketonato})(\text{CO})(\text{PPh}_3)]$ ($\beta\text{-diketonato} = \text{tta, bth, dtm}$ and acac) and the Monsanto catalyst. Experimental values of the kinetic rate constants (k_1) are also listed. The labels "A" and "B" refer to the two stereo isomers of tta and bth, as illustrated in Figure 3.16.

	tta-A	tta-B	bth-A	bth-B	dtm	acac	$[\text{Rh}(\text{CO})_2\text{I}_2(\text{CH}_3)(\text{I})]^{-i}$
Freq / cm^{-1}	222i	247i	257i	266i	239i	260i	323i
Intensity	-444	-473	-500	-515	-438	-520	-
Rh-C_{methyl} / Å	2.387	2.418	2.447	2.454	2.414	2.449	2.592
C_{methyl}-I / Å	2.723	2.676	2.606	2.640	2.710	2.654	2.577
Rh-C_{methyl}-I / °	175.7	174.8	176.3	174.0	174.4	175.2	176.7
C_{methine}-Rh-C_{methyl}-I / °	-9.1	52.1	-7.8	65.0	-12.7	21.1	-
ΔE^\ddagger / $\text{kJ}\cdot\text{mol}^{-1}$	33	33	28	29	25	27	32
k_1 / $\text{mol}^{-1}\cdot\text{dm}^3\cdot\text{s}^{-1}$	0.00171(4) ⁱⁱ		0.0265(6) ⁱⁱⁱ		0.029(1) ⁱⁱⁱ	0.024(3) ^{iv}	0.000068 ^v

ⁱ BP86/TZP/methanol, from reference [16].

ⁱⁱ UV spectrophotometry in chloroform, from reference [10].

ⁱⁱⁱ UV spectrophotometry in chloroform, from reference [8].

^{iv} IR spectrophotometry in DCM, from reference [4].

^v IR spectrophotometry in neat CH_3I , from reference [15].

Table 3.5: The PW91/TZP/chloroform calculated thermodynamic data of the reactants, TS and product during the oxidative addition reaction of methyl iodide to [Rh(β -diketonato)(CO)(PPh₃)] (β -diketonato = tta, bth, dtm and acac) and the Monsanto catalyst. The labels "A" and "B" refer to the two stereo isomers of tta and bth, as illustrated in Figure 3.16. All energy values are given compared to the reactants. Unbracketed values refer to theoretically determined values (this study); bracketed values refer to experimentally^{8,10,17} determined values.

	$\Delta H^{298K} / \text{kJ.mol}^{-1}$ ⁱ	$\Delta G^{298K} / \text{kJ.mol}^{-1}$ ⁱⁱ	$\Delta S^{298K} / \text{J.K}^{-1}.\text{mol}^{-1}$ ⁱⁱⁱ
$[\text{Rh}(\text{tta})(\text{CO})(\text{PPh}_3)]\text{-A} + \text{CH}_3\text{I} \rightarrow [\text{Rh}(\text{tta})(\text{CH}_3)(\text{CO})(\text{PPh}_3)(\text{I})]\text{-A}$			
Reactants	0	0	0
TS	39 {31.1(5)}	78 {89(1)}	-131 {-194(2)}
Product	-25	21	-156
$[\text{Rh}(\text{tta})(\text{CO})(\text{PPh}_3)]\text{-B} + \text{CH}_3\text{I} \rightarrow [\text{Rh}(\text{tta})(\text{CH}_3)(\text{CO})(\text{PPh}_3)(\text{I})]\text{-B}$			
Reactants	0	0	0
TS	37 {31.1(5)}	81 {89(1)}	-148 {-194(2)}
Product	-26	17	-145
$[\text{Rh}(\text{bth})(\text{CO})(\text{PPh}_3)]\text{-A} + \text{CH}_3\text{I} \rightarrow [\text{Rh}(\text{bth})(\text{CH}_3)(\text{CO})(\text{PPh}_3)(\text{I})]\text{-A}$			
Reactants	0	0	0
TS	32 {16.8(8)}	82 {82(2)}	-167 {-218(3)}
Product	-34	28	-209
$[\text{Rh}(\text{bth})(\text{CO})(\text{PPh}_3)]\text{-B} + \text{CH}_3\text{I} \rightarrow [\text{Rh}(\text{bth})(\text{CH}_3)(\text{CO})(\text{PPh}_3)(\text{I})]\text{-B}$			
Reactants	0	0	0
TS	31 {16.8(8)}	84 {82(2)}	-178 {-218(3)}
Product	-35	24	-197
$[\text{Rh}(\text{dtm})(\text{CO})(\text{PPh}_3)] + \text{CH}_3\text{I} \rightarrow [\text{Rh}(\text{dtm})(\text{CH}_3)(\text{CO})(\text{PPh}_3)(\text{I})]$			
Reactants	0	0	0
TS	26 {40(6)}	78 {80(3)}	-176 {-130(20)}
Product	-28	26	-180
$[\text{Rh}(\text{acac})(\text{CO})(\text{PPh}_3)] + \text{CH}_3\text{I} \rightarrow [\text{Rh}(\text{acac})(\text{CH}_3)(\text{CO})(\text{PPh}_3)(\text{I})]$			
Reactants	0	0	0
TS	33 {-}	72 {-}	-131 {-}
Product	-33	12	-150
$[\text{Rh}(\text{CO})_2\text{I}_2]^- + \text{CH}_3\text{I} \rightarrow [\text{Rh}(\text{CO})_2\text{I}_2(\text{CH}_3)(\text{I})]^{-\text{iv}}$			
Reactants	0	0	0
TS	34 {60}	80 {96}	-154 {-120}
Product	-	-	-

ⁱ Enthalpy, calculated by equation 4.2 (section 4.5.2.1, Chapter 4).

ⁱⁱ Gibbs free energy, calculated by equation 4.3 (section 4.5.2.1, Chapter 4).

ⁱⁱⁱ Entropy, calculated from the temperature dependent partition function in ADF at 298.15 K.

^{iv} BP86/TZP/methanol, from reference [16].

¹⁷ T.R. Griffin, D.B. Cook, A. Haynes, J.M. Pearson, D. Monti, G.E. Morris, *J. Am. Chem. Soc.* **1996** (118) 3029-3030.

RESULTS AND DISCUSSION

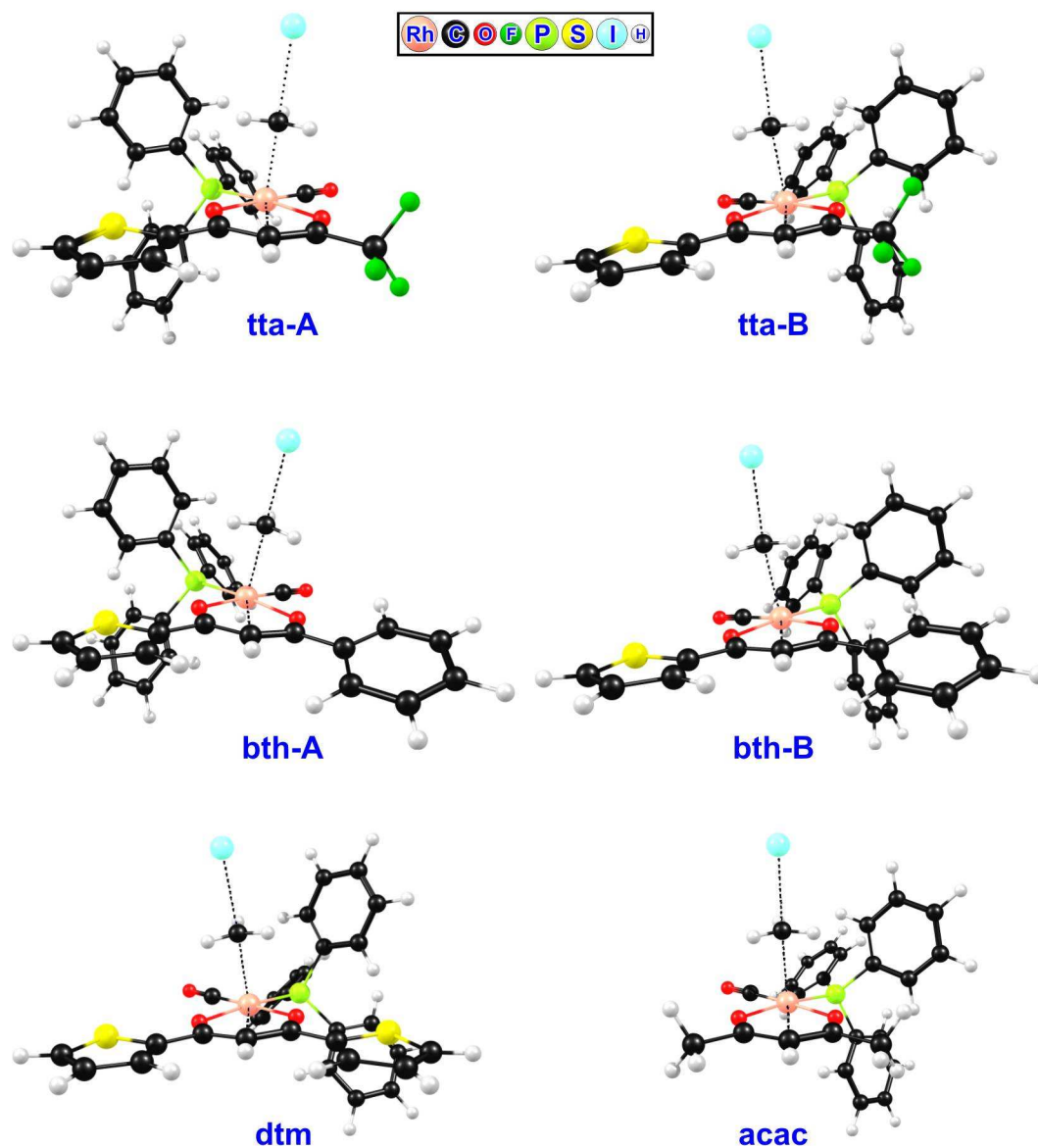


Figure 3.21: The PW91/TZP/chloroform calculated transition states of the oxidative addition reaction of methyl iodide to $[\text{Rh}(\beta\text{-diketonato})(\text{CO})(\text{PPh}_3)]$ (β -diketonato = tta, bth, dtm and acac). Note the angle at which the CH_3I molecule enters the environment of the Rh centre (represented by the $\text{C}_{\text{methine}}\text{-Rh-C}_{\text{methyl}}\text{-I}$ torsion angle indicated by the dotted black lines). The labels "A" and "B" refer to the two stereo isomers of tta and bth, as illustrated in Figure 3.16. The colour code of the atoms is as indicated.

3.1.4 [Rh(acac)(P(OPh)₃)₂] + CH₃I.

3.1.4.1 Introduction.

The reaction between methyl iodide and [Rh(β-diketonato)(P(OPh)₃)₂] is very similar to the reaction between methyl iodide and the [Rh(β-diketonato)(CO)(PPh₃)] complexes (section 3.1.2 and 3.1.3). In both cases, a neutral alkyl halide is added to a square planar rhodium(I) complex. The main difference between the reaction with the [Rh(β-diketonato)(P(OPh)₃)₂] and the [Rh(β-diketonato)(CO)(PPh₃)] complexes is that the former complex contains no carbonyl group bonded to the rhodium centre. Therefore, no methyl migration is possible after the oxidative addition of the alkyl halide. Another difference is the electronic and steric effect on the rate of the reaction of the bulky triphenylphosphite ligands.

The oxidative addition reaction between CH₃I and [Rh(β-diketonato)(P(OPh)₃)₂] complexes has only been studied experimentally,^{18,19} though no solid state X-ray crystal structure has been solved of the product.²⁰ Since the understanding of the mechanism of the activity of a catalyst requires an understanding of its structure in all reaction steps, a DFT computational study has been undertaken of the geometry of the reactant, transition state and possible products of the oxidative addition reaction of CH₃I to [Rh(acac)(P(OPh)₃)₂] (where Hacac = acetylacetonate). Due to the computational requirement of optimizing such a big molecular system, simplified models of [Rh(acac)(P(OPh)₃)₂] were also investigated to see whether these models give the same information regarding the nature of the transition state and possible reaction products of the oxidative addition reaction in this study. For the details of the computational methods used, see section 4.5.2.1 (Chapter 4).

3.1.4.2 General study of [Rh(β-diketonato)(P(OPh)₃)₂] complexes.

Since DFT computational methods are applied for the first time to [Rh(β-diketonato)(P(OPh)₃)₂] complexes, some measure of the reliability of the approach had to be obtained. This was addressed by comparing the known single crystal X-ray crystallographic structures (Figure 3.22)

¹⁸ G.J. van Zyl, G.J. Lamprecht, J.G. Leipoldt, T.W. Swaddle, *Inorg. Chim. Acta* **1988** (143) 223-227.

¹⁹ J.G. Leipoldt, E.C. Steynberg, R. van Eldik, R. *Inorg. Chem.* **1987** (26) 3068-3070.

RESULTS AND DISCUSSION

of $[\text{Rh}^{\text{I}}(\beta\text{-diketonato})(\text{P}(\text{OPh})_3)_2]$ ($\beta\text{-diketonato} = \text{acac},^{21} \text{tfba},^{22} \text{tfaa}^{23}$) and $[\text{Rh}^{\text{III}}(\beta\text{-diketonato})(\text{P}(\text{OPh})_3)_2(\text{I})_2]$ ($\beta\text{-diketonato} = \text{tfaa}^{24}$) (Hacac = acetylacetonone, Htfba = trifluorobenzoylacetone and Htfaa = trifluoroacetylacetonone) with the theoretically calculated structure of the same complex.

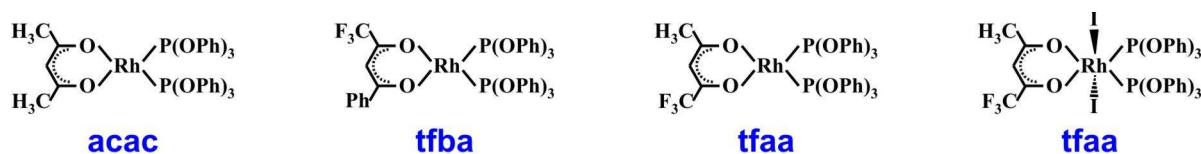


Figure 3.22: Schematic illustration of the β -diketonatobis(triphenylphosphite)rhodium complexes that have been solved by X-ray crystallography.

All these β -diketonatobis(triphenylphosphite)rhodium crystals contained two molecules in the asymmetric unit, except for β -diketonato tfba which had only one molecule in the asymmetric unit. When comparing the backbones of the two molecules in the asymmetric unit (that is $[\text{Rh}(\text{CCOCCOC})(\text{P})_2]$), a RMSD (root-mean-square distance) a value of 0.03, 0.06 and 0.13 Å is obtained respectively for $[\text{Rh}^{\text{I}}(\text{acac})(\text{P}(\text{OPh})_3)_2]$, $[\text{Rh}^{\text{I}}(\text{tfaa})(\text{P}(\text{OPh})_3)_2]$ and $[\text{Rh}^{\text{III}}(\text{tfaa})(\text{P}(\text{OPh})_3)_2(\text{I})_2]$. Inclusion of the O atoms on the P (that is $[\text{Rh}(\text{CCOCCOC})(\text{PO}_3)_2]$), gives a RMSD value of 0.04, 0.61 and 0.19 Å respectively. Note that the backbones of the two molecules in the asymmetric unit are near enantiomers and therefore the mirror symmetry of the one molecule of each was used for the fitting. The larger RMSD values, when the O atoms on the P are included, indicate that packing in the solid state may give rise to different orientations of the OPh groups, whereas in solution these OPh groups can rotate freely. Care should therefore be taken when optimizing these types of molecules when the geometry is not experimentally known (no experimental crystal structure), that the global minimum energy geometry is obtained and not a local minimum structure, due to the orientation of the OPh groups. The relative energy of the two enantiomeric molecules in the asymmetric unit, optimized with and without relativistic effects in methanol as solvent, is virtually the same, as would be expected for near enantiomers (Table 3.6).

²⁰ Cambridge Structural Database (CSD), Version 5.30, August 2008 update.

²¹ J.G. Leipoldt, G.J. Lamprecht, G.J. Van Zyl, *Inorg. Chim. Acta* **1985** (96) L31-L34.

²² G.J. Lamprecht, J.G. Leipoldt, G.J. Van Zyl, *Inorg. Chim. Acta* **1985** (97) 31-35.

²³ G.J. Van Zyl, G.J. Lamprecht, J.G. Leipoldt, *Inorg. Chim. Acta* **1985** (102) L1-L4.

²⁴ G.J. Van Zyl, G.J. Lamprecht, J.G. Leipoldt, *Inorg. Chim. Acta* **1986** (122) 75-79.

The theoretical and experimental geometrical data of the complexes $[\text{Rh}^{\text{I}}(\beta\text{-diketonato})(\text{P}(\text{OPh})_3)_2]$ ($\beta\text{-diketonato} = \text{acac}, \text{tfba}, \text{tfaa}$) and $[\text{Rh}^{\text{III}}(\beta\text{-diketonato})(\text{P}(\text{OPh})_3)_2(\text{I})_2]$ ($\beta\text{-diketonato} = \text{tfaa}$) are summarized in Table 3.7 and comparative information with signed deviations is given in Table 3.8 (atom numbering is as indicated in Figure 3.24). High agreement between experimental and theoretical structures is obtained, as reflected by the RMSD values of the calculated data superimposed on the experimental data of less than 0.11 Å. A key indicator in organometallic compounds is the bond lengths and angles involving the metal centre. The bonds in the coordination polyhedron of these four complexes were generally slightly overestimated by the DFT calculations (0.00-0.10 Å for Rh-O bonds and 0.02-0.10 Å for Rh-P bonds). It is well-known that GGA density functionals overestimate bonds lengths.²⁵ The angles around the Rh were calculated accurately within 2.9°. The calculations including relativistic effects gave more precise bond lengths than the calculation without relativistic effects (Table 3.8). Here it is informative to notice that the Rh-O and Rh-P bonds (or angles around the Rh) of the optimized geometries of the two enantiomeric molecules in the asymmetric unit differ by 0.00-0.01 Å (or 0-3°). Since comparisons of experimental metal-ligand bond lengths with calculated bond lengths below a threshold of 0.02 Å are considered as meaningless,²⁶ the methods employed in this study give a good account of the experimental bond lengths of both rhodium(I) and rhodium(III) $\beta\text{-diketonatobis}(\text{triphenylphosphite})$ complexes.

Oxidative addition of CH_3I to $[\text{Rh}(\text{acac})(\text{P}(\text{OPh})_3)_2]$ leads to an alkyl product $[\text{Rh}(\text{acac})(\text{P}(\text{OPh})_3)_2(\text{CH}_3)(\text{I})]$. Four possible rhodium(III) alkyl isomers are possible: one (Alkyl-A) if *trans* addition occurs and three possible isomers (Alkyl-B, Alkyl-C and Alkyl-D) if *cis* addition occurs (inserts in Figure 3.23).²⁷ Due to the computational requirement of

²⁵ (a) A.C. Scheiner, J. Baker, J.W. Andzelm, *J. Comput. Chem.* **1997** (18) 775-795. (b) J.R. Hill, C.M. Freeman, B. Delley, *J. Phys. Chem. A* **1999** (103) 3772-3777. (c) F. Furche, J.P. Perdew, *J. Chem Phys.* **2006** (124) 044103.

²⁶ W.J. Hehre, *A guide to molecular mechanics and quantum chemical calculations*, Wavefunction, Irvine, **2003**, p153.

²⁷ When optimizing the full experimental model, the influence of the rotating OPh groups must be taken into account so that the geometry of the global minimum energy structures (in solution) of $[\text{Rh}(\text{acac})(\text{P}(\text{OPh})_3)_2]$ and the four possible alkyl $[\text{Rh}(\text{acac})(\text{P}(\text{OPh})_3)_2(\text{CH}_3)(\text{I})]$ products can be obtained. A conformational search was therefore performed by calculating the energy of the molecules as a function of the $\text{O}_{\text{acac}}\text{-Rh-P-O}$ dihedral angle. The global minimum energy structure was then obtained by re-optimizing the minimum energy structure obtained from the dihedrally restricted optimizations, without any restraints.

optimizing such a big molecular system, two simplified models of $[\text{Rh}(\text{acac})(\text{P}(\text{OPh})_3)_2]$, which are $[\text{Rh}(\text{acac})(\text{P}(\text{OCH}_3)_3)_2]$ and $[\text{Rh}(\text{acac})(\text{P}(\text{OH})_3)_2]$, were introduced. The goal is to determine whether the simplified models give the same information regarding the nature, geometry and energetics of the transition state (TS) and products of oxidative addition.

3.1.4.3 Energy profile.

The PW91/TZP/methanol optimized relative energies of the rhodium(I) complex $[\text{Rh}(\text{acac})(\text{P}(\text{OPh})_3)_2]$ and the four possible rhodium(III) isomers $[\text{Rh}(\text{acac})(\text{P}(\text{OPh})_3)_2(\text{CH}_3)(\text{I})]$ of the full experimental model ($\text{R} = \text{Ph}$) are displayed in Figure 3.23. These results indicate (in agreement with experimental observation)^{18,19,28} that the *trans* product Alkyl-A is the product of oxidative addition of CH_3I to $[\text{Rh}(\text{acac})(\text{P}(\text{OPh})_3)_2]$. The two simplified systems, $[\text{Rh}(\text{acac})(\text{P}(\text{OCH}_3)_3)_2]$ and $[\text{Rh}(\text{acac})(\text{P}(\text{OH})_3)_2]$ (also displayed in Figure 3.23), show the same trend regarding the relative energies of the four possible rhodium(III) reaction products, *viz.* (most stable) Alkyl-A < Alkyl-D < Alkyl-C < Alkyl-B (least stable). Inclusion of relativistic effects in the DFT calculations did not change the relative stability of the four possible $[\text{Rh}(\text{acac})(\text{P}(\text{OR})_3)_2(\text{CH}_3)(\text{I})]$ products of all three models ($\text{R} = \text{Ph}$, CH_3 or H). The energetically preferred product of the oxidative addition reaction of CH_3I to $[\text{Rh}(\text{acac})(\text{P}(\text{OPh})_3)_2]$ therefore assumes an octahedral geometry, with the β -diketonato and the two triphenylphosphite groups located in the equatorial plane and the methyl and iodide ligands in the axial position. The *trans* addition of CH_3I to $[\text{Rh}(\beta\text{-diketonato})(\text{P}(\text{OPh})_3)_2]$ is also confirmed by the structure determination of a similar complex, *trans*- $[\text{Rh}(\text{benzoylphenylhydroxylamine})(\text{P}(\text{OPh})_3)_2(\text{CH}_3)(\text{I})]$.²⁹ Oxidative addition of I_2 to $[\text{Rh}(\text{tfaa})(\text{P}(\text{OPh})_3)_2(\text{I})_2]$ also gave the *trans* product (Figure 3.22, right).²⁴ This is also in agreement with the DFT calculations on the structurally similar monocarbonyltriphenylphosphine rhodium complexes, $[\text{Rh}(\beta\text{-diketonato})(\text{CO})(\text{PPh}_3)]$, where the CH_3I oxidative addition resulted in *trans* addition (section 3.1.3).

²⁸ G.J. van Zyl, G.J. Lamprecht, J.G. Leipoldt, *Inorg. Chim. Acta* **1987** (129) 35-37.

²⁹ G.J. Lamprecht, G.J. Van Zyl, J.G. Leipoldt, *Inorg. Chim. Acta* **1989** (164) 69-72.

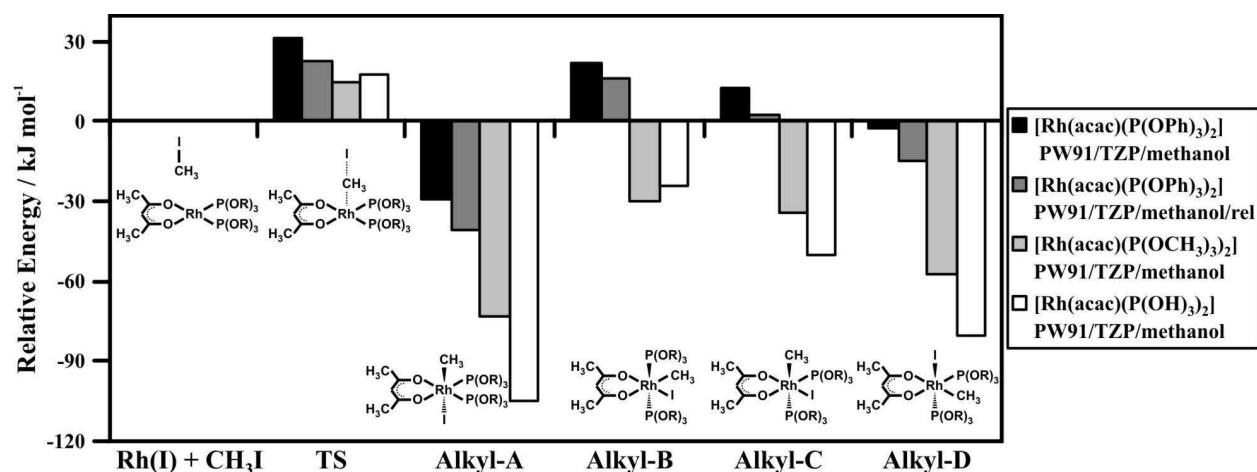


Figure 3.23: PW91/TZP/methanol calculated energies of the reactants $[\text{Rh}(\text{acac})(\text{P}(\text{OR})_3)_2] + \text{CH}_3\text{I}$, the transition state (TS) and the four possible $[\text{Rh}(\text{acac})(\text{P}(\text{OR})_3)_2(\text{CH}_3)(\text{I})]$ -alkyl reaction products. The energy of the reactants is taken as zero.

3.1.4.4 Geometry profile.

The PW91/TZP/methanol optimized geometrical data of the full experimental model ($\text{R} = \text{Ph}$) are illustrated in Figure 3.25 and the bond lengths and bond angles around the Rh centre of all three models ($\text{R} = \text{Ph}$, CH_3 or H) are given in Table 3.9. Introducing $\text{R} = \text{CH}_3$ or H instead of Ph , did not change the bond lengths around the Rh centre significantly - the calculated bond lengths were similar within 0.05 \AA . The bond angles around the Rh centre were within 8.5° (5%) of the corresponding angle of the three models. It is expected that the bond angles around the Rh centre will differ as the size of the R group increases from H to CH_3 to Ph . The $\text{C}_{\text{methyl}}\text{-Rh-I}$ angle of the full experimental model of Alkyl-A is 169.1° and is in the same order as the $\text{C}_{\text{methyl}}\text{-Rh-I}$ angle (174.2°) of *trans*- $[\text{Rh}(\text{benzoylphenylhydroxylamine})(\text{P}(\text{OPh})_3)_2(\text{CH}_3)(\text{I})]^{29}$ and the I-Rh-I angle (*ca.* 170°) in $[\text{Rh}(\text{tfaa})(\text{P}(\text{OPh})_3)_2(\text{I})_2]$.²⁴ The slightly distorted octahedral arrangement in $[\text{Rh}(\text{tfaa})(\text{P}(\text{OPh})_3)_2(\text{I})_2]$ is attributed to the steric interaction between the iodide and triphenylphosphite ligands. The calculated $\text{C}_{\text{methyl}}\text{-Rh-I}$ angle of the simplified models of Alkyl-A, however, increases as the $\text{P}(\text{OR})_3$ groups decrease in size - 171.7° and 176.5° for $[\text{Rh}(\text{acac})(\text{P}(\text{OCH}_3)_3)_2(\text{CH}_3)(\text{I})]$ and $[\text{Rh}(\text{acac})(\text{P}(\text{OH})_3)_2(\text{CH}_3)(\text{I})]$ respectively.

The deviation of the geometry of the two simplified models can also be evaluated by comparing the RMSD values of the key bonds of the $\text{Rh}(\text{CCOCCOC})(\text{P})_2$ backbone of the optimized simplified model, fitted on the backbone of the optimized full model (Table 3.9). The RMSD values of the simplified rhodium(I) models are exceptionally good (0.06 and 0.09 \AA

respectively). The RMSD values of the simplified rhodium(III) models (between 0.10 and 0.16 Å) are somewhat larger than the rhodium(I) values, as would be expected for the more complex molecules. Therefore, both simplified models (R = CH₃ or H) give a good account of the key bond lengths around the rhodium centre relative to that of the full experimental model.

3.1.4.5 Transition states.

Figure 3.26 displays the three types of transition state (TS) structures that have been reported for the oxidative addition of methyl iodide to square planar rhodium(I) complexes (especially the Monsanto catalyst [Rh(CO)₂I₂]⁻, section 2.4.2, Chapter 2). Two results from *trans* addition ("linear/back" and "bent") and one results from *cis* addition ("front"). The linear/back transition state structure corresponds to an S_N2 mechanism, characterized by a linear Rh-C_{methyl}-I arrangement and by an Rh-C_{methyl}-H angle close to 90°. The methyl hydrogen atoms are located in the equatorial plane of the five-coordinated carbon atom, resulting in a trigonal bipyramidal arrangement. The bent and front transition state structures correspond to a side-on approach of the C_{methyl}-I bond to the rhodium atom. The bent transition state structure leads to the same intermediate product as the linear/back transition state structure - a cationic five-coordinated rhodium complex and a free iodide ion. Both the mechanisms of the linear/back and the bent transition state structures are therefore described as S_N2 processes. The front transition state structure corresponds to a concerted three-centred oxidative addition mechanism, in which the Rh-I and Rh-C_{methyl} bonds form simultaneously as I-C_{methyl} bond breaks, resulting in the *cis* addition of the methyl iodide. Table 3.10 summarizes the main geometric parameters of the TS structures determined of the simplified models in the study, as well as the calculated geometric parameters of the Monsanto catalyst [Rh(CO)₂I₂]⁻.¹⁶

The three types of TS structures exhibit similar characteristics. The I-C_{methyl} bond length and the Rh-C_{methyl} bond length of all the [Rh(acac)(P(OH)₃)₂(CH₃)(I)] and [Rh(acac)(P(OCH₃)₃)₂(CH₃)(I)] TS structures, as well as the Monsanto TS structures, are very similar (2.51-2.85 Å and 2.54-2.78 Å respectively). The Rh-C_{methyl}-I angles are between 172.9-176.7° for the linear/back TS structures, 89.2-95.0° for the bent TS structures and 64.3-65.1° for the front TS structures. The linear/back transition states are favoured by a large margin of energy (> 90 kJ.mol⁻¹) with activation barriers (ΔE[‡]) of 14-32 kJ.mol⁻¹. The bent and front transition states were therefore not considered in further investigations. The calculated relative energies of the reactants, linear/back TS structures and products are summarized in Figure 3.23.

The thermodynamic data are summarized in Table 3.11. The calculated enthalpy of activation (ΔH^\ddagger) is between 19-37 kJ.mol⁻¹ for the different models. The large negative entropy of activation (ΔS^\ddagger) calculated for all models, is consistent with an associative mechanism. The activation free energy (ΔG^\ddagger) of the two simplified models (60 kJ.mol⁻¹ for both models) is lower than that of the full model (75 and 78 kJ.mol⁻¹, with and without relativistic effects).

The DFT optimized reactant complexes, the linear/back TS and the reaction intermediate of the [Rh(acac)(P(OPh)₃)₂] + CH₃I reaction are visualized in Figure 3.27. The metal centre attacks the methyl group in a S_N2-type fashion, approaching the methyl iodide *trans* to the leaving iodide group. During this process the metal-methyl bond is under development, whereas the methyl-iodide bond is substantially stretched. In the reactant [Rh(acac)(P(OPh)₃)₂], the large OPh groups are bent backwards so that the Ph groups are arranged above, below and in the square planar plane (formed by the acac-ligand, the rhodium atom and the two phosphor atoms). As the CH₃I group approaches the reactant, the "arms" of the OPh groups above the plane gradually open up to accept the incoming CH₃I group to proceed through the TS. The overall structure of the TS appears to be square pyramidal, with the CH₃⁺ group in the pyramidal position (Figure 3.27 middle). The optimized distance between the attacking rhodium atom and CH₃⁺ group at the point of the TS is 2.55, 2.61 and 2.54 Å respectively for R = Ph, CH₃ and H. The carbon-iodide bond distance of the CH₃I group increased from 2.18 Å in the reactant to 2.59, 2.51 and 2.55 Å in the products (R = Ph, CH₃ and H).

Rhodium(I) is a $d_{xz}^2 d_{xz}^2 d_{xy}^2 d_{z^2}^2 d_{x^2-y^2}^0$ complex of which the HOMO (highest occupied molecular orbital) exhibits mainly d_{z^2} character. The HOMO of the TS is visualized in Figure 3.27 (middle). The main contribution to the Rh-C_{CH3} bond in the TS comes from the overlap of the d_{z^2} HOMO of the rhodium atom with the p_z LUMO (lowest unoccupied molecular orbital) of the methyl carbon.

Following the TS, is the formation of the cationic five-coordinate [Rh(acac)(P(OPh)₃)₂(CH₃)]⁺ intermediate with the CH₃ group in the apical position (Figure 3.27, right) and with the iodide ion drifting away into the solvent sphere. The product, [Rh(acac)(P(OPh)₃)₂(CH₃)(I)] Alkyl-A, is octahedral with the methyl and iodide above and below the square planar plane in a *trans* arrangement (Figure 3.25, Alkyl-A). Inversion of the configuration at the methyl carbon occurred and the methyl group is fully bonded to rhodium atom.

3.1.4.6 Calculated *versus* experimental thermodynamic data.

The obtained thermodynamic data (Table 3.11) can be compared with experimental^{18,19,30} results. The activation enthalpy (ΔH^\ddagger) of the oxidative addition of CH_3I to $[\text{Rh}(\text{acac})(\text{P}(\text{OPh})_3)_2]$ is experimentally determined as $40(3) \text{ kJ}\cdot\text{mol}^{-1}$, which is in the same order as the calculated activation enthalpy value of 37 and $28 \text{ kJ}\cdot\text{mol}^{-1}$ (determined without and with relativistic effects respectively). The calculated values of the two simplified models are lower, 22 and $19 \text{ kJ}\cdot\text{mol}^{-1}$ for $[\text{Rh}(\text{acac})(\text{P}(\text{OCH}_3)_3)_2]$ and $[\text{Rh}(\text{acac})(\text{P}(\text{OH})_3)_2]$ respectively. The activation entropy (ΔS^\ddagger) of the reaction $[\text{Rh}(\text{acac})(\text{P}(\text{OPh})_3)_2] + \text{CH}_3\text{I}$ is experimentally determined as $-128(9) \text{ J}\cdot\text{K}^{-1}\cdot\text{mol}^{-1}$. This is in agreement with the large negative activation entropy observed as for all models here and the same as the calculated value of $-129 \text{ J}\cdot\text{K}^{-1}\cdot\text{mol}^{-1}$ for the full model. The activation free energy (ΔG^\ddagger) of the reaction $[\text{Rh}(\text{acac})(\text{P}(\text{OPh})_3)_2] + \text{CH}_3\text{I}$ is experimentally determined as $78 \text{ kJ}\cdot\text{mol}^{-1}$, which is in high agreement with the calculated values of 75 and $78 \text{ kJ}\cdot\text{mol}^{-1}$ for the full model (with and without relativistic effects). The calculated values of the two simplified models failed to accurately reproduce this value ($60 \text{ kJ}\cdot\text{mol}^{-1}$ for both $[\text{Rh}(\text{acac})(\text{P}(\text{OCH}_3)_3)_2]$ and $[\text{Rh}(\text{acac})(\text{P}(\text{OH})_3)_2]$). The agreement between experiment and theory for the individual components ΔH^\ddagger and ΔS^\ddagger to $\Delta G^\ddagger = \Delta H^\ddagger - T\Delta S^\ddagger$ is thus not as good as for ΔG^\ddagger itself. The large compensating variations in ΔH^\ddagger and ΔS^\ddagger , with a modest change in ΔG^\ddagger , were also found by Ziegler and was assigned to solvent effects.³¹

A reduction in the activation enthalpy associated with the oxidative addition reaction $[\text{Rh}(\text{acac})(\text{P}(\text{OR})_3)_2] + \text{CH}_3\text{I}$ is observed for $\text{R} = \text{CH}_3$ as compared to Ph. On the basis of Tolman's electronic parameter (Table 3.12), $\text{P}(\text{OCH}_3)_3$ is expected to be somewhat more electron-rich than $\text{P}(\text{OPh})_3$.³² Therefore, a nucleophilic attack of the rhodium atom of $[\text{Rh}(\text{acac})(\text{P}(\text{OCH}_3)_3)_2]$ on the CH_3^+ group is expected to be easier than that of $[\text{Rh}(\text{acac})(\text{P}(\text{OPh})_3)_2]$. The higher calculated activation enthalpy of $[\text{Rh}(\text{acac})(\text{P}(\text{OPh})_3)_2] + \text{CH}_3\text{I}$ is therefore as expected on electronic grounds. However, the bulkiness of the $\text{P}(\text{OPh})_3$ group could hinder the attack of the rhodium atom of $[\text{Rh}(\text{acac})(\text{P}(\text{OPh})_3)_2]$ on the CH_3^+ group, also leading to a higher energy barrier. The high agreement between the computed activation enthalpy of the full experimental model and the experimentally obtained value demonstrates that the use of the full $\text{P}(\text{OPh})_3$ groups are vital for obtaining accurate theoretical values.

³⁰ G.J. van Zyl, G.J. Lamprecht, J.G. Leipoldt, *Inorg. Chim. Acta* **1987** (129) 35-37.

³¹ M. Cheong, T. Ziegler, *Organometallics* **2005** (24) 3053-3058.

³² C.A. Tolman, *Chem. Rev.* **1977** (77) 313-384.

The calculated activation barrier, $\Delta E^\ddagger = 30 \text{ kJ.mol}^{-1}$, for the trans addition of CH_3I to $[\text{Rh}(\text{acac})(\text{P}(\text{OPh})_3)_2]$ in this study is of the same order as the reported DFT values for the Monsanto system 32 kJ.mol^{-1} (Table 3.10, BP86) by Feliz,¹⁶ but smaller than the value reported by Laasonen when using the hybrid B3LYP functional (68 kJ.mol^{-1}).³³ The calculated thermodynamic quantities (ΔH^\ddagger , ΔG^\ddagger , ΔS^\ddagger , 298 K) of this study compare well with experimental data of the Monsanto catalyst (60 kJ.mol^{-1} , 96 kJ.mol^{-1} and 120 J.mol^{-1} respectively).¹⁷ However, since the $[\text{Rh}(\text{acac})(\text{P}(\text{OPh})_3)_2]$ complex in this study does not contain a CO group, no methyl migration (the second step in the Monsanto catalytic cycle) is possible.

3.1.4.7 Conclusions.

Simplified model systems of the oxidative addition reaction $[\text{Rh}(\text{acac})(\text{P}(\text{OPh})_3)_2] + \text{CH}_3\text{I}$, *viz.* $[\text{Rh}(\text{acac})(\text{P}(\text{OCH}_3)_3)_2]$ and $[\text{Rh}(\text{acac})(\text{P}(\text{OH})_3)_2]$, give a good account of the Rh-L experimental bond lengths of both rhodium(I) and rhodium(III) β -diketonatobis(triphenylphosphite) complexes. All models give the same trend concerning the relative stability of the four possible rhodium(III) reaction products. The main features of the TS, *viz.* the nucleophilic attack of the rhodium atom on the CH_3^+ group and the cleavage of the carbon-iodide bond, are similar for all three systems. Therefore, in order to save on computational recourses, a simplified model system can be used to obtain preliminary information of the oxidative addition reaction of CH_3I to $[\text{Rh}(\beta\text{-diketonato})(\text{P}(\text{OPh})_3)_2]$ complexes. However, for the best agreement with experimental activation parameters, the full experimental system is necessary.

3.1.4.8 Graphs and tables.

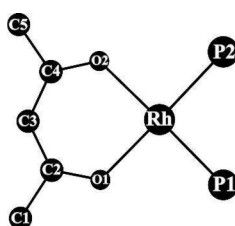


Figure 3.24: The core structure of $[\text{Rh}^{\text{I}}(\beta\text{-diketonato})(\text{P}(\text{OPh})_3)_2]$ (β -diketonato = acac, tfba, tfaa) and $[\text{Rh}^{\text{III}}(\beta\text{-diketonato})(\text{P}(\text{OPh})_3)_2(\text{I})_2]$ (β -diketonato = tfaa) indicating the numbering system used in Table 3.6. The R-groups attached to C_2 and C_4 are $(\text{CH}_3, \text{CH}_3)$ for acac, (Ph, CF_3) for tfba and $(\text{CF}_3, \text{CH}_3)$ for tfaa.

³³ T. Kinnunen, K. Laasonen, *J. Mol. Struct. (Theochem)* **2001** (542) 273-288.

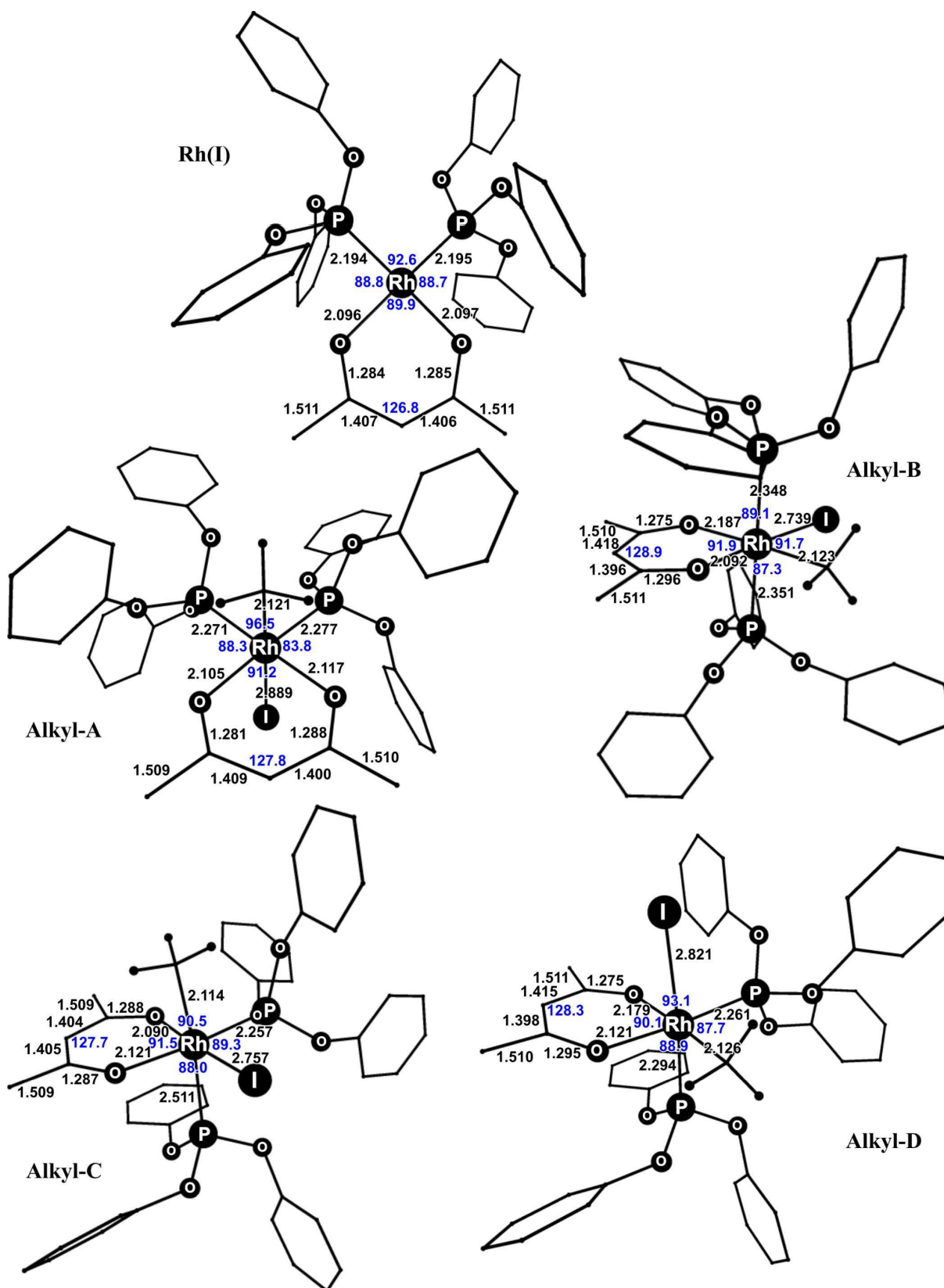


Figure 3.25: The PW91/TZP/methanol calculated minimum energy geometries of the $[\text{Rh}(\text{acac})(\text{P}(\text{OPh})_3)_2]$ complex and the four possible $[\text{Rh}(\text{acac})(\text{P}(\text{OPh})_3)_2(\text{CH}_3)(\text{I})]$ -alkyl reaction products. The H atoms are removed for clarity (except for the CH₃ group bonded to the rhodium). Bond angles (°) and bond lengths (Å) are as indicated. Only angles in the square planar plane are given.

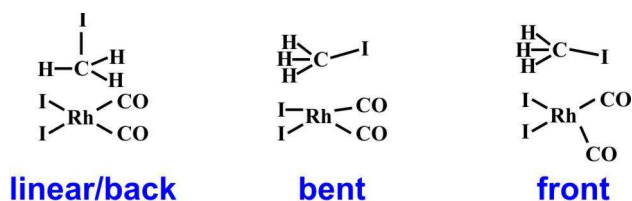


Figure 3.26: Schematic illustration of a "linear/back", "bent" and "front" transition states of the nucleophilic attack of square planar rhodium(I) on methyl iodide. The Monsanto catalyst $[\text{Rh}(\text{CO})_2\text{I}_2]^-$ is used as example for the square planar rhodium(I) complex.

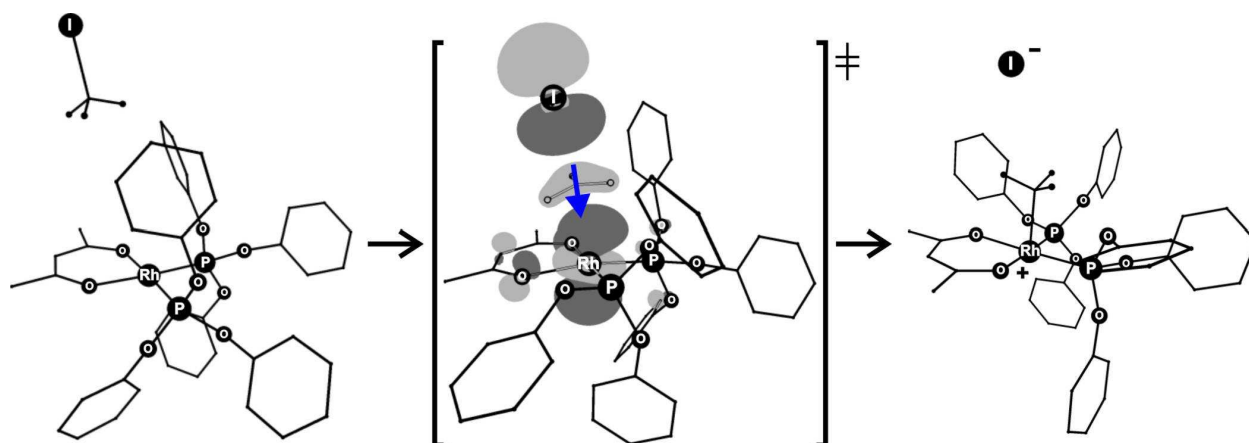


Figure 3.27: The PW91/TZP/methanol optimized structures of the oxidative addition of the reaction $[\text{Rh}(\text{acac})(\text{P}(\text{OPh})_3)_2] + \text{CH}_3\text{I}$. The H atoms are removed for clarity (except for the methyl group of the CH_3I). Left: The reactant complexes *viz.* $[\text{Rh}(\text{acac})(\text{P}(\text{OPh})_3)_2] + \text{CH}_3\text{I}$. Middle: The square pyramidal TS, involving the attack of rhodium atom on the CH_3^+ group with displacement vector (blue arrow), indicating movement of the CH_3^+ group at the negative frequency (-258.6 cm^{-1}). The HOMO of the TS is superimposed on the TS geometry - note the d_{z^2} -orbital on the rhodium centre. Right: The optimized reaction intermediate $[\text{Rh}(\text{acac})(\text{P}(\text{OPh})_3)_2(\text{CH}_3)]^+\text{I}^-$.

Table 3.6: The relative energies ($\text{kJ}\cdot\text{mol}^{-1}$) of the DFT optimized structures of the two enantiomeric molecules in the asymmetric unit of $[\text{Rh}^{\text{I}}(\text{acac})(\text{P}(\text{OPh})_3)_2]$, $[\text{Rh}^{\text{I}}(\text{tfaa})(\text{P}(\text{OPh})_3)_2]$ and $[\text{Rh}^{\text{III}}(\text{tfaa})(\text{P}(\text{OPh})_3)_2(\text{I})_2]$.

	$[\text{Rh}(\text{acac})(\text{P}(\text{OPh})_3)_2]$		$[\text{Rh}(\text{tfaa})(\text{P}(\text{OPh})_3)_2]$		$[\text{Rh}(\text{tfaa})(\text{P}(\text{OPh})_3)_2(\text{I})_2]$	
	Molecule 1	Molecule 2	Molecule 1	Molecule 2	Molecule 1	Molecule 2
PW91/TZP/methanol ⁱ	0.0	1.7	0.0	3.8	0.6	0.0
PW91/TZP/methanol/rel ⁱⁱ	0.0	2.5	0.0	1.7	2.4	0.0

ⁱ Geometry optimization was done with the PW91 functional and the TZP basis set in methanol as solvent.

ⁱⁱ Geometry optimization under the same conditions as (ⁱ), but with inclusion of relativistic effects.

RESULTS AND DISCUSSION

Table 3.7: Calculated and experimental bond lengths (Å) and bond angles (°) of $[\text{Rh}^{\text{I}}(\beta\text{-diketonato})(\text{P}(\text{O}^i\text{Ph})_3)_2]$ ($\beta\text{-diketonato} = \text{acac}, \text{tfba}, \text{tfaa}$) and $[\text{Rh}^{\text{III}}(\beta\text{-diketonato})(\text{P}(\text{O}^i\text{Ph})_3)_2(\text{I})_2]$ ($\beta\text{-diketonato} = \text{tfaa}$). Unbracketed values refer to the solution DFT values, round bracketed values refer to the solution DFT values including relativistic effects (PW91/TZP/methanol) and square bracket values refer to the X-ray crystal data. The atom numbering is as indicated in Figure 3.24.

	$[\text{Rh}(\text{acac})(\text{P}(\text{O}^i\text{Ph})_3)_2]^i$		$[\text{Rh}(\text{tfba})(\text{P}(\text{O}^i\text{Ph})_3)_2]$	$[\text{Rh}(\text{tfaa})(\text{P}(\text{O}^i\text{Ph})_3)_2]^i$		$[\text{Rh}(\text{tfaa})(\text{P}(\text{O}^i\text{Ph})_3)_2(\text{I})_2]^i$	
	Molecule 1	Molecule 2		Molecule 1	Molecule 2	Molecule 1	Molecule 2
<i>Bond lengths / Å</i>							
C1-C2	1.511 (1.509) [1.510]	1.510 (1.509) [1.548]	1.495 (1.493) [1.480]	1.543 (1.542) [1.500]	1.542 (1.540) [1.492]	1.546 (1.545) [1.517]	1.547 (1.544) [1.472]
C2-C3	1.407 (1.401) [1.406]	1.403 (1.400) [1.392]	1.416 (1.414) [1.407]	1.387 (1.384) [1.363]	1.387 (1.385) [1.367]	1.385 (1.383) [1.372]	1.387 (1.384) [1.450]
C3-C4	1.406 (1.405) [1.401]	1.408 (1.405) [1.401]	1.390 (1.388) [1.377]	1.421 (1.418) [1.386]	1.420 (1.417) [1.434]	1.418 (1.417) [1.428]	1.417 (1.416) [1.284]
C4-C5	1.513 (1.511) [1.519]	1.513 (1.511) [1.528]	1.545 (1.543) [1.512]	1.508 (1.507) [1.539]	1.507 (1.506) [1.548]	1.506 (1.505) [1.607]	1.507 (1.504) [1.535]
C2-O1	1.280 (1.289) [1.286]	1.288 (1.289) [1.271]	1.287 (1.284) [1.269]	1.280 (1.281) [1.240]	1.279 (1.281) [1.269]	1.280 (1.282) [1.226]	1.279 (1.280) [1.237]
C4-O2	1.284 (1.286) [1.279]	1.285 (1.287) [1.264]	1.277 (1.279) [1.285]	1.275 (1.277) [1.281]	1.277 (1.279) [1.254]	1.275 (1.277) [1.246]	1.275 (1.278) [1.286]
O1-Rh	2.098 (2.071) [2.067]	2.094 (2.070) [2.062]	2.101 (2.077) [2.066]	2.117 (2.092) [2.085]	2.117 (2.091) [2.083]	2.133 (2.113) [2.109]	2.135 (2.114) [2.036]
O2-Rh	2.101 (2.075) [2.081]	2.098 (2.074) [2.067]	2.107 (2.080) [2.071]	2.106 (2.080) [2.067]	2.096 (2.070) [2.089]	2.120 (2.101) [2.083]	2.114 (2.095) [2.055]
P1-Rh	2.202 (2.177) [2.142]	2.203 (2.175) [2.148]	2.205 (2.181) [2.150]	2.199 (2.174) [2.136]	2.203 (2.177) [2.137]	2.291 (2.263) [2.190]	2.299 (2.271) [2.221]
P2-Rh	2.200 (2.177) [2.150]	2.202 (2.177) [2.155]	2.206 (2.185) [2.162]	2.197 (2.174) [2.148]	2.209 (2.184) [2.144]	2.287 (2.259) [2.209]	2.286 (2.256) [2.200]
<i>Bond angles / °</i>							
C1-C2-C3	118.7 (119.2) [120.5]	119.1 (119.3) [120.4]	120.3 (120.5) [121.0]	117.9 (118.0) [119.2]	118.3 (118.6) [115.9]	117.3 (117.4) [115.2]	117.5 (117.7) [120.5]
C2-C3-C4	127.0 (126.8) [126.9]	127.3 (126.8) [125.6]	125.2 (124.7) [124.7]	125.2 (124.8) [124.3]	125.1 (124.7) [122.1]	126.0 (125.8) [125.4]	125.9 (125.6) [127.0]
C3-C4-C5	117.9 (118.3) [119.2]	118.0 (118.3) [119.1]	117.6 (117.8) [118.5]	117.9 (118.1) [120.2]	118.7 (118.9) [117.6]	117.7 (117.9) [121.5]	118.7 (118.8) [121.0]
O1-C2-C1	114.5 (114.4) [114.4]	114.3 (114.3) [112.5]	115.1 (115.2) [114.9]	111.8 (112.1) [110.5]	111.6 (111.7) [112.6]	111.8 (111.9) [113.4]	111.5 (111.6) [114.9]
O1-C2-C3	126.8 (126.4) [125.1]	126.6 (126.3) [127.0]	124.6 (124.3) [124.0]	130.3 (129.9) [130.3]	130.2 (129.8) [131.5]	130.9 (130.7) [128.8]	130.9 (130.7) [124.4]
O2-C4-C3	126.6 (126.1) [126.0]	126.6 (126.3) [125.7]	130.8 (130.4) [130.0]	125.8 (125.5) [126.0]	125.9 (125.6) [126.1]	126.4 (126.2) [127.0]	126.5 (126.2) [128.1]
O2-C4-C5	115.5 (115.5) [114.8]	115.5 (115.5) [115.2]	111.6 (111.8) [111.4]	116.3 (116.4) [113.8]	115.4 (115.4) [116.2]	115.8 (115.9) [111.3]	114.8 (114.9) [110.7]
O1-Rh-P1	86.9 (86.8) [87.1]	87.1 (87.1) [87.5]	86.4 (86.4) [87.9]	90.2 (89.9) [91.1]	87.2 (86.9) [87.4]	89.6 (89.5) [92.3]	88.7 (88.3) [89.3]
P1-Rh-P2	96.2 (96.4) [94.2]	95.0 (95.3) [93.8]	94.1 (94.4) [93.0]	91.7 (92.1) [90.6]	93.9 (94.3) [92.2]	92.5 (92.5) [91.4]	92.6 (93.0) [91.2]
P2-Rh-O2	87.5 (87.2) [89.9]	88.3 (88.0) [90.3]	90.7 (90.3) [90.8]	88.9 (88.7) [90.1]	89.7 (89.5) [92.4]	87.8 (87.5) [87.1]	88.4 (88.3) [90.0]
O2-Rh-O1	90.2 (90.5) [89.3]	90.5 (90.6) [88.8]	88.9 (89.0) [88.4]	89.3 (89.4) [88.1]	89.4 (89.6) [87.9]	90.2 (90.6) [89.3]	90.2 (90.5) [89.4]
I1-Rh-I2	-	-	-	-	-	171.1 (170.6) [172.6]	169.3 (168.9) [169.4]

ⁱ Contains two molecules per asymmetric unit.

CHAPTER 3

Table 3.8: Comparative information of the deviations between the calculated (PW91/TZP/methanol) and the experimental (X-ray crystal) structures. Signed deviations of the bond lengths (Å) and the bond angles (°) around the rhodium centre of [Rh^I(β-diketonato)(P(OPh)₃)₂] (β-diketonato = acac, tfba, tfaa) and [Rh^{III}(β-diketonato)(P(OPh)₃)₂(I)₂] (β-diketonato = tfaa) are given. Unbracket values refer to the solution DFT values and round bracket values refer to the solution DFT values including relativistic effects. The atom numbering is as indicated in Figure 3.24.

	[Rh(acac)(P(OPh) ₃) ₂] ⁱ		[Rh(tfba)(P(OPh) ₃) ₂]	[Rh(tfaa)(P(OPh) ₃) ₂] ⁱ		[Rh(tfaa)(P(OPh) ₃) ₂ (I) ₂] ⁱ	
	Molecule 1	Molecule 2		Molecule 1	Molecule 2	Molecule 1	Molecule 2
<i>Bond length deviationsⁱⁱ / Å</i>							
O1-Rh	-0.03 (0.00)	-0.03 (-0.01)	-0.04 (-0.01)	-0.03 (-0.01)	-0.03 (-0.01)	-0.02 (0.00)	-0.10 (-0.08)
O2-Rh	-0.02 (0.01)	-0.03 (-0.01)	-0.04 (-0.01)	-0.04 (-0.01)	-0.01 (0.02)	-0.04 (-0.02)	-0.06 (-0.04)
P1-Rh	-0.06 (-0.04)	-0.05 (-0.03)	-0.06 (-0.03)	-0.06 (-0.04)	-0.07 (-0.04)	-0.10 (-0.07)	-0.08 (-0.05)
P2-Rh	-0.05 (-0.03)	-0.05 (-0.02)	-0.04 (-0.02)	-0.05 (-0.03)	-0.06 (-0.04)	-0.08 (-0.05)	-0.09 (-0.06)
<i>Bond angle deviationsⁱⁱ / °</i>							
O1-Rh-P1	0.2 (0.3)	0.4 (0.4)	1.5 (1.5)	0.9 (1.2)	0.2 (0.5)	2.7 (2.8)	0.6 (1.0)
P1-Rh-P2	-2.0 (-2.2)	-1.2 (-1.5)	-1.1 (-1.4)	-1.1 (-1.5)	-1.7 (-2.1)	-1.1 (-1.1)	-1.4 (-1.8)
P2-Rh-O2	2.4 (2.7)	2.0 (2.3)	0.1 (0.5)	1.2 (1.4)	2.7 (2.9)	-0.7 (-0.4)	1.6 (1.7)
O2-Rh-O1	-0.9 (-1.2)	-1.7 (-1.8)	-0.5 (-0.6)	-1.2 (-1.3)	-1.5 (-1.7)	-0.9 (-1.3)	-0.8 (-1.1)
RMSD ⁱⁱⁱ	0.05 (0.05)	0.06 (0.05)	0.05 (0.03)	0.06 (0.05)	0.10 (0.11)	0.10 (0.09)	0.10 (0.09)

ⁱ Contains two molecules per asymmetric unit.

ⁱⁱ Experimental value - Calculated value (data from Table 3.7).

ⁱⁱⁱ RMSD values, in Å, are root-mean-square atom positional deviations, calculated for the non-hydrogen atoms and excluding the rotational groups (CF₃, Ph and OPh).

RESULTS AND DISCUSSION

Table 3.9: A comparison between the PW91/TZP/methanol calculated minimum energy geometries of the $[\text{Rh}(\text{acac})(\text{P}(\text{OR})_3)_2]$ complex and the four possible $[\text{Rh}(\text{acac})(\text{P}(\text{OR})_3)_2(\text{CH}_3)(\text{I})]$ -alkyl reaction products for $\text{R} = \text{Ph}$, CH_3 and H . Angles ($^\circ$), bond lengths (\AA) and RMSD values (\AA) are as indicated. All models were optimized without relativistic effects, except where indicated. The calculated energies (E , $\text{kJ}\cdot\text{mol}^{-1}$) are also listed with the energy of the reactant taken as zero (see Table 3.23).

		Ph	Ph (incl. rel.)	CH ₃	H	
Rh(I)		Rh-P	2.195	2.171	2.218	2.189
		Rh-P'	2.194	2.171	2.217	2.196
		Rh-O	2.097	2.071	2.113	2.119
		Rh-O'	2.096	2.071	2.111	2.117
		O-Rh-O'	89.9	90.0	89.1	90.6
		O'-Rh-P'	88.8	88.4	91.0	87.4
		P'-Rh-P	92.6	93.1	92.6	93.6
		P-Rh-O	88.7	88.5	87.3	87.9
		RMSD ⁱ	-	0.02	0.06	0.09
		E	0	0	0	0
		Alkyl-A		Rh-P	2.277	2.250
Rh-P'	2.271			2.240	2.270	2.244
Rh-O	2.117			2.099	2.127	2.143
Rh-O'	2.105			2.086	2.126	2.136
Rh-I	2.889			2.855	2.943	2.913
Rh-C	2.121			2.110	2.104	2.114
O-Rh-O'	91.2			91.4	90.1	90.6
O'-Rh-P'	88.3			88.3	88.5	85.6
P'-Rh-P	96.5			96.6	93.2	97.8
P-Rh-O	83.8			83.6	87.9	86.0
I-Rh-C	169.1			168.4	171.7	176.5
RMSD ⁱ	-	0.02	0.12	0.15		
E	-28	-40	-71	-101		
Alkyl-B		Rh-P	2.348	2.317	2.344	2.312
		Rh-P'	2.351	2.321	2.354	2.335
		Rh-O	2.187	2.165	2.203	2.190
		Rh-O'	2.092	2.075	2.086	2.107
		Rh-I	2.739	2.715	2.758	2.740
		Rh-C	2.123	2.112	2.112	2.121
		O-Rh-O'	91.9	92.5	91.7	91.7
		O'-Rh-C	87.3	86.8	86.6	86.7
		C-Rh-I	91.7	92.2	92.1	92.2
		I-Rh-O	89.1	88.6	89.6	89.5
		P-Rh-P'	173.0	173.8	179.7	176.4
RMSD ⁱ	-	0.02	0.10	0.13		
E	21	16	-29	-23		
Alkyl-C		Rh-P	2.511	2.457	2.416	2.460
		Rh-P'	2.257	2.229	2.227	2.260
		Rh-O	2.121	2.102	2.134	2.133
		Rh-O'	2.090	2.073	2.104	2.095
		Rh-I	2.757	2.732	2.742	2.761
		Rh-C	2.114	2.106	2.131	2.120
		O-Rh-O'	91.5	92.0	91.8	91.3
		O'-Rh-P'	90.5	90.2	85.2	89.6
		P'-Rh-I	89.3	89.7	93.9	93.5
		I-Rh-O	88.0	87.5	88.9	85.1
		P-Rh-C	167.6	167.6	175.6	172.2
RMSD ⁱ	-	0.03	0.16	0.16		
E	12	2	-33	-48		
Alkyl-D		Rh-P	2.294	2.267	2.277	2.251
		Rh-P'	2.261	2.232	2.264	2.236
		Rh-O	2.121	2.102	2.134	2.163
		Rh-O'	2.179	2.159	2.210	2.205
		Rh-I	2.821	2.795	2.847	2.853
		Rh-C	2.126	2.112	2.112	2.115
		O-Rh-O'	90.1	90.6	88.9	89.2
		O'-Rh-P'	93.1	92.5	96.0	85.9
		P'-Rh-C	87.7	88.5	88.4	94.5
		C-Rh-O	88.9	88.1	86.6	90.4
		P-Rh-I	166.6	166.9	174.6	175.1
RMSD ⁱ	-	0.02	0.12	0.12		
E	-3	-14	-56	-77		

ⁱ RMSD values, in \AA , are root-mean-square atom positional deviations, calculated by fitting the $\text{Rh}(\text{CCOCCOC})(\text{P})_2$ backbones of the simplified models on the backbone of the full model ($\text{R} = \text{Ph}$).

CHAPTER 3

Table 3.10: The PW91/TZP/methanol calculated selected geometrical parameters, TS imaginary frequencies and activation energies (ΔE^\ddagger) of the three possible transition states when methyl iodide is oxidatively added to the selected square planar rhodium(I) complexes.

	Freq / cm^{-1}	Intensity	Rh-C _{methyl} / Å	C _{methyl} -I / Å	Rh-C _{methyl} -I / °	I-C _{methyl} -H / °	ΔE^\ddagger / $\text{kJ}\cdot\text{mol}^{-1}$
[Rh(acac)(P(OH) ₃) ₂ (CH ₃)(I)]							
linear/back	242i	-523	2.541	2.554	172.9	93.2	14
bent	523i	-315	2.678	2.845	95.0	78.8, 149.6	155
front	253i	-43	2.689	2.617	65.1	83.0, 112.0	106
[Rh(acac)(P(OCH ₃) ₃) ₂ (CH ₃)(I)]							
linear/back	187i	-514	2.608	2.509	175.4	95.5	14
bent	311i	-305	2.684	2.862	94.0	70.4, 136.7	148
front	264i	-82	2.655	2.522	68.1	86.9, 119.9	161
[Rh(CO) ₂ I ₂ (CH ₃)(I)] ⁱ							
linear/back	323i	-	2.592	2.577	176.7	91.8	32
bent	386i	-	2.775	2.641	89.2	144.2, 81.9	160
front	306i	-	2.618	2.721	64.3	124.5, 95.5, 86.7	157

ⁱ BP86/TZP/methanol, from reference [16].

Table 3.11: The PW91/TZP/methanol calculated thermodynamic data of the reactants, TS and product during the oxidative addition reaction [Rh(acac)(P(OR)₃)₂] + CH₃I (where R = Ph, CH₃ or H). All energy values are given compared to the reactant. Unbracketed values refer to R = Ph, round bracketed values refer to R = Ph (including relativistic effects), square bracketed values refer to R = CH₃ and curved bracketed values refer to R = H.

	ΔE / $\text{kJ}\cdot\text{mol}^{-1}$	$\Delta H^{298\text{K}}$ / $\text{kJ}\cdot\text{mol}^{-1}$ ⁱ	$\Delta G^{298\text{K}}$ / $\text{kJ}\cdot\text{mol}^{-1}$ ⁱⁱ	$\Delta S^{298\text{K}}$ / $\text{J}\cdot\text{K}^{-1}\cdot\text{mol}^{-1}$ ⁱⁱⁱ
Reactants	0 (0) [0] {0}	0 (0) [0] {0}	0 (0) [0] {0}	0 (0) [0] {0}
TS	30 (22) [14] {17}	37 (28) [22] {19}	75 (78) [60] {60}	-129 (-168) [-125] {-137}
Product (Alkyl-A)	-28 (-40) [-71] {-101}	-16 (-27) [-56] {-95}	27 (18) [-2] {-47}	-144 (-151) [-180] {-163}

ⁱ Enthalpy, calculated by equation 4.2 (section 4.5.2.1, Chapter 4).

ⁱⁱ Gibbs free energy, calculated by equation 4.3 (section 4.5.2.1, Chapter 4).

ⁱⁱⁱ Entropy, calculated from the temperature dependent partition function in ADF at 298.15 K.

Table 3.12: Electronic (ν) and steric (cone angle, θ) parameters of P(OR)₃, R = Ph or CH₃ and computed relative activation enthalpies of oxidative addition reaction [Rh(acac)(P(OR)₃)₂] + CH₃I.

P(OR) ₃	ν / cm^{-1}	cone angle / °	$\Delta H^\ddagger^{298\text{K}}$ / $\text{kJ}\cdot\text{mol}^{-1}$
P(OPh) ₃	2085	128	37
P(OCH ₃) ₃	2080	107	22

3.1.5 Crystal structure of [Rh(bth)(CO)₂].

Transition metal complexes with a square planar geometry allow stacking in the solid state and allow the molecules to interact with another unit. As a consequence, the formation of metal chains is possible.^{34,35} Examples of metal chains with strong metal-metal bonds that are catalytically active in processes, such as the water gas shift reaction and CO₂ reduction, are known.³⁶ 16-Electron rhodium(I) complexes are electron deficient and coordinatively unsaturated, making these systems prone to stacking and allowing the formation of metal-metal bonds³⁷ and chains with weak metal-metal interactions between the rhodium atoms.^{38,39} The

³⁴ M. Jakonen, L. Oresmaa, M. Haukka, *Crystal Growth & Design*, **2007** (7) 2620-2626.

³⁵ (a) J.S. Miller, *Extended linear chain compounds*, Plenum Press: New York, **1982**, Vol. 1–3. (b) J.K. Bera, K.R. Dunbar, *Angew. Chem., Int. Ed.* **2002** (23) 4453-4457.

³⁶ (a) K. Tanaka, M. Morimoto, T. Tanaka, *Chem. Lett.* **1983** 901-904. (b) M. Haukka, J. Kiviaho, M. Ahlgrén, T.A. Pakkanen, *Organometallics* **1995** (14) 825-833. (c) S. Luukkanen, P. Homanen, M. Haukka, T.A. Pakkanen, A. Deronzier, S. Chardon-Noblat, D. Zsoldos, R. Ziessel, *Appl. Catal. A* **1995** (185) 157-164. (d) M. Haukka, T. Venäläinen, M. Kallinen, T.A. Pakkanen, *J. Mol. Catal. A: Chem.* **1998** (136) 127-134. (e) M.A. Moreno, M. Haukka, T. Venäläinen, T.A. Pakkanen, *Catal. Lett.* **2004** (96) 153-155. (f) H. Ishida, K. Tanaka, T. Tanaka, *Chem. Lett.* **1985** (3) 405-406. (g) H. Ishida, K. Tanaka, T. Tanaka, *Chem. Lett.* **1987** (16) 1035-1038. (h) M.-N. Collomb-Dunand-Sauthier, A. Deronzier, R. Ziessel, *Inorg. Chem.* **1994** (33) 2961-2967. (i) S. Chardon-Noblat, A. Deronzier, F. Hartl, J. van Slageren, T. Mahabiersig, *Eur. J. Inorg. Chem.* **2001** 613-617.

³⁷ (a) S.-S. Chern, G.-H. Lee, S.-M. Peng, *Chem. Commun.* **1994** 1645-1646. (b) G.M. Finnis, E. Candall, C. Campana, K.R. Dunbar, *Angew. Chem., Int. Ed.* **1996** (35) 2772-2774. (c) M. Mitsumi, H. Goto, S. Umabayashi, Y. Ozawa, M. Kobayashi, T. Yokoyama, H. Tanaka, S. Kuroda, K. Toriumi, *Angew. Chem., Int. Ed.* **2005** (44) 4164-4168.

³⁸ F. Huq, A.C. Skapski, *J. Cryst. Mol. Struct.* **1974** (4) 411-418.

³⁹ (a) M.J. Decker, D.O.K. Fjeldsted, S.R. Stobart, M.J. Zaworotko, *Chem. Commun.* **1983** 1525-1527. (b) C. Crotti, S. Cenini, B. Rindone, S. Tollari, F. Demartin, *Chem. Commun.* **1986** 784-786. (c) G.M. Villacorta, S.J. Lippard, *Inorg. Chem.* **1988** (27) 144-149. (d) G. Matsubayashi, K. Yokoyama, T. Tanaka, *J. Chem. Soc., Dalton Trans.* **1988** 253-256. (e) L.A. Oro, M.T. Pinillos, C. Tejel, M.C. Apreada, C. Foces-Foces, F.H. Cano, *J. Chem. Soc., Dalton Trans.* **1988** 1927-1933. (f) J. Pursiainen, T. Teppana, S. Rossi, T.A. Pakkanen, *Acta Chem. Scand.* **1993** (47) 416-418. (g) F. Ragaini, M. Pizzotti, S. Cenini, A. Abboto, G.A. Pagain, F. Demartin, *J. Organomet. Chem.* **1995** (489) 107-112. (h) A. Elduque, C. Finestra, J.A. López, F.J. Lahoz, F. Merchan, L.A. Oro, M.T. Pinillos, *Inorg. Chem.* **1998** (37) 824-829. (i) F.P. Pruchnik, P. Jakimowicz, Z. Ciunik, *Inorg. Chem. Commun.* **2001** (4) 726-729. (j) N.K. Kiriakidou-Kazemifar, M. Haukka, T.A. Pakkanen, S.P. Tunik, E. Nordlander, *J. Organomet. Chem.* **2001** (623) 65-73. (k) M.C. Torralba, M. Cano, J.A. Campo, J.V. Heras, E. Pinilla, M.R. Torres, *J. Organomet. Chem.* **2001** (633) 91-104. (l) F.A. Cotton, E.V. Dikarev, M.A. Petrukhina, *J. Organomet. Chem.* **2002** (596) 130-135.

extended interactions are the result of metal-metal σ -bonding between the square planar d^8 transitional metal complexes. The weak σ -bonding interactions are formed between occupied d_{z^2} -orbitals and unoccupied p_z -orbitals.⁴⁰ The typical distance between two rhodium(I) molecules in extended metal chains is in the range of 3.25-3.68 Å.^{38,39} The square planar rhodium(I) complexes can also form a dinuclear unit, which interacts with another similar dinuclear unit *via* weak metal-metal interactions,^{38,39,41} metal and ligand interactions,^{42,43} metal and aromatic π -interactions⁴³ or π - π interactions.³⁴ In these cases, the distance between the metals in the dinuclear unit varies from 3.23 to almost 4.00 Å.^{43,44}

The results of a single crystal structure determination of [Rh(bth)(CO)₂] (Hbth = benzoylthenoylacetone) are presented. The molecular diagram showing atom labelling of [Rh(bth)(CO)₂] is presented in Figure 3.28. Crystal data of the structure of [Rh(bth)(CO)₂] are summarized in Table 3.15, selected bond lengths, angles and torsion angles can be found in Table 3.14. The cif file with the complete crystallographic data, is given in Appendix B. Selected comparative geometric data of the square planar complexes of the type [Rh(β -diketonato)(CO)₂] (β -diketonato = bth, acac,³⁸ tfba⁴⁵ and fctfa⁴⁶) are given in Table 3.13.

⁴⁰ S.T. Trzaska, T.M. Swager, *Chem. Mater.* **1998** (10) 438-443.

⁴¹ (a) V. Schurig, W. Pille, W. Winter, *Angew. Chem., Int. Ed.* **1983** (22) 327-328. (b) A.F. Heyduk, D.J. Krodell, E.E. Meyer, D.G. Nocera, *Inorg. Chem.* **2002** (41) 634-636.

⁴² J.F. Berry, F.A. Cotton, P. Huang, C.A. Murillo, X. Wang, *Dalton Trans.* **2005** 3713-3715.

⁴³ (a) R.J. Doendes, *Inorg. Chem.* **1978** (17) 1315-1318. (b) P.W. de Haeven, V.L. Goedken, *Inorg. Chem.* **1979** (18) 827-831. (c) Y. Yamamoto, Y. Wakatsuki, H. Yamazaki, *Organometallics* **1983** (2) 1604-1607. (d) F.A. Cotton, K.-B. Shiu, *Rev. Chem. Miner.* **1986** (23) 14-19. (e) W.S. Sheldrick, P. Bell, *Inorg. Chim. Acta* **1987** (137) 181-188. (f) W.S. Sheldrick, B. Gunther, *Inorg. Chim. Acta* **1988** (151) 237-241. (g) E. Corradi, N. Masciocchi, G. Palyi, R. Ugo, A. Vizi-Orosz, C. Zucchi, A. Sironi, *J. Chem. Soc., Dalton Trans.* **1997** 4651-4655. (h) A. Elduque, Y. Garces, F.J. Lahoz, J.A. Lopéz, L.A. Oro, T. Pinillos, C. Tejel, *Inorg. Chem. Commun.* **1999** (2) 414-418. (i) T. Mochida, R. Torigoe, T. Koinuma, C. Asano, T. Satou, K. Koike, T. Nikaido, *Eur. J. Inorg. Chem.* **2006** 558-565.

⁴⁴ F.H. Allen, *Acta Crystallogr., Sect. B* **2002** (58) 380-388.

⁴⁵ J.G. Leipoldt, L.D.C. Bok, S.S. Basson, J.S. van Vollenhoven, T.I.A. Gerber, *Inorg. Chim. Acta* **1977** (25) L63-L64.

⁴⁶ J. Conradie, T.S. Cameron, M.A.S. Aquino, G.J. Lambrecht, J.C. Swarts, *Inorg. Chim. Acta* **2005** (358) 2530-2542.

RESULTS AND DISCUSSION

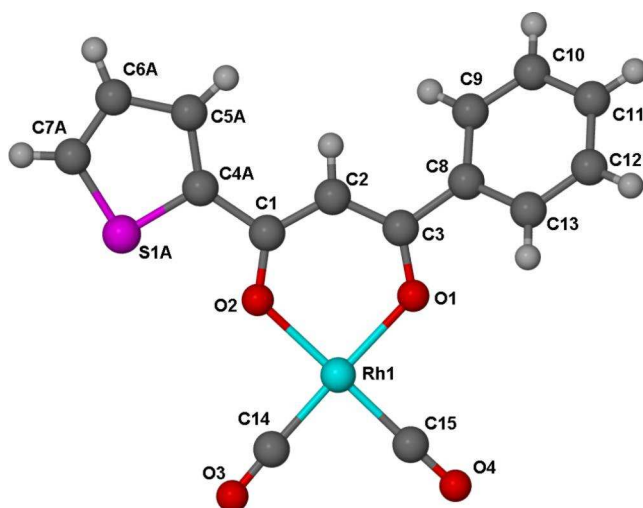


Figure 3.28: Molecular diagram of $[\text{Rh}(\text{bth})(\text{CO})_2]$ (Hbth = benzoylthenoylacetone) showing atom numbering.

Table 3.13: Selected geometric and crystallographic data of square planar complexes $[\text{Rh}(\beta\text{-diketonato})(\text{CO})_2]$ ($\beta\text{-diketonato}$ = bth, acac,³⁸ tfba⁴⁵ and fctfa⁴⁶) with R^1 and R^2 groups as indicated.

$\beta\text{-diketonate}$ $\text{R}_1\text{COCH}_2\text{COR}_2$	R_1	R_2	Rh-O / Å	$\text{Rh-O}'$ / Å	Rh-C / Å	$\text{Rh-C}'$ / Å	$\text{O-Rh-O}'$ / °	$\text{C-Rh-C}'$ / °	Space group
Hbth benzoylthenoylacetone	Ph	$\text{C}_4\text{H}_3\text{S}$	2.028(6)	2.041(5)	1.866(9)	1.846(9)	90.4(2)	88.1(3)	$P2_12_12_1$
Hacac acetylacetone	CH_3	CH_3	2.040(4)	2.044(4)	1.831(7)	1.831(7)	90.8(2)	88.9(3)	$P\bar{1}$
Htfba trifluorobenzoylacetone	CF_3	Ph	2.02(2)	2.02(2)	1.79(3)	1.82(3)	89.8(7)	87(1)	$Pbca$
Hfctfa ferrocenyltrifluoroacetone	Fc	CF_3	2.016(9)	2.049(8)	1.84(1)	1.83(2)	90.2(3)	89.1(6)	$C2/c$

The $[\text{Rh}(\text{bth})(\text{CO})_2]$ molecules pack in the $P2_12_12_1$ space group with $Z = 4$. The Rh(I) atom has a square planar coordination sphere. The $[\text{Rh}(\text{bth})(\text{CO})_2]$ molecule as a whole is non-planar. The thenoyl ($\text{C}_4\text{H}_3\text{S}$) and benzoyl (Ph) groups bonded to the $\beta\text{-diketonate}$ backbone are both rotated out of the plane formed by the rest of the molecule by 2° and 15° respectively. This might possibly be due to packing effects (Figure 3.29) as different interactions of the two groups are observed with neighbouring molecules. Although both the groups are aromatic, the angle of the benzoyl which is larger than the angle of the thenoyl, implies that the conjugation between the pseudo aromatic $\beta\text{-diketonate}$ ring and the thenoyl is stronger. The bonds around the rhodium centre of the $[\text{Rh}(\text{bth})(\text{CO})_2]$ molecule were in the same range as the other $[\text{Rh}(\beta\text{-diketonato})(\text{CO})_2]$ molecules (Table 3.13).

The packing diagrams of the $[\text{Rh}(\beta\text{-diketonato})(\text{CO})_2]$ molecules are given in Figure 3.29. The $[\text{Rh}(\text{bth})(\text{CO})_2]$ molecules stack in an infinite chain of rhodium atoms along the a -axis with a $\text{Rh}\cdots\text{Rh}$ distance of 3.250 Å. Neighbouring units are oriented with an angle of 180° in the opposite direction due to an inversion symmetry operation (Figure 3.30). The rhodium atoms

that form the core of a column are stacked in a zigzag fashion with an angle between Rh...Rh vectors of 167.38° . The distance between Rh atoms in $[\text{Rh}(\text{bth})(\text{CO})_2]$ is therefore too long to be considered as a true metal-metal bond, but indicates clearly that interactions between metal atoms exist. In the examples presented in the literature, the distance between the two Rh(I) centres is typically within a range of $3.25\text{-}3.68 \text{ \AA}$ ^{34,38,39} in the stacked Rh(I) chains that have no covalent metal-metal bonds and contain meaningful weak metal-metal interactions. Similar Rh...Rh interactions were observed for the other $[\text{Rh}(\beta\text{-diketonato})(\text{CO})_2]$ molecules ($\beta\text{-diketonato} = \text{acac}, \text{tfba}$ and fctfa), as illustrated in Figure 3.29.

The $[\text{Rh}(\text{acac})(\text{CO})_2]$ molecules consist of weak dimeric units with a Rh...Rh distance of 3.253 \AA . These dimers are stacked along the *a*-axis in a linear fashion, with a distance of 3.271 \AA between the dimers. The neighbouring atoms in a dimeric unit are oriented with an angle of 180° in the opposite direction due to an inversion symmetry operation. A stereoview of this stacking arrangement is given in Figure 3.30. The rhodium atoms that form the core of a column are not perfectly aligned on top of one another with an angle between Rh...Rh vectors of 175.28° .

The $[\text{Rh}(\text{tfba})(\text{CO})_2]$ molecules stack in infinite arrays along the *c*-axis, with a Rh...Rh distance of 3.537 \AA between the molecules. Different from $[\text{Rh}(\text{bth})(\text{CO})_2]$ and $[\text{Rh}(\text{acac})(\text{CO})_2]$, neighbouring $[\text{Rh}(\text{tfba})(\text{CO})_2]$ molecules are staggered with an O-Rh...Rh-O torsion angle of $\sim 115^\circ$ between them (Figure 3.30). The orientation of the neighbouring molecules is antieclipsed. That is, the ligands are oriented in opposite directions. The angle between Rh...Rh vectors forming the core of a column is 170.0° . The benzoyl (Ph) group bonded to the $\beta\text{-diketonato}$ backbone in $[\text{Rh}(\text{tfba})(\text{CO})_2]$ is rotated out of the plane formed by the rest of the molecule by 22° , slightly more than the 15° rotation of the benzoyl in $[\text{Rh}(\text{bth})(\text{CO})_2]$.

The $[\text{Rh}(\text{fctfa})(\text{CO})_2]$ molecules form weak dimeric units with a Rh...Rh distances of 3.346 . Like $[\text{Rh}(\text{tfba})(\text{CO})_2]$, the two units of a $[\text{Rh}(\text{fctfa})(\text{CO})_2]$ dimer are staggered with a an O-Rh...Rh-O torsion angle of $\sim 96^\circ$ between them (Figure 3.30) and the orientation of the neighbouring molecules is antieclipsed. The dimeric units are further supported by $\pi\text{-}\pi$ interactions that exist between the neighbouring cyclopentadienyl rings of the ferrocenyl (Fc) groups. The cyclopentadienyl rings are displaced from each other, in a slipped or offset alignment⁴⁷ with a

⁴⁷ C. Janiak, *J. Chem. Soc., Dalton Trans.* **2000** 3885-3896.

RESULTS AND DISCUSSION

centroid-centroid separation of 3.585 Å. One main difference between the $[\text{Rh}(\text{fctfa})(\text{CO})_2]$ and the other three $[\text{Rh}(\beta\text{-diketonato})(\text{CO})_2]$ complexes discussed here is that the dimeric units do not stack with the rhodium as a central axis. The dimeric units additionally rotate a further 180° so that the rhodium centre of the one pair stacks on the β -diketonato backbone of the adjacent pair. Such an arrangement allows Rh- π interactions between the Rh of one dimeric unit and the cyclopentadienyl ring of another unit. The Rh-centroid separation is 3.599 Å. The stacking is illustrated by the blue spheres in Figure 3.29.

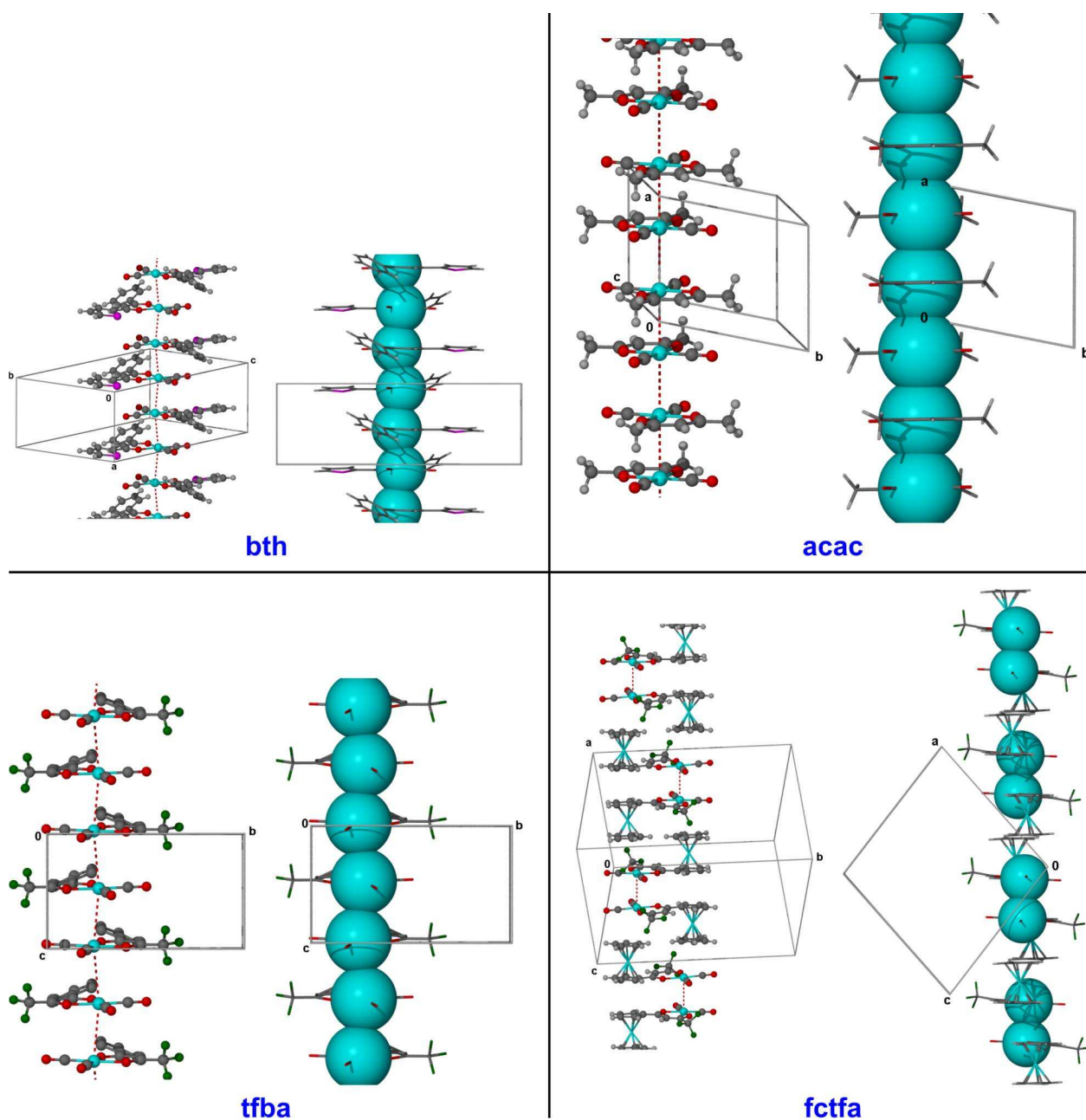


Figure 3.29: Packing diagrams of the $[\text{Rh}(\beta\text{-diketonato})(\text{CO})_2]$ molecules (β -diketonato = bth, acac, tfba and fctfa). Note the different types of stacking, accentuated by the blue spheres around the rhodium centre.

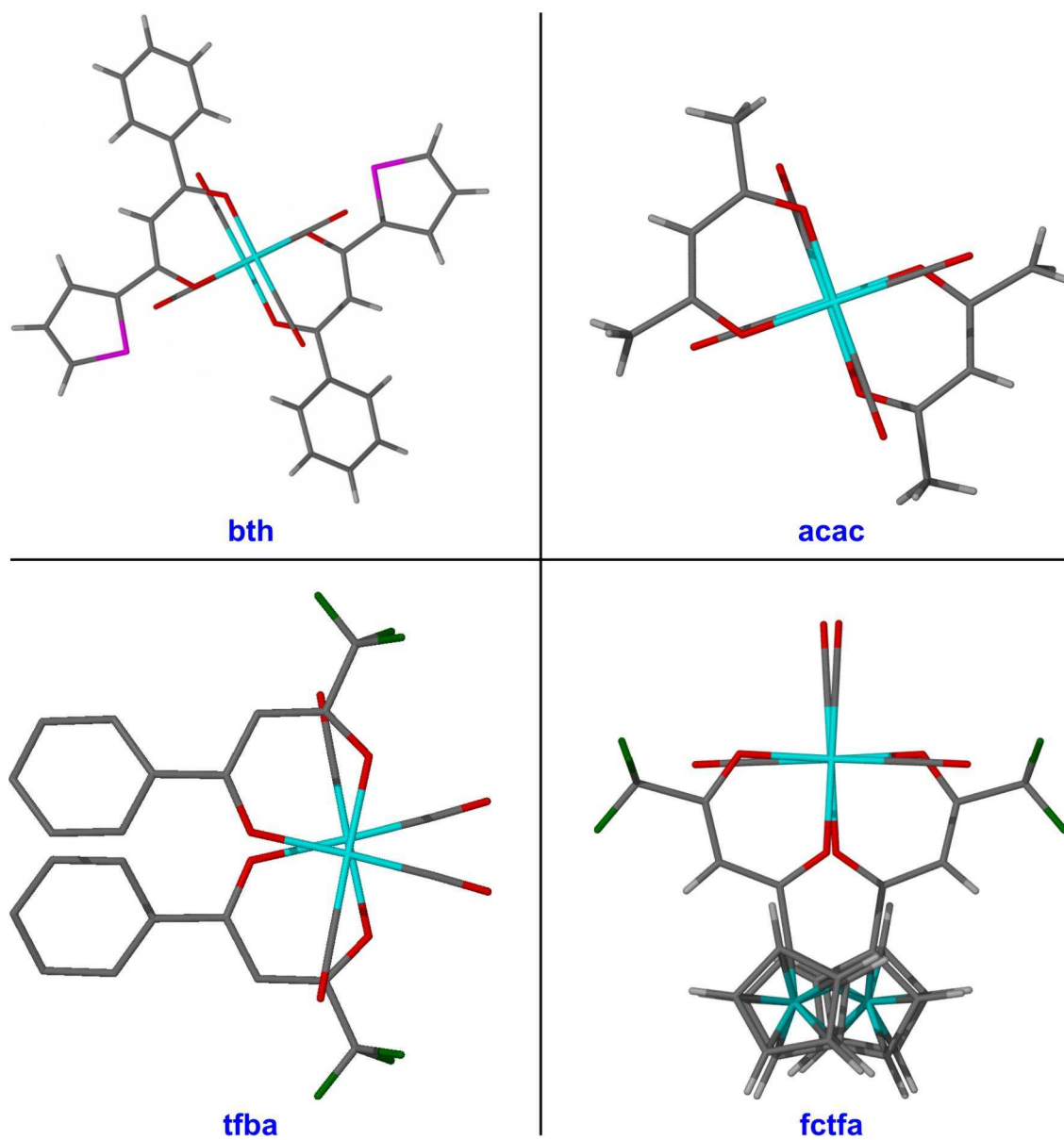


Figure 3.30: Two closest interacting $[\text{Rh}(\beta\text{-diketonato})(\text{CO})_2]$ molecules ($\beta\text{-diketonato} = \text{bth}, \text{acac}, \text{tfba}$ and fctfa), viewed perpendicularly to the coordination plane. Note the orientation between the two molecules.

RESULTS AND DISCUSSION

Table 3.14: Selected bond lengths (Å), bond angles (°) and torsion angles (°) of [Rh(bth)(CO)₂]. Geometric parameters involving hydrogen atoms are omitted from this table. Atom numbering is as indicated in Figure 3.28.

Bond lengths / Å					
Rh1-C14	1.846 (9)	C1-C4B	1.485 (16)	C12-C13	1.383 (12)
Rh1-C15	1.866 (9)	C2-C3	1.391 (11)	S1A-C7A	1.684 (10)
Rh1-O1	2.028 (6)	C3-C8	1.496 (12)	S1A-C4A	1.714 (11)
Rh1-O2	2.041 (5)	C4B-C5B	1.438 (17)	C5A-C4A	1.421 (17)
O1-C3	1.265 (10)	C4B-S1B	1.728 (17)	C5A-C6A	1.431 (17)
O2-C1	1.250 (9)	C8-C9	1.397 (12)	C6A-C7A	1.359 (13)
O3-C14	1.140 (9)	C8-C13	1.438 (13)	S1B-C7B	1.695 (19)
O4-C15	1.128 (10)	C9-C10	1.360 (12)	C5B-C6B	1.415 (18)
C1-C2	1.401 (10)	C10-C11	1.373 (14)	C6B-C7B	1.325 (18)
C1-C4A	1.483 (10)	C11-C12	1.366 (14)		
Bond angles / °					
C14-Rh1-C15	88.1 (3)	C3-C2-C1	126.5 (7)	C12-C13-C8	118.2 (8)
C14-Rh1-O1	177.5 (3)	O1-C3-C2	125.3 (8)	O3-C14-Rh1	178.2 (7)
C15-Rh1-O1	90.4 (3)	O1-C3-C8	114.8 (7)	O4-C15-Rh1	178.7 (8)
C14-Rh1-O2	91.2 (3)	C2-C3-C8	119.8 (7)	C7A-S1A-C4A	91.9 (5)
C15-Rh1-O2	177.6 (4)	C5B-C4B-C1	133.3 (16)	C4A-C5A-C6A	110.0 (14)
O1-Rh1-O2	90.4 (2)	C5B-C4B-S1B	113.3 (12)	C7A-C6A-C5A	112.7 (11)
C3-O1-Rh1	126.1 (6)	C1-C4B-S1B	113.4 (13)	C6A-C7A-S1A	113.8 (8)
C1-O2-Rh1	125.3 (5)	C9-C8-C13	118.1 (8)	C7B-S1B-C4B	90.4 (11)
O2-C1-C2	126.3 (7)	C9-C8-C3	124.3 (8)	C6B-C5B-C4B	106.2 (15)
O2-C1-C4A	116.5 (8)	C13-C8-C3	117.6 (7)	C7B-C6B-C5B	117.1 (19)
C2-C1-C4A	117.2 (8)	C10-C9-C8	120.7 (9)	C6B-C7B-S1B	113.0 (18)
O2-C1-C4B	106.6 (10)	C9-C10-C11	121.7 (9)	C5A-C4A-C1	133.2 (12)
C2-C1-C4B	126.9 (11)	C12-C11-C10	118.9 (9)	C5A-C4A-S1A	111.6 (9)
C4A-C1-C4B	11.2 (10)	C11-C12-C13	122.4 (9)	C1-C4A-S1A	115.2 (8)
Torsion angles / °					
C14-Rh1-O1-C3	-133 (7)	C2-C1-C4B-S1B	-21 (3)	C4A-C5A-C6A-C7A	-0.4 (15)
C15-Rh1-O1-C3	175.0 (8)	C4A-C1-C4B-S1B	11 (7)	C5A-C6A-C7A-S1A	-0.6 (14)
O2-Rh1-O1-C3	-2.7 (8)	O1-C3-C8-C9	154.6 (9)	C4A-S1A-C7A-C6A	1.1 (11)
C14-Rh1-O2-C1	179.8 (7)	C2-C3-C8-C9	-28.7 (14)	C5B-C4B-S1B-C7B	0 (3)
C15-Rh1-O2-C1	-109 (7)	O1-C3-C8-C13	-27.1 (11)	C1-C4B-S1B-C7B	178 (3)
O1-Rh1-O2-C1	1.7 (7)	C2-C3-C8-C13	149.5 (10)	C1-C4B-C5B-C6B	-179 (4)
Rh1-O2-C1-C2	-0.1 (13)	C13-C8-C9-C10	0.9 (13)	S1B-C4B-C5B-C6B	-1.0 (17)
Rh1-O2-C1-C4A	-179.1 (7)	C3-C8-C9-C10	179.1 (8)	C4B-C5B-C6B-C7B	1 (2)
Rh1-O2-C1-C4B	175.3 (16)	C8-C9-C10-C11	0.4 (14)	C5B-C6B-C7B-S1B	-1 (4)
O2-C1-C2-C3	-1.4 (17)	C9-C10-C11-C12	-1.5 (15)	C4B-S1B-C7B-C6B	0 (3)
C4A-C1-C2-C3	177.5 (10)	C10-C11-C12-C13	1.4 (16)	C6A-C5A-C4A-C1	-179.5 (13)
C4B-C1-C2-C3	-176 (2)	C11-C12-C13-C8	-0.1 (15)	C6A-C5A-C4A-S1A	1.2 (14)
Rh1-O1-C3-C2	2.3 (14)	C9-C8-C13-C12	-1.0 (13)	O2-C1-C4A-C5A	172.4 (13)
Rh1-O1-C3-C8	178.7 (6)	C3-C8-C13-C12	-179.4 (8)	C2-C1-C4A-C5A	-6.6 (17)
C1-C2-C3-O1	0.2 (18)	C15-Rh1-C14-O3	22 (27)	C4B-C1-C4A-C5A	-159 (10)
C1-C2-C3-C8	-176.0 (8)	O1-Rh1-C14-O3	-31 (32)	O2-C1-C4A-S1A	-8.2 (13)
O2-C1-C4B-C5B	-19 (4)	O2-Rh1-C14-O3	-160 (27)	C2-C1-C4A-S1A	172.7 (8)
C2-C1-C4B-C5B	157 (2)	C14-Rh1-C15-O4	-171 (41)	C4B-C1-C4A-S1A	21 (9)
C4A-C1-C4B-C5B	-172 (12)	O1-Rh1-C15-O4	7 (41)	C7A-S1A-C4A-C5A	-1.3 (11)
O2-C1-C4B-S1B	163.8 (17)	O2-Rh1-C15-O4	118 (39)	C7A-S1A-C4A-C1	179.2 (9)

CHAPTER 3

Table 3.15: Crystal data and structure refinement of [Rh(bth(CO)₂)].

Empirical formula	C ₁₅ H ₉ O ₄ RhS	Theta range for data collection	3.5-40.5°
Formula weight	388.19 g mol ⁻¹	Index ranges	8<=h<=8 15<=k<=15 26<=l<=26
Temperature	100(2) K	Reflections collected	25770
Wavelength	0.71073 Å	Independent reflections	3596 [R _{int} = 0.152]
Crystal system	Orthorhombic	Theta maximum	28.5°
Space group	<i>P2₁2₁2₁</i>	Absorption correction	multi-scan
Unit cell dimensions	a = 6.4610(9) Å b = 11.4245(18) Å c = 19.557(3) Å α = 90° β = 90° γ = 90°	Max. and min. transmission	0.937 and 0.620
Volume	1443.57 Å ³	Refinement method	Full-matrix least-squares on F ²
Z	4	Data / restraints / parameters	3596 / 26 / 185
Density (calculated)	1.786 Mg m ⁻³	Goodness-of-fit on F²	1.06
Absorption coefficient (μ)	1.34 mm ⁻¹	Final R indices [I > 2σ(I)]	R1 = 0.074
F(000)	768	R indices (all data)	R1 = 0.0979 wR2 = 0.1948
Crystal size	0.40 x 0.09 x 0.05 mm ³	Largest diff. peak and hole	3.46 and -1.60 e.Å ⁻³
-	-	Absolute structure parameter	0.46(10)

3.2 Iron complexes.

3.2.1 [Fe(β -diketonato)₃].

3.2.1.1 Synthesis.

Two new [Fe(β -diketonato)₃] complexes (β -diketonato = bth {3} and dtm {4}) and eight known [Fe(β -diketonato)₃] complexes (β -diketonato = acac {1}, ba {2}, dbm {5}, tfaa {6}, tffu {7}, tfba {8}, tta {9} and hfaa {10}) were synthesized by a general adapted method.^{48,49,50} The general method is given in Figure 3.31.

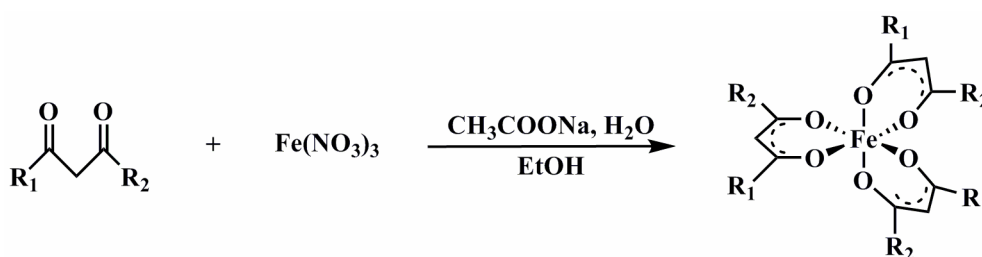


Figure 3.31: General method to synthesize [Fe(β -diketonato)₃] complexes.

The method involves buffering the aqueous metal solution of Fe(NO₃)₃ with sodium acetate. The result of this reaction, 2 Fe(NO₃)₃ + 4 CH₃COONa, is a paddle wheel complex [Fe₂(CH₃COO)₄] (Figure 3.32). Bridging occurs since the CH₃COO⁻ ligand forms a four membered ring with a bite angle of ~68°. Since a bite angle of ~90° (as with a six membered ring) is necessary for overlap with the *d*-orbitals of the iron centre (as with the final product), a paddle wheel complex forms. This keeps the iron soluble in water without reacting with the water itself.

⁴⁸ E.W. Berg, J.T. Truemper, *J. Phys. Chem.* **1960** (64) 487-490.

⁴⁹ K. Endo, M. Furukawa, H. Yamatera, H Sano, *Bull. Chem. Soc. Jpn* **1980** (53) 407-410.

⁵⁰ G.S. Hammond, D.C. Nonhebel, C.S. Wu, *Inorg. Chem.* **1963** (2) 73-76.

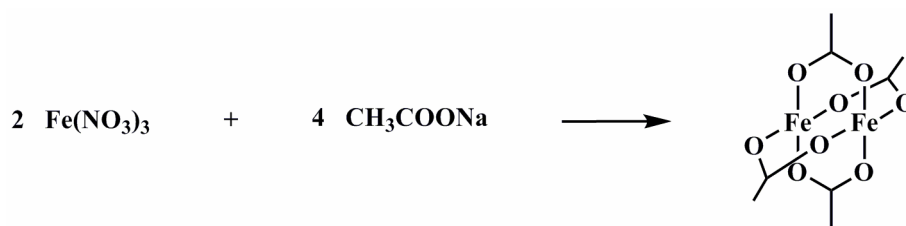


Figure 3.32: The paddle wheel complex $[\text{Fe}_2(\text{CH}_3\text{COO})_4]$.

For complexes {2}, {3}, {8} and {9}, the aqueous buffered metal solution was used as is. For complexes {1}, {4}, {5}, {6}, {7} and {10}, ethanol was added additionally to the aqueous buffered metal solution to make a 1:1 $\text{H}_2\text{O}:\text{EtOH}$ solution. This was done for the purpose of the next step for one of the following two reasons: the β -diketone is already a liquid and was therefore not dissolved in ethanol or the β -diketone is insoluble in pure water. The next step therefore is to add the β -diketone to the buffered metal solution. For {2}, {3}, {8} and {9}, the β -diketones were first dissolved in ethanol and then added to the buffered solution. For {1}, {6}, {7} and {10}, the β -diketones were added direct with a syringe, since they are liquid at room temperature. For {4} and {5}, the β -diketones were first dissolved in DCM and then added to the 1:1 $\text{H}_2\text{O}:\text{EtOH}$ solution. The resulting solution in all the cases was stirred well for 30 minutes and was left overnight in a fume hood. The precipitate was collected the next day by filtration and thorough washing with water. The complexes were confirmed by mass spectroscopy and elemental analysis (section 4.3.3, Chapter 4). Since the complexes are paramagnetic, no ^1H NMR characterization was possible. A comparison table with the different characteristics of the different $[\text{Fe}(\beta\text{-diketonato})_3]$ complexes is given in Table 3.16.

In general, good yields (71-96%) were obtained, except for {4} and {10} which had yields of 39% and 51% respectively. The poor yield for {4} is due to solubility problems of the β -diketone. DCM was the only solvent that reasonably could dissolve the β -diketone and still could mix with the buffered metal solution. The poor yield for {10} is probably due to the fact that the β -diketone is extremely volatile at room temperature.

The complexes had all red-like colours, varying from light orange to black. This is due to the crystal field splitting exhibited by the high spin octahedral complexes, which will be discussed in section 3.2.1.4. The melting points of the known complexes were in the same range as the reported values,^{48,51,52,53,54,55,56} except for {8} which was found to melt much earlier than the reported value. Since the elemental analysis of this compound was within 99% accurate for

RESULTS AND DISCUSSION

carbon, it is assumed that the compound is clean. The melting point was determined three times and is therefore accepted to be 58.4-60.1 °C and not 128-129 °C, as reported by Berg *et al.*⁴⁸ in 1960.

Table 3.16: Characteristic data and results of the synthesis of [Fe(β -diketonato)₃] complexes.

[Fe(β -diketonato) ₃]		Yield	Colour	$\lambda_{\max} / \text{nm}^i$ ($\epsilon_{\max} / \text{mol}^{-1} \cdot \text{dm}^3 \cdot \text{cm}^{-1}$)	M.p.
acac {1}	acetylacetone	73%	red	270 (25842)	180.0-182.0 °C (reported: 179 °C, ⁴⁸ 180 °C ⁵¹)
ba {2}	benzoylacetone	84%	red-orange	298 (40256)	218.5-220.3 °C (reported: 222-224 °C ⁴⁸)
bth {3}	benzoylthenoylacetylacetone	85%	red-brown	361 (30956)	220.0-222.0 °C
dtm {4}	dithenoylmethane	39%	black	260 (35301)	63.7-66.4 °C
dbm {5}	dibenzoylmethane	71%	dark red	336 (48608)	264.0-265.2 °C (reported: 261 °C, ⁵² 257 °C ⁵³)
tfaa {6}	trifluoroacetylacetone	91%	red-brown	271 (48996)	113.5-116.1 °C (reported: 115 °C ^{48,54})
tffu {7}	trifluorofuroylacetone	92%	dark red	333 (53476)	205.0-208.0 °C (reported: 201-208 °C ⁴⁸)
tfba {8}	trifluorobenzoylacetone	96%	orange	304 (30788)	58.4-60.1 °C (reported: 128-129 °C ⁴⁸)
tta {9}	thenoyltrifluoroacetone	78%	dark red	333 (48461)	158.0-161.0 °C (reported: 159-160 °C, ⁴⁸ 162.5 °C ⁵⁵)
hfaa {10}	hexafluoroacetylacetone	51%	light orange	- ⁱⁱ	56.0-58.0 °C (reported: 55 °C ⁵⁶)

i In CH₃CN solution.

ii Insoluble in CH₃CN.

3.2.1.2 Cyclic Voltammetry (CV).

In this section, the electrochemistry of [Fe^{III}(β -diketonato)₃] (β -diketonato = acac {1}, ba {2}, bth {3}, dtm {4}, dbm {5}, tfaa {6}, tffu {7}, tfba {8}, tta {9} and hfaa {10}, Table 3.18) is described. The only redox active centre in the complexes studied was the iron centre. The oxidation state of iron changes reversibly between Fe(III) and Fe(II). The overall electrochemical reaction is: [Fe^{III}(β -diketonato)₃] + e⁻ \rightleftharpoons [Fe^{II}(β -diketonato)₃]⁻. The different redox potentials of the [Fe^{III}(β -diketonato)₃] series are due to the different electronic densities at the metal centre due to the different substituents on the β -diketonato ligands. The details of the methods used are given in section 4.2.5 (Chapter 4).

⁵¹ M.-L. Hu, Z.-M. Jin, Q. Miao, L.-P. Fang, *Z. Kristallogr. - New Cryst. Struct.* **2001** (216) 597-598.

⁵² B. Kaitner, B. Kamenar, *Cryst. Struct. Commun.* **1980** (9) 487-492.

⁵³ I.A. Baidina, P.A. Stabnikov, I.K. Igumenov, S.V. Borisov, *Koord. Khim. (Russ.) (Coord. Chem.)* **1986** (12) 258-265.

⁵⁴ I.A. Baidina, P.A. Stabnikov, I.K. Igumenov, S.V. Borisov, *Koord. Khim. (Russ.) (Coord. Chem.)* **1986** (12) 404-408.

⁵⁵ H. Soling, *Acta Chem. Scand. A* **1976** (30) 163-170.

⁵⁶ C.E. Pfluger, P.S. Haradem, *Inorg. Chim. Acta* **1983** (69) 141-146.

The electrochemical data of [Fe(acac)₃] {1} (at varying scan rates) are summarized in Table 3.17 and the cyclic voltammograms are shown in Figure 3.33. One iron-related reduction half reaction in the cathodic sweep (the peaks pointing downward) and one oxidation half reaction in the anodic sweep (the peaks pointing upward) were observed. The [Fe(acac)₃] {1} complex shows reversible electrochemical behaviour at the slower scan rates ($\Delta E_p < 90$ mV). However, at a higher scan rate of 1000 mV.s⁻¹, the difference in peak potentials increased to 109 mV. A slow increase of ΔE_p with scan rate is consistent with electrode adsorption. The current ratios ($i_{pa}/i_{pc} \approx 1$) indicate that this redox reaction is chemically reversible.

Table 3.17: Electrochemical dataⁱ of [Fe(acac)₃] {1}.

Scan Rate / mV.s ⁻¹	E _{pa} / V	E _{pc} / V	ΔE _p / V	E ^{0'} / V	i _{pa} / μA	i _{pc} / μA	i _{pa} /i _{pc}
50	-1.002	-1.076	0.074	-1.039	10.56	10.75	0.98
100	-1.002	-1.074	0.072	-1.038	14.66	14.72	1.00
150	-1.000	-1.077	0.077	-1.038	17.58	18.51	0.95
200	-0.997	-1.078	0.081	-1.037	20.25	20.50	0.99
250	-0.997	-1.078	0.081	-1.037	22.73	22.92	0.99
300	-0.993	-1.081	0.088	-1.037	24.47	25.03	0.98
1000	-0.983	-1.092	0.109	-1.037	42.42	43.35	0.98

ⁱ Solvent CH₃CN, supporting electrolyte TBAPF₆ ([NBu₄][PF₆]), versus Fc/Fc⁺, scan rate as indicated.

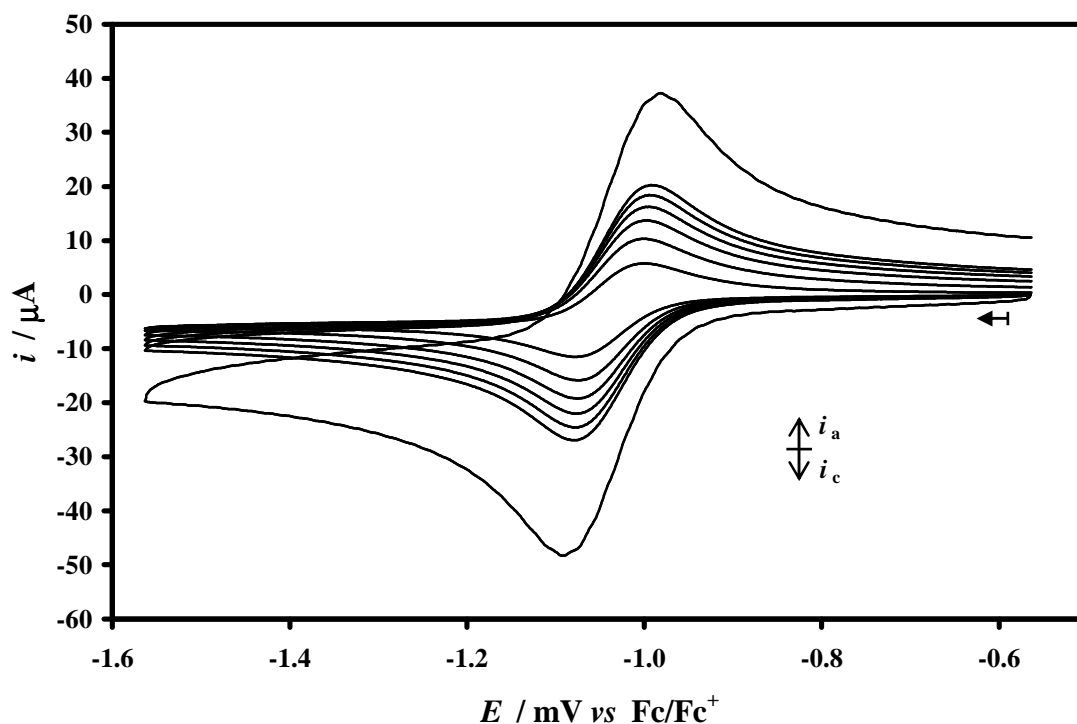


Figure 3.33: Cyclic voltammograms (versus Fc/Fc⁺) of 1 mmol.dm⁻³ [Fe(acac)₃] {1} at scan rates 50, 100, 150, 200, 250, 300 and 1000 mV.s⁻¹. Scans initiated in the direction of the arrow. Measured in 100 mmol.dm⁻³ TBAPF₆/CH₃CN on a glassy carbon working electrode at 25 °C.

RESULTS AND DISCUSSION

Selected electrochemical data of all the $[\text{Fe}^{\text{III}}(\beta\text{-diketonato})_3]$ complexes in this study are summarized in Table 3.18 and the comparative cyclic voltammograms are shown in Figure 3.34. The complete cyclic voltammograms of the $[\text{Fe}^{\text{III}}(\beta\text{-diketonato})_3]$ complexes in this study, along with the tables with the complete electrochemical data, are given in Appendix A. Complexes {2} - {10} show electrochemistry similar to that of $[\text{Fe}(\text{acac})_3]$ {1}, producing electrochemically and chemically reversible behaviour, except for $[\text{Fe}(\text{tfaa})_3]$ {6}. The $[\text{Fe}(\text{tfaa})_3]$ {6} complex shows quasi-reversible electrochemical behaviour ($88 \text{ mV} < \Delta E_p < 147 \text{ mV}$). A quasi-reversible redox couple indicates that both the oxidation and reduction processes still take place, but there is a slow electron exchange between the electrode and the redox species in solution. $[\text{Fe}(\text{hfaa})_3]$ {10} is insoluble in CH_3CN . A sufficient amount was, however, dissolved in DCM to perform an electrochemical analysis. The results of {1} - {9} in $\text{TBAPF}_6/\text{CH}_3\text{CN}$ and {10} in $\text{TBAPF}_6/\text{DCM}$ are much better than in TBAP/DMF , reported by Endo *et. al.*⁴⁹ In our study, all the $[\text{Fe}^{\text{III}}(\beta\text{-diketonato})_3]$ complexes (except {6}) show reversible electrochemical behaviour ($62 \text{ mV} < \Delta E_p < 72 \text{ mV}$ at $100 \text{ mV}\cdot\text{s}^{-1}$). Endo *et. al.*⁴⁹ found that $[\text{Fe}(\text{dbm})_3]$ {5} showed electrochemically reversible behaviour ($\Delta E_p = 60 \text{ mV}$ at $500 \text{ mV}\cdot\text{s}^{-1}$), whereas those of the other $[\text{Fe}^{\text{III}}(\beta\text{-diketonato})_3]$ complexes in his study (Table 2.10, section 2.5.1, Chapter 2) showed electrochemically irreversible behaviour ($130 < \Delta E_p < 500 \text{ mV}$). The formal reduction potentials (E^0 , versus saturated Ag/AgCl), had the same sequence as in the table below.

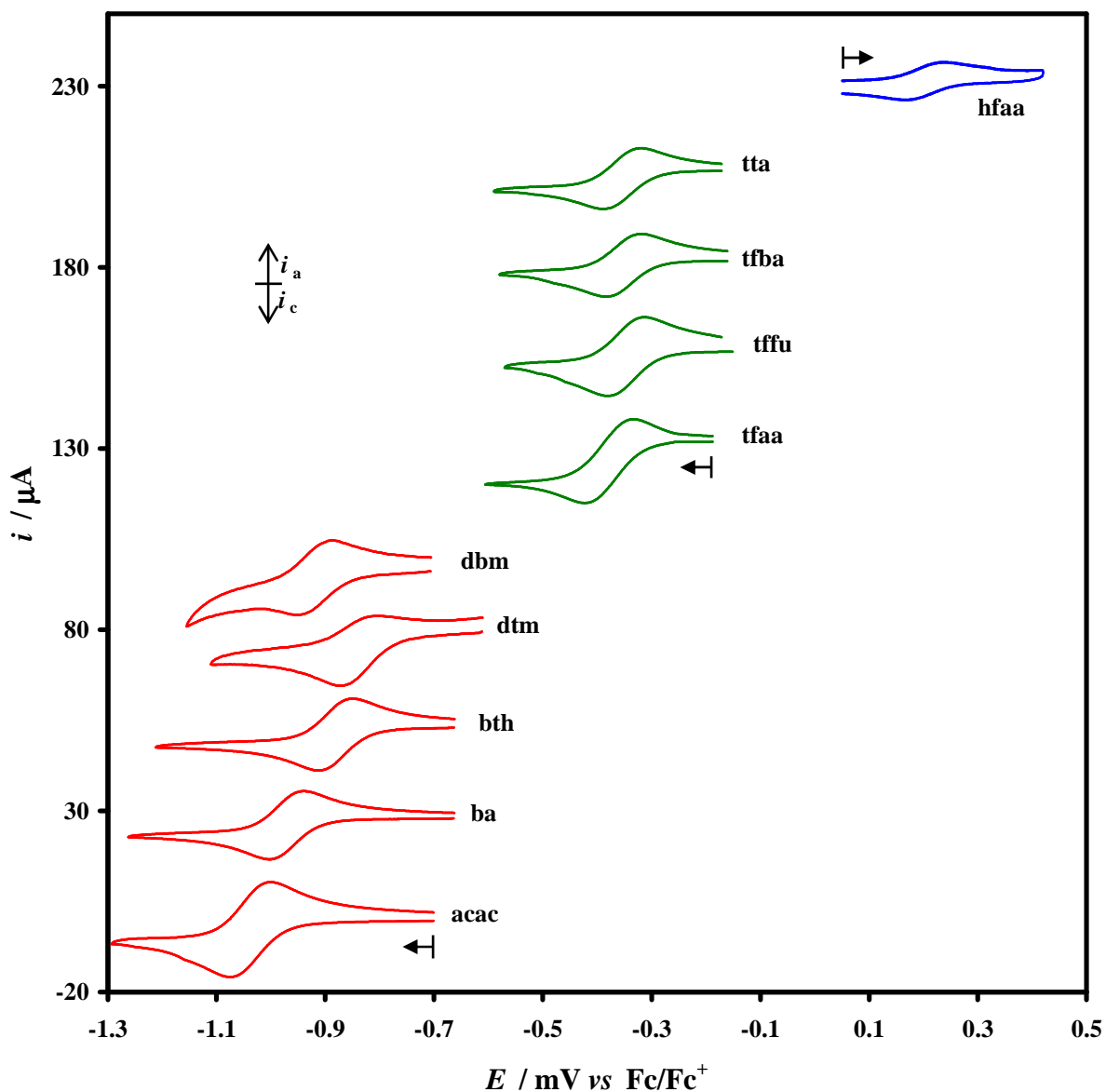


Figure 3.34: Comparative cyclic voltammograms (*versus* Fc/Fc^+) of $1 \text{ mmol}\cdot\text{dm}^{-3}$ of the indicated $[\text{Fe}^{\text{III}}(\beta\text{-diketonato})_3]$ complexes at a scan rate of $100 \text{ mV}\cdot\text{s}^{-1}$. Scans initiated in the direction of the arrow. The β -diketonato ligands in the red, green and blue groups contain respectively none, one and two CF_3 side groups.

RESULTS AND DISCUSSION

Table 3.18: Acid dissociation constant (pK_a), total group electronegativities on the Gordy scale ($\chi_{R1} + \chi_{R2}$) and selected electrochemical data of the $[\text{Fe}^{\text{III}}(\beta\text{-diketonato})_3]$ complexes.

		$\beta\text{-diketone (R}_1\text{COCH}_2\text{COR}_2)$				$[\text{Fe}^{\text{III}}(\beta\text{-diketonato})_3]$	
		R_1	R_2	pK_a	$\chi_{R1} + \chi_{R2}$	$\Delta E_p / \text{mV}$	$E^{0'} / \text{V}$
acac {1}	acetylacetone	CH ₃	CH ₃	8.95 ⁵⁷	4.68 ⁵⁸	72 ⁱ	-1.038 ⁱ
ba {2}	benzoylacetone	CH ₃	Ph	8.70 ⁵⁷	4.55 ^{58,60}	63 ⁱ	-0.971 ⁱ
bth {3}	benzoylthienoylacetylacetone	Ph	C ₄ H ₃ S	9.01 ⁵⁹	4.31 ^{60,59}	62 ⁱ	-0.881 ⁱ
dtm {4}	dithenoylmethane	C ₄ H ₃ S	C ₄ H ₃ S	8.89 ⁵⁹	4.20 ⁵⁹	70 ⁱ	-0.844 ⁱ
dbm {5}	dibenzoylmethane	Ph	Ph	9.35 ⁵⁷	4.42 ⁶⁰	68 ⁱ	-0.921 ⁱ
tfaa {6}	trifluoroacetylacetone	CF ₃	CH ₃	6.30 ⁵⁷	5.35 ^{60,58}	88 ⁱ	-0.377 ⁱ
tffu {7}	trifluorofuroylacetone	CF ₃	C ₄ H ₃ O	6.48 ⁱⁱⁱ	5.13 ⁱⁱⁱ	67 ⁱ	-0.347 ⁱ
tfba {8}	trifluorobenzoylacetone	CF ₃	Ph	6.30 ⁵⁷	5.22 ⁶⁰	64 ⁱ	-0.351 ⁱ
tta {9}	thienoyltrifluoroacetone	CF ₃	C ₄ H ₃ S	6.50 ⁵⁹	5.11 ^{60,59}	70 ⁱ	-0.355 ⁱ
hfaa {10}	hexafluoroacetylacetone	CF ₃	CF ₃	4.35 ⁶¹	6.02 ⁶⁰	70 ⁱⁱ	0.202 ⁱⁱ

ⁱ Solvent CH₃CN, supporting electrolyte TBAPF₆ ([NBu₄][PF₆]), versus Fc/Fc⁺, scan rate 100 mV.s⁻¹.

ⁱⁱ Solvent DCM, supporting electrolyte TBAPF₆ ([NBu₄][PF₆]), versus Fc/Fc⁺, scan rate 100 mV.s⁻¹.

ⁱⁱⁱ This study, calculated from the relationships in Figure 3.35.

According to Figure 3.34, the $[\text{Fe}^{\text{III}}(\beta\text{-diketonato})_3]$ complexes in this study can be divided into three distinctive groups. The red group: containing $[\text{Fe}^{\text{III}}(\beta\text{-diketonato})_3]$ complexes where the $\beta\text{-diketonato}$ ligand has no CF₃ side groups. The green group: containing $[\text{Fe}^{\text{III}}(\beta\text{-diketonato})_3]$ complexes where the $\beta\text{-diketonato}$ ligand has one CF₃ side group. The blue group: containing a $[\text{Fe}^{\text{III}}(\beta\text{-diketonato})_3]$ complex where the $\beta\text{-diketonato}$ ligand has two CF₃ side groups. The CF₃ group has a higher group electronegativity than the other groups (CF₃ = 3.01,⁶⁰ CH₃ = 2.34,⁵⁸ Ph = 2.21,⁶⁰ C₄H₃O = 2.12⁶² and C₄H₃S = 2.10⁵⁹). Therefore, an increase in the number of CF₃ groups results in an increase of the total group electronegativity ($\chi_{R1} + \chi_{R2}$) of the $\beta\text{-diketonato}$ ligands bonded to the iron centre. In general, as the total group electronegativity increases, the formal reduction potential ($E^{0'}$) also increases (Table 3.18). This is expected since the more electron-withdrawing the R group becomes, the more electron density is removed from the $\beta\text{-diketonato}$ backbone, making the iron centre relatively more positive and more difficult to reduce.

Parameters that are related to the electron density of the metal centre of $[\text{Fe}^{\text{III}}(\beta\text{-diketonato})_3]$, such as the acid dissociation constant (pK_a) of the uncoordinated $\beta\text{-diketone}$, the total group

⁵⁷ J. Starý, *The Solvent Extraction of Metal Chelates*, MacMillan Company, New York, **1964**, Appendix.

⁵⁸ R.E. Kagarise, *J. Am. Chem. Soc.* **1955** (77) 1377-1379.

⁵⁹ M.M. Conradie, A.J. Muller, J. Conradie, *S. Afr. J. Chem.* **2008** (61) 13-21.

⁶⁰ W.C. du Plessis, T.G. Vosloo, J.C. Swarts, *J. Chem. Soc. Dalton Trans.* **1998** 2507-2514.

⁶¹ M. Ellinger, H. Duschner, K. Starke, *J. Inorg. Nucl. Chem.* **1978** (40) 1063-1067.

⁶² This study, calculated from the relationships in Figure 3.35.

electronegativities ($\chi_{R1} + \chi_{R2}$) of the R_1 and R_2 side groups on the β -diketonato ligand and the formal reduction potentials (E^0) of the redox active metal Fe(III)/Fe(II) in $[\text{Fe}^{\text{III}}(\beta\text{-diketonato})_3]$, are also included in Table 3.18. The relationships of the formal reduction potential (E^0) with $\text{p}K_a$ and $\chi_{R1} + \chi_{R2}$ are shown graphically in Figure 3.35.

The correlation of the formal reduction potentials shows the following trends:

E^0 versus $\text{p}K_a$: Shows that the E^0 increases linearly with a decreasing $\text{p}K_a$. The iron centre is relatively more electron-deficient (with smaller $\text{p}K_a$) and consequently more energy is needed to reduce $[\text{Fe}^{\text{III}}(\beta\text{-diketonato})_3]$.

E^0 versus $\chi_{R1} + \chi_{R2}$: Three separate trends were found for the red, green and blue groups, where the β -diketonato ligands contain respectively none, one and two CF_3 side groups. In general, the E^0 increases for the three groups as the number of CF_3 groups increase. The trend within a group, however, shows an opposite behaviour. The E^0 decreases slightly linearly with the increase in total group electronegativities.

The linear equations ($y = mx + c$) in Figure 3.35, defining the relationships between E^0 and the parameters above are:

$$\text{p}K_a = (-4.164) E^0 + 5.033$$

$$\chi_{R1} + \chi_{R2} = (-2.483) E^0 + 2.120 \quad (\text{red group, } R_1 \text{ and } R_2 \neq \text{CF}_3)$$

$$\chi_{R1} + \chi_{R2} = (-6.990) E^0 + 2.703 \quad (\text{green group, } R_1 \text{ or } R_2 = \text{CF}_3)$$

$$\chi_{R1} + \chi_{R2} = 6.020 \quad (\text{blue group, } R_1 = R_2 = \text{CF}_3)$$

This allows one to determine the acid dissociation constant ($\text{p}K_a$) of the uncoordinated β -diketone and the total group electronegativities ($\chi_{R1} + \chi_{R2}$) of the R_1 and R_2 side groups, when the formal reduction potential (E^0) is known. These newly found relationships were used on $[\text{Fe}(\text{tffu})_3]$ {7}, where neither the acid dissociation constant of Htffu nor the group electronegativity of furyl ($\text{C}_4\text{H}_3\text{O}$) was known. Using the experimental value of -0.347 V for the E^0 of $[\text{Fe}(\text{tffu})_3]$ {7}, the $\text{p}K_a$ of Htffu was calculated as 6.48 and the $\chi_{\text{C}_4\text{H}_3\text{O}}$ of furyl was calculated as 2.12.

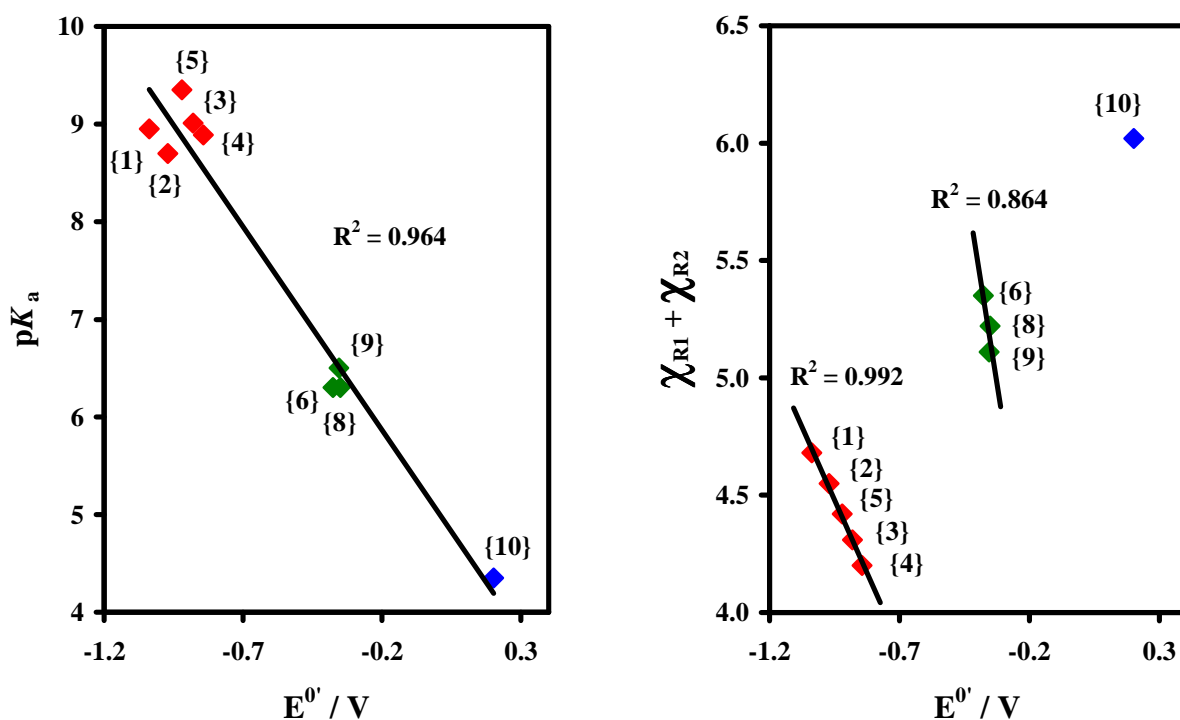


Figure 3.35: The correlation of the formal reduction potentials (E^0') of $[\text{Fe}^{\text{III}}(\beta\text{-diketonato})_3]$ complexes with the acid dissociation constants (pK_a) of the uncoordinated β -diketones ($\text{R}_1\text{COCH}_2\text{COR}_2$) and the total group electronegativities ($\chi_{R1} + \chi_{R2}$) of the R_1 and R_2 side groups. The β -diketonato ligands in the red, green and blue groups contain respectively none, one and two CF_3 side groups.

From the DFT computational study (section 3.2.1.4), it is clear that both the facial (*fac*) and meridional (*mer*) isomers exist in appreciable quantities for the $[\text{Fe}^{\text{III}}(\beta\text{-diketonato})_3]$ complexes with unsymmetrical β -diketonato ligands. However, it was impossible to distinguish between the two stereo isomers electrochemically. This entirely expected result indicates that molecular geometry does not significantly influence the potential required to oxidise the iron centre, but bond delocalisation does transmit electron donating or electron withdrawing effects of molecular fragments to and from the iron centre.

3.2.1.3 Spectroelectrochemistry (SEC).

To further investigate the electrochemical properties of the $[\text{Fe}^{\text{III}}(\beta\text{-diketonato})_3]$ complexes (β -diketonato = acac {1}, ba {2}, bth {3}, dtm {4}, dbm {5}, tfaa {6}, tfu {7}, tfba {8} and tta {9}), a spectroelectrochemical study was conducted. Spectroelectrochemistry (SEC) combines the two quite different techniques, electrochemistry and spectroscopy, to study the influence of the redox chemistry of the $[\text{Fe}^{\text{III}}(\beta\text{-diketonato})_3]$ complexes on their UV/vis absorption spectra.

The oxidation state is changed electrochemically (in an OTTLE cell) by the addition of an electron. The product of the redox transformation is then simultaneously monitored *in situ* by UV/vis spectroscopy (200-600 nm). The details of the methods used are given in section 4.2.5 (Chapter 4).

From the cyclic voltammetry study (section 3.2.1.2), we already know that $[\text{Fe}^{\text{III}}(\beta\text{-diketonato})_3]$ complexes undergo a single one-electron iron-related reduction reaction. This reaction is electrochemically and chemically reversible. The voltammograms are given in Figure 3.34 and Appendix A and the electrochemical data are summarized in Table 3.18.

Iron(III) complexes have strong absorption bands in the near ultraviolet region. Iron(III) porphyrins have a typical Soret⁶³ band at ~400nm,^{64,65,66,67} whereas tris(β -diketonato) iron(III) complexes have a strong absorption band at ~300nm.⁶⁸ The intensity of the bands change as the iron(III) complexes are reduced or oxidized.^{64,65,66,67} The spectral changes obtained during the Fe(III)/Fe(II) reduction of complexes {1} - {9} are presented graphically in Figure 3.36. The study was conducted in CH_3CN and since $[\text{Fe}(\text{hfaa})_3]$ {10} is insoluble in CH_3CN , it is excluded from this study.

⁶³ J.L. Soret, *Comptes Rendus* **1883** (97) 1269-1273.

⁶⁴ K.M. Kadish, E. van Caemelbecke, E. Gueletti, S. Fukuzumi, K. Miyamoto, T. Suenobu, A. Tabard, R. Guilard, *Inorg. Chem.* **1998** (37) 1759-1766.

⁶⁵ P.W Crawford, M.D. Ryan, *Inorg. Chem.* **1991** (179) 25-33.

⁶⁶ K.M. Kadish, E. van Caemelbecke, F. D'Souza, C.J. Medforth, K.M. Smith, A. Tabard, R. Guilard, *Inorg. Chem.* **1995** (34) 2984-2989.

⁶⁷ D. Lancon, P. Cocolios, R. Guilard, K.M. Kadish, *Inorg. Chem.* 1984 (106) 4472-4478.

⁶⁸ G. Gumbel, H. Elias, *Inorg. Chim. Acta* **2003** (342) 97-106.

RESULTS AND DISCUSSION

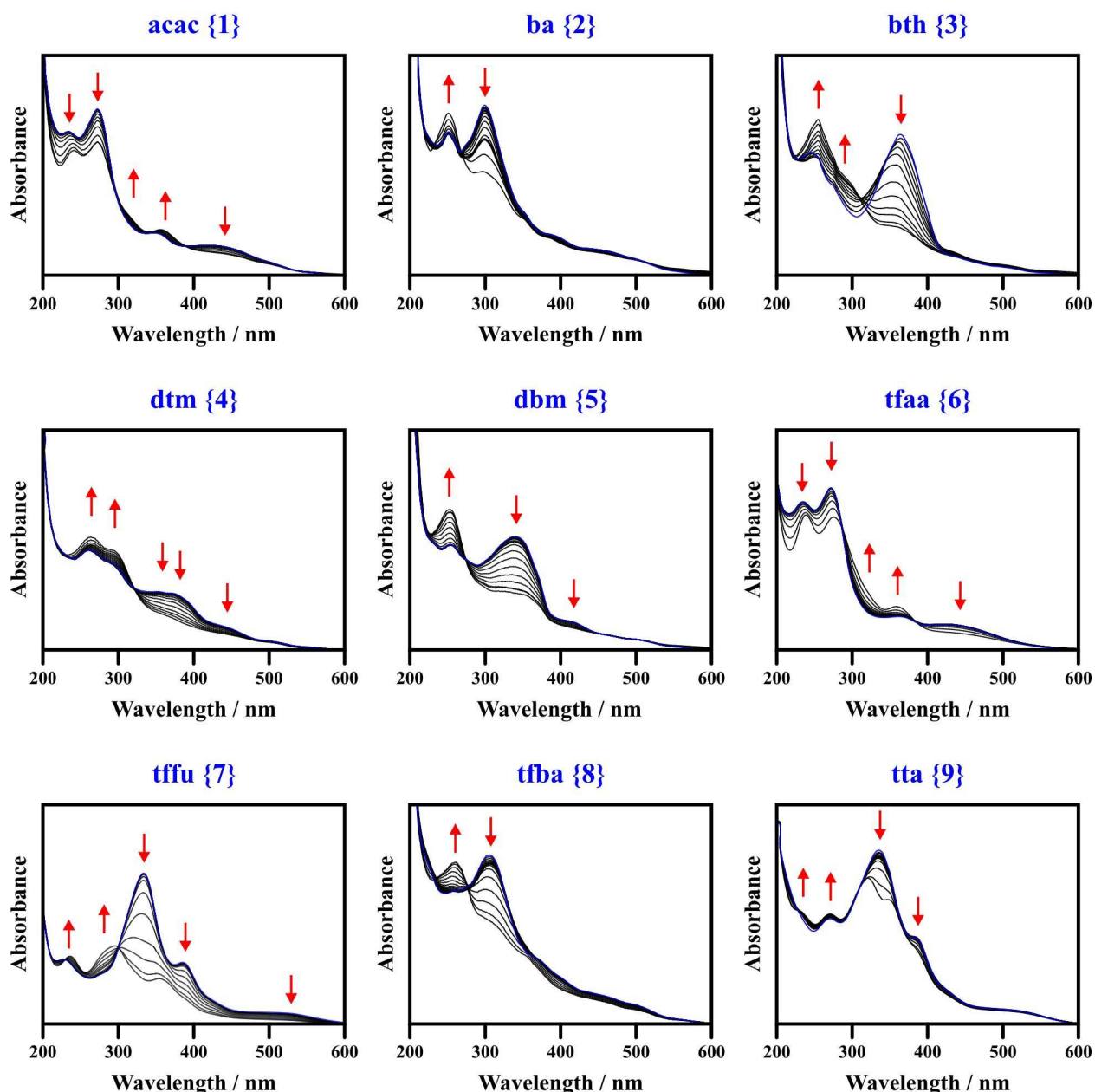


Figure 3.36: UV/vis thin-layer spectral changes during the one-electron Fe(III)/Fe(II) reduction of $[\text{Fe}^{\text{III}}(\beta\text{-diketonato})_3]$ complexes {1} - {9}, measured in $\text{TBAPF}_6/\text{CH}_3\text{CN}$ in an OTTLE cell at 25 °C. First scans are marked blue and the peak increase/decrease is as indicated by the arrows.

Similar spectra for $[\text{Fe}(\text{acac})_3]$ {1} and $[\text{Fe}(\text{tfaa})_3]$ {6} were observed. The β -diketonato ligands acac and tfaa have respectively CH_3/CH_3 and CH_3/CF_3 side groups. Changing the one side group from CH_3 to CF_3 had very little effect on the spectral absorption of these two complexes. This is also the case with $[\text{Fe}(\text{ba})_3]$ {2} and $[\text{Fe}(\text{tfba})_3]$ {8}, which also have very similar spectra. The β -diketonato ligands ba and tfba have respectively Ph/CH_3 and Ph/CF_3 side groups. Introduction of one Ph or two Ph side groups successively causes a red shift of ~ 30 nm:

$[\text{Fe}(\text{acac})_3] \{1\}$ (270 nm) \rightarrow $[\text{Fe}(\text{ba})_3] \{2\}$ (298 nm) \rightarrow $[\text{Fe}(\text{dbm})_3] \{5\}$ (336 nm)

$[\text{Fe}(\text{tfaa})_3] \{6\}$ (271 nm) \rightarrow $[\text{Fe}(\text{tfba})_3] \{8\}$ (304 nm) \rightarrow $[\text{Fe}(\text{dbm})_3] \{5\}$ (336 nm)

The spectral changes during the reduction of $[\text{Fe}(\text{acac})_3] \{1\}$ and $[\text{Fe}(\text{tfaa})_3] \{6\}$, as well as of $[\text{Fe}(\text{ba})_3] \{2\}$ and $[\text{Fe}(\text{tfba})_3] \{8\}$, were very similar. Changing the one side group from CH_3 to CF_3 not only had very little effect on the spectral absorption of the $[\text{Fe}^{\text{III}}(\beta\text{-diketonato})_3]$ complexes, but also on the $[\text{Fe}^{\text{II}}(\beta\text{-diketonato})_3]^-$ complexes.

The other complexes, all containing one or two aromatic side groups, had unique spectra and spectral changes and no further trends were observed. Each complex is discussed in detail in the following paragraphs.

$[\text{Fe}(\text{acac})_3] \{1\}$: This complex has a strong band at 270 nm, two smaller bands at 235 and 355 nm and a shoulder at 440 nm. Upon reduction of the complex, the 235, 270 and 440 nm bands decrease in intensity and the 355 nm band increases. The 235 and 335 nm bands also have a red shift of 5 and 25 nm respectively. Additionally, a new shoulder appears at 320 nm. Two isobestic points are visible at 295 and 390 nm. These spectral changes are similar to that of $[\text{Fe}(\text{tfaa})_3] \{6\}$.

$[\text{Fe}(\text{ba})_3] \{2\}$: This complex has a strong band at 298 nm and a smaller band at 250 nm. Upon reduction of the complex, the 298 and 250 nm bands respectively decrease and increase in intensity. One isobestic point is visible at 265 nm. These spectral changes are similar to that of $[\text{Fe}(\text{tfba})_3] \{8\}$.

$[\text{Fe}(\text{bth})_3] \{3\}$: This complex has a strong band at 361 nm, a smaller band at 245 nm and a shoulder at 275 nm. Upon reduction of the complex, the 361 nm band decreases in intensity. The 245 nm band initially slightly decreases with a red shift of 10 nm and then strongly increases at 255 nm. The shoulder at 275 nm increases with a red shift of 25 nm. One isobestic point is visible at ~300 nm.

$[\text{Fe}(\text{dtm})_3] \{4\}$: This complex has a band at 260 nm and four shoulders at 295, 350, 375 and 445 nm. Upon reduction of the complex, the 350, 375 and 445 nm shoulders decrease in intensity and the 260 nm band with the 295 nm shoulder increases in intensity. One isobestic point is visible at 320 nm.

RESULTS AND DISCUSSION

[Fe(dbm)₃] {5}: This complex has a strong band at 336 nm, a smaller band at 251 nm and a shoulder at 415 nm. Upon reduction of the complex, the 336 nm band decreases in intensity and the shoulder at 415 nm disappears completely. The 251 nm band increases in intensity with a slight blue shift of 3 nm. One isobestic point is visible at 270 nm.

[Fe(tfaa)₃] {6}: This complex has a strong band at 271 nm, two smaller bands at 235 and 360 nm and a shoulder at 450 nm. Upon reduction of the complex, the 235, 271 and 450 nm bands decrease in intensity and the 360 nm band increases. The 235 and 271 nm bands also both have a red shift of 4 nm. Additionally, a new shoulder appears at 315 nm. Two isobestic points are visible at 290 and 390 nm. These spectral changes are similar to that of Fe(acac)₃ {1}.

[Fe(tffu)₃] {7}: This complex has a strong band at 333 nm, two smaller bands at 230 and 385 nm and a shoulder at ~520 nm. Upon reduction of the complex, the 333, 385 and ~520 nm bands disappear completely. A new strong band at 295 nm and a shoulder at 350 nm appear. The 230 nm band increases with a red shift of 5 nm. Two isobestic points are visible at 230 and 300 nm.

[Fe(tfba)₃] {8}: This complex has a strong band at 304 nm and a shoulder at 259 nm. Upon reduction of the complex, the 304 and 259 nm bands respectively decrease and increase in intensity. Two isobestic points are visible at 230 and 275 nm. These spectral changes are similar to that of Fe(ba)₃ {2}.

[Fe(tta)₃] {9}: This complex has a strong band at 333 nm, a smaller band at 270 nm and a shoulder at 385 nm. Upon reduction of the complex, the 333 nm band decreases in intensity to form a band at 320 nm with a shoulder at 350 nm. The shoulder at 385 nm also decreases in intensity. The band at 270 nm slightly increases in intensity and a new shoulder at 230 nm appears. Two isobestic points are visible at 225 and 300 nm.

3.2.1.4 DFT computational study.

In this DFT computational study, we investigate the electrochemical behaviour of the redox reaction: $[\text{Fe}^{\text{III}}(\beta\text{-diketonato})_3] + e^- \rightleftharpoons [\text{Fe}^{\text{II}}(\beta\text{-diketonato})_3]^-$ (β -diketonato = acac {1}, ba {2}, bth {3}, dtm {4}, dbm {5}, tfaa {6}, tffu {7}, tfba {8}, tta {9} and hfaa {10}, Table 3.18). Tris(β -diketonato) iron(III) complexes are stable molecules with the metal in a high spin state

($S = 5/2$).^{69,70} In the reduced form, $[\text{Fe}^{\text{II}}(\beta\text{-diketonato})_3]^-$, it is also high-spin ($S = 2$). These complexes can have either a D_3 (complexes with symmetrical β -diketone ligand), C_3 (complexes with unsymmetrical β -diketone ligand, arranged in such a way that they have a 3-fold rotational axis) or C_1 (complexes with unsymmetrical β -diketone ligand, arranged in such a way that they have no symmetry operation) symmetry. The details of the computational methods used are given in section 4.5.3.1 (Chapter 4).

To validate the DFT computational method, the $S = 1/2$, $3/2$ and $5/2$ states of $[\text{Fe}(\text{acac})_3]$ were optimized with a variety of functionals (PW91, OLYP, B3LYP and B3LYP*), to see which functional can correctly predict the $S = 5/2$ state. The relative energies are given in Table 3.19. To further validate the DFT computational method, the bond lengths and bond angles of $[\text{Fe}(\text{acac})_3]$ ($S = 5/2$) were compared to known experimental^{70,71} and calculated⁷⁰ data (Table 3.20). OLYP, B3LYP and B3LYP* successfully predict a sextet ground state with the other states approximately $90 \text{ kJ}\cdot\text{mol}^{-1}$ higher in energy (Table 3.19). PW91, however, incorrectly predicts a doublet state with the sextet state $30 \text{ kJ}\cdot\text{mol}^{-1}$ higher in energy. The functional OLYP was therefore used in further calculations. The OLYP optimization of $[\text{Fe}(\text{acac})_3]$ ($S = 5/2$) with D_3 , C_2 and C_1 symmetry constraint gave virtually the same energies. The OLYP geometries are in close agreement with known experimental and calculated data (Table 3.20). The calculated bond lengths are slightly longer than those obtained from X-ray crystallography, but it is well-known that GGA density functionals overestimate bonds lengths.²⁵

Table 3.19: Relative energies ($\text{kJ}\cdot\text{mol}^{-1}$) of the different spin states (default occupations) of $[\text{Fe}(\text{acac})_3]$, optimized under a D_3 symmetry constraint with a selection of functionals.

Spin	PW91	OLYP	B3LYP	B3LYP*
1/2	-30	61	132	89
3/2	30	76	135	109
5/2	0	0	0	0

⁶⁹ F.A. Cotton, G. Wilkinson, *Advanced inorganic chemistry*, Second edition, John Wiley & Sons, New York, **1966**, p875.

⁷⁰ I. Diaz-Acosta, J. Baker, W. Cordes, P. Pulay, *J. Phys. Chem. A* **2001** (105) 238-244.

⁷¹ J. Iball, C.H. Morgan, *Acta Cryst.* **1967** (23) 239-244.

RESULTS AND DISCUSSION

Table 3.20: Selected experimental and calculated geometrical parameters of [Fe(acac)₃] (*S* = 5/2), optimized under a *D*₃ symmetry.

Properties	OLYP	B3LYP ^{70 i}	Crystal ⁷⁰	Crystal ⁷¹
Fe-O(Å)	2.064	2.011	1.992(21)	1.992(6)
O-C (Å)	1.276	1.275	1.262(4)	1.258(12)
C-C (Å)	1.408	1.405	1.382(5)	1.377(19)
C-CH ₃ (Å)	1.517	1.512	1.504(5)	1.530(21)
O-Fe-O (°)	85.9	87.1	87.43(9)	87.1(3)
Fe-O-C (°)	129.8	129.8	129.12(20)	129.3(6)
O-C-C (°)	125.1	124.9	124.5(3)	125.0(15)
C-C-C (°)	124.3	123.5	124.8(3)	124.8(8)

i PQS parallel *ab initio* programme, B3LYP functional, 6-31G* basis set and *D*₃ symmetry.

The coordination of the metal in tris(β-diketonato) iron(III) complexes with a symmetrical β-diketone ligand ({1}, {4}, {5} and {10}) is approximately of octahedral *D*₃ symmetry. Figure 3.37 shows a qualitative diagram of the *d*-orbital energies of the metal ion and the effect on the relative energies upon distortion of the ligand field (section 2.2.3, Chapter 2). The symmetry-breaking distortion is zero at the middle, corresponding to octahedral symmetry. Distortion towards *D*₃ ligand symmetry splits the degenerate *t*_{2g}-orbitals into *a* and *e* components. Qualitatively, a positive *D*₃ distortion corresponds to the flattening of the octahedron and a negative distortion corresponds to an increase of its height. Depending on the sign of the *D*₃ distortion, either the *a* or the *e* component is lower in energy. Complexes {1}, {4}, {5} and {10} all show negative distortion as depicted in Figure 3.37 9 (left), with the lowest *d*-orbital having *a* symmetry. Therefore, when [Fe(β-diketonato)₃] with *D*₃ symmetry is reduced to become [Fe(β-diketonato)₃][−], the lower *a* component of the *d*-orbital will gain an electron. Gaining only one electron is not allowed for the *e* component, since the *e* component has to be doubly occupied.

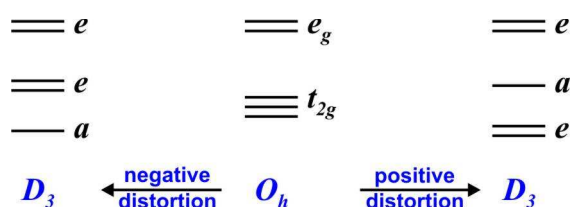


Figure 3.37: Alteration of octahedral orbital energies (*O_h*) under *D*₃ distortion.

For tris(β-diketonato) iron(III) complexes with a unsymmetrical β-diketone ligand ({2}, {3}, {6}, {7}, {8} and {9}), two stereo isomers are possible: a facial isomer (*fac*), where the three ligands are symmetrically arranged, and a meridional isomer (*mer*) (Figure 3.38). The ratios of the

isomers were calculated with the Boltzmann equation (Equation 2.1, Chapter 2) and are tabulated in Table 3.21. The population of the *fac* and *mer* isomers were used in calculating the effective ionization potential (IP) of the complex.

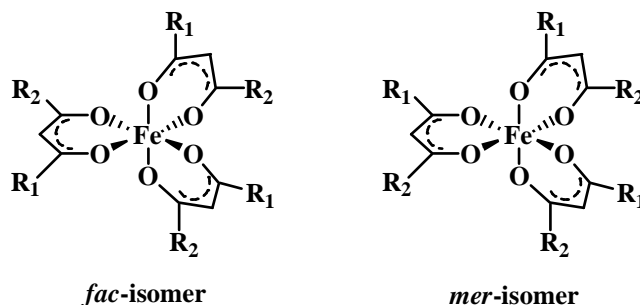


Figure 3.38: The facial (*fac*) and meridional (*mer*) isomers of $[\text{Fe}(\beta\text{-diketonato})_3]$ complexes with unsymmetrical β -diketonato ligands.

Table 3.21: The calculated *fac* and *mer* isomer distribution of $[\text{Fe}(\beta\text{-diketonato})_3]$ and $[\text{Fe}(\beta\text{-diketonato})_3]^-$. The ionization potential of the redox reaction is also given.

	$[\text{Fe}(\beta\text{-diketonato})_3]$				$[\text{Fe}(\beta\text{-diketonato})_3]^-$				Ionization potential / $\text{kJ}\cdot\text{mol}^{-1}$
	% <i>fac</i>	$E_{\text{fac}} / \text{kJ}\cdot\text{mol}^{-1}$	% <i>mer</i>	$E_{\text{mer}} / \text{kJ}\cdot\text{mol}^{-1}$	% <i>fac</i>	$E_{\text{fac}} / \text{kJ}\cdot\text{mol}^{-1}$	% <i>mer</i>	$E_{\text{mer}} / \text{kJ}\cdot\text{mol}^{-1}$	
acac {1}	100.0	-24433	-	-	100.0	-24593	-	-	160
ba {2}	45.8	-38849	54.2	-38849	44.3	-39037	55.7	-39037	188
bth {3}	88.6	-47158	11.4	-47153	73.3	-47367	26.7	-47365	209
dtm {4}	100.0	-41049	-	-	100.0	-41259	-	-	210
dbm {5}	100.0	-53259	-	-	100.0	-53475	-	-	216
tfaa {6}	65.4	-24637	34.6	-24636	65.9	-24896	34.1	-24894	259
tffu {7}	64.5	-33680	35.5	-33679	42.3	-33943	57.7	-33944	264
tfba {8}	45.8	-39059	54.2	-39059	70.5	-39330	29.5	-39328	270
tta {9}	32.5	-32949	67.5	-32951	42.6	-33223	57.4	-33224	273
hfaa {10}	100.0	-24806	-	-	100.0	-25165	-	-	360

The ionization potential (IP) of the $[\text{Fe}^{\text{III}}(\beta\text{-diketonato})_3]$ complexes, calculated according to



as the amount of energy required to add an electron to $[\text{Fe}^{\text{III}}(\beta\text{-diketonato})_3]$ to form $[\text{Fe}^{\text{II}}(\beta\text{-diketonato})_3]^-$, is also tabulated in Table 3.21. The forward reaction is the reduction reaction and the backward reaction is the oxidation reaction. The formal reduction potentials (E^0) of the redox active metal Fe(III)/Fe(II) in $[\text{Fe}^{\text{III}}(\beta\text{-diketonato})_3]$, are included in Table 3.18 (section 3.2.1.2). The relationship between the calculated ionization potential (IP) and E^0 is shown graphically in Figure 3.39.

The correlation of the calculated ionization potentials shows that IP increases with increasing (less negative) formal reduction potential. A larger E^0 implies that more energy is needed to reduce $[\text{Fe}^{\text{III}}(\beta\text{-diketonato})_3]$. In other words, more energy is needed to add an electron to

$[\text{Fe}^{\text{III}}(\beta\text{-diketonato})_3]$ and thus a larger IP. The linear equation ($y = mx + c$) defining this relationship is: $E^0 = (6.933 \times 10^{-3}) \text{IP} + 2.258$. This allows one to determine the formal reduction potentials (E^0) of $[\text{Fe}^{\text{III}}(\beta\text{-diketonato})_3]$ complexes when the calculated IP is known.

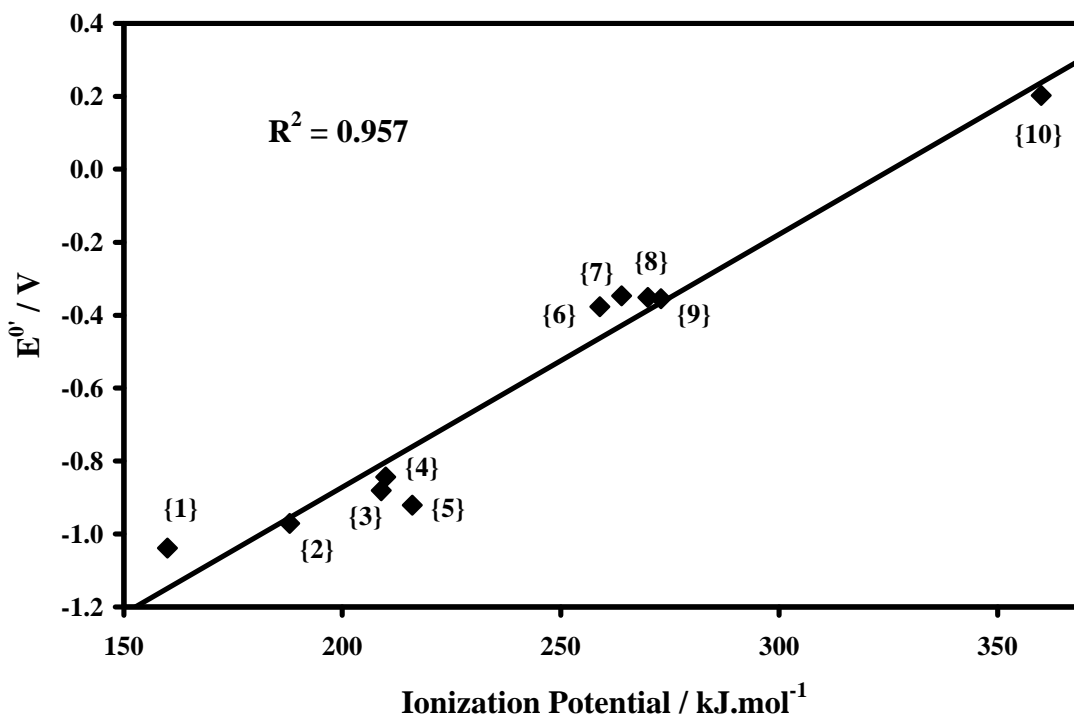


Figure 3.39: A plot of the ionization potentials *versus* the formal reduction potentials (E^0) of the redox reaction $[\text{Fe}^{\text{III}}(\beta\text{-diketonato})_3] + e^- \rightleftharpoons [\text{Fe}^{\text{II}}(\beta\text{-diketonato})_3]^- + \text{IP}$ for the $[\text{Fe}^{\text{III}}(\beta\text{-diketonato})_3]$ {1} - {10}.

3.2.2 $[\text{Fe}(\text{salen})(\text{CH}_3)_2(\text{COCH}_3)_2(\text{py})_2]$.

3.2.2.1 Introduction.

For researchers involved in DFT calculations on open-shell transition metal complexes, including many important bioinorganic systems, a lasting question stays the choice of the exchange-correlation functional.^{72,73,74} Unfortunately, there have been only a few comparative studies of different functionals in relation to the energetics of low-lying spin states of transition

⁷² A. Ghosh, P.R. Taylor, *Curr. Opin. Chem. Biol.* **2003** (91) 113-124.

⁷³ J.N. Harvey, *Struct. Bonding* **2004** (112) 151-183.

⁷⁴ A. Ghosh, *J. Biol. Inorg. Chem.* **2006** (11) 712-724.

metal complexes.^{75,76,77} Nevertheless, the limited amount of data suggests that, whereas the “classic” pure functionals such as BLYP,^{78,79} PW91,⁸⁰ and BP86^{79,81} favour somewhat unduly spincoupled, covalent descriptions, hybrid functionals such as B3LYP⁸² err in the other direction. To correct for the latter tendency, the amount of Hartree-Fock exchange in B3LYP has been reduced from the standard 20% to 15%. The resulting B3LYP*⁸³ functional has been found to yield improved results in certain cases. These stereotypes of the different functionals were further confirmed in a recent study of first-row transition metal β -diketiminato (nacnac) imido complexes, where the classic pure functionals led to unduly low-multiplicity spin states, whereas the hybrid functionals B3LYP and O3LYP⁸⁴ resulted in unduly high-multiplicity ground states.⁸⁵

-
- 75** Selected studies comparing the performance of different functionals *vis-à-vis* transition metal spin state energetics: (a) M. Swart, A.R. Groenhof, A.W. Ehlers, K. Lammertsma, *J. Phys. Chem. A* **2004** (108) 5479-5483. (b) R.J. Deeth, N. Fey, *J. Comp. Chem.* **2004** (25) 1840-1848. (c) A.R. Groenhof, M. Swart, A.W. Ehlers, K. Lammertsma, *J. Phys. Chem. A* **2005** (109) 3411-3417. (d) L.M.L. Daku, A. Vargas, A. Hauser, A. Fouqueau, M.E. Casida, *ChemPhysChem* **2005** (6) 1393-1410. (e) G. Ganzenmuller, N. Berkaine, A. Fouqueau, M.E. Casida, M. Reiher, *J. Chem. Phys.* **2005** (122) 234321-234332. (f) F. De Angelis, N. Jin, R. Car, J.T. Groves, *Inorg. Chem.* **2006** (45) 4268-4276. (g) A. Vargas, M. Zerara, E. Krausz, A. Hauser, L.M.L. Daku, *J. Chem. Theory Comput.* **2006** (2) 1342-1359. (h) C.Y. Rong, S.X. Lian, D.L. Yin, B. Shen, A.G. Zhong, L. Bartolotti, S.B. Liu, *J. Chem. Phys.* **2006** (125) 174102-174108. (i) N. Strickland, J.N. Harvey, *J. Phys. Chem. B* **2007** (111) 841-852.
- 76** J. Conradie, A. Ghosh, *J. Phys. Chem. B* **2007** (111) 12621-12624.
- 77** M. Swart, A.W. Ehlers, K. Lammertsma, *Mol. Phys.* **2004** (102) 2467-2474.
- 78** (a) C. Lee, W. Yang, R.G. Parr, *Phys. Rev. B* **1988** (37) 785-789. (b) B.G. Johnson, P.M.W. Gill, J.A. Pople, *J. Chem. Phys.* **1993** (98) 5612-5626. (c) T.V. Russo, R.L. Martin, P.J. Hay, *J. Chem. Phys.* **1994** (101) 7729-7737.
- 79** A.D. Becke, *Phys. Rev.* **1988** (A38) 3098-3100.
- 80** J.P. Perdew, J.A. Chevary, S.H. Vosko, K.A. Jackson, M.R. Pederson, D.J. Singh, C. Fiolhais, *Phys. Rev. B* **1992** (46) 6671-6687. Erratum: J.P. Perdew, J.A. Chevary, S.H. Vosko, K.A. Jackson, M.R. Pederson, D.J. Singh, C. Fiolhais, *Phys. Rev. B* **1993** (48) 4978.
- 81** J.P. Perdew, *Phys. Rev.* **1986** (B33) 8822-8824; Erratum: J.P. Perdew, *Phys. Rev.* **1986** (B34) 7406.
- 82** P.J. Stephens, F.J. Devlin, C.F. Chabalowski, M.J. Frisch, *J. Phys. Chem.* **1994** (98) 11623-11627.
- 83** M. Reiher, O. Salomon, B.A. Hess, *Theor. Chem. Acc.* **2001** (107) 48-55.
- 84** A.J. Cohen, N.C. Handy, *Mol. Phys.* **2001** (99) 607-615.
- 85** J. Conradie, A. Ghosh, *J. Chem. Theory Comput.* **2007** (3) 689-702.

RESULTS AND DISCUSSION

Interestingly, the OLYP^{78,86} and OPBE^{77,86} pure functionals, based on the new OPTX⁸⁶ exchange functional, yielded the correct ground states for all of the complexes examined, notably $S = 0$ for $\text{Co}^{\text{III}}(\text{nacnac})(\text{NR})$ and $S = 3/2$ for $\text{Fe}^{\text{III}}(\text{nacnac})(\text{NR})$. This finding led us to speculate, though on the basis of a limited amount of data, that exchange-correlation functionals based on the OPTX-based exchange functional may be among the best from the point of view of transition metal spin state energetics.⁸⁵ To further test this proposal, DFT calculations were carried out with different functionals on the spin crossover complex $[\text{Fe}(\text{salen})(\text{CH}_3)_2(\text{COCH}_3)_2(\text{py})_2]$. The question to be addressed in this study is: which functional best reproduces accurate geometry and equi-energetic $S = 0$ (high spin, HS) and 2 (low spin, LS) states of this complex?

All DFT calculations in this study have been performed on two different conformations of $[\text{Fe}(\text{salen})(\text{CH}_3)_2(\text{COCH}_3)_2(\text{py})_2]$ with the pyridine groups oriented either vertically or dihedrally relative to the symmetry plane through the salen ligand, as illustrated in Figure 3.40. Both conformations gave very similar results throughout the study. Since the conformation with the vertical pyridines is energetically preferred, only results of this conformation will be given. For the details of the computational methods used, see section 4.5.3.2 (Chapter 4).

⁸⁶ N.C. Handy, A.J. Cohen, *Mol. Phys.* **2001** (99) 403-412.

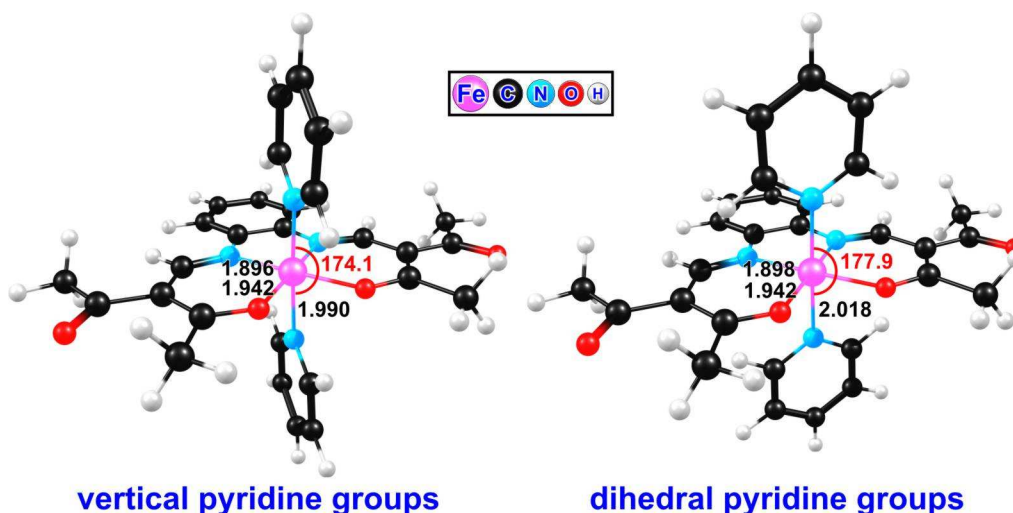


Figure 3.40: PW91 optimized geometries (C_{2v} symmetry constraint) of two different conformations of $[\text{Fe}(\text{salen})(\text{CH}_3)_2(\text{COCH}_3)_2(\text{py})_2]$ - pyridine groups oriented vertically or dihedrally. The conformation with the vertical pyridines is energetically preferred. The distances (Å, black), the angles ($^\circ$, red) and the colour code of the atoms are as indicated.

3.2.2.2 Geometry profile of default occupations.

The $S = 0, 1$ and 2 states of $[\text{Fe}(\text{salen})(\text{CH}_3)_2(\text{COCH}_3)_2(\text{py})_2]$, with default occupation, were optimized with a selection of functionals (PW91, BP86, BLYP, PBE, OLYP, OPBE and B3LYP). The bond lengths and bond angles around the Fe(II) centre, a key indicator of the structure in organometallic complexes, are tabulated in Table 3.22. Focussing on the Fe- N_{py} bond length, one would expect a longer bond length for high spin complexes compared to low spin complexes.⁸⁷ The Fe- N_{py} bond lengths of all the singlet states are more or less the same for all the studied functionals, varying between 1.970 and 2.043 Å. Though, the Fe- N_{py} bond lengths of the quintet state vary between 2.265 and 2.498 Å. According to the high spin octahedral crystal structure of $[\text{Fe}(\text{py})_6]^{2+}$,⁸⁸ Fe- N_{py} bond lengths should be in the range of 2.22-2.29 Å. Therefore, only the PW91 functional (2.298 Å for TZP basis set and 2.265 Å for 6-311G** basis set) is able to produce a good geometry of the high spin $[\text{Fe}(\text{salen})(\text{CH}_3)_2(\text{COCH}_3)_2(\text{py})_2]$ complex. BP86, PBE⁸⁹ and B3LYP slightly overestimated the Fe- N_{py} bond length with very similar geometries (2.307, 2.308 and 2.312 respectively). OLYP, which is known to be one of

⁸⁷ M.B. Darkhovskii, I.V. Pletnev, A.L. Tchougréeff, *J. Comp. Chem.* **2003** (24) 1703-1719.

⁸⁸ R.J. Doedens, L.F. Dahl, *J. Am. Chem. Soc.* **1966** (88) 4847-4855.

⁸⁹ J.P. Perdew, K. Burke, M. Ernzerhof, *Phys. Rev. Lett.* **1996** (77) 3865-3868; Erratum: J.P. Perdew, K. Burke, M. Ernzerhof, *Phys. Rev. Lett.* **1997** (78) 1396.

the best functionals for transition metal systems,^{75,85} performed the worst geometry optimization of all with an Fe-N_{py} bond length of 2.498 Å, indicating that the pyridine groups have basically fallen off.

3.2.2.3 Energy profile of default occupations.

For spin crossover to be possible, the relative energies of the different spin states of [Fe(salen)(CH₃)₂(COCH₃)₂(py)₂] have to be within 30 kJ.mol⁻¹ (0.3 eV) of each other. The relative energies of the *S* = 0, 1 and 2 states of [Fe(salen)(CH₃)₂(COCH₃)₂(py)₂], with default occupation and a selection of functionals, are tabulated in Table 3.22. The energy profile, compared to the geometry profile, shows a completely opposite performance by the functionals. OLYP, OPBE and B3LYP performed the best with an energy range of 5, 14 and 23 kJ.mol⁻¹ respectively. The other studied functionals, including PW91 (energy range of 103 kJ.mol⁻¹ for TZP basis set and 115 kJ.mol⁻¹ for 6-311G** basis set), produced an unacceptable energy profile.

Therefore, the functional with the best geometry profile, PW91, gave the worst energy profile and the functional with the best energy profile, OLYP, gave the worst geometry profile. In this light, a linear transit was performed on the *S* = 2 state of [Fe(salen)(CH₃)₂(COCH₃)₂(py)₂], with OLYP, to see whether the geometry of a specific functional has a large influence on its energy profile. The stepwise changing of the Fe-N_{py} bond length of 2.50-2.30 Å resulted in a stepwise energy increase of only 8 kJ.mol⁻¹. Therefore, the precise geometry does not have a large influence on the energy profile of a specific functional. Therefore one can conduct single-point calculations on the PW91 geometry, with different functionals, to obtain an accurate energy profile with a good geometry profile.

3.2.2.4 Energy profile of alternative occupations.

Single-point OLYP, B3LYP and B3LYP* calculations were carried out for the PW91 optimized geometries of *S* = 0, 1 and 2. Subsequently, alternative occupations of the triplet and quintet states were also calculated. The energy profiles of these calculations are tabulated in Table 3.23. As mentioned before, for spin crossover to be possible, the different spin states of [Fe(salen)(CH₃)₂(COCH₃)₂(py)₂] have to be equi-energetic, especially the low spin *S* = 0 and the high spin *S* = 2.⁹⁰ B3LYP exhibits the best energy profile with all quintet states (⁵B₂, ⁵A₂ and

⁹⁰ B. Weber, F.A. Walker, *Inorg. Chem.* **2007** (46) 6794-6803.

5A_1) within the energy range of the singlet state (1A_1). PW91 once again exhibits the worst energy profile, with no high spin states in the range of the low spin state.

3.2.2.5 Spin density profile.

Figure 3.41 presents a comparison of the PW91, OLYP, B3LYP and B3LYP* spin density profiles of $S = 2$ [Fe(salen)(CH₃)₂(COCH₃)₂(py)₂]. Contrary to that which was found for similar salen complexes ($S = 1/2$),⁷⁶ the different functionals exhibit a qualitatively similar electron description for both $S = 1$ (as example: Figure 3.42, top row, left) and $S = 2$ (Figure 3.41). For all functionals, the $S = 2$ iron centre carries approximately 3.7 of majority electron spin and the N of the pyridine carries approximately 0.03. The O and N in the salen ligand carries approximately 0.06-0.08 majority electron spin.

Figure 3.42 represents the B3LYP spin density profiles of [Fe(salen)(CH₃)₂(COCH₃)₂(py)₂] for all the triplet and quintet states. The Mullikan spin density around the iron centre, of each triplet and quintet state, is a combination of mainly the singly occupied d -orbitals (SOMO). For instance, the Mullikan spin density of the triplet state $1: ^3A_2$ (Figure 3.42, top row, left) consists of 48.4% d_{xz} and 46.0% d_{z^2} d -orbital character, as illustrated by the form of the majority spin density in cyan. In the same way, the triplet state 3A_1 (Figure 3.42, top row, middle) consists of 47.7% $d_{x^2-y^2}$ and 49.1% d_{z^2} d -orbital character. This pattern is repeated for the other triplet states. The quintet states are mostly a fine mesh of four of the five d -orbitals, resulting in an almost round shape of Mullikan spin density around the iron centre (Figure 3.42, bottom row).

3.2.2.6 Conclusions.

The pure functional PW91 gives a good geometry optimization of both the low and high spin states of the spin crossover complex [Fe(salen)(CH₃)₂(COCH₃)₂(py)₂]. The pure functionals OLYP, OPBE, BLYP, PBE and BP86 and the hybrid functional B3LYP only succeeded in giving a good geometry optimization of the low spin complex. For the high spin geometry, OLYP performed the worst. Though, an opposite performance by functionals was obtained for the spin-state energetics. OLYP, B3LYP and B3LYP* provided the best spin-state energetics for spin crossover with similar spin density profiles. So, to answer the question stated in the beginning: which functional best reproduces accurate geometry and equi-energetic $S = 0$ (high spin, HS) and 2 (low spin, LS) states of this complex? Although OLYP is known to be one of the best functionals for transition metal systems,^{75,85} it failed to perform for the spin crossover

RESULTS AND DISCUSSION

complex $[\text{Fe}(\text{salen})(\text{CH}_3)_2(\text{COCH}_3)_2(\text{py})_2]$. Failures like these inspire researchers to constantly improve old functionals and hence developing new ones.⁹¹

3.2.2.7 Tables and graphs.

Table 3.22: Relative energies ($\text{kJ}\cdot\text{mol}^{-1}$) of the different spin states of $[\text{Fe}(\text{salen})(\text{CH}_3)_2(\text{COCH}_3)_2(\text{py})_2]$ (pyridine groups vertically oriented), optimized under a C_{2v} symmetry constraint. Calculated bond lengths (\AA) and bond angles ($^\circ$) around the Fe(II) centre are also tabulated.

Basis Set		STO-TZP						6-311G**	
Functional		PW91	BP86	BLYP	PBE	OLYP	OPBE	PW91	B3LYP
State	Properties								
1A_1	E ($\text{kJ}\cdot\text{mol}^{-1}$)	0	0	0	0	0	0	0	0
	Fe-N _{py} (\AA)	1.990	1.994	2.034	1.994	2.043	2.002	1.970	2.036
	Fe-N _s (\AA)	1.896	1.899	1.924	1.897	1.897	1.874	1.890	1.925
	Fe-O _s (\AA)	1.942	1.945	1.968	1.945	1.963	1.946	1.930	1.958
	N _{py} -Fe-N _{py} ($^\circ$)	174.1	173.3	173.0	173.7	173.5	172.2	173.8	172.9
	N _s -Fe-N _s ($^\circ$)	85.2	85.1	85.0	85.2	85.7	85.5	85.7	85.1
	N _s -Fe-O _s ($^\circ$)	93.7	93.5	92.9	93.6	92.7	92.7	93.5	92.2
	O _s -Fe-O _s ($^\circ$)	87.4	87.9	89.2	87.5	88.9	89.0	87.2	90.5
$1: ^3A_2$	E ($\text{kJ}\cdot\text{mol}^{-1}$)	75	70	52	71	1	14	83	23
	Fe-N _{py} (\AA)	2.383	2.401	2.476	2.406	2.847	3.481	2.345	2.427
	Fe-N _s (\AA)	1.894	1.896	1.915	1.894	1.889	1.862	1.887	1.919
	Fe-O _s (\AA)	1.931	1.931	1.948	1.933	1.934	1.905	1.918	1.941
	N _{py} -Fe-N _{py} ($^\circ$)	171.0	170.9	171.2	169.2	167.6	160.4	170.8	170.8
	N _s -Fe-N _s ($^\circ$)	85.0	85.0	85.1	85.1	85.4	85.6	85.6	85.1
	N _s -Fe-O _s ($^\circ$)	93.8	93.7	93.3	93.8	93.2	93.8	93.7	92.5
	O _s -Fe-O _s ($^\circ$)	87.4	87.5	88.3	87.4	88.3	86.8	87.0	90.0
5B_2	E ($\text{kJ}\cdot\text{mol}^{-1}$)	103	95	77	95	-5	8	115	-2
	Fe-N _{py} (\AA)	2.298	2.307	2.365	2.308	2.498	2.494	2.265	2.312
	Fe-N _s (\AA)	2.083	2.088	2.108	2.086	2.093	2.068	2.070	2.106
	Fe-O _s (\AA)	2.001	2.001	2.013	2.006	2.013	2.001	1.991	2.021
	N _{py} -Fe-N _{py} ($^\circ$)	172.1	171.9	171.9	170.0	168.7	168.9	170.9	169.8
	N _s -Fe-N _s ($^\circ$)	79.3	79.2	79.3	79.2	79.2	79.3	80.2	79.5
	N _s -Fe-O _s ($^\circ$)	87.5	87.3	86.9	87.3	86.7	87.1	87.4	86.1
	O _s -Fe-O _s ($^\circ$)	105.8	106.2	106.8	106.2	107.5	106.5	105.0	108.3

⁹¹ E.J. Baerends, O.V. Gritsenko, *J. Chem. Phys.* **2005** (123) 62202-62218.

CHAPTER 3

Table 3.23: Relative energies (kJ.mol⁻¹) of the different spin states of [Fe(salen)(CH₃)₂(COCH₃)₂(py)₂] (pyridine groups vertically oriented), optimized under a C_{2v} symmetry constraint with PW91. Single-point OLYP, B3LYP and B3LYP* calculations were carried out on the PW91 optimized geometries. Note alternative occupations.

State	Occupation	Configuration	PW91	OLYP	B3LYP	B3LYP*
¹ A ₁	A1 = 40//40 A2 = 11//11 B1 = 27//27 B2 = 22//22	$d_{z^2}^0 d_{xy}^0$ $d_{x^2-y^2}^2 d_{xz}^2 d_{yz}^2$	0	0	0	0
1: ³ A ₂	A1 = 41//40 A2 = 11//10 B1 = 27//27 B2 = 22//22	$d_{z^2}^1 d_{xy}^0$ $d_{x^2-y^2}^2 d_{xz}^1 d_{yz}^2$	75	14	10	25
³ A ₁	A1 = 41//39 A2 = 11//11 B1 = 27//27 B2 = 22//22	$d_{z^2}^1 d_{xy}^0$ $d_{x^2-y^2}^1 d_{xz}^2 d_{yz}^2$	102	44 ⁱ	56	68
1: ³ B ₂	A1 = 41//40 A2 = 11//11 B1 = 27//27 B2 = 22//21	$d_{z^2}^1 d_{xy}^0$ $d_{x^2-y^2}^2 d_{xz}^2 d_{yz}^1$	128 ⁱ	68 ⁱ	45	65
2: ³ B ₂	A1 = 40//40 A2 = 11//10 B1 = 28//27 B2 = 22//22	$d_{z^2}^0 d_{xy}^1$ $d_{x^2-y^2}^2 d_{xz}^1 d_{yz}^2$	174 ⁱ	156 ⁱ	137	152
³ B ₁	A1 = 40//39 A2 = 11//11 B1 = 28//27 B2 = 22//22	$d_{z^2}^0 d_{xy}^1$ $d_{x^2-y^2}^1 d_{xz}^2 d_{yz}^2$	112	79	62	77
2: ³ A ₂	A1 = 40//40 A2 = 11//11 B1 = 28//27 B2 = 22//21	$d_{z^2}^0 d_{xy}^1$ $d_{x^2-y^2}^2 d_{xz}^2 d_{yz}^1$	189 ⁱ	155 ⁱ	137	149
⁵ B ₂	A1 = 41//39 A2 = 11//10 B1 = 28//27 B2 = 22//22	$d_{z^2}^1 d_{xy}^1$ $d_{x^2-y^2}^1 d_{xz}^1 d_{yz}^2$	189	2	-19	12
⁵ A ₂	A1 = 41//39 A2 = 11//11 B1 = 28//27 B2 = 22//21	$d_{z^2}^1 d_{xy}^1$ $d_{x^2-y^2}^1 d_{xz}^2 d_{yz}^1$	135	34	10	42
⁵ A ₁	A1 = 41//40 A2 = 11//10 B1 = 28//27 B2 = 22//21	$d_{z^2}^1 d_{xy}^1$ $d_{x^2-y^2}^2 d_{xz}^1 d_{yz}^1$	166 ⁱ	63 ⁱ	18	54

ⁱ Non Aufbau.

RESULTS AND DISCUSSION

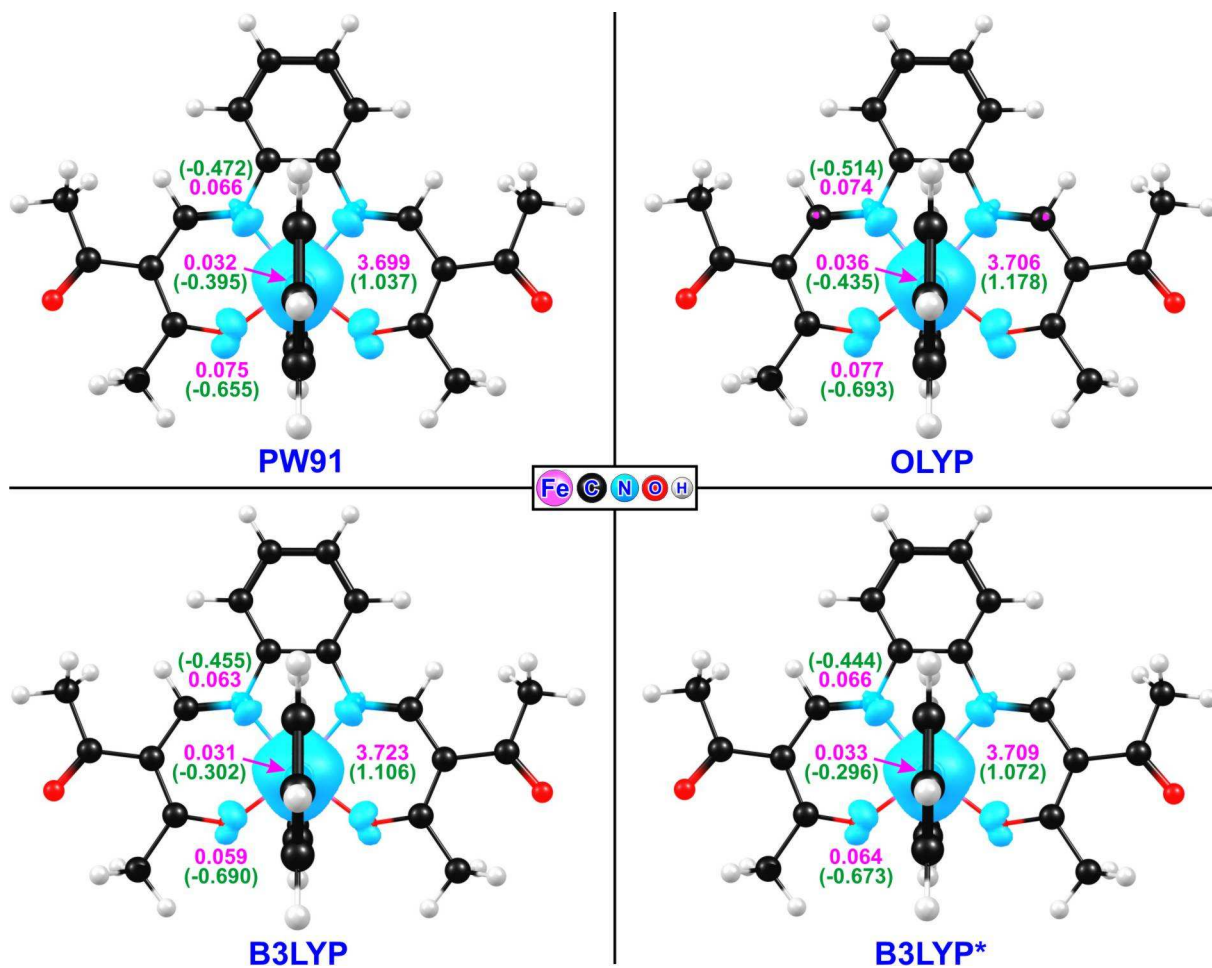


Figure 3.41: Spin density profiles of $S = 2$ $[\text{Fe}(\text{salen})(\text{CH}_3)_2(\text{COCH}_3)_2(\text{py})_2]$ (pyridine groups vertically oriented) of the different functionals on the PW91 optimized geometry. Majority and minority spin densities shown in cyan and magenta, respectively. The spin (magenta), the charge (green) and the colour code of atoms are as indicated.

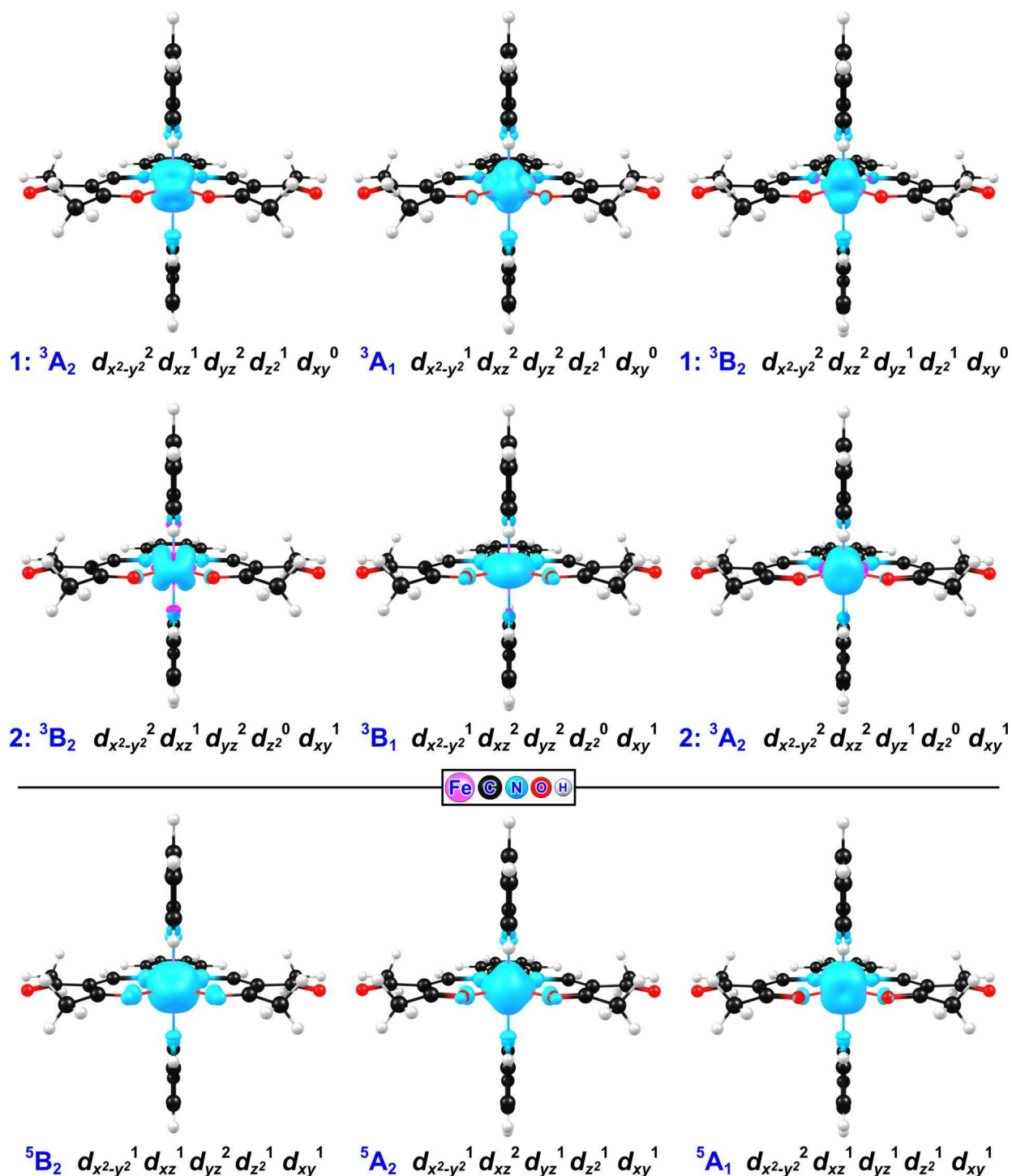


Figure 3.42: B3LYP spin density profiles of $[\text{Fe}(\text{salen})(\text{CH}_3)_2(\text{COCH}_3)_2(\text{py})_2]$ (pyridine groups vertically oriented) for alternative occupations of $S = 1$ and 2 on the PW91 optimized geometry. Majority and minority spin densities shown in cyan and magenta, respectively. The occupation and the colour code of the atoms are as indicated.

RESULTS AND DISCUSSION



3.2.3 [Fe(porphyrin)(Ar)].

3.2.3.1 Introduction.

One of the triumphs of modern density functional theory (DFT) is that it provides good to excellent results on open-shell transition metal systems at a fraction of the cost of high-quality multiconfigurational *ab initio* methods.^{72,74,92} A key imperfection in this otherwise encouraging picture, however, is that DFT often does not do a particularly good job of describing the spin-state energetics of transition metal complexes. The problem is particularly acute for iron complexes and iron porphyrins appear to be some of the worst offenders in this regard.^{93,94} This problem came to light in the course of a combined DFT and *ab initio* study of the chloroiron(III) porphyrin, [Fe^{III}(porphyrin)(Cl)], which is essentially an $S = 5/2$ system. The then popular pure functional PW91, however, predicted an $S = 3/2$ ground state. In contrast, *ab initio* CASPT2 calculations on [Fe^{III}(porphyrin)(Cl)] and CCSD(T) calculations on a small model complex yielded the expected $S = 5/2$ ground state by a clear margin of energy.⁹³ Since that time, experience with other transition metal systems have been gained, but the five-coordinate iron(III) porphyrins with a variety of currently popular exchange-correlation functionals have not been revisited.⁹⁵ This is therefore the aim of this study, to focus on an intriguing series of remarkable aryliron(III) porphyrins, [Fe^{III}(porphyrin)(Ar)], reported by Kadish *et al.* in 1995.⁹⁶ Such species are also of significant biological interest: aryliron-porphyrins have been implicated as reactive

⁹² (a) For an introduction to DFT as applied to transition metal systems, see: F. Neese, *J. Biol. Inorg. Chem.* **2006** (11) 702-711. (b) For a biochemically oriented review, see: L. Noodleman, T. Lovell, W.-H. Han, J. Li, F. Himo, *Chem. Rev.* **2004** (104) 459-508. (c) J.N. Harvey, *Struct. Bonding* **2004** (112) 151-183.

⁹³ (a) A. Ghosh, T. Vangberg, E. Gonzalez, P.R. Taylor, *J. Porph. Phth.* **2001** (5) 345-356. (b) A. Ghosh, B.J. Persson, P.R. Taylor, *J. Biol. Inorg. Chem.* **2003** (8) 507-511.

⁹⁴ (a) A. Ghosh, P.R. Taylor, *J. Chem. Theory Comput.* **2005** (1) 597-600. (b) M. Radon, K. Pierloot, *J. Phys. Chem. A* **2008** (112) 11824-11832. (c) B.O. Roos, V. Veryazov, J. Conradie, P.R. Taylor, A. Ghosh, *J. Phys. Chem. B* **2008** (112) 14099-14102.

⁹⁵ Notable, recent theoretical studies on five-coordinate iron porphyrins, see: (a) N. Strickland, J.N. Harvey, *J. Phys. Chem. B* **2007** (111) 841-852. (b) D.A. Scherlis, M. Cococcioni, P. Sit, N. Marzari, *J. Phys. Chem. B* **2007** (111) 7834-7391. (c) P. Rydberg, L. Olsen, *J. Phys. Chem. A* **2009** (113) 11949-11953.

⁹⁶ K.M. Kadish, E. van Caemelbecke, E. Gueletti, S. Fukuzumi, K. Miyamoto, T. Suenobu, A. Tabard, R. Guillard, *Inorg. Chem.* **1998** (37) 1759-1766.

RESULTS AND DISCUSSION

intermediates in the metabolism of arylhydrazines by cytochromes P450⁹⁷ and their reactivity patterns provide significant insights into the active site topologies of membrane-bound P450s whose crystal structures remain to be solved.^{98,99}

Ferrous and ferric hemes exhibit a wide variety of electronic structures and spin states.^{100,101} A useful rule of thumb, however, is that five-coordinate iron porphyrins are generally high spin, whereas six-coordinate ones are generally low spin. There are some exceptions to this generalization,^{102,103} even though it applies quite broadly. Aryliron(III) porphyrins are particularly interesting in this regard because the spin state of the complex depends on the substitution pattern of the aryl group. All known [Fe^{III}(porphyrin)(Ph)] complexes are low spin, whereas all known [Fe^{III}(porphyrin)(C₆F₅)] and [Fe^{III}(porphyrin)(C₆F₄H)] derivatives are high spin. For the trifluorophenyl derivatives, the spin state energies appear to be exceedingly finely balanced: Fe^{III}(OEP)(2,4,6-C₆F₃H₂) is $S = 5/2$, but Fe^{III}(OEP)(3,4,5-C₆F₃H₂) is $S = 1/2$.⁹⁶ How well do different DFT functionals capture this remarkable spin state diversity? Briefly put, some functionals do not do well, whereas others do not do badly...

⁹⁷ P.R. Ortiz de Montellano, In: P.R. Ortiz de Montellano (Editor), *Cytochrome P450*, Kluwer, New York, **2005**, Chapter 7, p247-322.

⁹⁸ Key references to the original literature on P450-hydrazine interactions, see: (a) R. Raag, B.S. Swanson, T.L. Poulos, P.R. Ortiz de Montellano, *Biochemistry* **1990** (29) 8119-8126. (b) K.L. Kunze, P.R. Ortiz de Montellano, *J. Am. Chem. Soc.* **1983** (105) 1380-1381. (c) D. Ringe, G.A. Petsko, D.E. Kerr, P.R. Ortiz de Montellano, *Biochemistry* **1984** (23) 2-4.

⁹⁹ For relevant synthetic model studies, see: (a) P. Battioni, J.P. Mahy, G. Gillet, D. Mansuy, *J. Am. Chem. Soc.* **1983** (105) 1380-1381. (b) D. Lancon, P. Cocolios, R. Guilard, K.M. Kadish, *J. Am. Chem. Soc.* **1984** (106) 4472-4478. (c) R. Guilard, B. Boisselier-Cocolios, A. Tabard, P. Cocolios, B. Simonet, K.M. Kadish, *Inorg. Chem.* **1985** (24) 2509-2520.

¹⁰⁰ F.A. Walker, In: K.M. Kadish, K.M. Smith, R. Guilard (Editors), *The Porphyrin Handbook*, Academic, San Diego, **2000**, Chapter 36, p81-183.

¹⁰¹ (a) M. Nakamura, *Coord. Chem. Rev.* **2006** (250) 2271-2294. (b) A. Ikezaki, Y. Ohgo, M. Nakamura, *Coord. Chem. Rev.* **2009** (253) 2056-2069.

¹⁰² Nakamura has recently reported a route to intermediate-spin iron(III) porphyrins: T. Sakai, Y. Ohgo, T. Ikeue, M. Takahashi, M. Takeda, M. Nakamura, *J. Am. Chem. Soc.* **2003** (125) 13028-13029.

¹⁰³ The N-nitrito ligand gives rise to (highly reactive) low spin iron(III) porphyrin intermediates: J. Conradie, A. Ghosh, *Inorg. Chem.* **2006** (45) 4902-4909.

DFT calculations in this study have been performed on $[\text{Fe}^{\text{III}}(\text{porphyrin})(\text{Ar})]$ complexes ($\text{Ar} = \text{aryl} = \text{Cl}, \text{Ph}, \text{C}_6\text{F}_5, 3,4,5\text{-C}_6\text{F}_3\text{H}_2$ and $2,4,6\text{-C}_6\text{F}_3\text{H}_2$) (Figure 3.43 and Figure 3.44). For the details of the computational methods used, see section 4.5.3.3 (Chapter 4). A number of classic pure functionals were used (PW91,⁸⁰ BLYP,^{78,79} BP86^{79,81} and TPSS¹⁰⁴). However, because the results obtained with these functionals were all in near-perfect mutual agreement, only the PW91 results are shown for all the complexes studied, as representative of the older pure functionals. The newer pure functionals (OLYP^{78,86} and OPBE^{77,86}), based on the improved OPTX exchange functional, were also examined, as were the hybrid functionals (B3LYP⁸² and B3LYP*⁸³) which contain 20 and 15% Hartree-Fock exchange respectively. The OPBE results will not be presented, since they are nearly identical to those obtained with OLYP. Finally, the hybrid meta-GGA functional TPSSh¹⁰⁴ (which contains 10% Hartree-Fock exchange) was also examined.

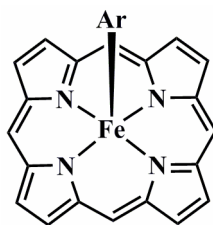


Figure 3.43: Chemical structure of $[\text{Fe}^{\text{III}}(\text{porphyrin})(\text{Ar})]$, the porphyrin used in this study.

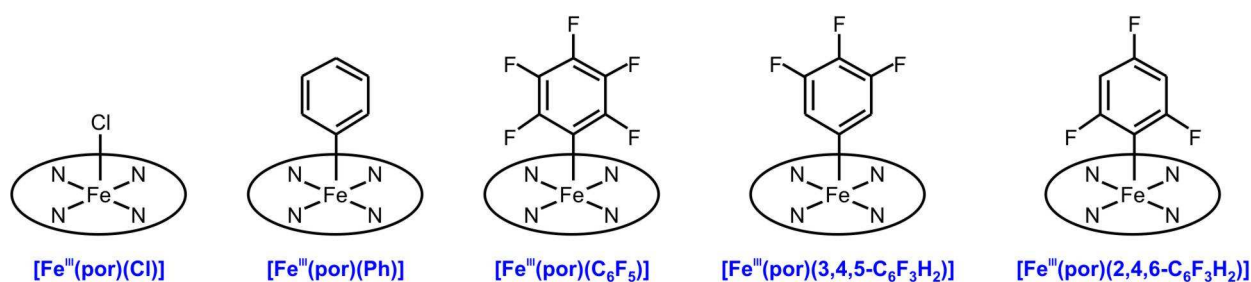


Figure 3.44: $[\text{Fe}^{\text{III}}(\text{porphyrin})(\text{Ar})]$ complexes studied in this work.

¹⁰⁴ (a) J. Tao, J.P. Perdew, V.N. Staroverov and G.E. Scuseria, *Phys. Rev. Lett.* **2003** (91) 146401-146404. (b) V.N. Staroverov, G.E. Scuseria, J. Tao and J.P. Perdew, *J. Chem. Phys.* **2003** (119) 12129-12137.

3.2.3.2 Geometry profile.

The [Fe^{III}(porphyrin)(Ar)] (Ar = aryl = Cl, Ph, C₆F₅, 3,4,5-C₆F₃H₂ and 2,4,6-C₆F₃H₂) complexes were optimized with a selection of functionals. The bond lengths around the Fe(III) centre, a key indicator of the structure in organometallic complexes, of the low spin ($S = 1/2$) and high spin ($S = 5/2$) complexes (with default occupation) are tabulated in Table 3.24. All the functionals give satisfactory results for the geometries of the different spin states. Focussing on the Fe-N_{por} bond length, one would expect that the bond length becomes longer as the spin state increases from $S = 1/2$ to $5/2$.⁸⁷ Consequently the porphyrin becomes more dome deformed (section 2.5.3, figure 2.5.1, Chapter 2), with the iron centre shifted out of the plane (Figure 3.45). The Fe-N_{por} bond lengths of the doublet state are more or less the same for all the studied functionals, varying between 1.97-2.00 Å (difference of 0.03 Å). This is also the case for the Fe-N_{por} bond lengths of the quintet state, where the elonged bond lengths vary between 2.09-2.13 Å (difference of 0.04 Å). The axial bond lengths, Fe-Ar, differ from each other in as the aryl substituents change, but are virtually the same for all functionals used (difference of 0.04 Å). This axial bond length also becomes longer as the spin state increases from $S = 1/2$ to $5/2$ (Table 3.24, Figure 3.45).

3.2.3.3 Energy profile.

Tables 3.24-3.28 present the calculated spin-state energetics of the above five complexes, with the $S = 5/2$ state as the energy zero level in each case. The shapes of the *d*-type frontier orbitals are very similar throughout and are shown, along with their irreducible representations, for the high spin state of [Fe^{III}(porphyrin)(Ph)] in Figure 3.46. The following are the results obtained of these molecules.

[Fe^{III}(porphyrin)(Cl)]: As found in an earlier study,⁹³ PW91 predicts a ⁴A₁ state for [Fe^{III}(porphyrin)(Cl)], with the expected ⁶A₁ state approximately 36 kJ.mol⁻¹ higher in energy (see Table 3.25). Interestingly, both OLYP and B3LYP successfully predict a sextet ground state, although the ⁴A₁ state is just over 10 kJ.mol⁻¹ higher in energy with both functionals. With B3LYP*, the ⁶A₁ and ⁴A₁ states are equi-energetic and TPSSh incorrectly favours the ⁴A₁ state as the ground state. However, although OLYP, B3LYP and B3LYP* are clearly better than PW91 (and other classic pure functionals), they still significantly underestimate the sextet-quartet splitting relative to both CASPT2 and CCSD(T), which indicate that it is around 70 kJ.mol⁻¹.

[Fe^{III}(porphyrin)(Ph)]:⁹⁶ For [Fe^{III}(porphyrin)(Ph)], Table 3.26 presents full results from all the functionals examined. All functionals successfully predict an $S = 1/2$ ground state for this complex, as expected on the basis of experimental results. Moreover, all the functionals agree among themselves in yielding a 2B_2 ground state, with a 2B_1 state only 2-6 kJ.mol⁻¹ higher in energy. These two states correspond to the $d_{x^2-y^2}^2 d_{xz}^2 d_{yz}^1$ and $d_{x^2-y^2}^2 d_{xz}^1 d_{yz}^2$ configurations respectively. The 2A_1 state with the $d_{x^2-y^2}^1 d_{xz}^2 d_{yz}^2$ configuration is somewhat higher in energy, 23-40 kJ.mol⁻¹ relative to the ground state, depending on the functional.

OLYP, OPBE, B3LYP and B3LYP* are in remarkable agreement vis-à-vis the energy of the sextet state, which is found to be 26-49 kJ.mol⁻¹ higher, relative to the ground state. In the absence of other results to the contrary, one is inclined to regard a doublet-sextet splitting in the order of ~50 kJ.mol⁻¹ as representative of reality for this complex. These results, however, need to be taken with a pinch of salt, given the apparently poor performance of all the functionals for [Fe^{III}(porphyrin)(Cl)]. With the classic pure functionals, which tend to unduly pair up electrons, the sextet energy is much higher, > 100 kJ.mol⁻¹ relative to the ground state.

[Fe^{III}(porphyrin)(C₆F₅)]:⁹⁶ The fact that [Fe^{III}(OEP)(C₆F₅)] is an $S = 5/2$ complex, suggests that [Fe^{III}(porphyrin)(C₆F₅)] should also be a high spin complex. As shown in Table 3.27, only OLYP appears to be consistent with this expectation - it predicts a sextet ground state with the 2B_2 state 12 kJ.mol⁻¹ higher in energy. With B3LYP, the two states are almost exactly equi-energetic, whereas with B3LYP*, the 2B_2 state appears to be favoured by close to 15 kJ.mol⁻¹. TPSSh performs distinctly differently (worse), favoring the 2B_2 state by 34 kJ.mol⁻¹, relative to the sextet state. With PW91, the sextet state is nearly 74 kJ.mol⁻¹ above the 2B_2 state and similarly poor results are obtained with other pure functionals. Interestingly, all the functionals predict a low-lying quartet state - 4A_2 , of which the electronic configuration may be described as $d_{x^2-y^2}^2 d_{xz}^1 d_{yz}^1 d_{z^2}^1$, where the double occupancy of the $d_{x^2-y^2}$ orbital may be ascribed to a π -backbonding interaction with the C₆F₅ group.

[Fe^{III}(porphyrin)(3,4,5-C₆F₃H₂)] and [Fe^{III}(porphyrin)(2,4,6-C₆F₃H₂)]:⁹⁶ As mentioned above, these two regioisomeric complexes are expected to be low spin and high spin, respectively. The spin state energetics of these two complexes would appear to present a stringent test of the performance of any functional. However, as in the case of [Fe^{III}(porphyrin)(Ph)], all the functionals examined appear to correctly indicate a low spin (2B_2) ground state for

[Fe^{III}(porphyrin)(3,4,5-C₆F₃H₂)] (Table 3.28). The energy of the sextet state is 24-29 kJ.mol⁻¹ with OLYP, TPSSh and B3LYP, 46 kJ.mol⁻¹ with B3LYP* and > 100 kJ.mol⁻¹ with PW91, all relative to the ground state. The fact that OLYP, B3LYP and B3LYP* are in reasonably good agreement suggests that the sextet-doublet splitting obtained with these functionals should be reasonably good.

With [Fe^{III}(porphyrin)(2,4,6-C₆F₃H₂)] (Table 3.29), as with [Fe^{III}(porphyrin)(C₆F₅)], the lowest doublet and sextet states seem to be very finely balanced indeed. Once again, only OLYP appears to indicate a sextet ground state by a reasonable margin of energy, approximately 8 kJ.mol⁻¹. B3LYP appears to predict either a doublet or a sextet state. B3LYP* favors a doublet ground state, with the sextet state nearly 18 kJ.mol⁻¹ higher, as does TPSSh with the sextet state 44 kJ.mol⁻¹ above the doublet ground state. Once again, PW91 is the worst, placing the sextet some 79 kJ.mol⁻¹ above the doublet ground state.

3.2.3.4 Spin density.

Figure 3.47 presents spin density plots of the lowest-energy low spin (²B₂) and high spin (⁶A₁) states of the complexes studied. Note that the axial aryl groups carry little spin density. This implies, as does a detailed examination of the valence molecular orbitals, that there is little π -interaction between the aryl π -systems and the iron d_{π} -orbitals. The aryl groups are therefore reasonably viewed as relatively pure, strong σ -donating ligands. Studies of spin state energetics as a function of the Fe-C distance (details not shown) indicate that the high-spin state of [Fe^{III}(porphyrin)(2,4,6-C₆F₃H₂)] (as opposed to the low-spin state of its 3,4,5- regioisomer) owes more to the *steric* requirements of the 2,6-fluoro substituents than to the slightly weaker *s*-donor ability of the 2,4,6-C₆F₃H₂ ligand. Thus, note from Figure 3.45 that for a given spin state, the axial Fe-C bond is roughly 0.03 Å longer for the 2,6-fluorinated complexes relative to their 2,6-unfluorinated counterparts. It is a relatively small difference but it apparently suffices to tip the delicately poised spin-state energies in favor of a high-spin state for the 2,6-fluorinated complexes.

3.2.3.5 Conclusions.

A series of closely related complexes such as the aryliron porphyrins, which exhibit different spin states, provide a powerful calibration of the performance of DFT functionals vis-à-vis the issue of transition metal spin state energetics.^{93,94,95} These approaches provide an attractive

alternative to the much more demanding strategy of calibrating DFT-derived spin-state energetics against high-level *ab initio* methods such as CASPT2 and CCSD(T).¹⁰⁵

Which functionals perform best for the complexes examined here? The newer pure functional (OLYP or OPBE) appears to have performed best, closely followed by B3LYP. Both OLYP and B3LYP appear to have performed distinctly better than B3LYP*, which is somewhat of a surprise, given that B3LYP* usually performs significantly better than B3LYP. Somewhat surprisingly, OLYP, B3LYP and B3LYP* have all performed better than the hybrid functional TPSSh. Classic pure functionals such as PW91 are clearly the worst, as far as spin state energetics is concerned.^{73,74} Unfortunately, the reasons as to why one functional performs better than another are not easy to fathom, given the empirical manner in which most functionals are designed. The preponderance of evidence, however, suggests that the OPTX exchange functional, which provides the exchange part of OLYP and OPBE, is a particularly good one.

3.2.3.6 Graphs and tables.

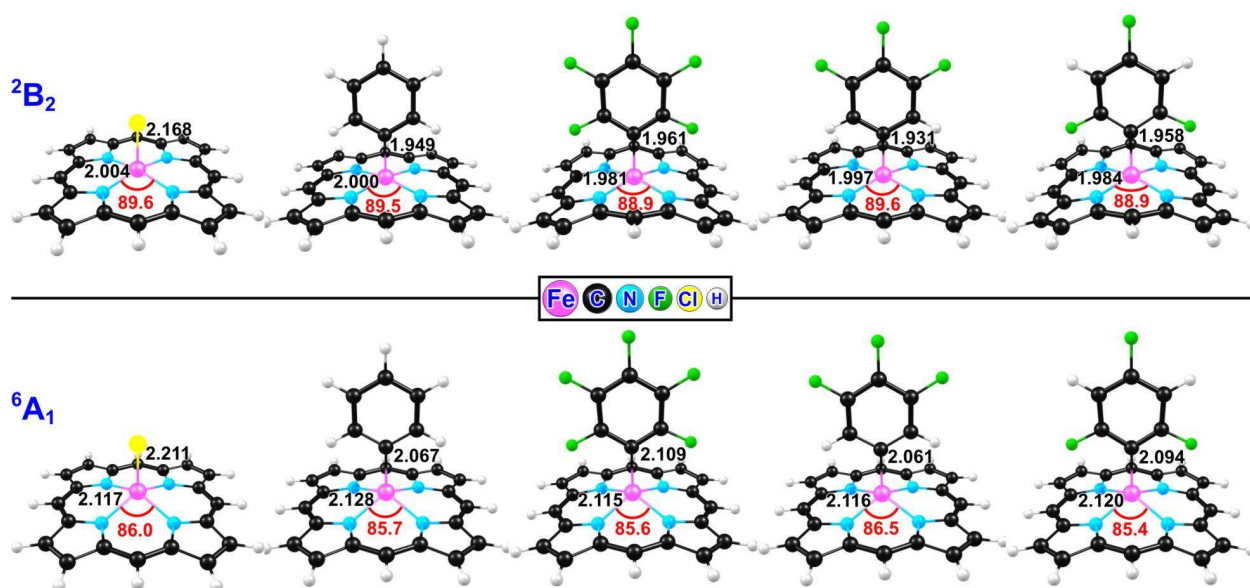


Figure 3.45: OLYP optimized geometries of the lowest-energy low spin (2B_2 , top) and high spin (6A_1 , bottom) states of the $[Fe^{III}(\text{porphyrin})(\text{Ar})]$ complexes (Ar = aryl = Cl, Ph, C_6F_5 , 3,4,5- $C_6F_3H_2$ and 2,4,6- $C_6F_3H_2$). Distances (\AA) and angles ($^\circ$) are indicated in black and red, respectively.

¹⁰⁵ Selected DFT/*ab initio* comparisons for transition metal systems: (a) K.P. Jensen, *J. Phys. Chem. B* **2005** (109) 10505-10512. (b) A. Ghosh, E. Gonzalez, E. Tangen, B.O. Roos, *J. Phys. Chem. A* **2008** (112) 12792-12798. (c) M. Swart, *J. Chem. Theory Comput.* **2008** (4) 2057-2066. (d) T. Takatani, J.S. Sears, C.D. Sherrill, *J. Phys. Chem. A* **2009** (113) 9231-9236.

RESULTS AND DISCUSSION

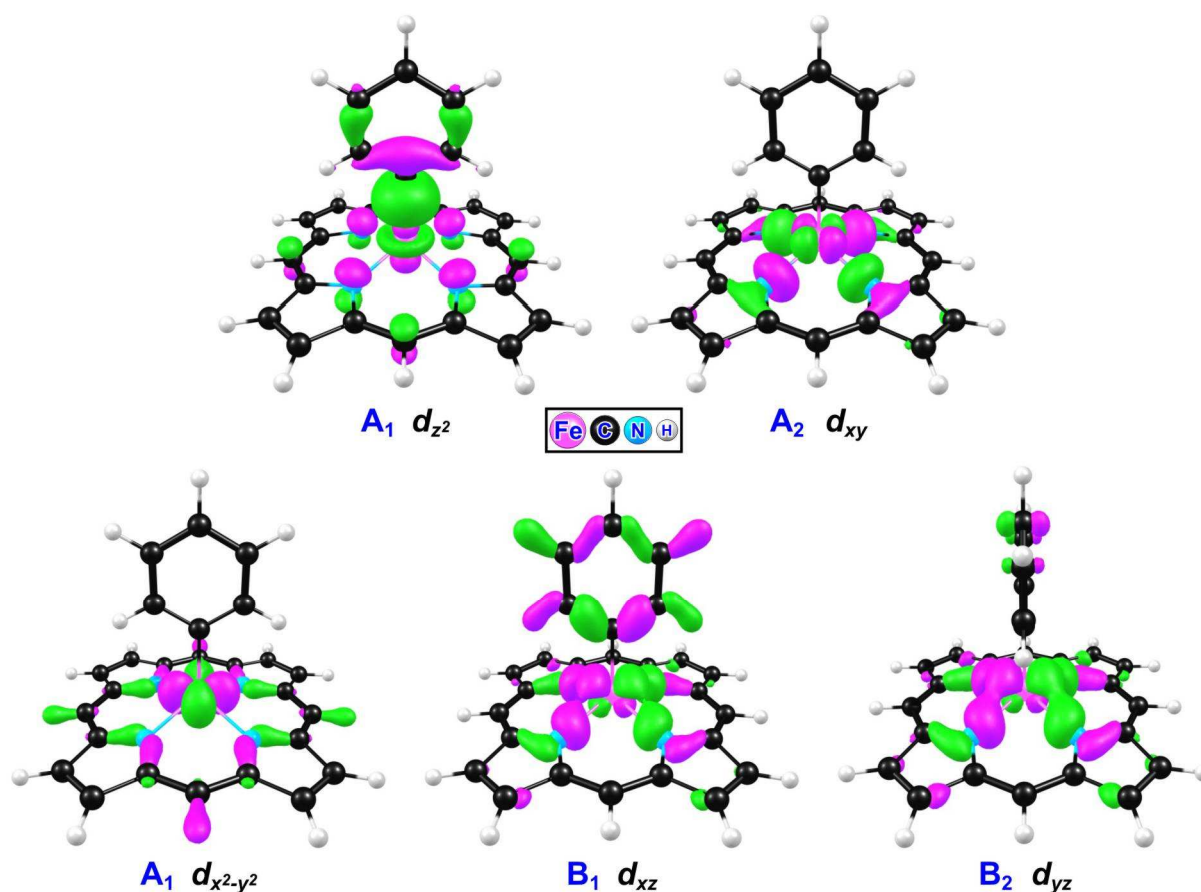


Figure 3.46: The shapes of the d -type frontier orbitals, along with their irreducible representations, of the high spin state 6A_1 of $[\text{Fe}^{\text{III}}(\text{porphyrin})(\text{Ph})]$, optimized with OLYP.

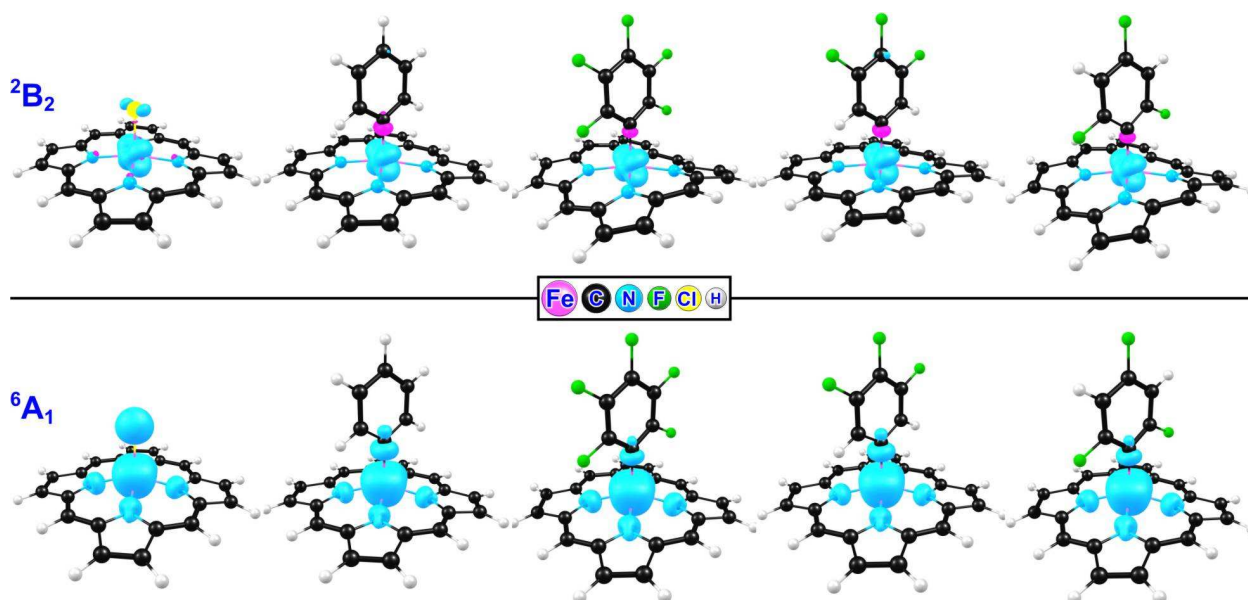


Figure 3.47: OLYP spin density profiles of the lowest-energy low spin (2B_2 , top) and high spin (6A_1 , bottom) states of the $[\text{Fe}^{\text{III}}(\text{porphyrin})(\text{Ar})]$ complexes (Ar = aryl = Cl, Ph, C_6F_5 , 3,4,5- $\text{C}_6\text{F}_3\text{H}_2$ and 2,4,6- $\text{C}_6\text{F}_3\text{H}_2$). Majority and minority spin densities shown in cyan and magenta, respectively.

CHAPTER 3

Table 3.24: Calculated bond lengths (Å) around the Fe(III) centre of the $S = 1/2$ and $5/2$ states (default occupations) of the $[\text{Fe}^{\text{III}}(\text{porphyrin})(\text{Ar})]$ complexes (Ar = aryl = Cl, Ph, C_6F_5 , 3,4,5- $\text{C}_6\text{F}_3\text{H}_2$ and 2,4,6- $\text{C}_6\text{F}_3\text{H}_2$), optimized under a C_{2v} symmetry constraint.

Basis Set		STO-TZP		6-311G**
		PW91 ⁱ	OLYP ⁱⁱ	B3LYP
$[\text{Fe}^{\text{III}}(\text{porphyrin})(\text{Cl})]$				
² B ₂	Fe-N _{por} (Å)	1.987	2.004	1.999
	Fe-Cl (Å)	2.156	2.168	2.200
⁶ A ₁ ⁱⁱⁱ	Fe-N _{por} (Å)	2.099	2.117	2.088
	Fe-Cl (Å)	2.194	2.211	2.232
$[\text{Fe}^{\text{III}}(\text{porphyrin})(\text{Ph})]$				
² B ₂	Fe-N _{por} (Å)	1.985	2.000	2.003
	Fe-Ph (Å)	1.939	1.949	1.956
⁶ A ₁	Fe-N _{por} (Å)	2.105	2.128	2.099
	Fe-Ph (Å)	2.044	2.067	2.071
$[\text{Fe}^{\text{III}}(\text{porphyrin})(\text{C}_6\text{F}_5)]$				
² B ₂	Fe-N _{por} (Å)	1.972	1.981	1.989
	Fe-C _{Ar} (Å)	1.951	1.961	1.975
⁶ A ₁	Fe-N _{por} (Å)	2.098	2.115	2.091
	Fe-C _{Ar} (Å)	2.079	2.109	2.103
$[\text{Fe}^{\text{III}}(\text{porphyrin})(3,4,5\text{-C}_6\text{F}_3\text{H}_2)]$				
² B ₂	Fe-N _{por} (Å)	1.985	1.997	2.001
	Fe-C _{Ar} (Å)	1.931	1.931	1.947
⁶ A ₁	Fe-N _{por} (Å)	2.102	2.116	2.094
	Fe-C _{Ar} (Å)	2.050	2.061	2.077
$[\text{Fe}^{\text{III}}(\text{porphyrin})(2,4,6\text{-C}_6\text{F}_3\text{H}_2)]$				
² B ₂	Fe-N _{por} (Å)	1.974	1.984	1.990
	Fe-C _{Ar} (Å)	1.947	1.958	1.967
⁶ A ₁	Fe-N _{por} (Å)	2.105	2.120	2.096
	Fe-C _{Ar} (Å)	2.066	2.094	2.089

ⁱ As representation of classic pure functionals. BLYP and BP86 results are in near-perfect mutual agreement.

ⁱⁱ As representation of newer pure functionals. OPBE results are in near-perfect mutual agreement.

ⁱⁱⁱ C_{4v} symmetry constraint.

RESULTS AND DISCUSSION

Table 3.25: Spin-state energetics (kJ.mol⁻¹) of [Fe^{III}(porphyrin)(Cl)] with the ⁶A₁ state as the energy zero level. All-electron occupancies (α/β) as well as individual d-orbital occupancies are indicated.

State	Occupation	d _{x2-y2}	d _{xz}	d _{yz}	d _{z2}	d _{xy}	PW91 ⁱ	OLYP ⁱⁱ	TPSSh	B3LYP	B3LYP*
² B ₂	A1: 34//34 A2: 18//18 B1: 25//25 B2: 25//24	2	2	1	0	0	-11	65	18	61	43
² B ₁	A1: 34//34 A2: 18//18 B1: 25//24 B2: 25//25	2	1	2	0	0	-10	65	19	63	44
² A ₁	A1: 34//33 A2: 18//18 B1: 25//25 B2: 25//25	1	2	2	0	0	34 ⁱⁱⁱ	107 ⁱⁱⁱ	72	107	89
⁴ A ₁ ^{iv}	A1: 25//24 A2: 7//7 B1: 10//10 B2: 11//11 E: 50//48	2	1	1	1	0	-36	13	-11	10	-2
⁶ A ₁ ^{iv}	A1: 25//24 A2: 7//7 B1: 10//9 B2: 12//11 E: 50//48	1	1	1	1	1	0	0	0	0	0

ⁱ As representation of classic pure functionals. BLYP, BP86 and TPSS results are in near-perfect mutual agreement.

ⁱⁱ As representation of newer pure functionals. OPBE results are in near-perfect mutual agreement.

ⁱⁱⁱ Non Aufbau.

^{iv} C_{4v} symmetry constraint.

CHAPTER 3

Table 3.26: Spin-state energetics (kJ.mol⁻¹) of [Fe^{III}(porphyrin)(Ph)] with the ⁶A₁ state as the energy zero level. All-electron occupancies (α/β) as well as individual d-orbital occupancies are indicated.

State	Occupation	d _{x2-y2}	d _{xz}	d _{yz}	d _{z2}	d _{xy}	PW91	TPSS	BLYP	BP86	OLYP	OPBE	TPSSh	B3LYP	B3LYP*
² B ₂	A1: 40//40 A2: 19//19 B1: 30//30 B2: 25//24	2	2	1	0	0	-115	-111	-103	-107	-31	-33	-64	-26	-49
² B ₁	A1: 40//40 A2: 19//19 B1: 30//29 B2: 25//25	2	1	2	0	0	-111	-107	-99	-104	-27	-31	-60	-20	-44
² A ₁	A1: 40//39 A2: 19//19 B1: 30//30 B2: 25//25	1	2	2	0	0	-85 ⁱ	-70	-69 ⁱ	-77 ⁱ	-3 ⁱ	-10 ⁱ	-24	14	-10
⁴ A ₂	A1: 41//40 A2: 19//19 B1: 30//29 B2: 25//24	2	1	1	1	0	-30 ⁱ	-29	-29 ⁱ	-26 ⁱ	23 ⁱ	27 ⁱ	-6	14	2
⁴ B ₁	A1: 40//39 A2: 20//19 B1: 30//30 B2: 25//24	1	2	1	0	1	-15	-9	-10	-12	21	22	12	24	15
⁴ B ₁	A1: 40//40 A2: 20//19 B1: 30//29 B2: 25//24	2	1	1	0	1	-5 ⁱ	-4	-2 ⁱ	-2 ⁱ	34 ⁱ	37 ⁱ	17	31	22
⁴ B ₂	A1: 41//39 A2: 19//19 B1: 30//30 B2: 25//24	1	2	1	1	0	25 ⁱ	31	30 ⁱ	30 ⁱ	78 ⁱ	78 ⁱ	59	86	71
⁴ B ₂	A1: 40//39 A2: 20//19 B1: 30//29 B2: 25//25	1	1	2	0	1	-16	-9	-10	-13	20	20	12	26	17
⁴ B ₁	A1: 41//39 A2: 19//19 B1: 30//29 B2: 25//24	1	1	2	1	0	24 ⁱ	26	29 ⁱ	28 ⁱ	76 ⁱ	75 ⁱ	59	84	69
⁶ A ₁	A1: 41//39 A2: 20//19 B1: 30//29 B2: 25//24	1	1	1	1	1	0 ⁱ	0	0 ⁱ	0 ⁱ	0	0	0	0	0

ⁱ Non Aufbau.

RESULTS AND DISCUSSION

Table 3.27: Spin-state energetics (kJ.mol⁻¹) of [Fe^{III}(porphyrin)(C₆F₅)] with the ⁶A₁ state as the energy zero level. All-electron occupancies (α/β) as well as individual d-orbital occupancies are indicated.

State	Occupation	d _{x2-y2}	d _{xz}	d _{yz}	d _{z2}	d _{xy}	PW91 ⁱ	OLYP ⁱⁱ	TPSSh	B3LYP	B3LYP*
² B ₂	A1: 48//48 A2: 21//21 B1: 37//37 B2: 28//27	2	2	1	0	0	-74	12	-34	6	-15
² B ₁	A1: 48//48 A2: 21//21 B1: 37//36 B2: 28//28	2	1	2	0	0	-63	22	-21	18	-4
² A ₁	A1: 48//47 A2: 21//21 B1: 37//37 B2: 28//28	1	2	2	0	0	-47	38	4	42	19
⁴ A ₂	A1: 49//48 A2: 21//21 B1: 37//36 B2: 28//27	2	1	1	1	0	-38	14	-13	5	-7
⁴ B ₁	A1: 48//47 A2: 22//21 B1: 37//37 B2: 28//27	1	2	1	0	1	31 ⁱⁱⁱ	67 ⁱⁱⁱ	53	66	56
⁴ B ₁	A1: 48//48 A2: 22//21 B1: 37//36 B2: 28//27	2	1	1	0	1	41 ⁱⁱⁱ	75 ⁱⁱⁱ	56	66	61
⁴ B ₂	A1: 49//47 A2: 21//21 B1: 37//37 B2: 28//27	1	2	1	1	0	13 ⁱⁱⁱ	66 ⁱⁱⁱ	45	67	53
⁴ B ₂	A1: 48//47 A2: 22//21 B1: 37//36 B2: 28//28	1	1	2	0	1	37 ⁱⁱⁱ	70 ⁱⁱⁱ	58	69	61
⁴ B ₁	A1: 49//47 A2: 21//21 B1: 37//36 B2: 28//28	1	1	2	1	0	11 ⁱⁱⁱ	65 ⁱⁱⁱ	43	67	53
⁶ A ₁	A1: 49//47 A2: 22//21 B1: 37//36 B2: 28//27	1	1	1	1	1	0	0	0	0	0

ⁱ As representation of classic pure functionals. BLYP, BP86 and TPSS results are in near-perfect mutual agreement.

ⁱⁱ As representation of newer pure functionals. OPBE results are in near-perfect mutual agreement.

ⁱⁱⁱ Non Aufbau.

CHAPTER 3

Table 3.28: Spin-state energetics (kJ.mol⁻¹) of [Fe^{III}(porphyrin)(3,4,5-C₆F₃H₂)] with the ⁶A₁ state as the energy zero level. All-electron occupancies (α/β) as well as individual d-orbital occupancies are indicated.

State	Occupation	d _{x2-y2}	d _{xz}	d _{yz}	d _{z2}	d _{xy}	PW91 ⁱ	OLYP ⁱⁱ	TPSSh	B3LYP	B3LYP*
² B ₂	A1: 45//45 A2: 20//20 B1: 34//34 B2: 27//26	2	2	1	0	0	-109	-25	-29	-24	-46
² B ₁	A1: 45//45 A2: 20//20 B1: 34//33 B2: 27//27	2	1	2	0	0	-106	-22	-25	-19	-41
² A ₁	A1: 45//44 A2: 20//20 B1: 34//34 B2: 27//27	1	2	2	0	0	-80 ⁱⁱⁱ	1 ⁱⁱⁱ	8	14	-10
⁴ A ₂	A1: 46//45 A2: 20//20 B1: 34//33 B2: 27//26	2	1	1	1	0	-35 ⁱⁱⁱ	18	23	9	-3
⁴ B ₁	A1: 45//44 A2: 21//20 B1: 34//34 B2: 27//26	1	2	1	0	1	-7	30	52	32	22
⁴ B ₁	A1: 45//45 A2: 21//20 B1: 34//33 B2: 27//26	2	1	1	0	1	4 ⁱⁱⁱ	44 ⁱⁱⁱ	59	41	32
⁴ B ₂	A1: 46//44 A2: 20//20 B1: 34//34 B2: 27//26	1	2	1	1	0	20 ⁱⁱⁱ	72 ⁱⁱⁱ	88	79	64
⁴ B ₂	A1: 45//44 A2: 21//20 B1: 34//33 B2: 27//27	1	1	2	0	1	-6	30	53	33	24
⁴ B ₁	A1: 46//44 A2: 20//20 B1: 34//33 B2: 27//27	1	1	2	1	0	18 ⁱⁱⁱ	71 ⁱⁱⁱ	84	78	62
⁶ A ₁	A1: 46//44 A2: 21//20 B1: 34//33 B2: 27//26	1	1	1	1	1	0	0	0	0	0

ⁱ As representation of classic pure functionals. BLYP, BP86 and TPSS results are in near-perfect mutual agreement.

ⁱⁱ As representation of newer pure functionals. OPBE results are in near-perfect mutual agreement.

ⁱⁱⁱ Non Aufbau.

RESULTS AND DISCUSSION

Table 3.29: Spin-state energetics (kJ.mol⁻¹) of [Fe^{III}(porphyrin)(2,4,6-C₆F₃H₂)] with the ⁶A₁ state as the energy zero level. All-electron occupancies (α/β) as well as individual d-orbital occupancies are indicated.

State	Occupation	d _{x²-y²}	d _{xz}	d _{yz}	d _{z²}	d _{xy}	PW91 ⁱ	OLYP ⁱⁱ	TPSSh	B3LYP	B3LYP*
² B ₂	A1: 45//45 A2: 20//20 B1: 34//34 B2: 27//26	2	2	1	0	0	-79	8	-44	4	-18
² B ₁	A1: 45//45 A2: 20//20 B1: 34//33 B2: 27//27	2	1	2	0	0	-65	20	-30	17	-5
² A ₁	A1: 45//44 A2: 20//20 B1: 34//34 B2: 27//27	1	2	2	0	0	-49	36 ⁱⁱⁱ	-4	42	19
⁴ A ₂	A1: 46//45 A2: 20//20 B1: 34//33 B2: 27//26	2	1	1	1	0	-34	19 ⁱⁱⁱ	-19	10	-3
⁴ B ₁	A1: 45//44 A2: 21//20 B1: 34//34 B2: 27//26	1	2	1	0	1	26	62 ⁱⁱⁱ	39	60	52
⁴ B ₁	A1: 45//45 A2: 21//20 B1: 34//33 B2: 27//26	2	1	1	0	1	35 ⁱⁱⁱ	70 ⁱⁱⁱ	44	63	58
⁴ B ₂	A1: 46//44 A2: 20//20 B1: 34//34 B2: 27//26	1	2	1	1	0	18 ⁱⁱⁱ	71 ⁱⁱⁱ	41	74	60
⁴ B ₂	A1: 45//44 A2: 21//20 B1: 34//33 B2: 27//27	1	1	2	0	1	33	67 ⁱⁱⁱ	46	67	58
⁴ B ₁	A1: 46//44 A2: 20//20 B1: 34//33 B2: 27//27	1	1	2	1	0	18 ⁱⁱⁱ	71	41	76	61
⁶ A ₁	A1: 46//44 A2: 21//20 B1: 34//33 B2: 27//26	1	1	1	1	1	0	0	0	0	0

ⁱ As representation of classic pure functionals. BLYP, BP86 and TPSS results are in near-perfect mutual agreement.

ⁱⁱ As representation of newer pure functionals. OPBE results are in near-perfect mutual agreement.

ⁱⁱⁱ Non Aufbau.

4

Experimental

4.1 Materials.

Reagents were obtained from Merck and Sigma-Aldrich. Solid reagents employed in preparations were used direct without further purification. Liquid reactants and solvents were distilled prior to use. Doubly distilled H₂O was used. Organic solvents were dried and distilled before use.

4.2 Techniques and apparatus.

4.2.1 Melting point (m.p.) determination.

Melting points (m.p.) were determined with an Olympus BX51 system microscope assembled on top of a Linkam THMS600 stage and connected to a Linkam TMS94 temperature programmer.

4.2.2 Analysis.

Elemental analysis was performed by Canadian Microanalytical Service Ltd, Canada. Mass spectroscopy was performed by Dr. Charlene Marais, University of the Free State, South Africa. Crystal determination was performed by Dr. Jan-André Gertenbach, University of Stellenbosch, South Africa.

4.2.3 Spectroscopic measurements.

NMR measurements at 298 K were recorded on a Bruker Advance II 600 NMR spectrometer [¹H (600.130 MHz)]. The chemical shifts were reported relative to SiMe₄ (0.00 ppm) for the ¹H spectra. Positive values indicate downfield shift and negative values correspond to upfield shifts. Spectral processing was done by means of TOPSPIN.¹

¹ TOPSPIN - Bruker NMR Software, Version 1.3, 2005.

MALDI-TOF-MS (matrix assisted laser desorption/ionization time-of-flight mass spectrometry) spectra were collected by a Bruker Microflex LRF20 in the negative and positive reflection mode (independently) with the minimum laser power required to observe signals.

4.2.4 Spectrophotometric measurements.

IR spectra were recorded on a Bruker Tensor 27 infrared spectrophotometer fitted with a Pike MIRacle single bounce and a diamond ATR. Both solid and liquid samples were recorded by placing a small amount of the pure material on the diamond of the ATR.

UV/vis spectra were recorded on a Varian Cary 50 Conc ultra-violet/visible spectrophotometer. CH₃CN was used as solvent for spectroelectrochemical (SEC) measurements.

Spectral processing was done with Microsoft Office Excel 2003.

4.2.5 Electrochemistry.

Cyclic voltammetric (CV) and spectroelectrochemical (SEC) measurements were done on a BAS100B Electrochemical Analyzer linked to a personal computer utilizing the BAS100W Version 2.3 software. Measurements were done at 293 K and the temperature was kept constant within 0.5 K. Successive experiments under the same experimental conditions showed that all formal reduction and oxidation potentials were reproducible within 5 mV. Data processing was done with Microsoft Office Excel 2003.

Cyclic voltammetric (CV) measurements were performed on 1 mmol.dm⁻³ solutions of the complex dissolved in CH₃CN as solvent containing 100 mmol.dm⁻³ tetrabutylammonium hexafluorophosphate (TBAPF₆, [NBu₄][PF₆]) as supporting electrolyte. Measurements were conducted under a blanket of purified Argon. A three-electrode cell, consisting of a Pt auxiliary electrode, a glassy carbon (surface area 0.0707 cm²) working electrode and a Ag/Ag⁺ (10 mmol.dm⁻³ AgNO₃ in CH₃CN) reference electrode² mounted on a Luggin capillary, was used.^{3,4} The working electrode was polished with 3 μm followed by 1 μm Diapat diamond paste

² D.T. Sawyer, J.L. Roberts Jr, *Experimental electrochemistry for chemists*, Wiley, New York, **1974**, p54.

³ D.H. Evans, K.M. O'Connell, R.A. Peterson, M.J. Kelly, *J. Chem. Educ.* **1983** (60) 290-293.

⁴ G.A. Mabbott, *J. Chem. Educ.* **1983** (60) 697-702.

on an abrasive cloth (in a figure of 8 motions), rinsed with EtOH, H₂O and CH₃CN and dried before each experiments. Scan rates were between 50 and 1000 mV.s⁻¹. All cited potentials are referenced against the Fc/Fc⁺ couple as suggested by IUPAC.⁵

Spectroelectrochemical (SEC) measurements were performed on 0.3 mmol.dm⁻³ solutions of the complex dissolved in CH₃CN as solvent containing 200 mmol.dm⁻³ tetra-n-butylammonium hexafluorophosphate as supporting electrolyte. An optically transparent thin layer electrochemical (OTTLE) Omni cell system fitted with NaCl liquid Omni windows, connected to a Cary 50 Conc ultra-violet/visible spectrophotometer, was used. The scan rate was set at 500 μV.s⁻¹. Spectra were collected every 5 minutes between 200-600 nm.

4.3 Synthesis.

4.3.1 β-diketones.

The β-diketones dithenoylmethane (Hdtm) and benzoylthenoylacetone (Hbth) were synthesized according to published methods.⁶ All other β-diketones in this study were obtained from Merck and Sigma-Aldrich.

4.3.2 Rhodium complexes.

All Rhodium complexes used in this study were synthesized according to published methods.^{7,8}

4.3.3 [Fe(β-diketonato)₃] complexes {1}-{10}.

[Fe(β-diketonato)₃] complexes {2}, {3}, {8} and {9} were prepared by the following adapted procedure:⁹

⁵ G. Gritzner, J. Kuta, *Pure Appl. Chem.* **1984** (56) 461-466.

⁶ M.M. Conradie, A.J. Muller, J. Conradie, *S. Afr. J. Chem.* **2008** (61) 13-21.

⁷ M.M. Conradie, J. Conradie, *Inorg. Chim. Acta* **2008** (361) 2285–2295.

⁸ S.S. Basson, J.G. Leipoldt, J.T. Nel, *Inorg. Chim. Acta* **1984** (84) 167-172.

EXPERIMENTAL

A metal solution of 0.15 mmol $\text{Fe}(\text{NO}_3)_3 \cdot 9\text{H}_2\text{O}$ (dissolved in 10 ml H_2O) was buffered with 0.45 mmol $\text{CH}_3\text{COONa} \cdot 3\text{H}_2\text{O}$ (dissolved in 10 ml H_2O). To this buffered metal solution, an 0.53 mmol β -diketone solution (dissolved in 10 ml EtOH) was added. The resulting solution was stirred well for 30 minutes and was left overnight in a fume hood. The precipitate was collected by filtration and washing with H_2O .

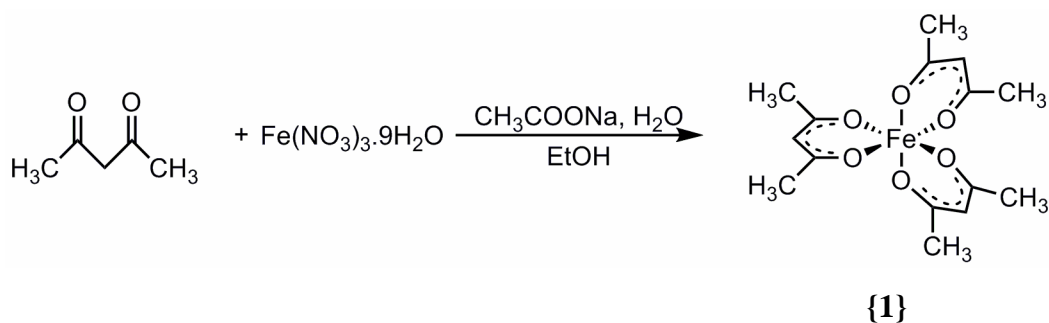
$[\text{Fe}(\beta\text{-diketonato})_3]$ complexes {1}, {6}, {7} and {10} were prepared by the following adapted procedure:⁹

A metal solution of 0.15 mmol $\text{Fe}(\text{NO}_3)_3 \cdot 9\text{H}_2\text{O}$ was buffered with 0.45 mmol $\text{CH}_3\text{COONa} \cdot 3\text{H}_2\text{O}$ (dissolved in minimal H_2O). To this, EtOH was added to make a 1:1 H_2O :EtOH solution. With the aid of a syringe, liquid 0.53 mmol β -diketone was added. The resulting solution was stirred well (with a lid on) for 30 minutes and was left overnight in a fume hood (without lid). The precipitate was collected by filtration and washing with H_2O .

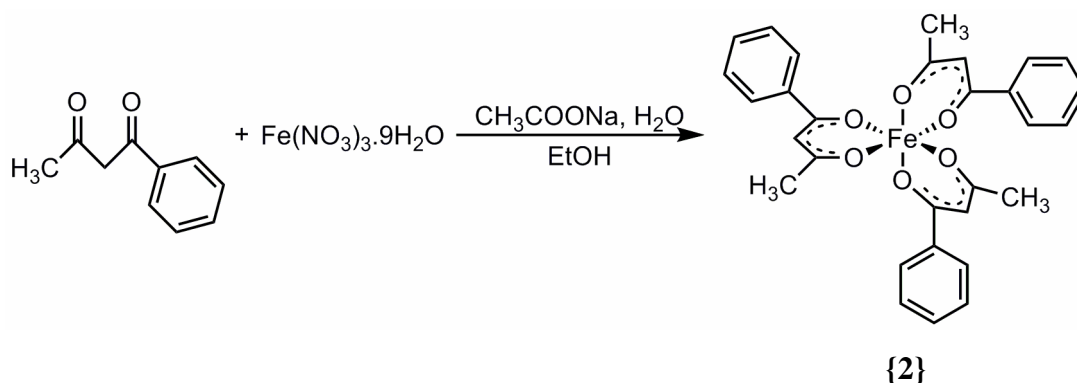
$[\text{Fe}(\beta\text{-diketonato})_3]$ complexes {4} and {5} were prepared by the following adapted procedure:⁹

A metal solution of 0.15 mmol $\text{Fe}(\text{NO}_3)_3 \cdot 9\text{H}_2\text{O}$ was buffered with 0.45 mmol $\text{CH}_3\text{COONa} \cdot 3\text{H}_2\text{O}$ (dissolved in minimal H_2O). To this, EtOH was added to make a 1:1 H_2O :EtOH solution. An 0.53 mmol β -diketone solution (dissolved in 10 ml DCM) was added to the above. The resulting solution was stirred well for 30 minutes and was left overnight in a fume hood. The precipitate was collected by filtration and washing with H_2O .

⁹ (a) E.W. Berg, J.T. Truemper, *J. Phys. Chem.* **1960** (64) 487-490 (b) K. Endo, M. Furukawa, H. Yamatera, H Sano, *Bull. Chem. Soc. Jpn* **1980** (53) 407-410 (c) G.S. Hammond, D.C. Nonhebel, C.S. Wu, *Inorg. Chem.* **1963** (2) 73-76.

4.3.3.1 Tris(acetylacetonato- $\kappa^2\text{O},\text{O}'$)iron(III) [$\text{Fe}(\text{acac})_3$] {1}.

Yield 73%. Colour: red. M.p. 180.0-182.0 °C (reported: 179 °C,¹⁰ 180 °C¹¹). UV: λ_{max} 270 nm, ϵ_{max} 25842 mol⁻¹.dm³.cm⁻¹ (CH₃CN). MS Calcd. ([M]⁺, positive mode): m/z 352.2. Found: m/z 351.9. Anal. Calcd. for FeC₁₅H₂₁O₆: C, 51.01; H, 5.99. Found: C, 50.42; H, 5.91.

4.3.3.2 Tris(benzoylacetonato- $\kappa^2\text{O},\text{O}'$)iron(III) [$\text{Fe}(\text{ba})_3$] {2}.

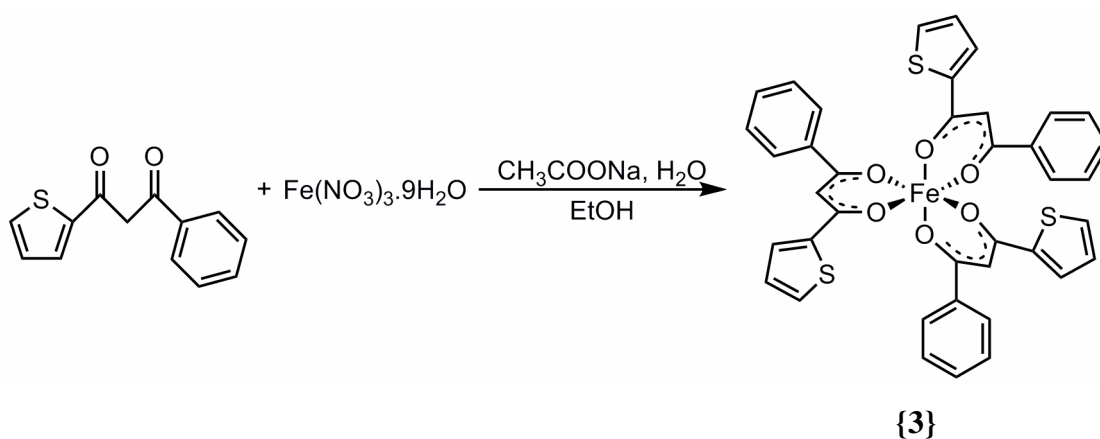
Yield 84%. Colour: red-orange. M.p. 218.5-220.3 °C (reported: 222-224 °C¹⁰). UV: λ_{max} 298 nm, ϵ_{max} 40256 mol⁻¹.dm³.cm⁻¹ (CH₃CN). MS Calcd. ([M]⁺, positive mode): m/z 539.4. Found: m/z 539.1. Anal. Calcd. for FeC₃₀H₂₇O₆: C, 66.80; H, 5.05. Found: C, 66.46; H, 5.10.

¹⁰ E.W. Berg, J.T. Truemper, *J. Phys. Chem.* **1960** (64) 487-490.

¹¹ M.-L. Hu, Z.-M. Jin, Q. Miao, L.-P. Fang, *Z. Kristallogr. - New Cryst. Struct.* **2001** (216) 597-598.

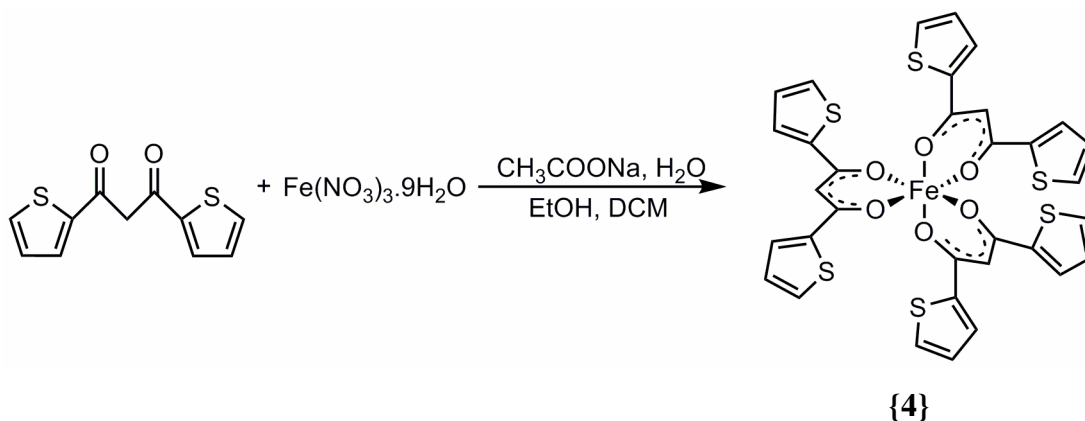
EXPERIMENTAL

4.3.3.3 Tris(benzoylthienylacetonato- $\kappa^2\text{O},\text{O}'$)iron(III) [Fe(bth)₃] {3}.

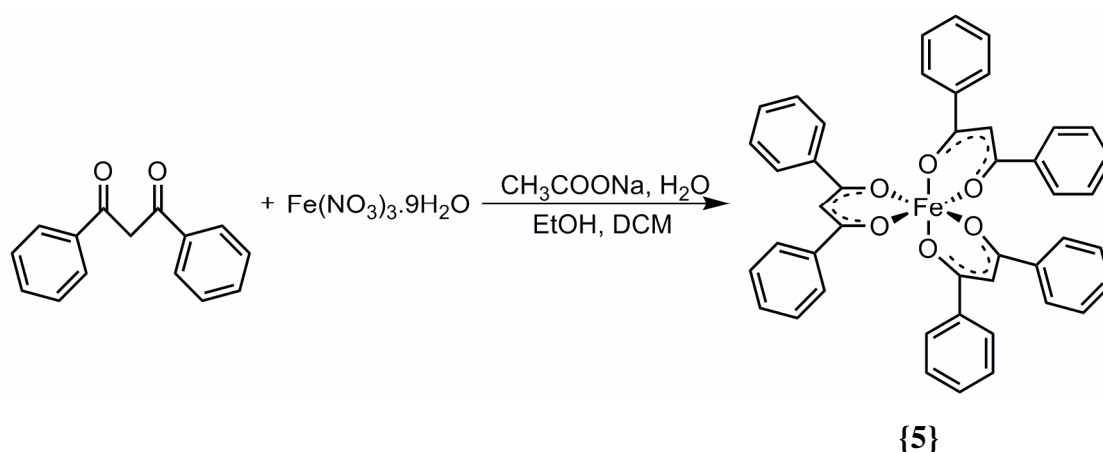


Yield 85%. Colour: red-brown. M.p. 220.0-222.0 °C. UV: λ_{max} 361 nm, ϵ_{max} 30956 mol⁻¹.dm³.cm⁻¹ (CH₃CN). MS Calcd. ([M], positive mode): m/z 743.7. Found: m/z 743.2. Anal. Calcd. for FeC₃₉H₂₇S₃O₆: C, 62.99; H, 3.66. Found: C, 61.44; H, 3.71.

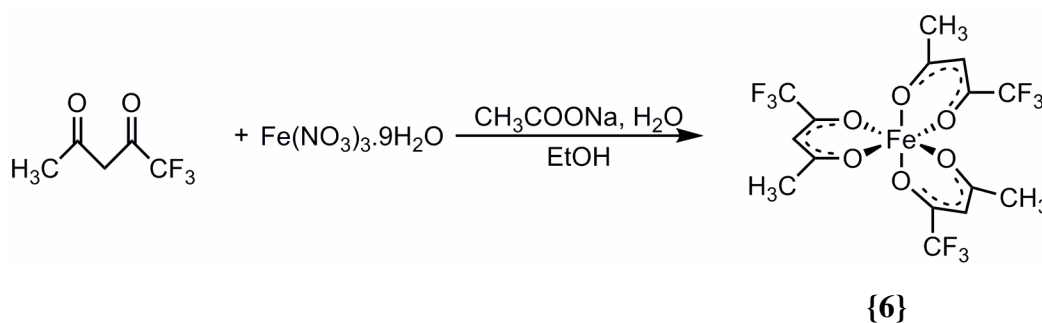
4.3.3.4 Tris(dithenoylmethanato- $\kappa^2\text{O},\text{O}'$)iron(III) [Fe(dtm)₃] {4}.



Yield 39%. Colour: black. M.p. 63.7-66.4 °C. UV: λ_{max} 260 nm, ϵ_{max} 35301 mol⁻¹.dm³.cm⁻¹ (CH₃CN). This complex could not be ionized for an MS analysis. Anal. Calcd. for FeC₃₃H₂₁S₆O₆: C, 52.03; H, 2.78. Found: C, 51.27; H, 2.71.

4.3.3.5 Tris(dibenzoylmethanato- $\kappa^2\text{O},\text{O}'$)iron(III) [$\text{Fe}(\text{dbm})_3$] {5}.

Yield 71%. Colour: dark red. M.p. 264.0-265.2 °C (reported: 261 °C,¹² 257 °C¹³). UV: λ_{max} 336 nm, ϵ_{max} 48608 mol⁻¹.dm³.cm⁻¹ (CH₃CN). MS Calcd. ([M], positive mode): m/z 725.6. Found: m/z 725.3. Anal. Calcd. for FeC₄₅H₃₃O₆: C, 74.49; H, 4.58. Found: C, 75.29; H, 4.51.

4.3.3.6 Tris(trifluoroacetylacetonato- $\kappa^2\text{O},\text{O}'$)iron(III) [$\text{Fe}(\text{tfaa})_3$] {6}.

Yield 91%. Colour: red-brown. M.p. 113.5-116.1 °C (reported: 115 °C^{10,14}). UV: λ_{max} 271 nm, ϵ_{max} 48996 mol⁻¹.dm³.cm⁻¹ (CH₃CN). MS Calcd. ([M]⁻, negative mode): m/z 514.1. Found: m/z 513.5. Anal. Calcd. for FeC₁₅H₁₂O₆F₉: C, 34.98; H, 2.35. Found: C, 34.48; H, 2.30.

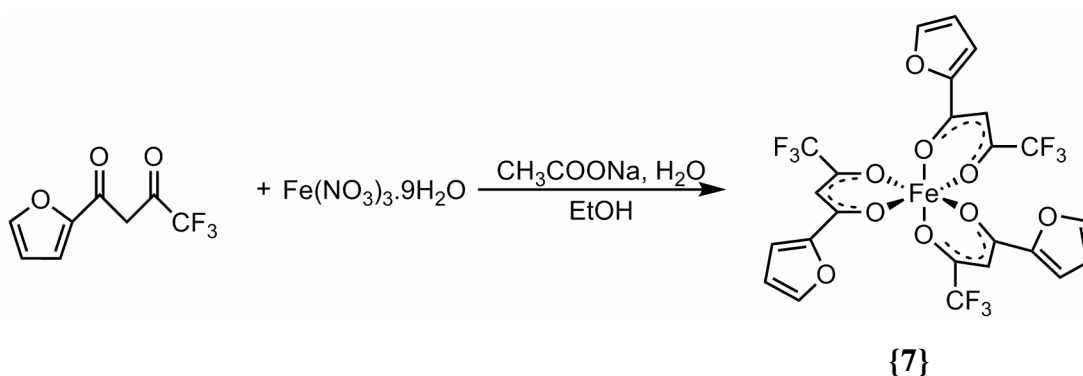
¹² B. Kaitner, B. Kamenar, *Cryst. Struct. Commun.* **1980** (9) 487-492.

¹³ I.A. Baidina, P.A. Stabnikov, I.K. Igumenov, S.V. Borisov, *Koord. Khim. (Russ.) (Coord. Chem.)* **1986** (12) 258-265.

¹⁴ I.A. Baidina, P.A. Stabnikov, I.K. Igumenov, S.V. Borisov, *Koord. Khim. (Russ.) (Coord. Chem.)* **1986** (12) 404-408.

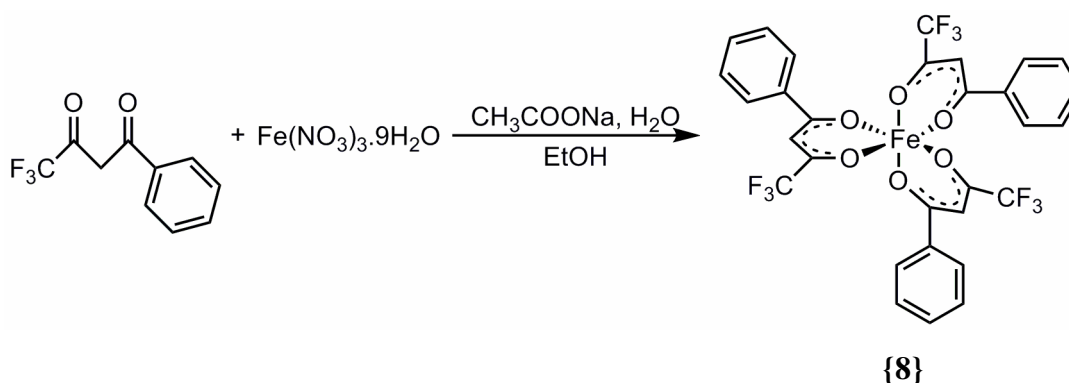
EXPERIMENTAL

4.3.3.7 Tris(trifluorofuroylacetonato- $\kappa^2\text{O},\text{O}'$)iron(III) [$\text{Fe}(\text{tffu})_3$] {7}.

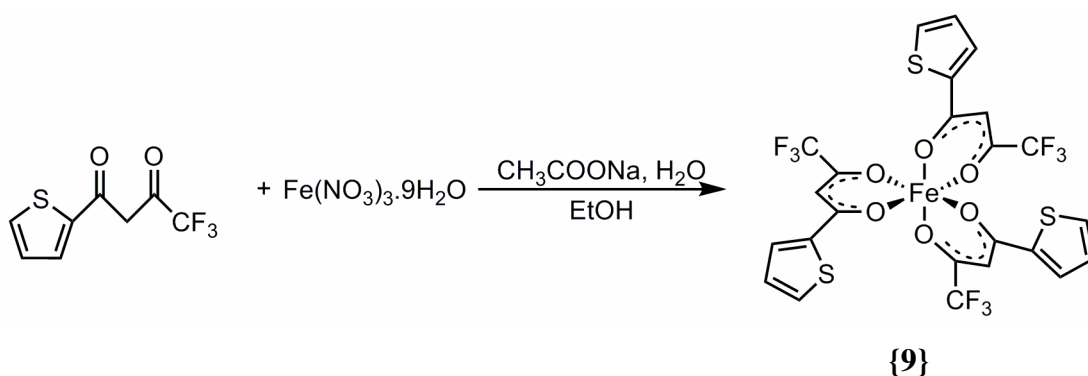


Yield 92%. Colour: dark red. M.p. 205.0-208.0 °C (reported: 201-208 °C¹⁰). UV: λ_{max} 333 nm, ϵ_{max} 53476 mol⁻¹.dm³.cm⁻¹ (CH₃CN). MS Calcd. ([M], positive mode): m/z 671.2. Found: m/z 671.1. Anal. Calcd. for FeC₂₄H₁₂O₉F₉: C, 42.95; H, 1.80. Found: C, 42.91; H, 1.83.

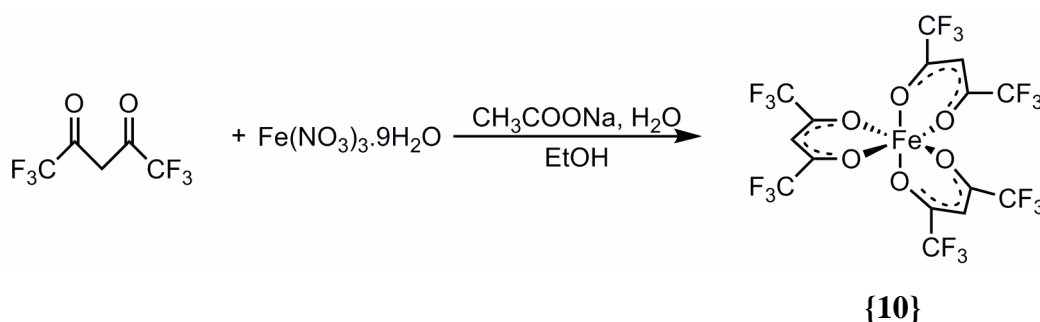
4.3.3.8 Tris(trifluorobenzoylacetonato- $\kappa^2\text{O},\text{O}'$)iron(III) [$\text{Fe}(\text{tfba})_3$] {8}.



Yield 96%. Colour: orange. M.p. 58.4-60.1 °C (reported: 128-129 °C¹⁰). UV: λ_{max} 304 nm, ϵ_{max} 30788 mol⁻¹.dm³.cm⁻¹ (CH₃CN). MS Calcd. ([M], negative mode): m/z 701.3. Found: m/z 701.1. Anal. Calcd. for FeC₃₀H₁₈O₆F₉: C, 51.38; H, 2.59. Found: C, 50.66; H, 2.53.

4.3.3.9 Tris(thenoyltrifluoroacetato- $\kappa^2\text{O},\text{O}'$)iron(III) [Fe(tta)₃] {9}.

Yield 78%. Colour: dark red. M.p. 158.0-161.0 °C (reported: 159-160 °C,¹⁰ 162.5 °C¹⁵). UV: λ_{max} 333 nm, ϵ_{max} 48461 mol⁻¹.dm³.cm⁻¹ (CH₃CN). MS Calcd. ([M], negative mode): m/z 719.4. Found: m/z 718.9. Anal. Calcd. for FeC₂₄H₁₂S₃O₆F₉: C, 40.07; H, 1.68. Found: C, 39.51; H, 1.70.

4.3.3.10 Tris(hexafluoroacetylacetonato- $\kappa^2\text{O},\text{O}'$)iron(III) [Fe(hfaa)₃] {10}.

Yield 51%. Colour: light orange. M.p. 56.0-58.0 °C (reported: 55 °C¹⁶). MS Calcd. ([M], negative mode): m/z 677.0. Found: m/z 676.8. Anal. Calcd. for FeC₁₅H₃O₆F₁₈: C, 26.61; H, 0.45. Found: C, 26.17; H, 0.51.

¹⁵ H. Soling, *Acta Chem. Scand. A* **1976** (30) 163-170.

¹⁶ C.E. Pfluger, P.S. Haradem, *Inorg. Chim. Acta* **1983** (69) 141-146.

4.4 Crystallography.

4.4.1 Structure determination of [Rh(bth)(CO)₂].

Crystals of [Rh(bth)(CO)₂] (Hbth = benzoylthenoylacetone) were obtained by recrystallization from acetone and water. The red crystal was mounted on a glass fibre and used for the X-ray crystallographic analysis. The X-ray intensity data were measured on a Bruker X8 Apex II 4K Kappa CCD diffractometer area detector system equipped with a graphite monochromator and a Mo K_α fine-focus sealed tube ($\lambda = 0.71073 \text{ \AA}$) operated at 1.5 kW power (50 kV, 30 mA). The detector was placed at a distance of 3.75 cm from the crystal. The crystal temperature during the data collection was kept constant at 100(2) K using an Oxford 700 series cryostream cooler.

The initial unit cell and data collection was achieved by the Apex2 software¹⁷ utilizing COSMO¹⁸ for optimum collection of more than a hemisphere of reciprocal space. A total of 1778 frames were collected with a scan width of 0.5° in ϕ and ω and an exposure time of 40 s.frame⁻¹. The frames were integrated using a narrow-frame integration algorithm and reduced with the Bruker SAINT-Plus¹⁹ and XPREP¹⁹ software packages respectively. The integration of the data using a monoclinic cell yielded a total of 25770 reflections to a maximum θ angle of 28.5°, of which 3596 were independent with a $R_{\text{int}} = 0.1523$. Analysis of the data showed no significant decay during the data collection. Data were corrected for absorption effects using the multi-scan technique SADABS²⁰ with minimum and maximum transmission coefficients of 0.620 and 0.937 respectively.

The structure was solved by the direct methods package SHELXS²¹ and refined using the X-Seed software package²² incorporating SHELXL.²¹ The final anisotropic full-matrix least-squares refinement on F^2 with 235 variables converged at $R1 = 0.0842$ for the observed data and $wR2 = 0.1948$ for all data. The GOF was 1.002. The largest peak on the final difference electron

¹⁷ Apex2., Bruker AXS Inc., Madison, Wisconsin, USA, Version 1.0-27, **2005**.

¹⁸ COSMO, Bruker AXS Inc., Madison, Wisconsin, USA, Version 1.48, **2003**.

¹⁹ SAINT-Plus, Bruker AXS Inc., Madison, Wisconsin, USA, Version 7.68a (including XPREP), **2009**.

²⁰ SADABS, Bruker AXS Inc., Madison, Wisconsin, USA, Version 2008/1, **2009**.

²¹ G.M. Sheldrick, *Acta Cryst.* **2008** (A64) 112-122.

²² J.L. Atwood, L.J. Barbour, *Cryst. Growth Des.* **2003** (3) 3-8.

density synthesis was $3.11 \text{ e.}\text{\AA}^{-3}$ at 0.5 \AA from Rh1 and the deepest hole $-1.621.576 \text{ e.}\text{\AA}^{-3}$ at 0.77 \AA from Rh1.

The aromatic H atoms were placed in geometrically idealized positions ($\text{C-H} = 0.95 \text{ \AA}$) and constrained to ride on their parent atoms with $U_{\text{iso}}(\text{H}) = 1.2U_{\text{eq}}(\text{C})$. Non-hydrogen atoms were refined with anisotropic displacement parameters. Atomic scattering factors were taken from the International Tables for Crystallography Volume C.²³ The molecular plot was drawn using the X-Seed programme.²²

4.5 Computational.

4.5.1 Resources.

4.5.1.1 Computational Facilities.²⁴

The Norwegian Metacenter for Computational Science (Notur) project provides the national infrastructure for computational science in Norway. The project provides computational resources and services to individuals or groups involved in education and research at Norwegian universities and colleges, operational forecasting and research at the Meteorological Institute and to institutes and industries that collaborate with the project. The university partners of the Notur consortium operate a number of High Performance Computing (HPC) facilities. Some characteristics of all the available facilities are given in Table 4.1.

Each of the facilities consists of a computer resource (a number of compute nodes each with a number of processors and internal shared-memory, plus an interconnect that connects the nodes), a central storage resource that is accessible to all the nodes, and a secondary storage resource for back-up (and in few cases also for archiving). All facilities use variants of the UNIX operating system (Linux, AIX, etc.).

²³ *International Tables for Crystallography*, Kluwer Academic Publishers, Dordrecht, The Netherlands, Vol. C, p1002.

²⁴ www.notur.no.

EXPERIMENTAL

Table 4.1: Some characteristics of all the available facilities at the Notur consortium.

	System	Type	No. of Nodes	No. of cores	CPU type	Theoretical total peak	Total memory	Total disk capacity
Hexagon	Cray XT4	MPP ⁱ	1388	2 776	Opteron	12214 Gflop	6064 GB	288 TB
Njord	IBM p575+	distributed SMP	62	992	Power5+	7500 Gflop	1984 GB	70 TB
Stallo	HP BL 460c	cluster	704	5 632	Xeon 2	60 000 Gflop	12 064 GB	128 TB
Titan	Dell 1425	cluster	180	360	Xeon	2304 Gflop	720 GB	28 TB + 12 TB GPFS
	Sun X2200		448	1872	Opteron	9539 Gflop	7620 GB	336 TB + 120 TB GPFS

ⁱ MPP = Massively Parallel Processor.

For the research of the projects in this thesis, the facility Stallo was used. This was made possible through collaboration between Prof. J. Conradie at the University of the Free State (UFS)²⁵ and the Centre for Theoretical and Computational Chemistry (CTCC).²⁶ The key numbers of the facility Stallo are given in Table 4.2.

Table 4.2: Key numbers about the facility Stallo, a Linux cluster.

	Aggregated	Per node
Peak performance	60 Teraflop/s	85.12 Gigaflop/s
No. of Nodes	704 x HP BL460c blade servers	1 x HP BL460c blade server
No. of CPUs / No. of Cores	1408 / 5632	2 / 8
Processors	1408 x 2.66 GHz Intel Xeon X5355 Quad Core	2 x 2.66 GHz Intel Xeon X5355 Quad Core
Total memory	12 TB	16 GB (50 nodes with 32 GB)
Internal storage	84.5 TB	120 GB
Centralized storage	128 TB	128 TB
Interconnect	Gigabit Ethernet + Infiniband ⁱ	Gigabit Ethernet + Infiniband ⁱ
Compute racks	11	
Infrastructure racks	2	
Storage racks	4	
Dimensions (w x d x h)	15 m x 1.3 m x 2 m	
Weight	16 tons	

ⁱ All nodes in the cluster are connected with Gigabit Ethernet and 384 nodes are also connected with Infiniband.

4.5.1.2 Scaling of ADF 2007.²⁷

Geometry optimization calculations were performed on a caffeine molecule (24 atoms, closed shell, BP86/DZP) and a ring-substituted iron-porphyrin with axial ligands (125 atoms, open shell, D_{2d} symmetry, PW91/TZP) with the ADF 2007 programme on Stallo. Tests were made on 1, 2, 4, 8, 16, 24, 30, 40, 60, 80 and 100 processors and repeated twice.

²⁵ www.ufs.ac.za.

²⁶ www.ctcc.no.

²⁷ Performed by Dr. Espen Tangen, University of Trømsø, Trømsø, Norway, 2008.

CHAPTER 4

In general, ADF 2007 appears to be very stable, though somewhat memory-demanding. Energies varied slightly, but showed satisfactory reliability when running on 40 processors or less. In the initial tests, default values for the convergence criteria and the numerical integration were used. This proved to be a rather poor test for ADF 2007, since the results were unreliable. It is therefore recommended to use a tighter convergence geometry criterion, in other words a tighter SCF convergence and a higher integration accuracy. A general rule of thumb: by increasing the default integration by one, one should also decrease both the grad in the geometry cycle and the SCF convergence by an order of magnitude. The default value for the SCF iterations (50) was also found to be too low for jobs to work realistically. It is therefore recommended to use a value of at least 200 as a standard number and it can be increased up to 3000.

Results are summarized in Table 4.3 and Table 4.4. The speed-up is calculated by dividing the real-time for the job on one processor by the real-time for the job on the given amount of processors. Therefore, the higher the value for speed-up, the better. The scale factor is the reported real time, multiplied by the number of processors and then divided by the reported real-time for the job on one processor. This number should ideally be as close to 1 as possible. Time-Save is the time-difference between the reported real-time and the shortest time reported.

Table 4.3: Scaling results of the small molecule (caffeine, 24 atoms). Best performance is indicated in bold.

No. of processors	Real	Speed-up	Scale-factor	Time-Save
1	0:49:45	1.00	1.00	0:23:59
2	0:40:57	1.21	1.65	0:15:11
4	0:25:46	1.93	2.07	0:00:00
8	0:32:43	1.52	5.26	0:06:57
16	0:46:04	1.08	14.82	0:20:18
24	0:53:30	0.93	25.81	0:27:44
30	0:57:28	0.87	34.66	0:31:42
40	1:02:11	0.80	50.00	0:36:25
60	1:15:14	0.66	90.73	0:49:28
80	1:17:34	0.64	124.73	0:51:48
100	1:22:25	0.60	165.66	0:56:39

EXPERIMENTAL

Table 4.4: Scaling results of the large molecule (iron-porphyrin, 125 atoms). Best performance is indicated in bold.

No. of processors	Real	Speed-up	Scale-factor	Time-Save
1	23:28:51	1.00	1.00	20:11:57
2	10:41:01	2.20	0.91	7:24:07
4	8:15:08	2.85	1.41	4:58:14
8	5:17:12	4.44	1.80	2:00:18
16	3:38:51	6.44	2.49	0:21:57
24	3:25:40	6.85	3.50	0:08:46
30	3:37:15	6.48	4.63	0:20:21
40	3:21:25	6.99	5.72	0:04:31
60	4:57:38	4.73	12.68	1:40:44
80	4:24:42	5.32	15.03	1:07:48
100	3:16:54	7.16	13.98	0:00:00

From the above results, it is recommended to use 4 to 8 processors (1/2 to 1 node) for small jobs and 40 processors (5 nodes) for large jobs. Exceeding these recommended amounts of processors only increase the wall time consumption.

4.5.2 Rhodium complexes.

4.5.2.1 [Rh(β -diketonato)(CO)(PPh₃)] and [Rh(acac)(P(OR)₃)₂].

DFT calculations were carried out on [Rh(β -diketonato)(CO)(PPh₃)] (β -diketone = Hacac, Htta, Hbth or Hdtm) and [Rh(acac)(P(OR)₃)₂] complexes using the ADF (Amsterdam Density Functional) 2007 programme²⁸ with the GGA (Generalized Gradient Approximation) functional PW91.²⁹ The TZP (Triple ζ polarized) basis set, with a fine mesh for numerical integration, a spin-restricted formalism and a full geometry optimization with tight convergence criteria, was used for minimum energy and transition state (TS) searches. Approximate structures of the TS have been determined with linear transit (LT) scans, with a constraint optimization along a chosen reaction coordinate, to sketch an approximate path over the TS between reactants and products. Throughout, all calculations have been performed with no symmetry constraint (C_1) and all structures have been calculated as singlet states.

²⁸ G. Te Velde, F.M Bickelhaupt, E.J. Baerends, C.F. Guerra, S.J.A. Van Gisbergen, J.G. Snijders, T. Ziegler, *J. Comput. Chem.* **2001** (22) 931-967.

²⁹ J.P. Perdew, J.A. Chevary, S.H. Vosko, K.A. Jackson, M.R. Pederson, D.J. Singh, C. Fiolhais, *Phys. Rev. B* **1992** (46) 6671-6687. Erratum: J.P. Perdew, J.A. Chevary, S.H. Vosko, K.A. Jackson, M.R. Pederson, D.J. Singh, C. Fiolhais, *Phys. Rev. B* **1993** (48) 4978.

Numerical frequency analyses,^{30,31} where the frequencies are computed numerically by differentiation of energy gradients in slightly displaced geometries, have been performed to verify the TS geometries. A TS has one imaginary frequency.

Zero point energy and thermal corrections (vibrational, rotational and translational) were made in the calculation of the thermodynamic parameters. The enthalpy (H) and Gibbs free energy (G) were calculated from

$$U = E_{\text{TBE}} + E_{\text{ZPE}} + E_{\text{IE}} \quad \text{(Equation 4.1)}$$

$$H = U + RT \text{ (gas phase) or } H = U \text{ (solution)} \quad \text{(Equation 4.2)}$$

$$G = H - TS \quad \text{(Equation 4.3)}$$

where U is the total energy, E_{TBE} is total bonding energy, E_{ZPE} is zero point energy, E_{IE} is internal energy, R is the gas constant, T is temperature and S is entropy. The entropy (S) was calculated from the temperature dependent partition function in ADF at 298.15 K. The computed results assume an ideal gas.

Solvent effects were taken into account for all optimized structures reported here. The COSMO (Conductor like Screening Model) model of solvation^{32,33,34} was used as implemented in ADF.³⁵ The COSMO model is a dielectric model in which the solute molecule is embedded in a molecule-shaped cavity surrounded by a dielectric medium with a given dielectric constant (ϵ_0). The type of cavity used is Esurf³⁶ and the solvent used is methanol ($\epsilon_0 = 32.6$) and chloroform ($\epsilon_0 = 4.8$). Where applicable, scalar relativistic effects were used with the ZORA^{37,38,39,40,41} (Zero Order Regular Approximation) formalism.

³⁰ L. Fan, T. Ziegler, *J. Chem. Phys.* **1992** (96) 9005-9012.

³¹ L. Fan, T. Ziegler, *J. Amer. Chem. Soc.* **1992** (114) 10890-10897.

³² A. Klamt, G. Schüürmann, *J. Chem. Soc., Perkin Trans. 2* **1993** 799-805.

³³ A. Klamt, *J. Phys. Chem.* **1995** (99) 2224-2235.

³⁴ A. Klamt, V. Jones, *J. Chem. Phys.* **1996** (105) 9972-9981.

³⁵ C.C. Pye, T. Ziegler, *Theor. Chem. Acc.* **1999** (101) 396-408.

³⁶ J.L. Pascual-Ahuir, E. Silla, I. Tuñon, *J. Comput. Chem.* **1994** (15) 1127-1138.

³⁷ E. van Lenthe, A.E. Ehlers, E.J. Baerends, *J. Chem. Phys.* **1999** (110) 8943-8953.

³⁸ E. van Lenthe, E.J. Baerends, J.G. Snijders, *J. Chem. Phys.* **1993** (99) 4597-4610.

³⁹ E. van Lenthe, E.J. Baerends, J.G. Snijders, *J. Chem. Phys.* **1994** (101) 9783-9792.

⁴⁰ E. van Lenthe, J.G. Snijders, E.J. Baerends, *J. Chem. Phys.* **1996** (105) 6505-6516.

⁴¹ E. van Lenthe, R. van Leeuwen, E.J. Baerends, J.G. Snijders, *Int. J. Quantum Chem.* **1996** (57) 281-293.

The accuracy of the computational approach was evaluated by comparing the root-mean-square distances (RMSDs) as calculated by the "RMS Compare Structures" utility in ChemCraft.⁴² The RMSD values were calculated for the best three-dimensional superposition of optimized molecular structures on experimental crystal structures, using only the non-hydrogen atoms and the non-rotational groups of the molecule.

4.5.3 Iron complexes.

4.5.3.1 [Fe(β -diketonato)₃].

DFT calculations were carried out on [Fe(β -diketonato)₃] (β -diketone = Hacac, Hba, Hdtm, Hbth, Hdbm, Htfaa, Htffu, Htfba, Htta or Hhfaa) complexes using the ADF 2007 programme²⁸ with the GGA functional OLYP.^{43,44} The TZP basis set, with a fine mesh for numerical integration and a full geometry optimization with tight convergence criteria, was used. Initial calculations on [Fe(acac)₃] were performed with a D_3 symmetry constraint and a selection of spin states ($S = 1/2$, $3/2$ and $5/2$). Final calculations on all [Fe(β -diketonato)₃] and [Fe(β -diketonato)₃]⁻ complexes have been performed with a D_3 (complexes with symmetrical β -diketone ligand), C_3 (complexes with unsymmetrical β -diketone ligand, arranged in such a way that they have a 3-fold rotational axis) or C_1 (complexes with unsymmetrical β -diketone ligand, arranged in such a way that they have no symmetry operation) symmetry constraint. Both [Fe(β -diketonato)₃] ($S = 5/2$) and [Fe(β -diketonato)₃]⁻¹ ($S = 2$) complexes were calculated, with the expected spin states in parentheses.

⁴² G.A. Zhurko, D.A. Zhurko, *CHEMCRAFT*, Version 1.6 (Build 304), **2009**.

⁴³ N.C. Handy, A.J. Cohen, *Mol. Phys.* **2001** (99) 403-412.

⁴⁴ (a) C. Lee, W. Yang, R.G. Parr, *Phys. Rev. B* **1988** (37) 785-789. (b) B.G. Johnson, P.M.W. Gill, J.A. Pople, *J. Chem. Phys.* **1993** (98) 5612-5626. (c) T.V. Russo, R.L. Martin, P.J. Hay, *J. Chem. Phys.* **1994** (101) 7729-7737.

4.5.3.2 [Fe(salen)(CH₃)₂(COCH₃)₂(py)₂].

DFT calculations were carried out on two different conformations of the Fe(salen)(CH₃)₂(COCH₃)₂(py)₂ complex using the ADF 2007 programme²⁸ with a selection of GGA functionals, namely PW91,²⁹ BLYP,^{44,45} BP86,^{45,46} PBE,⁴⁷ OLYP^{43,44} and OPBE.^{43,48} The TZP basis set, with a fine mesh for numerical integration and a full geometry optimization with tight convergence criteria, was used. DFT and hybrid DFT calculations were also carried out using the Gaussian 03 programme⁴⁹. These calculations were performed with tight convergence criteria using the PW91²⁹ and B3LYP⁵⁰ functionals and the 6-311G**⁵¹ basis set. Subsequently, single-point OLYP,^{43,44} B3LYP⁵⁰ and B3LYP*⁵² calculations were performed on the PW91²⁹ geometries with the ADF 2007 programme²⁸ using the TZP basis set and alternative occupations. Throughout, all ADF calculations have been performed with a C_{2v} symmetry constraint and both conformations have been calculated as singlet, triplet and quintet states for a variety of low-energy *d*-electron configurations, which were manually worked out. The *xy* symmetry plane

⁴⁵ A.D. Becke, *Phys. Rev.* **1988** (A38) 3098-3100.

⁴⁶ J.P. Perdew, *Phys. Rev.* **1986** (B33) 8822-8824; Erratum: J.P. Perdew, *Phys. Rev.* **1986** (B34) 7406.

⁴⁷ J.P. Perdew, K. Burke, M. Ernzerhof, *Phys. Rev. Lett.* **1996** (77) 3865-3868; Erratum: J.P. Perdew, K. Burke, M. Ernzerhof, *Phys. Rev. Lett.* **1997** (78) 1396.

⁴⁸ M. Swart, A.W. Ehlers, K. Lammertsma, *Mol. Phys.* **2004** (102) 2467-2474.

⁴⁹ Gaussian 03, Revision C.02, M.J. Frisch, G.W. Trucks, H.B. Schlegel, G.E. Scuseria, M.A. Robb, J.R. Cheeseman, J.A. Montgomery Jr., T. Vreven, K.N. Kudin, J.C. Burant, J.M. Millam, S.S. Iyengar, J. Tomasi, V. Barone, B. Mennucci, M. Cossi, G. Scalmani, N. Rega, G.A. Petersson, H. Nakatsuji, M. Hada, M. Ehara, K. Toyota, R. Fukuda, J. Hasegawa, M. Ishida, T. Nakajima, Y. Honda, O. Kitao, H. Nakai, M. Klene, X. Li, J.E. Knox, H.P. Hratchian, J.B. Cross, V. Bakken, C. Adamo, J. Jaramillo, R. Gomperts, R.E. Stratmann, O. Yazyev, A.J. Austin, R. Cammi, C. Pomelli, J.W. Ochterski, P.Y. Ayala, K. Morokuma, G.A. Voth, P. Salvador, J.J. Dannenberg, V.G. Zakrzewski, S. Dapprich, A.D. Daniels, M.C. Strain, O. Farkas, D.K. Malick, A.D. Rabuck, K. Raghavachari, J.B. Foresman, J.V. Ortiz, Q. Cui, A.G. Baboul, S. Clifford, J. Cioslowski, B.B. Stefanov, G. Liu, A. Liashenko, P. Piskorz, I. Komaromi, R.L. Martin, D.J. Fox, T. Keith, M.A. Al-Laham, C. Peng, A. Nanayakkara, M. Challacombe, P.M.W. Gill, B. Johnson, W. Chen, M.W. Wong, C. Gonzalez, J.A. Pople, Gaussian, Inc., Wallingford CT, **2004**.

⁵⁰ P.J. Stephens, F.J. Devlin, C.F. Chabalowski, M.J. Frisch, *J. Phys. Chem.* **1994** (98) 11623-11627.

⁵¹ (a) R.C. Binning Jr., L.A. Curtiss, *J. Comp. Chem.* **1990** (11) 1206-1216. (b) L.A. Curtiss, M.P. McGrath, J.-P. Blaudeau, N.E. Davis, R.C. Binning Jr., L. Radom, *J. Chem. Phys.* **1995** (103) 6104-6113. (c) M.P. McGrath, L. Radom, *J. Chem. Phys.* **1991** (94) 511-516.

⁵² M. Reiher, O. Salomon, B.A. Hess, *Theor. Chem. Acc.* **2001** (107) 48-55.

is defined to be in the plane of the salen ligand with the y -axis as the 2-fold rotational axis. The z -axis is defined to point upwards towards the pyridine ligand.

4.5.3.3 [Fe(porphyrin)(Ar)].

DFT calculations were carried out on [Fe(porphyrin)(Ar)] complexes (Ar = aryl = Cl, Ph, C₆F₅, 3,4,5-C₆F₃H₂ and 2,4,6-C₆F₃H₂) using the ADF 2007 programme²⁸ with a selection of GGA, meta-GGA and meta-hybrid functionals, namely PW91,²⁹ BLYP,^{44,45} BP86,^{45,46} OLYP,^{43,44} OPBE,^{43,48} TPSS⁵³ and TPSSh.⁵³ Subsequently, single-point B3LYP⁵⁰ and B3LYP*⁵² hybrid calculations were performed on the OLYP^{43,44} geometries. The TZP basis set, with a fine mesh for numerical integration and a full geometry optimization with tight convergence criteria, was used. Hybrid DFT calculations were also carried out using the Gaussian 03 programme⁴⁹. These calculations were performed with tight convergence criteria using the B3LYP⁵⁰ functional and the 6-311G**⁵¹ basis set. Throughout, all ADF calculations have been performed with a C_{2v} symmetry constraint (unless else indicated) and all structures have been calculated as doublet, quartet and sextet states for a variety of low-energy d -electron configurations, which were manually worked out.

⁵³ (a) J. Tao, J.P. Perdew, V.N. Staroverov and G.E. Scuseria, *Phys. Rev. Lett.* **2003** (91) 146401-146404. (b) V.N. Staroverov, G.E. Scuseria, J. Tao and J.P. Perdew, *J. Chem. Phys.* **2003** (119) 12129-12137.

5 Concluding remarks and future perspectives

5.1 Concluding remarks.

Rhodium complexes.

The oxidative addition reaction of methyl iodide to square planar rhodium(I) complexes has been studied. Two types of rhodium complexes were investigated: monocarbonyltriphenylphosphine rhodium complexes $[\text{Rh}(\beta\text{-diketonato})(\text{CO})(\text{PPh}_3)]$ and triphenylphosphite rhodium complexes $[\text{Rh}(\beta\text{-diketonato})(\text{P}(\text{OPh})_3)_2]$ (where β -diketonato is a monoanionic bidentate ligand with two oxygen donor atoms $(\text{R}_1\text{COCHCOR}_2)^-$).

The reaction, $[\text{Rh}(\beta\text{-diketonato})(\text{CO})(\text{PPh}_3)] + \text{CH}_3\text{I}$ (β -diketonato = acac, tta, bth and dtm), consists of many steps with numerous transition states, intermediate products and reaction products. Experimental studies indicate that the reaction occurs according to the following reaction scheme:

$$[\text{Rh}^{\text{I}}(\beta\text{-diketonato})(\text{CO})(\text{PPh}_3)] + \text{CH}_3\text{I} \rightarrow \text{Rh}^{\text{III}}\text{-alkyl1} \rightarrow \text{Rh}^{\text{III}}\text{-acyl1} \rightarrow \text{Rh}^{\text{III}}\text{-alkyl2} \rightarrow \text{Rh}^{\text{III}}\text{-acyl2}$$

$[\text{Rh}(\text{acac})(\text{CO})(\text{PPh}_3)]$ (Hacac = acetylacetonate) was used to study the stereochemistry of the reaction products and the complete reaction mechanism. An *in situ* ^1H NMR experimental study revealed the following information about the stereochemistry of the reaction products: $\text{Rh}^{\text{III}}\text{-alkyl1}$ has an octahedral geometry around the rhodium centre with the CH_3 group in the apical position and the PPh_3 group in the plane of the acac ligand, $\text{Rh}^{\text{III}}\text{-acyl1}$ has a square pyramidal geometry around the rhodium centre with the PPh_3 groups in the plane of the acac ligand, $\text{Rh}^{\text{III}}\text{-alkyl2}$ has an octahedral geometry around the rhodium centre with the PPh_3 group in the apical position and the CH_3 group in the plane of the acac ligand and $\text{Rh}^{\text{III}}\text{-acyl2}$ has a square pyramidal geometry around the rhodium centre with the PPh_3 group in the plane of the acac ligand. A DFT computational study on the relative stability of the possible reaction products is in agreement with these findings of the ^1H NMR experimental study. The DFT computational study gave additional insight into the relative positions of the I and the CO group in each of the above reaction products. On the grounds of the ^1H NMR experimental study and the DFT

CONCLUDING REMARKS AND FUTURE PERSPECTIVES

computational study, a general reaction scheme with specific stereochemistry for the reaction $[\text{Rh}(\beta\text{-diketonato})(\text{CO})(\text{PPh}_3)] + \text{CH}_3\text{I}$ could be constructed (Figure 5.1). For $[\text{Rh}(\beta\text{-diketonato})(\text{CO})(\text{PPh}_3)]$ complexes with symmetrical β -diketonato ligands, only one isomer in the reaction scheme has to be considered.

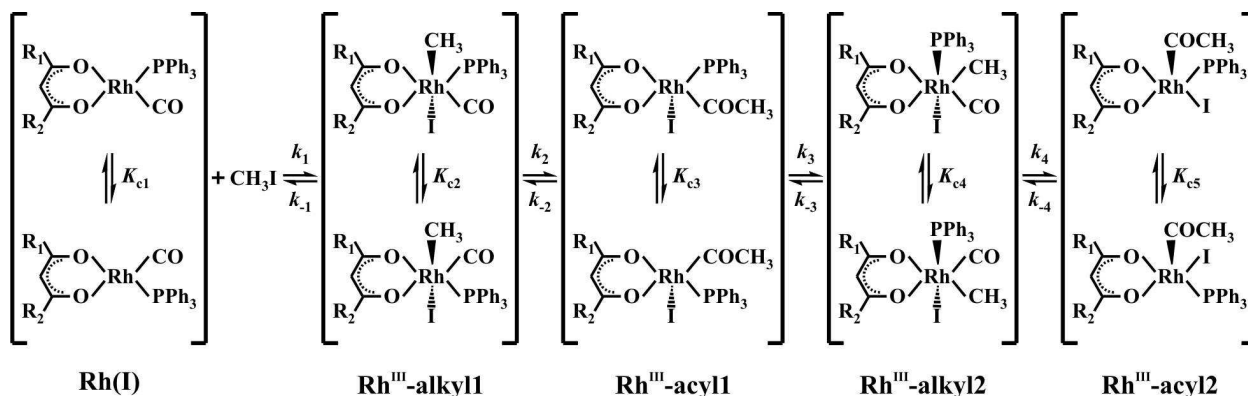


Figure 5.1: The proposed reaction scheme of the reaction of methyl iodide with $[\text{Rh}(\beta\text{-diketonato})(\text{CO})(\text{PPh}_3)]$, showing specific stereochemistry.

A DFT computational study of the multistep reaction mechanism of the reaction $[\text{Rh}(\text{acac})(\text{CO})(\text{PPh}_3)] + \text{CH}_3\text{I}$ was conducted. The DFT computational study revealed that the oxidative addition of methyl iodide to the square planar rhodium(I) complex corresponds to an $\text{S}_{\text{N}}2$ nucleophilic attack by the rhodium metal centre on the methyl iodide and that the multistep reaction mechanism consists of fourteen distinctive steps with the $\text{Rh}^{\text{III}}\text{-acyl1} \rightarrow \text{Rh}^{\text{III}}\text{-alkyl2}$ step as the rate-determining step. The multistep reaction mechanism is given in Figure 5.2.

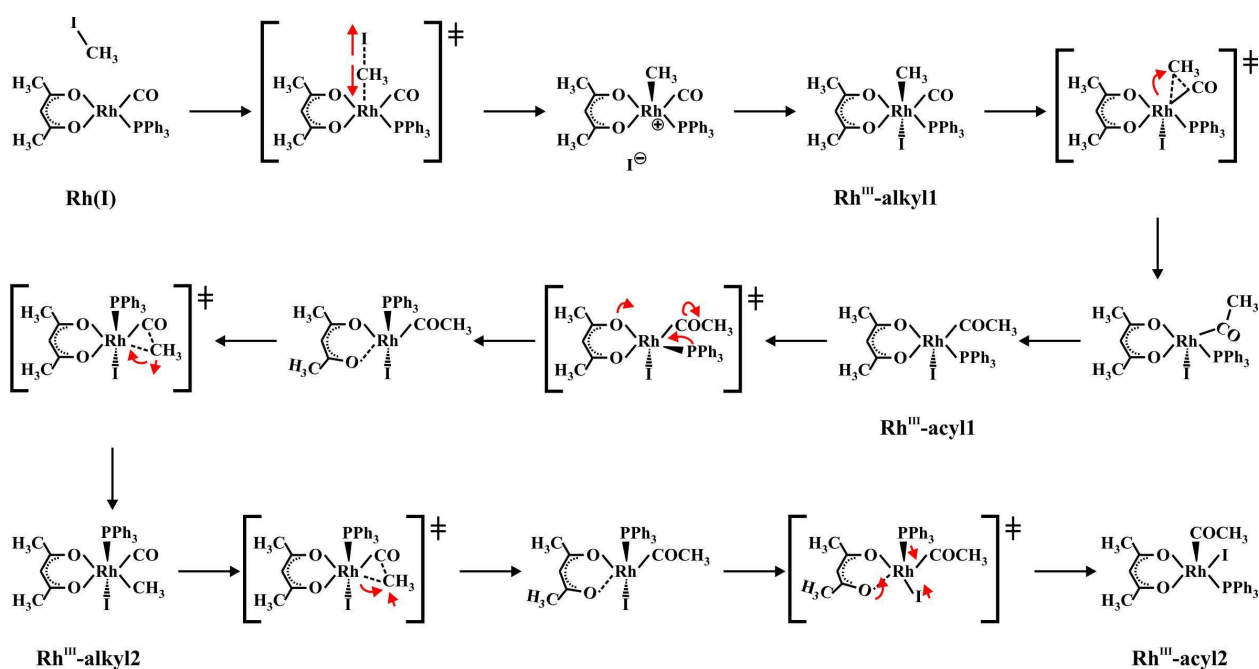


Figure 5.2: The multistep reaction mechanism of the reaction $[\text{Rh}(\text{acac})(\text{CO})(\text{PPh}_3)] + \text{CH}_3\text{I}$.

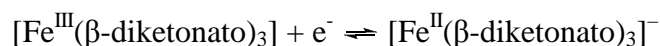
The oxidative addition reaction was generalized by investigating the first part of this multistep reaction mechanism with DFT computational methods for a selected series of $[\text{Rh}(\beta\text{-diketonato})(\text{CO})(\text{PPh}_3)]$ complexes. The oxidative addition of CH_3I to the square planar $[\text{Rh}(\beta\text{-diketonato})(\text{CO})(\text{PPh}_3)]$ ($\beta\text{-diketonato} = \text{acac, tta, bth and dtm}$) complexes corresponds to an $\text{S}_{\text{N}}2$ nucleophilic attack by the rhodium metal centre on the methyl iodide. The transition states of these complexes all exhibit similar geometrical and thermodynamical data. The experimental kinetic rate constants (k_1) and the theoretical activation energies (ΔE^\ddagger) exhibited a linear relationship due to the different electronic effect of the R_1 and R_2 side groups of the $\beta\text{-diketonato}$ ligands coordinated to the $[\text{Rh}(\beta\text{-diketonato})(\text{CO})(\text{PPh}_3)]$ complexes. The $[\text{Rh}(\beta\text{-diketonato})(\text{CO})(\text{PPh}_3)]$ complexes showed rapid oxidative addition compared to the Monsanto catalyst and it is recommended to further investigate these complexes as promising rhodium based catalysts.

Finally, a DFT computational study of the oxidative addition of methyl iodide to the bulky $[\text{Rh}(\text{acac})(\text{P}(\text{OPh})_3)_2]$ was performed. Due to the computational requirement of optimizing such a big molecular system, simplified models, *viz.* $[\text{Rh}(\text{acac})(\text{P}(\text{OCH}_3)_3)_2]$ and $[\text{Rh}(\text{acac})(\text{P}(\text{OH})_3)_2]$, were also investigated. The models have similar geometrical features and energy profiles of the reactants, transition state and possible reaction products. Methyl iodide is added *trans* to the square planar rhodium(I) complex with $[\text{Rh}(\text{acac})(\text{P}(\text{OR})_3)_2(\text{CH}_3)(\text{I})]$ -alkyl ($\text{R} = \text{Ph, CH}_3, \text{H}$) as the product. The $[\text{Rh}(\text{acac})(\text{P}(\text{OR})_3)_2(\text{CH}_3)(\text{I})]$ -alkyl product has an octahedral geometry around the rhodium centre with the I and CH_3 group in the apical position and the $\text{P}(\text{OR})_3$ groups in the plane of the acac ligand. The main features of the transition state, *viz.* the nucleophilic attack of the rhodium atom on the CH_3^+ group and the cleavage of the carbon-iodide bond, were also similar for all the models. Though, only the full model gave thermodynamic data about the oxidative addition reaction in agreement with experimental data. Therefore, in order to save on computational recourses, simplified models can be used to obtain preliminary information on the geometrical features and the energy profile of the oxidative addition reaction $[\text{Rh}(\beta\text{-diketonato})(\text{P}(\text{OPh})_3)_2] + \text{CH}_3\text{I}$. But in order to compare thermodynamic results with the experimental data, the full model is needed.

Iron complexes.

A series of [Fe^{III}(β-diketonato)₃] (β-diketonato = acac, ba, bth, dtm, dbm, tfaa, tffu, tfba, tta and hfaa) complexes were studied by experimental and computational methods. Two new and eight known [Fe(β-diketonato)₃] complexes were successfully synthesized. The DFT computational study indicated that these complexes can occur as two isomers, the facial (*fac*) and meridional (*mer*) isomers. These complexes were all characterized with UV/vis spectrophotometry, mass spectroscopy, elemental analysis and by their melting points.

The [Fe(β-diketonato)₃] complexes were further electrochemically characterized by using cyclic voltammetry and spectroelectrochemistry. Cyclic voltammetric studies on the [Fe(β-diketonato)₃] complexes were performed in the weakly coordinating CH₃CN/TBAPF₆ medium. The only redox active centre in the complexes studied was the iron centre. The overall electrochemical reaction can be expressed as:



The redox process was found to be electrochemically and chemically reversible at a scan rate of 100 mV.s⁻¹. The different redox potentials of the [Fe^{III}(β-diketonato)₃] series are due to the different electronic densities at the metal centre which are due to the different substituents on the β-diketonato ligands. The formal reduction potential (E⁰) of the redox active metal Fe(III)/Fe(II) in the [Fe^{III}(β-diketonato)₃] complexes was correlated to parameters related to electron density on the iron centre, such as the acid dissociation constant (pK_a) of the uncoordinated β-diketone (R₁COCH₂COR₂), the total group electronegativities (χ_{R1} + χ_{R2}) of the R₁ and R₂ side groups on the β-diketonato ligand (R₁COCHCOR₂)⁻ and the calculated ionization potentials of the [Fe^{III}(β-diketonato)₃] complexes. The linear equations (y = mx + c) defining these relationships can be expressed as:

$$\begin{aligned} \text{p}K_{\text{a}} &= (-4.164) E^0 + 5.033 \\ \chi_{\text{R1}} + \chi_{\text{R2}} &= (-2.483) E^0 + 2.120 \quad (\text{R}_1 \text{ and } \text{R}_2 \neq \text{CF}_3) \\ \chi_{\text{R1}} + \chi_{\text{R2}} &= (-6.990) E^0 + 2.703 \quad (\text{R}_1 \text{ or } \text{R}_2 = \text{CF}_3) \\ E^0 &= (6.933 \times 10^{-3}) \text{IP} + 2.258 \end{aligned}$$

This allows one to predict the electronegativities of the R₁ and R₂ side groups, the acid dissociation constant of the uncoordinated β-diketone and the formal reduction potential of the [Fe^{III}(β-diketonato)₃] complexes, if the calculated ionization potentials are known. Electrochemical and spectroscopic techniques were combined in a spectroelectrochemistry study of the [Fe^{III}(β-diketonato)₃] complexes. The influence of the reduction reactions on the UV/vis

absorption spectra was monitored. The intensity of the bands in the near ultraviolet region (200-600 nm) changed as the iron(III) complexes were reduced. Complexes without aromatic side groups had similar absorption spectra and spectral changes during the reduction reaction. Introduction of one Ph or two Ph side groups successively caused a red shift of ~30 nm on the maximum absorbance band of the iron(III) complexes. Inclusion of aromatic groups such as C₄H₃S or C₄H₃O resulted in different spectra.

In the final two studies, the performance of different DFT functionals, in relation to the energetics of different spin states of iron complexes, was tested. The spin crossover complex [Fe(salen)(CH₃)₂(COCH₃)₂(py)₂] and low/high spin five-coordinate iron(III) porphyrins were used to conduct this research.

For the spin crossover complex [Fe(salen)(CH₃)₂(COCH₃)₂(py)₂], no single functional could accurately reproduce the geometry of both the low and high spin states as well as provide an energy profile with equi-energetic low and high spin states. The functional PW91 gave a good geometry optimization of both the low and high spin states, whereas the functionals BP86, BLYP, PBE, OLYP, OPBE and B3LYP only succeeded in giving a good geometry optimization of the low spin complex. For the high spin geometry, OLYP and OPBE performed the worst. An opposite performance by functionals was obtained for the spin-state energetics. OLYP, OPBE and B3LYP provided the best spin-state energetics for spin crossover, whereas the functionals PW91, BP86, BLYP and PBE could not reproduce equi-energetic low and high spin states. Although OLYP is known to be one of the best functionals for transition metal systems, it failed to perform for the spin crossover complex [Fe(salen)(CH₃)₂(COCH₃)₂(py)₂]. Failures like these inspire researchers to constantly improve old functionals and hence to develop new ones.

A series of closely related five-coordinate iron(III) porphyrins, [Fe^{III}(porphyrin)(Ar)] (Ar = aryl = Cl, Ph, C₆F₅, 3,4,5-C₆F₃H₂ and 2,4,6-C₆F₃H₂), was also used to test the performance of different DFT functionals. These complexes are an excellent calibration tool, since even though they are closely related, they exhibit different spin states. The newer pure functionals (OLYP and OPBE) performed the best in predicting the applicable spin states of the porphyrin complexes, closely followed by B3LYP. Both OLYP and B3LYP appeared to have performed distinctly better than B3LYP*, which was somewhat of a surprise, given that B3LYP* usually performs significantly better than B3LYP. The classic pure functionals (such as PW91) performed the worst, as far as spin state energetics were concerned.

5.2 Future perspectives.

The rhodium studies can be extended as follow:

- (i) DFT calculation of the oxidative addition reaction $[\text{Rh}(\beta\text{-diketonato})(\text{CO})(\text{PPh}_3)] + \text{CH}_3\text{I}$ for a series of β -diketonato ligands and compare data to known experimental values.
- (ii) Investigate whether the proposed mechanism of the reaction $[\text{Rh}(\text{acac})(\text{CO})(\text{PPh}_3)] + \text{CH}_3\text{I}$ also applies to $[\text{Rh}(\beta\text{-diketonato})(\text{CO})(\text{PPh}_3)]$ complexes with an unsymmetrical β -diketone backbone, using DFT calculations.
- (iii) Determination of the molecular structures of rhodium(III) reaction products, using X-ray crystallography
- (iv) Electrochemical characterization of the $[\text{Rh}(\beta\text{-diketonato})(\text{CO})(\text{PPh}_3)]$ complexes using cyclic voltammetry and spectroelectrochemistry. Evaluation of the peak anodic potential (E_{pa}), as well as the electrochemical and chemical reversibility/irreversibility, of the redox active rhodium(I) centre. Determination whether these Rh(I) complexes are oxidized to Rh(II) or Rh(III), using bulk electrolysis. Determination of the effect of the electron donation/withdrawal of the different R side groups of the β -diketonato ligands on the peak anodic potential (E_{pa}).
- (v) Determination of the relationships between experimentally determined and DFT calculated properties, such as the acid dissociation constant ($\text{p}K_{\text{a}}$) of the β -diketone coordinated to the rhodium complex, the total group electronegativities ($\chi_{\text{R1}} + \chi_{\text{R2}}$) of the R_1 and R_2 side groups on the β -diketonato ligand, the peak anodic potential (E_{pa}) of the redox active metal Rh(I)/Rh(II) or Rh(I)/Rh(III) in $[\text{Rh}(\beta\text{-diketonato})(\text{CO})(\text{PPh}_3)]$ and the calculated ionization potentials.

The iron studies can be extended as follow:

- (i) Synthesize a series of tris(β -diketonato) metal complexes (where metal = Cr, Mn, Co, Ni and Cu) to explore electrochemical trends of metals in the same row in the periodic table.
- (ii) Calculate the ionization potential of a series of tris(β -diketonato) metal complexes (where metal = Cr, Mn, Co, Ni and Cu) and compare with experimental data.
- (iii) Synthesize a series of tris(β -diketonato) metal complexes (where metal = Ru and Os) to explore electrochemical trends of metals in the same group in the periodic table.
- (iv) Calculate the ionization potential of a series of tris(β -diketonato) metal complexes (where metal = Ru and Os) and compare with experimental data.

A

Appendix

A.1 Infrared spectrophotometry (IR).

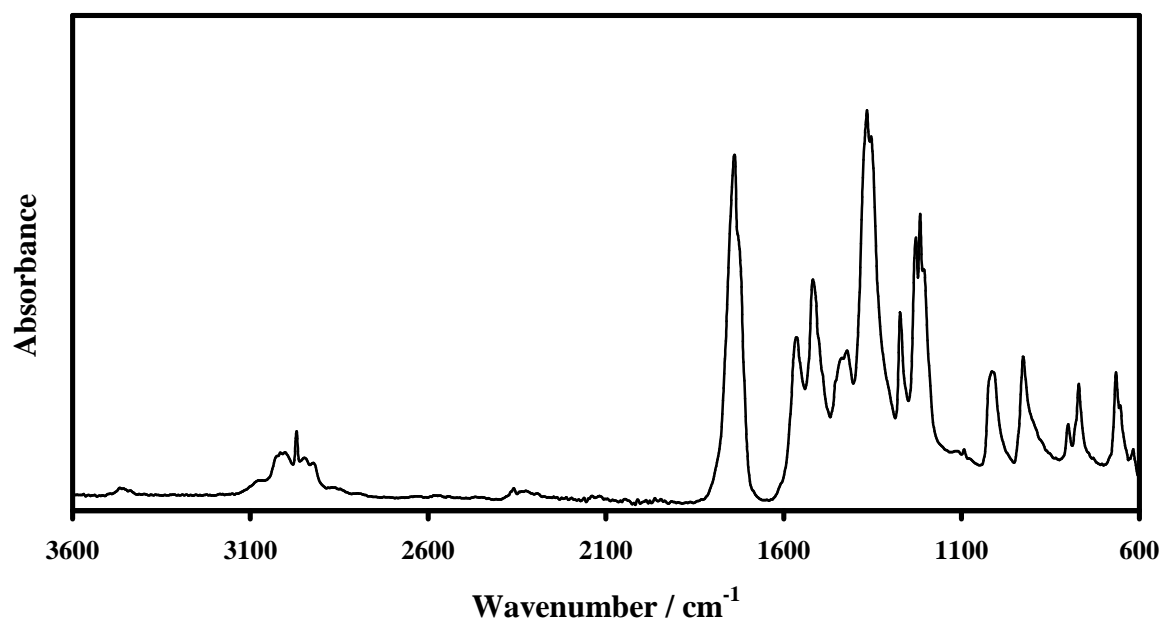


Figure A.1: Infrared spectrum of powder [Fe(acac)₃] {1}.

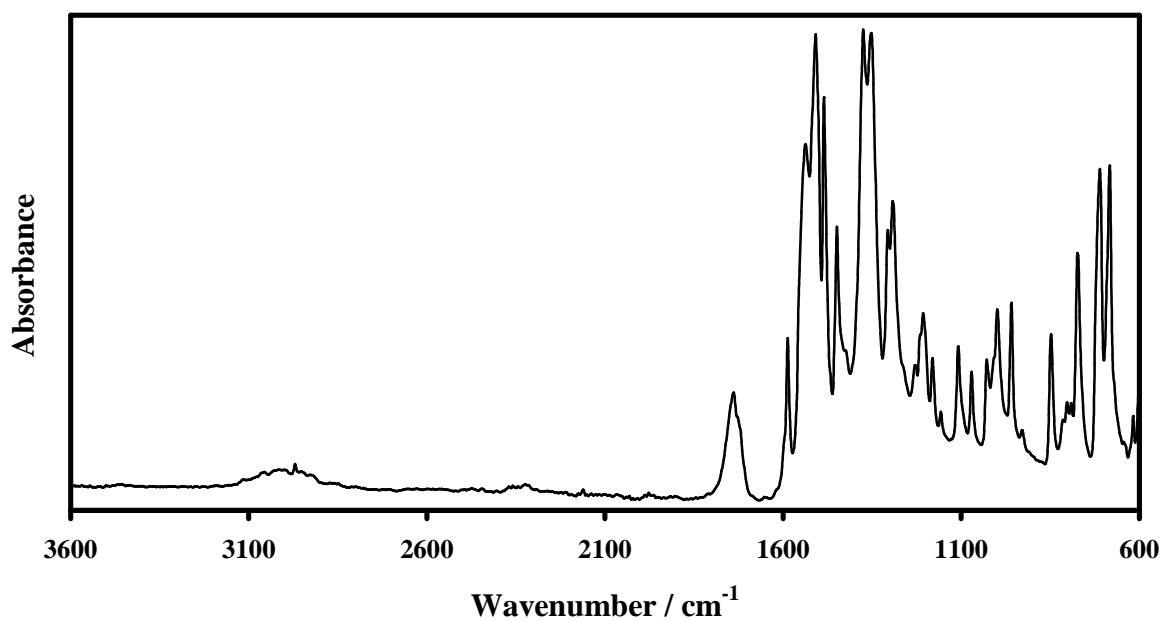


Figure A.2: Infrared spectrum of powder [Fe(ba)₃] {2}.

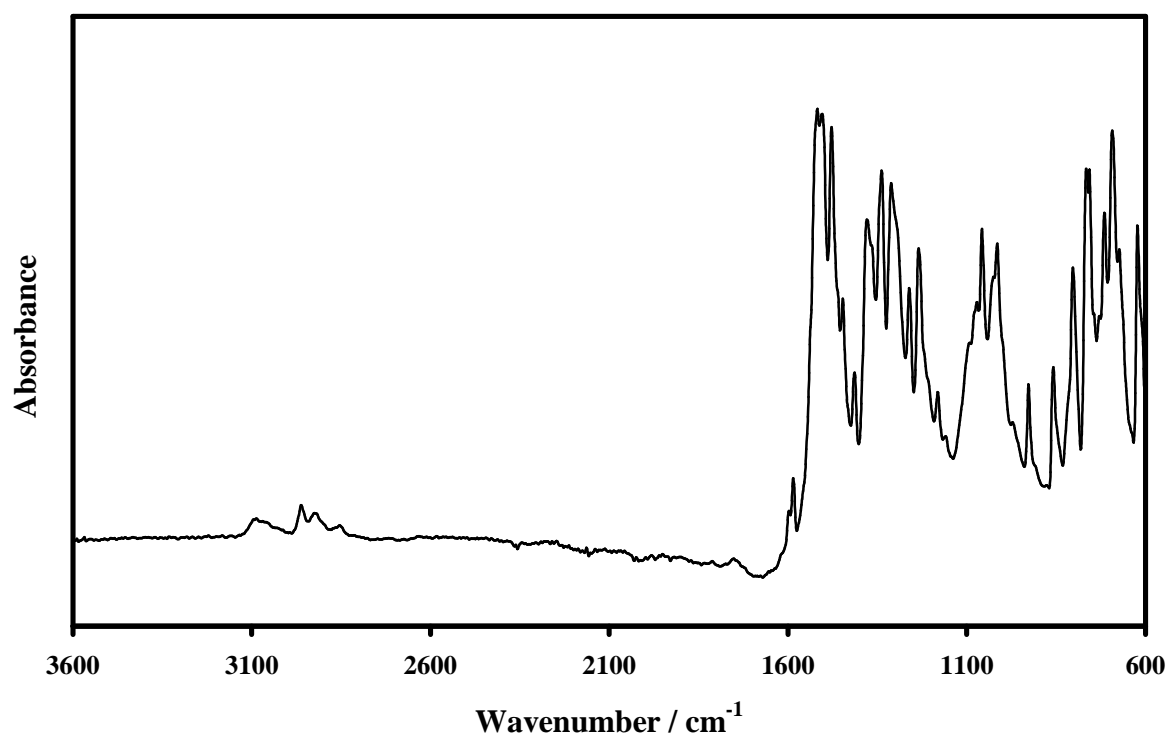


Figure A.3: Infrared spectrum of powder [Fe(bth)₃] {3}.

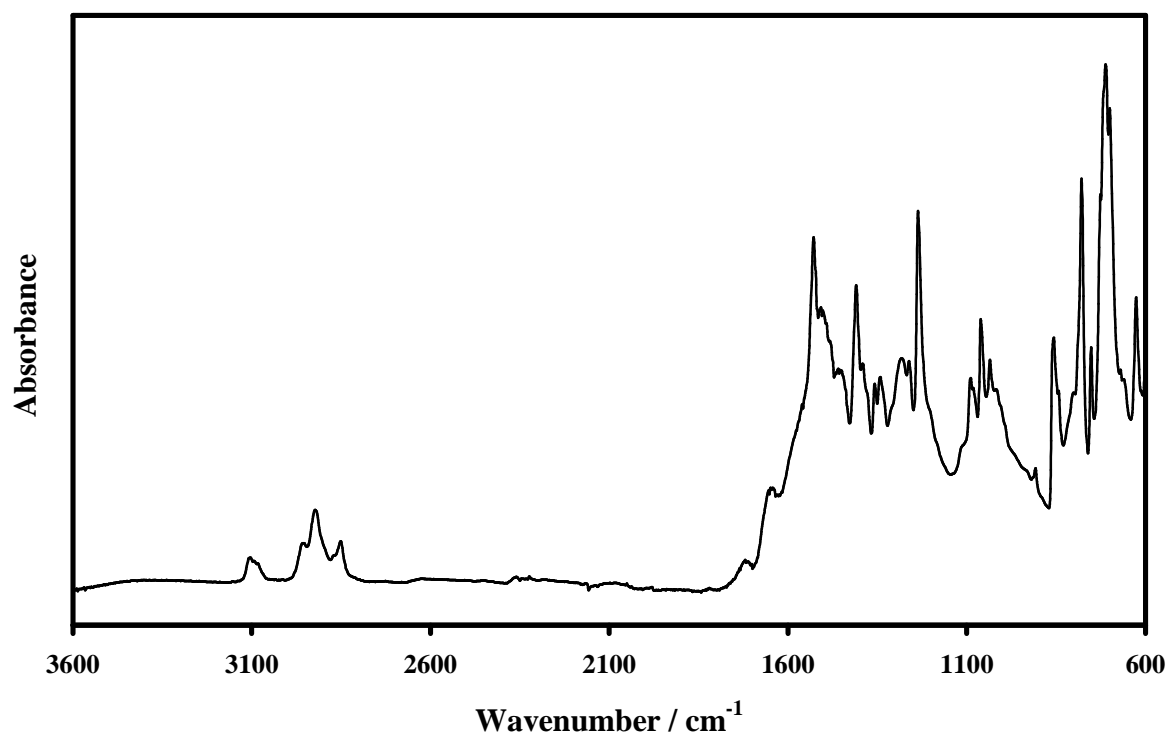


Figure A.4: Infrared spectrum of powder [Fe(dtm)₃] {4}.

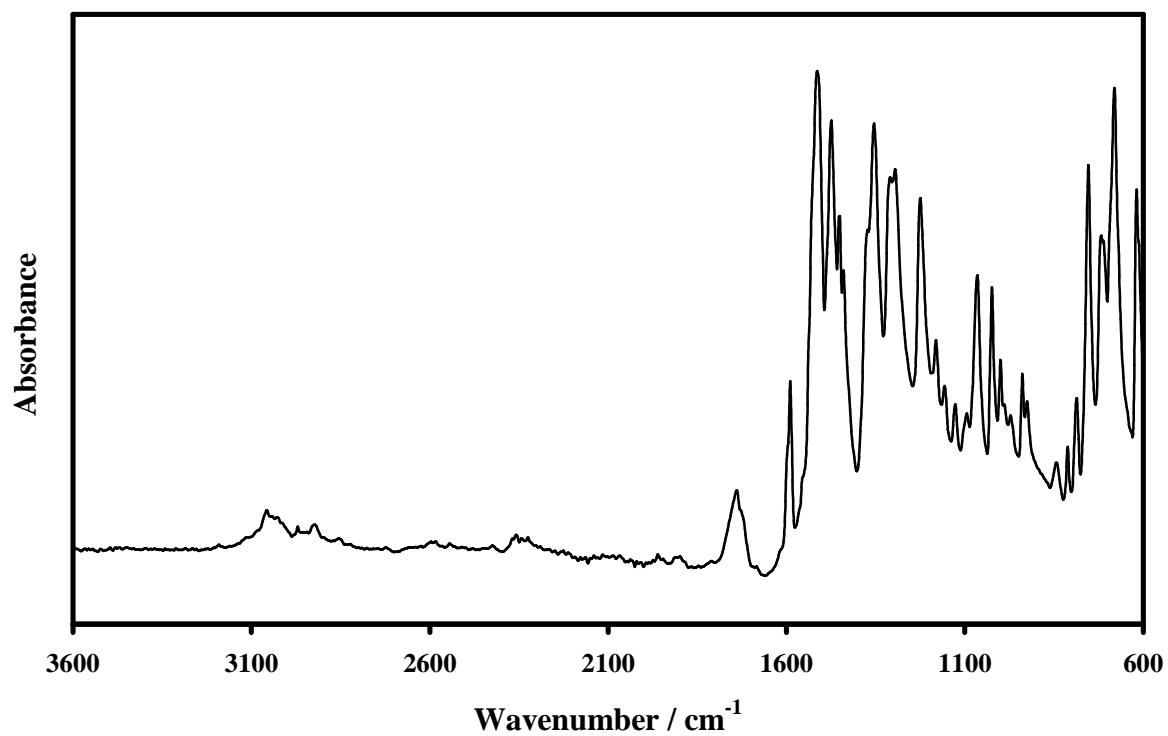


Figure A.5: Infrared spectrum of powder [Fe(dbm)₃] {5}.

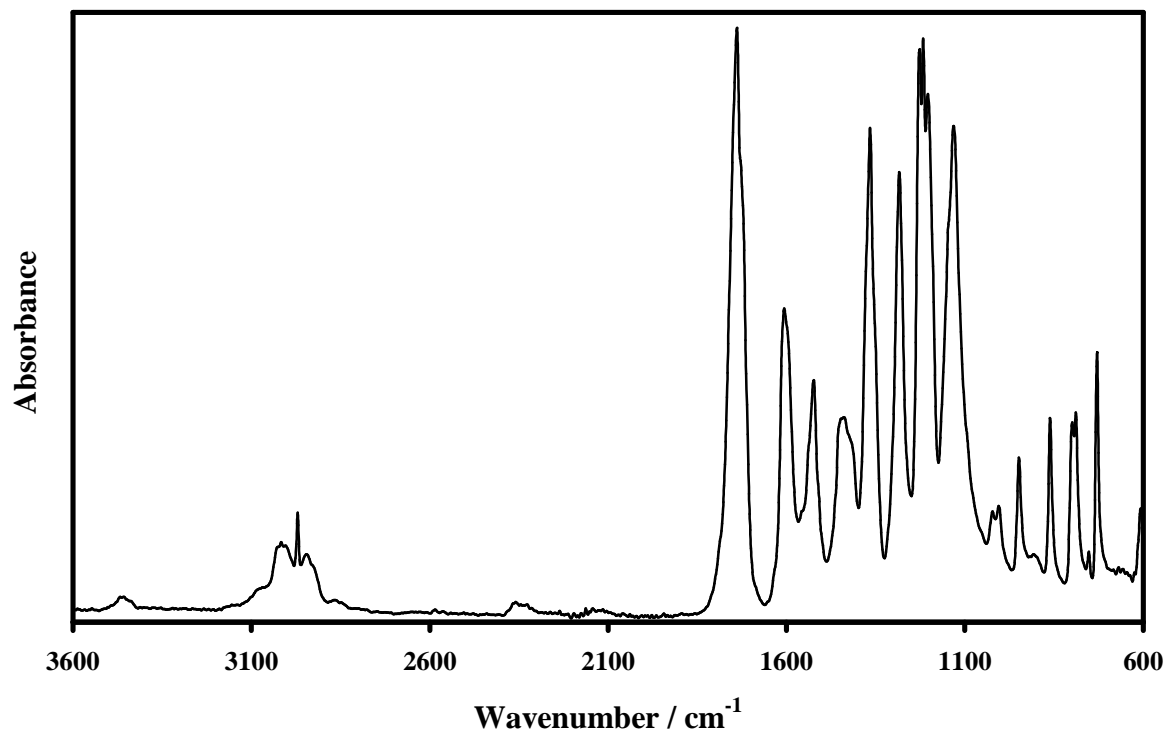


Figure A.6: Infrared spectrum of powder [Fe(tfaa)₃] {6}.

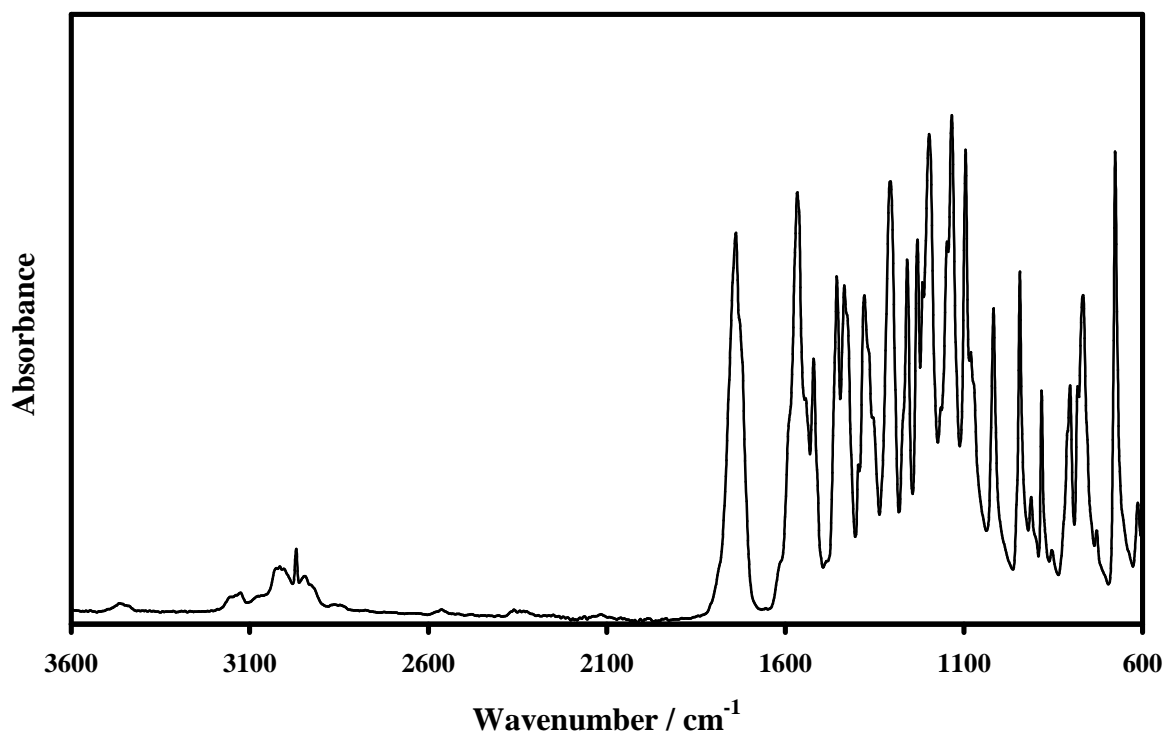


Figure A.7: Infrared spectrum of powder $[\text{Fe}(\text{tffu})_3]$ {7}.

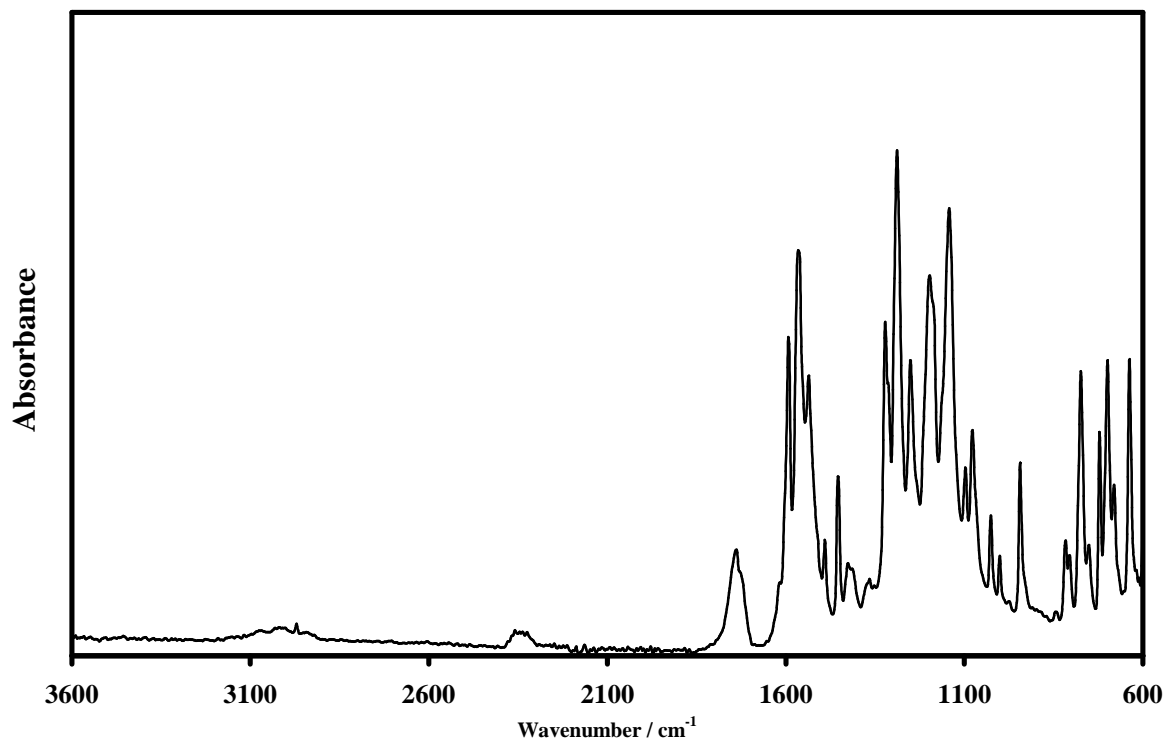


Figure A.8: Infrared spectrum of powder $[\text{Fe}(\text{tfba})_3]$ {8}.

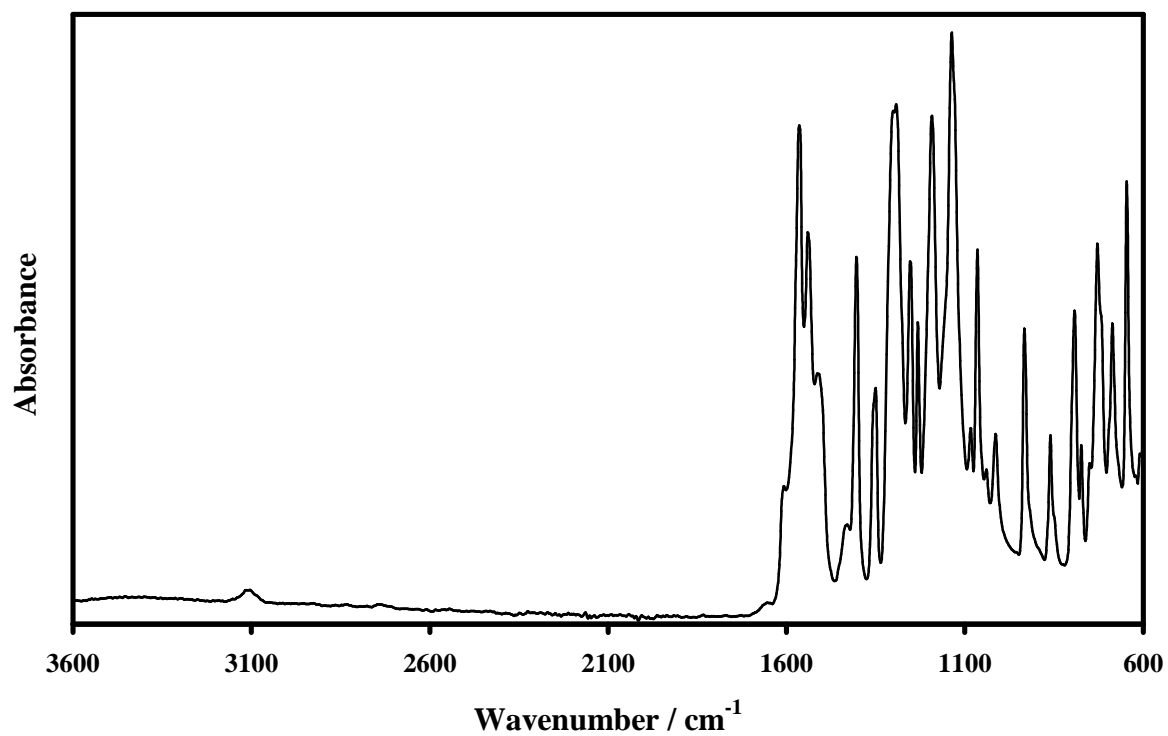


Figure A.9: Infrared spectrum of powder $[\text{Fe}(\text{tta})_3]$ {9}.

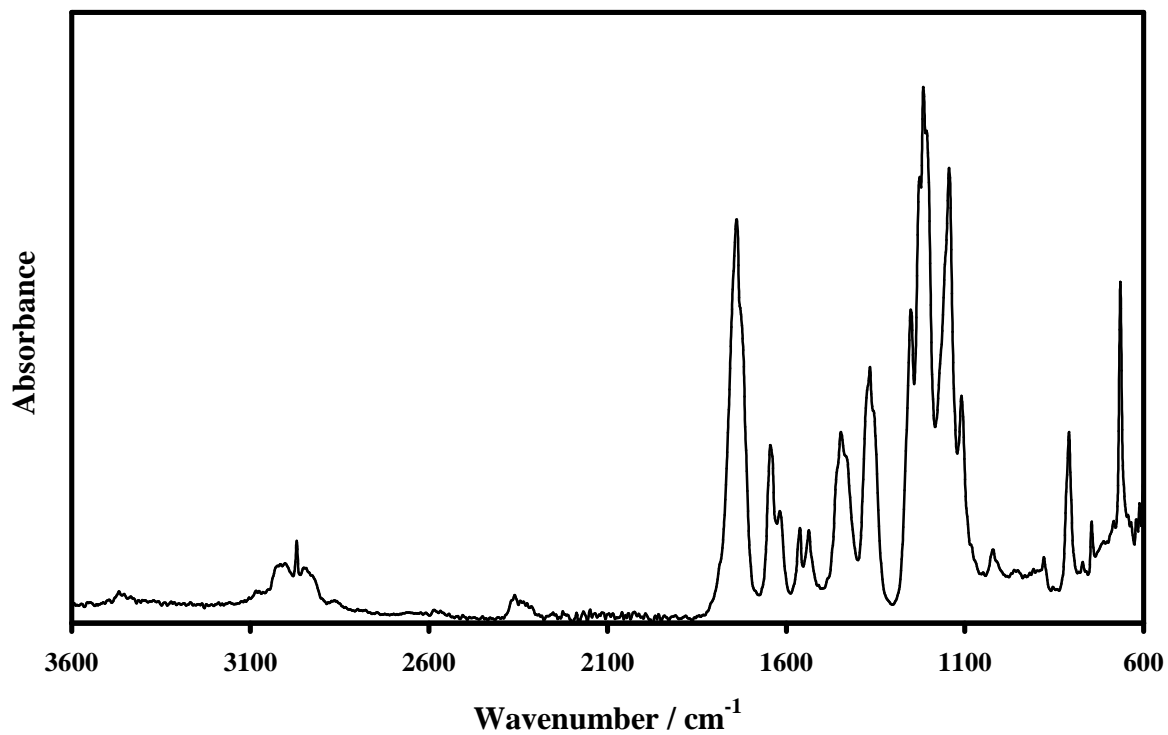


Figure A.10: Infrared spectrum of powder $[\text{Fe}(\text{hfaa})_3]$ {10}.

A.2 Ultraviolet spectrophotometry (UV).

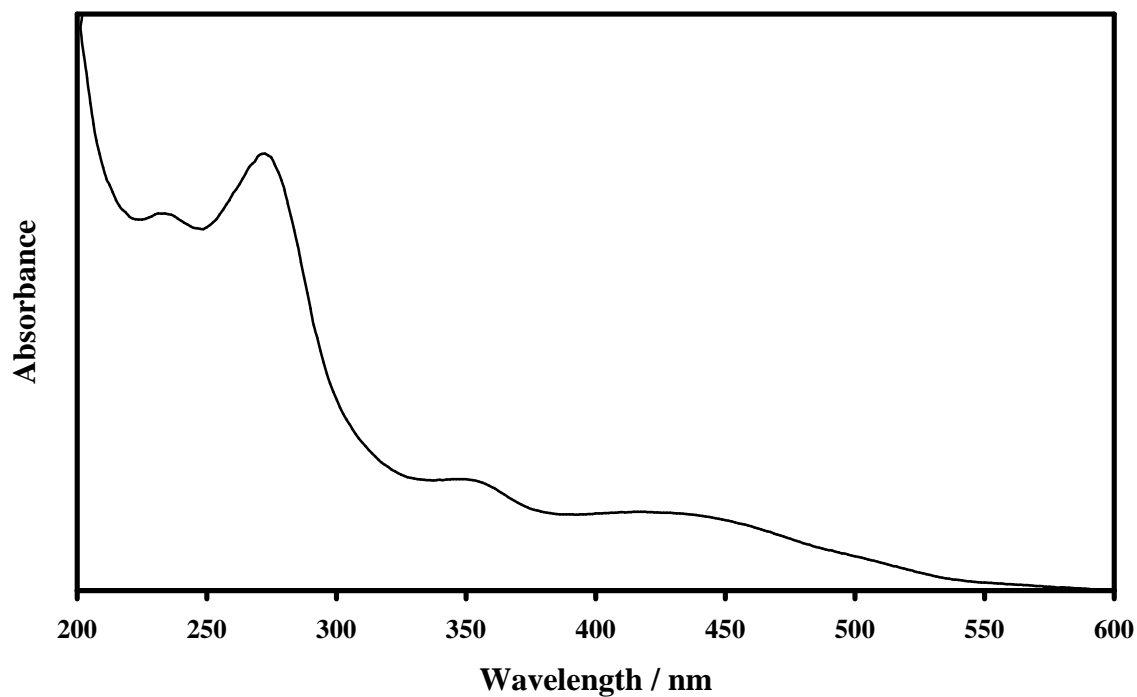


Figure A.11: Ultraviolet spectrum of [Fe(acac)₃] {1}, measured in CH₃CN at 25 °C.

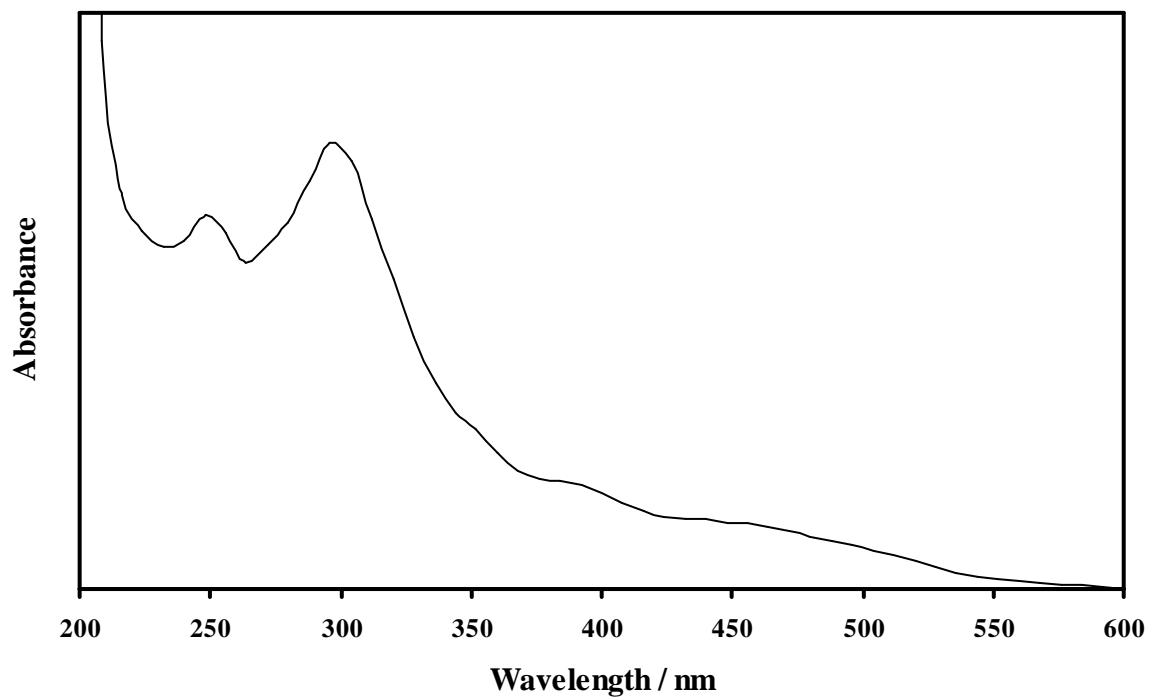


Figure A.12: Ultraviolet spectrum of [Fe(ba)₃] {2}, measured in CH₃CN at 25 °C.

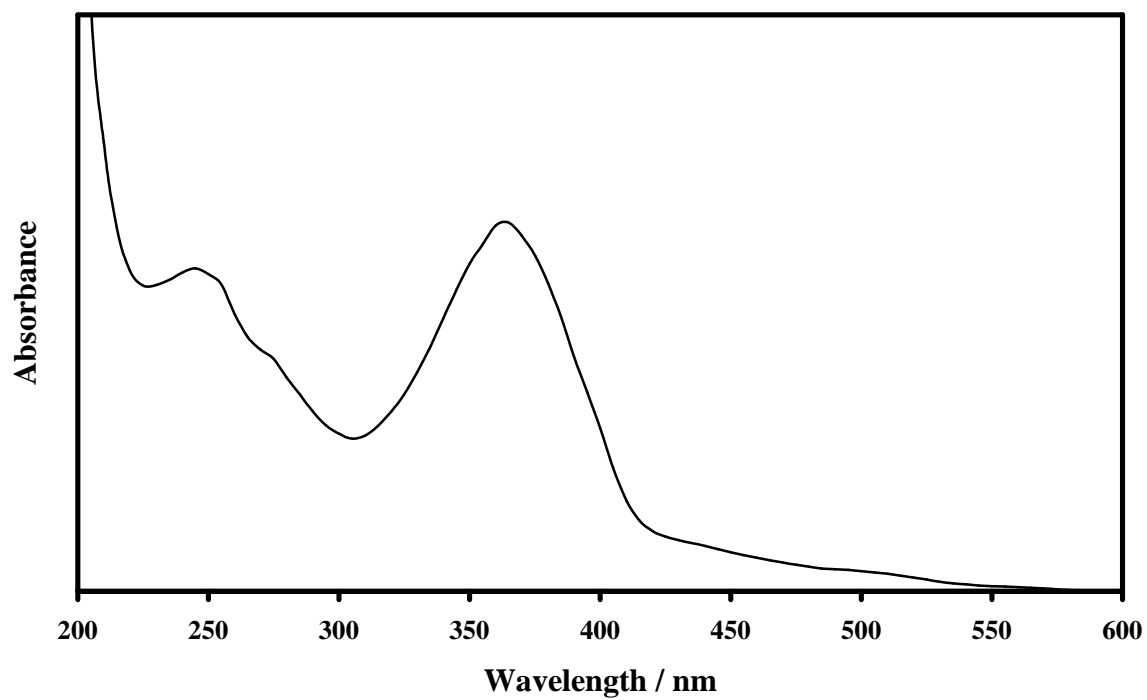


Figure A.13: Ultraviolet spectrum of [Fe(bth)₃] {3}, measured in CH₃CN at 25 °C.

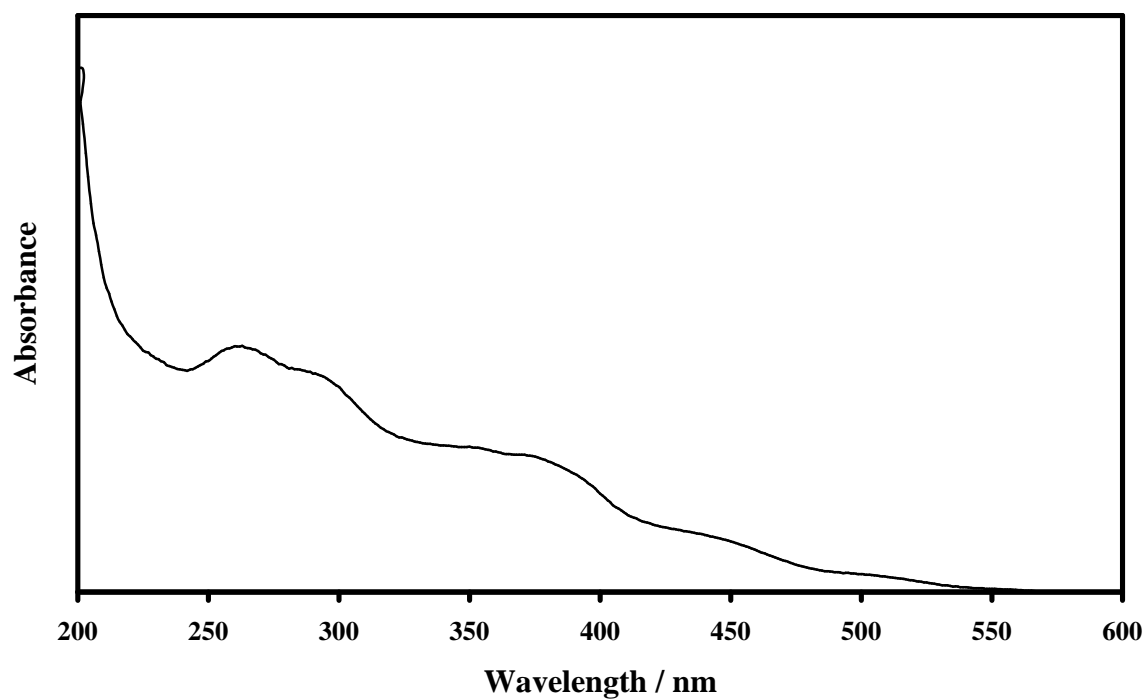


Figure A.14: Ultraviolet spectrum of [Fe(dtm)₃] {4}, measured in CH₃CN at 25 °C.

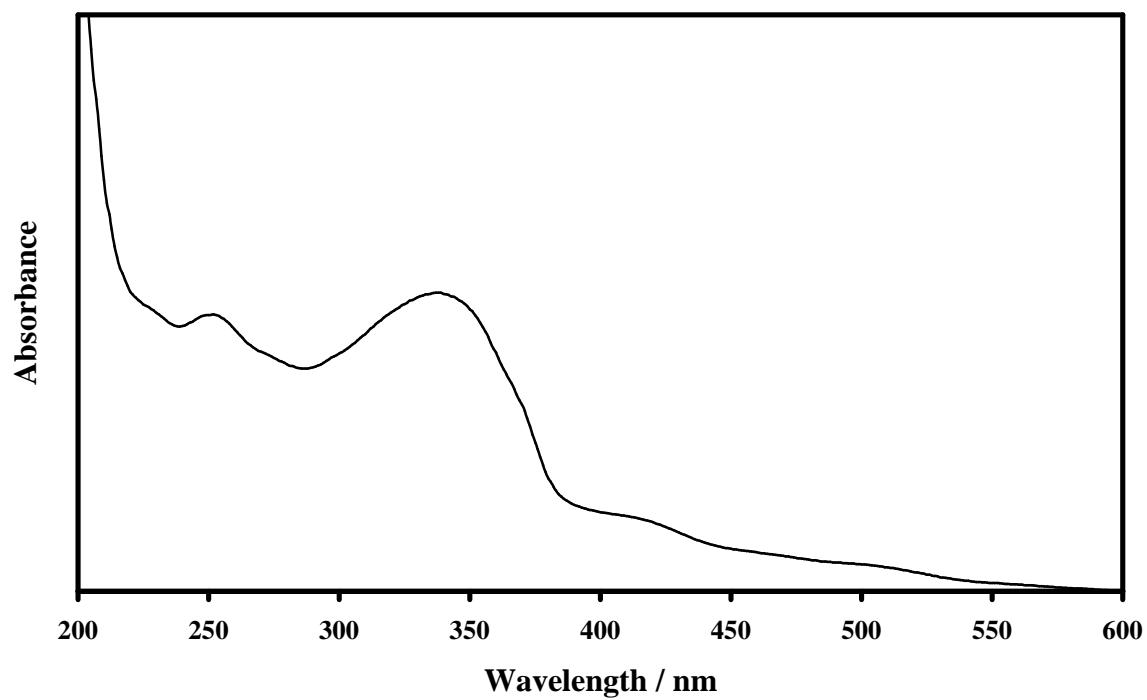


Figure A.15: Ultraviolet spectrum of [Fe(dbm)₃] (5), measured in CH₃CN at 25 °C.

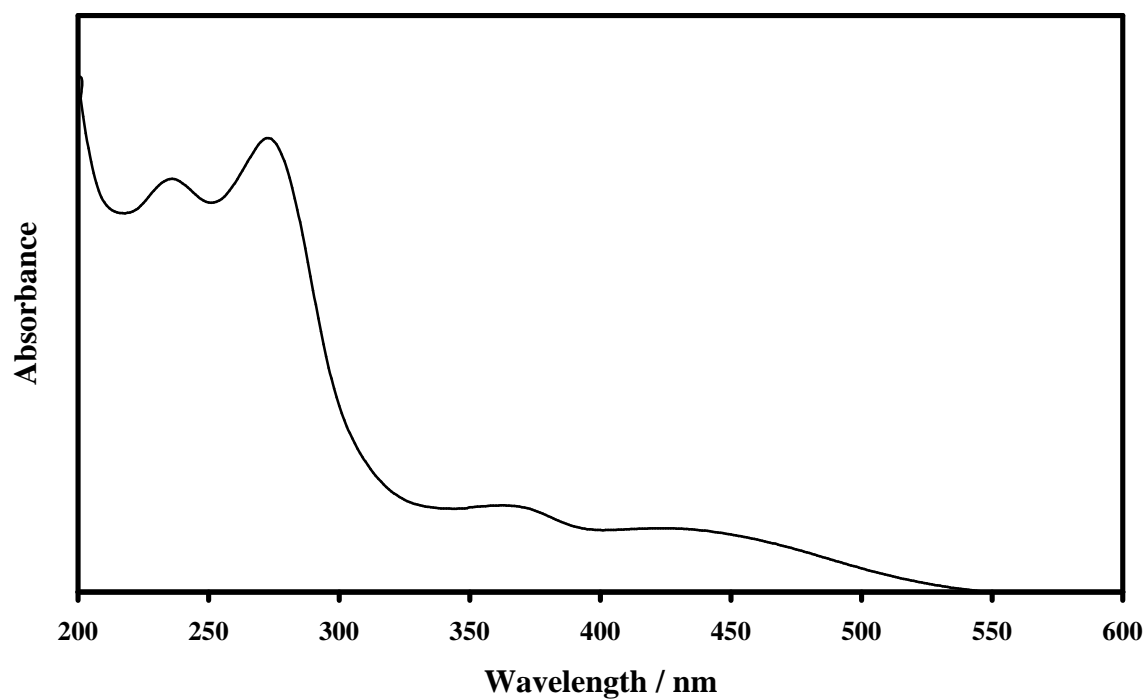


Figure A.16: Ultraviolet spectrum of [Fe(tfaa)₃] (6), measured in CH₃CN at 25 °C.

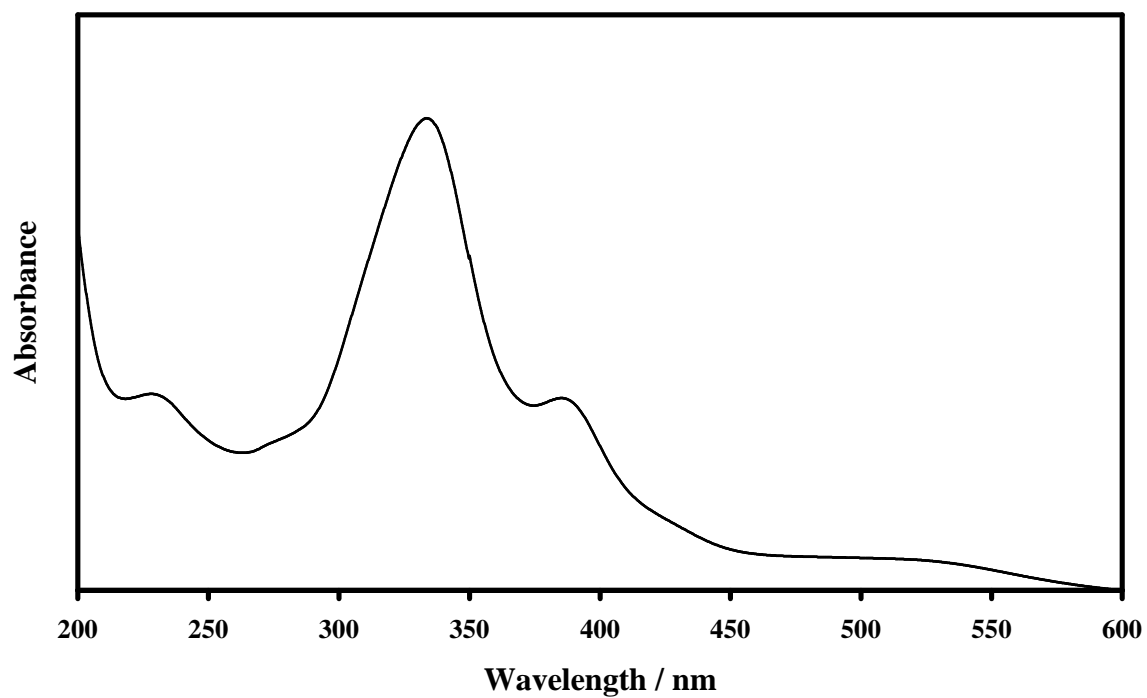


Figure A.17: Ultraviolet spectrum of [Fe(tffu)₃] {7}, measured in CH₃CN at 25 °C.

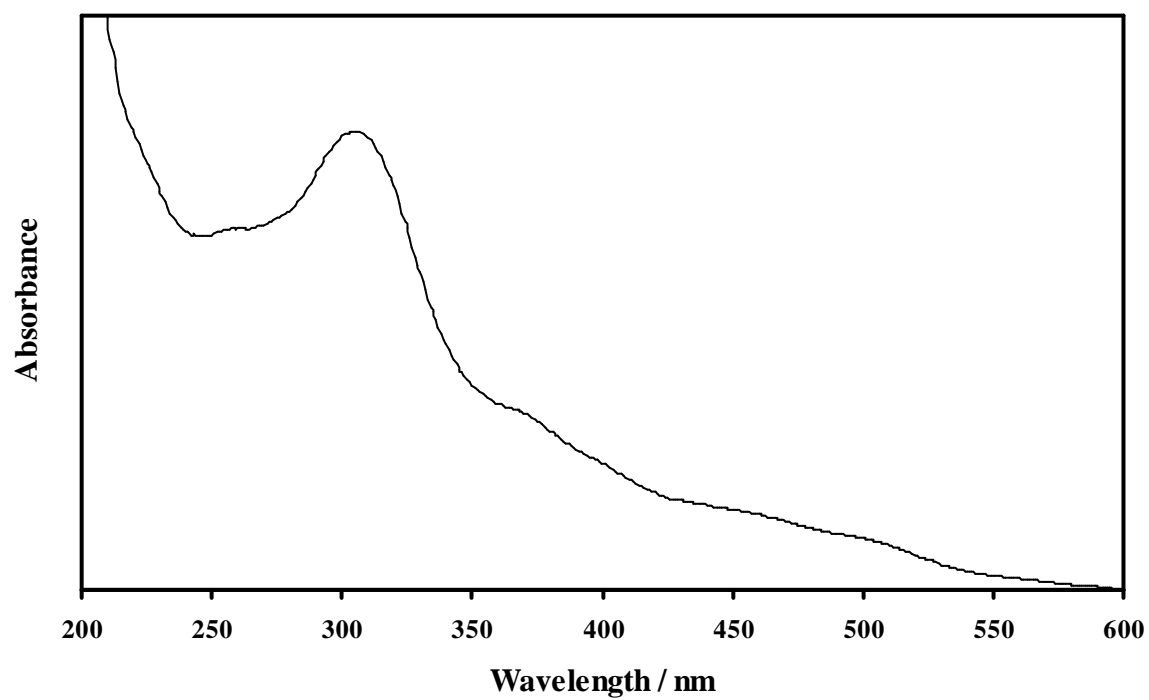


Figure A.18: Ultraviolet spectrum of [Fe(tfba)₃] {8}, measured in CH₃CN at 25 °C.

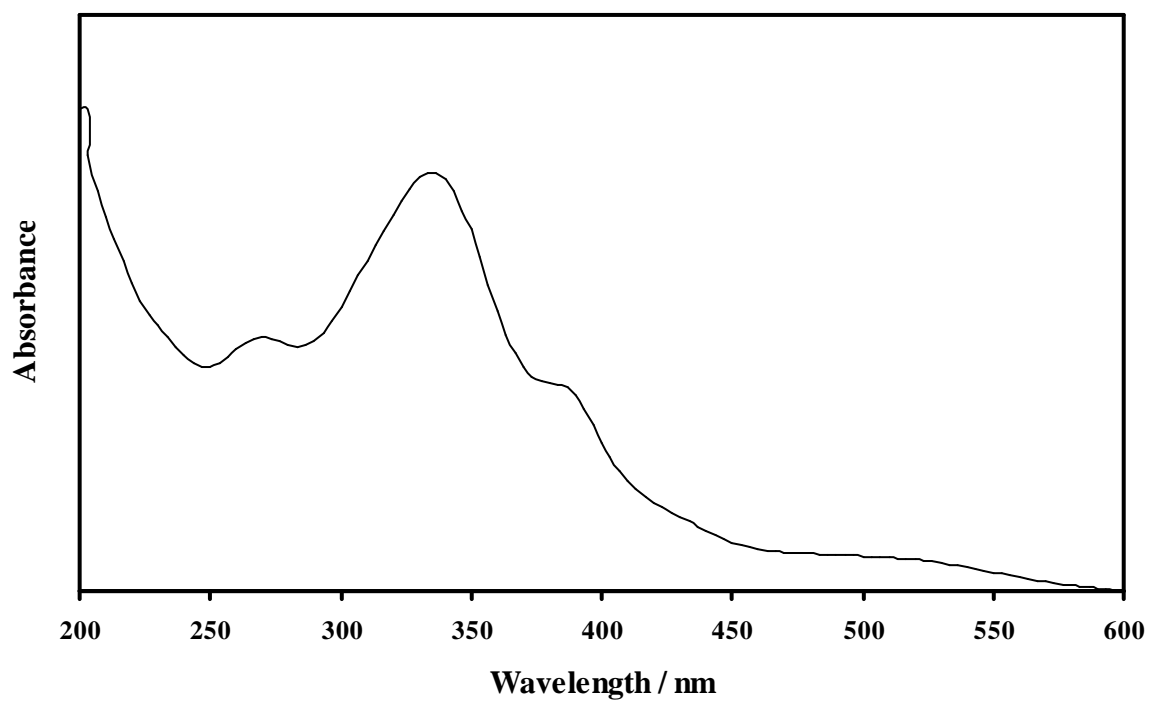


Figure A.19: Ultraviolet spectrum of [Fe(tta)₃] {9}, measured in CH₃CN at 25 °C.

A.3 Mass spectrometry (MS).

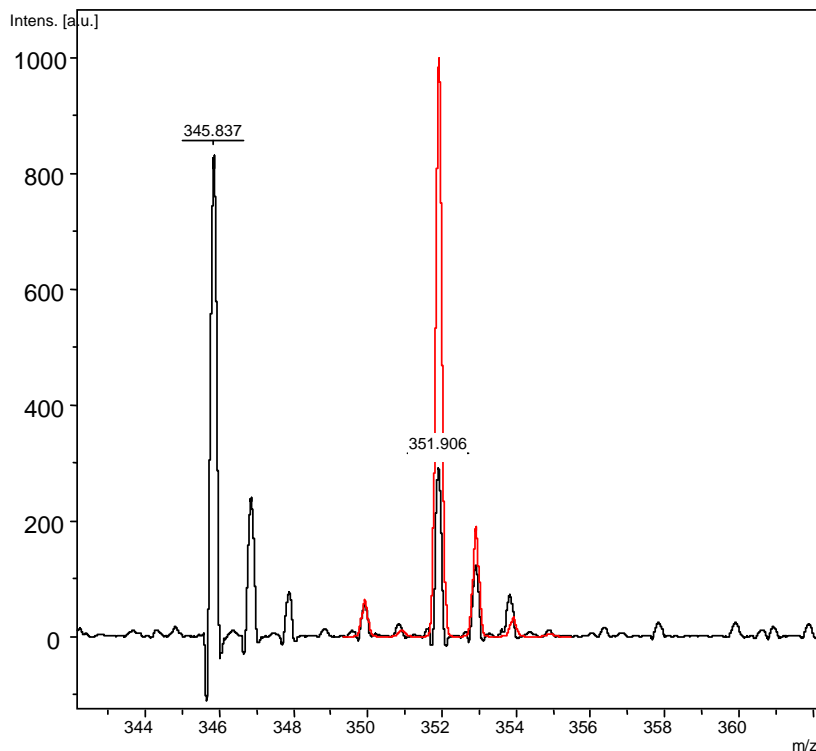


Figure A.20: MALDI mass spectrum of $[\text{Fe}(\text{acac})_3]^- \{1\}$ in the positive reflection mode. Calculated in red.

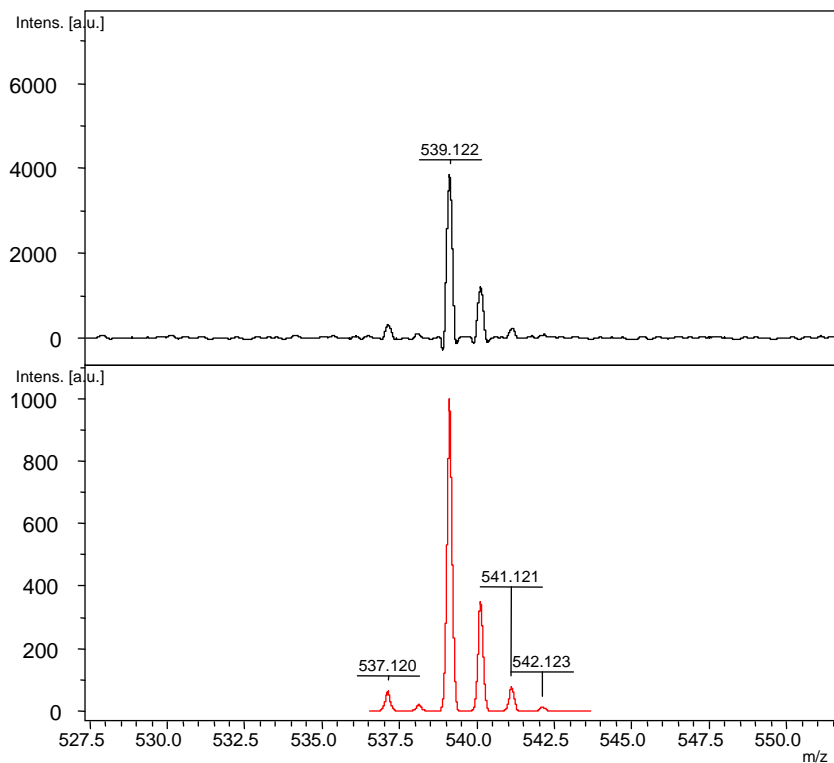


Figure A.21: MALDI mass spectrum of $[\text{Fe}(\text{ba})_3] \{2\}$ in the positive reflection mode. Calculated in red.

APPENDIX A

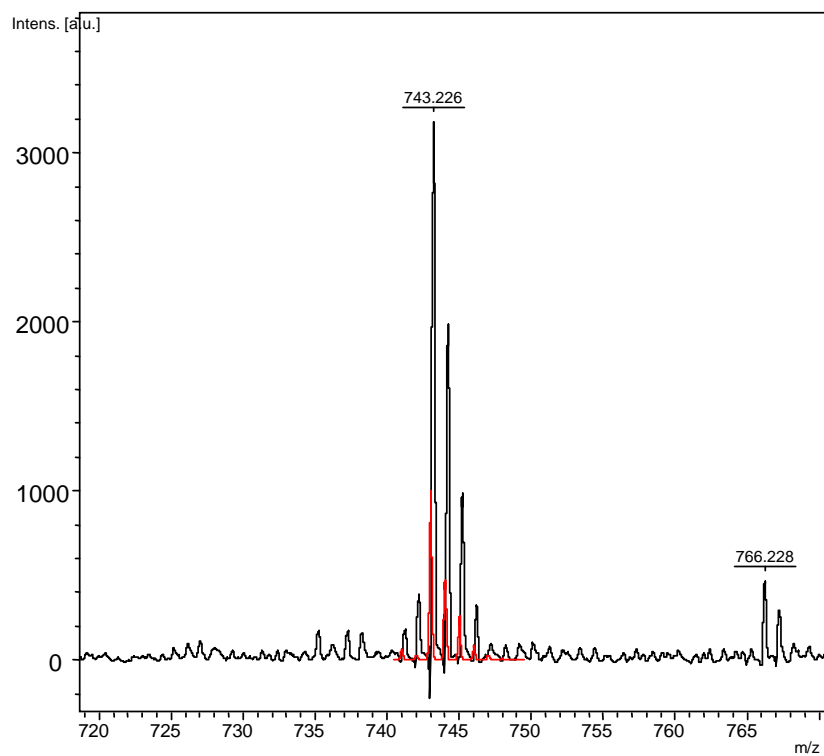


Figure A.22: MALDI mass spectrum of [Fe(bth)₃] {3} in the positive reflection mode. Calculated in red.

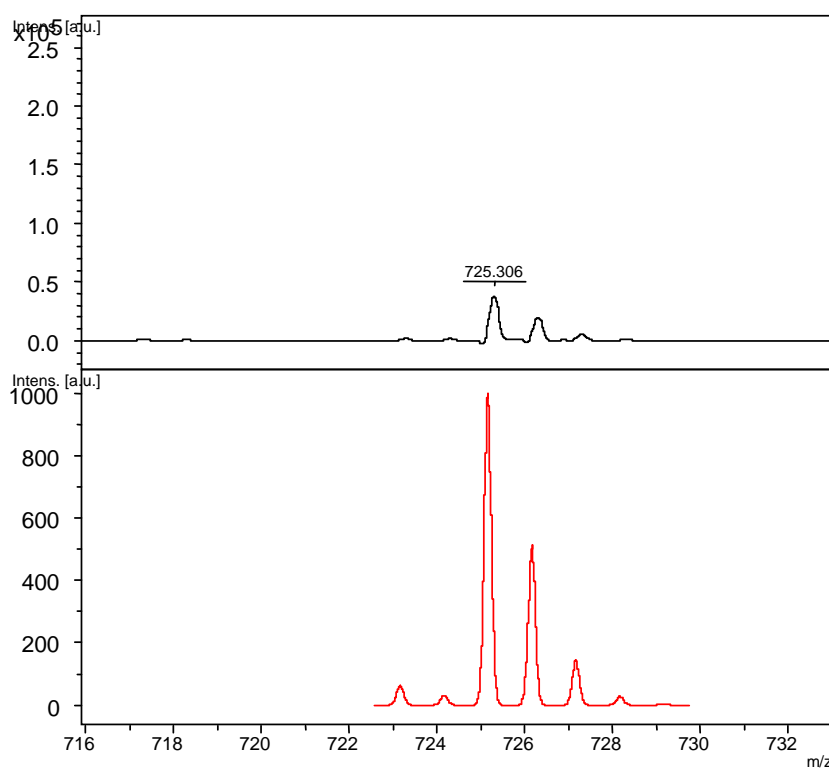


Figure A.23: MALDI mass spectrum of [Fe(dbm)₃] {5} in the positive reflection mode. Calculated in red.

APPENDIX A

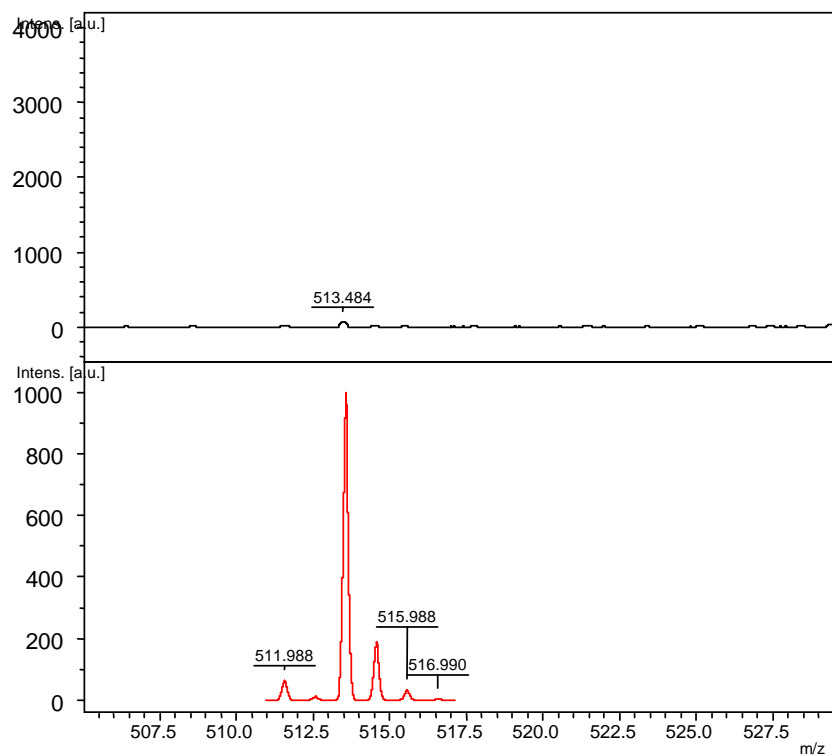


Figure A.24: MALDI mass spectrum of $[\text{Fe}(\text{tfaa})_3]^-$ {6} in the negative reflection mode. Calculated in red.

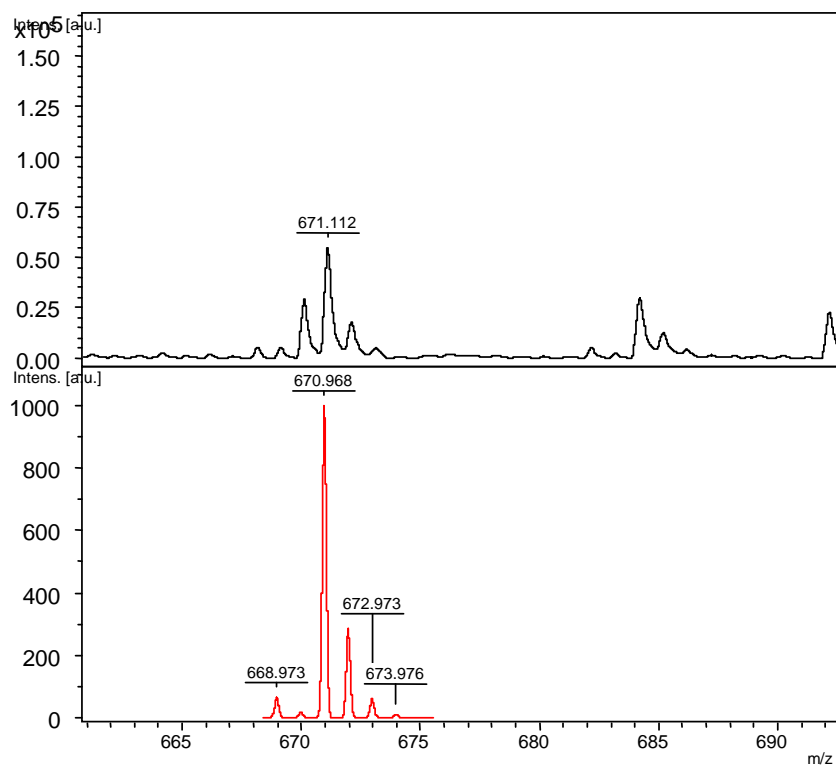


Figure A.25: MALDI mass spectrum of $[\text{Fe}(\text{tffu})_3]^+$ {7} in the positive reflection mode. Calculated in red.

APPENDIX A

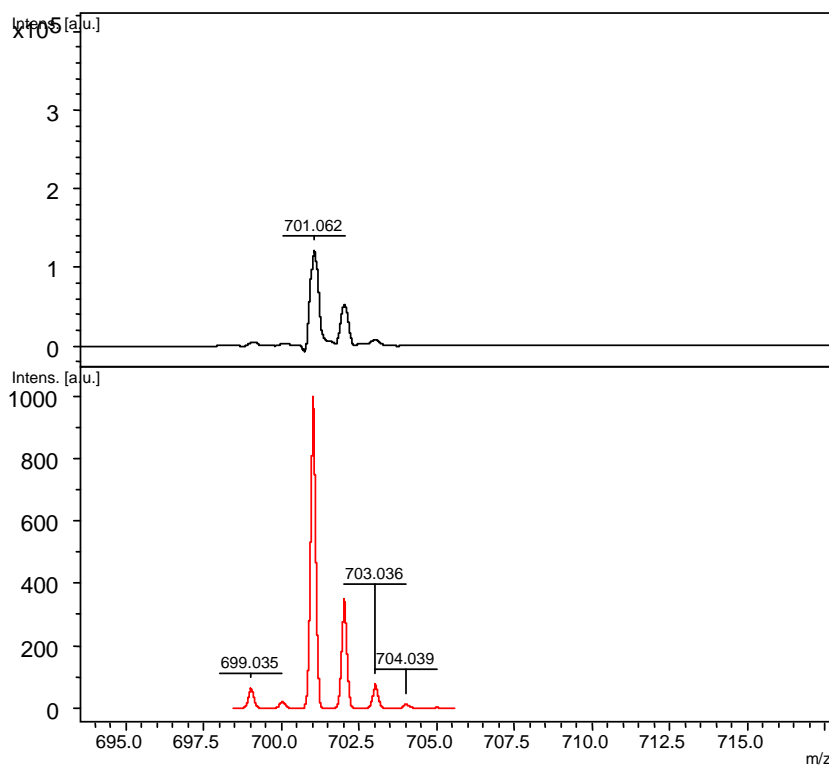


Figure A.26: MALDI mass spectrum of [Fe(tfba)₃] (8) in the negative reflection mode. Calculated in red.

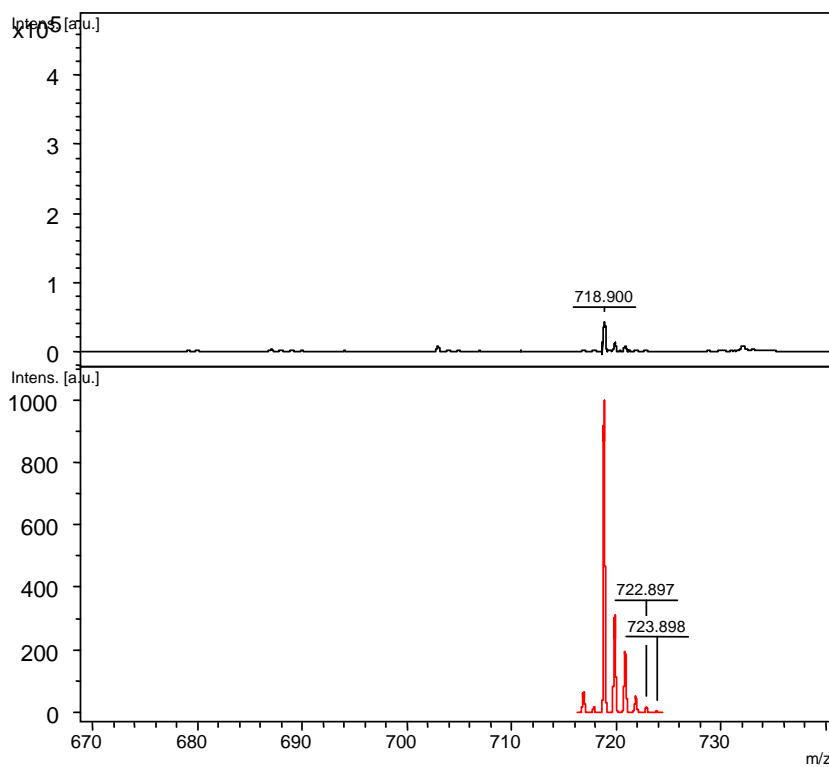


Figure A.27: MALDI mass spectrum of [Fe(tta)₃] (9) in the negative reflection mode. Calculated in red.

APPENDIX A

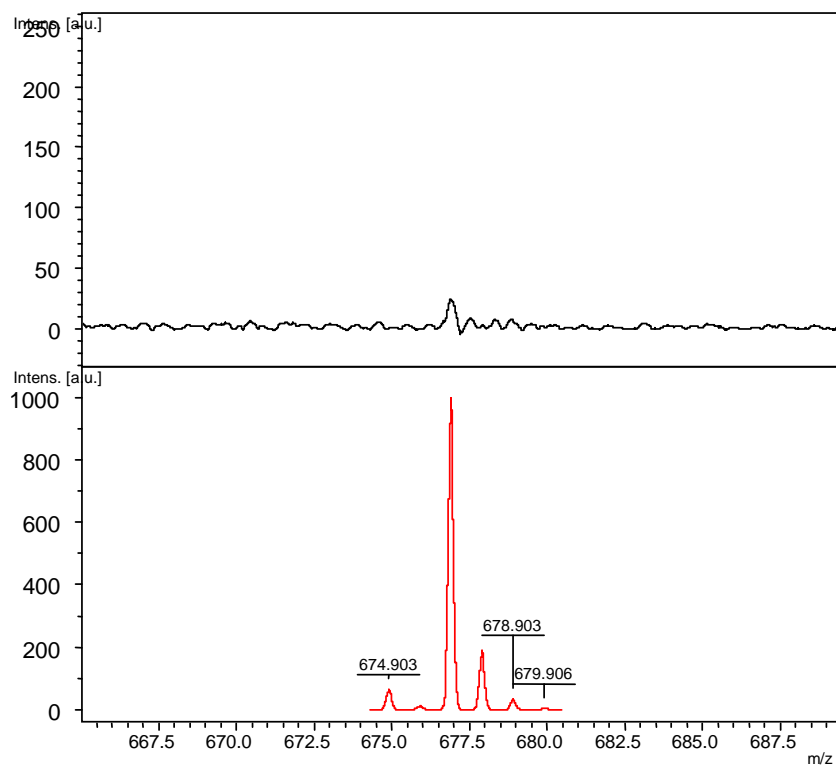


Figure A.28: MALDI mass spectrum of [Fe(hfaa)₃] {10} in the negative reflection mode. Calculated in red.

A.4 Cyclic voltammetry (CV).

Table A.1: Electrochemical data of $[\text{Fe}(\text{acac})_3]$ {1}. Solvent CH_3CN , supporting electrolyte TBAPF_6 ($[\text{NBu}_4][\text{PF}_6]$), versus Fc/Fc^+ , scan rate as indicated.

Scan Rate	E_{pa} / V	E_{pc} / V	$\Delta E_{\text{p}} / \text{V}$	$E^{0'} / \text{V}$	$i_{\text{pa}} / \mu\text{A}$	$i_{\text{pc}} / \mu\text{A}$	$i_{\text{pa}}/i_{\text{pc}}$
50	-1.002	-1.076	0.074	-1.039	10.56	10.75	0.98
100	-1.002	-1.074	0.072	-1.038	14.66	14.72	1.00
150	-1.000	-1.077	0.077	-1.038	17.58	18.51	0.95
200	-0.997	-1.078	0.081	-1.037	20.25	20.50	0.99
250	-0.997	-1.078	0.081	-1.037	22.73	22.92	0.99
300	-0.993	-1.081	0.088	-1.037	24.47	25.03	0.98
1000	-0.983	-1.092	0.109	-1.037	42.42	43.35	0.98

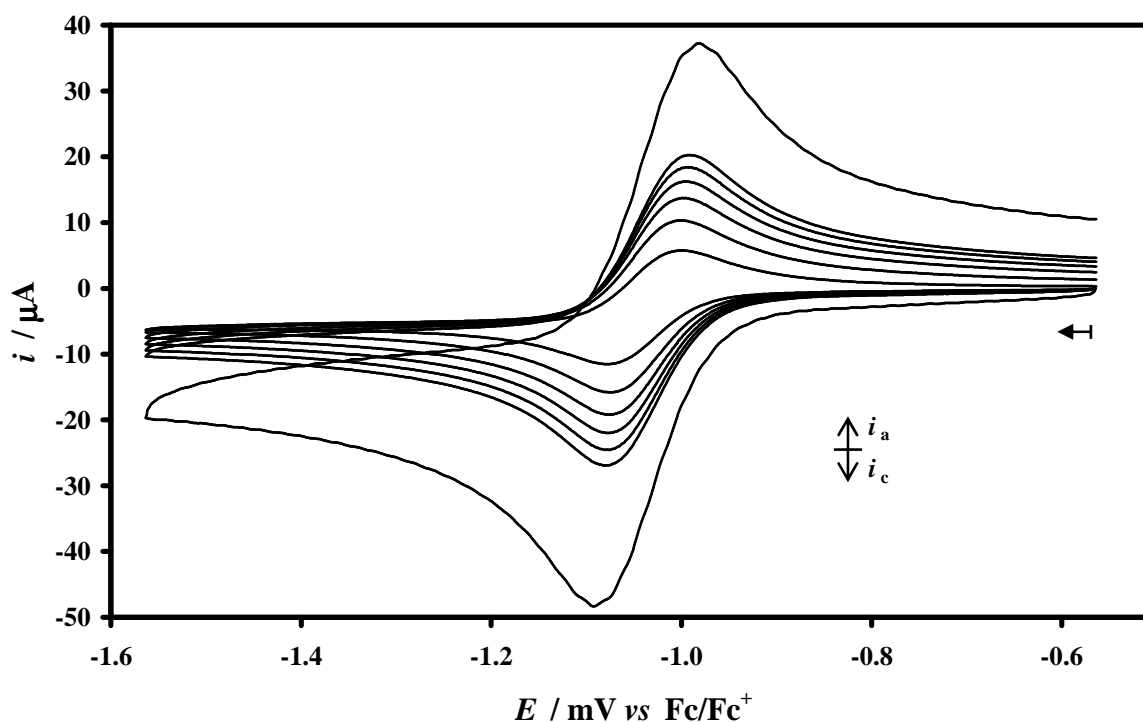


Figure A.29: Cyclic voltammograms (versus Fc/Fc^+) of $1 \text{ mmol}\cdot\text{dm}^{-3}$ $[\text{Fe}(\text{acac})_3]$ {1} at scan rates 50, 100, 150, 200, 250, 300 and $1000 \text{ mV}\cdot\text{s}^{-1}$. Scans initiated in the direction of the arrow. Measured in $100 \text{ mmol}\cdot\text{dm}^{-3}$ $\text{TBAPF}_6/\text{CH}_3\text{CN}$ on a glassy carbon working electrode at 25°C .

APPENDIX A

Table A.2: Electrochemical data of [Fe(ba)₃] {2}. Solvent CH₃CN, supporting electrolyte TBAPF₆ ([NBu₄][PF₆]), versus Fc/Fc⁺, scan rate as indicated.

Scan Rate	E _{pa} / V	E _{pc} / V	ΔE _p / V	E ⁰ / V	i _{pa} / μA	i _{pc} / μA	i _{pa} /i _{pc}
50	-0.938	-1.004	0.066	-0.971	7.14	7.22	0.99
100	-0.940	-1.003	0.063	-0.971	10.43	10.65	0.98
150	-0.939	-1.003	0.064	-0.971	12.55	12.55	1.00
200	-0.937	-1.003	0.066	-0.970	14.16	14.60	0.97
250	-0.936	-1.006	0.070	-0.971	16.02	16.69	0.96
300	-0.934	-1.005	0.071	-0.969	17.45	17.81	0.98
1000	-0.932	-1.008	0.076	-0.970	30.81	31.12	0.99

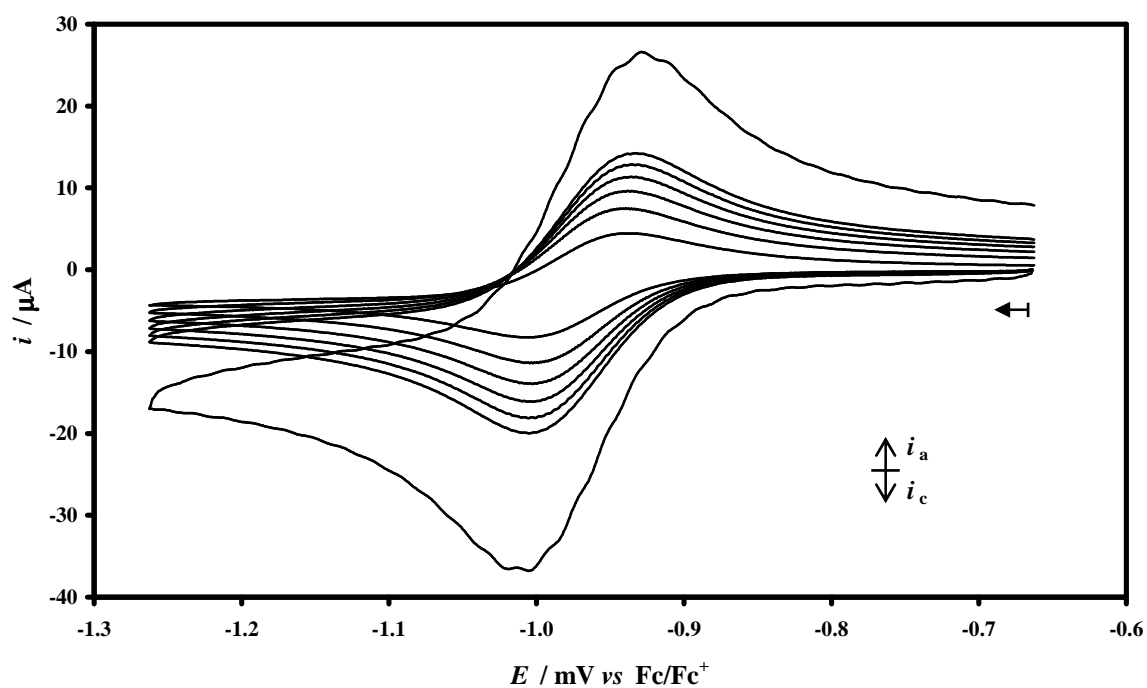


Figure A.30: Cyclic voltammograms (*versus* Fc/Fc⁺) of 1 mmol.dm⁻³ [Fe(ba)₃] {2} at scan rates 50, 100, 150, 200, 250, 300 and 1000 mV.s⁻¹. Scans initiated in the direction of the arrow. Measured in 100 mmol.dm⁻³ TBAPF₆/CH₃CN on a glassy carbon working electrode at 25 °C.

APPENDIX A

Table A.3: Electrochemical data of [Fe(bth)₃] {3}. Solvent CH₃CN, supporting electrolyte TBAPF₆ ([NBu₄][PF₆]), versus Fc/Fc⁺, scan rate as indicated.

Scan Rate	E _{pa} / V	E _{pc} / V	ΔE _p / V	E ^{0'} / V	i _{pa} / μA	i _{pc} / μA	i _{pa} /i _{pc}
50	-0.848	-0.913	0.065	-0.881	0.58	0.60	0.97
100	-0.850	-0.912	0.062	-0.881	0.78	0.78	1.00
150	-0.847	-0.914	0.067	-0.881	1.17	1.18	0.99
200	-0.848	-0.913	0.065	-0.881	1.38	1.39	0.99
250	-0.846	-0.915	0.069	-0.881	1.47	1.50	0.98
300	-0.847	-0.913	0.066	-0.880	1.71	1.74	0.98
1000	-0.843	-0.920	0.077	-0.882	2.47	2.54	0.97

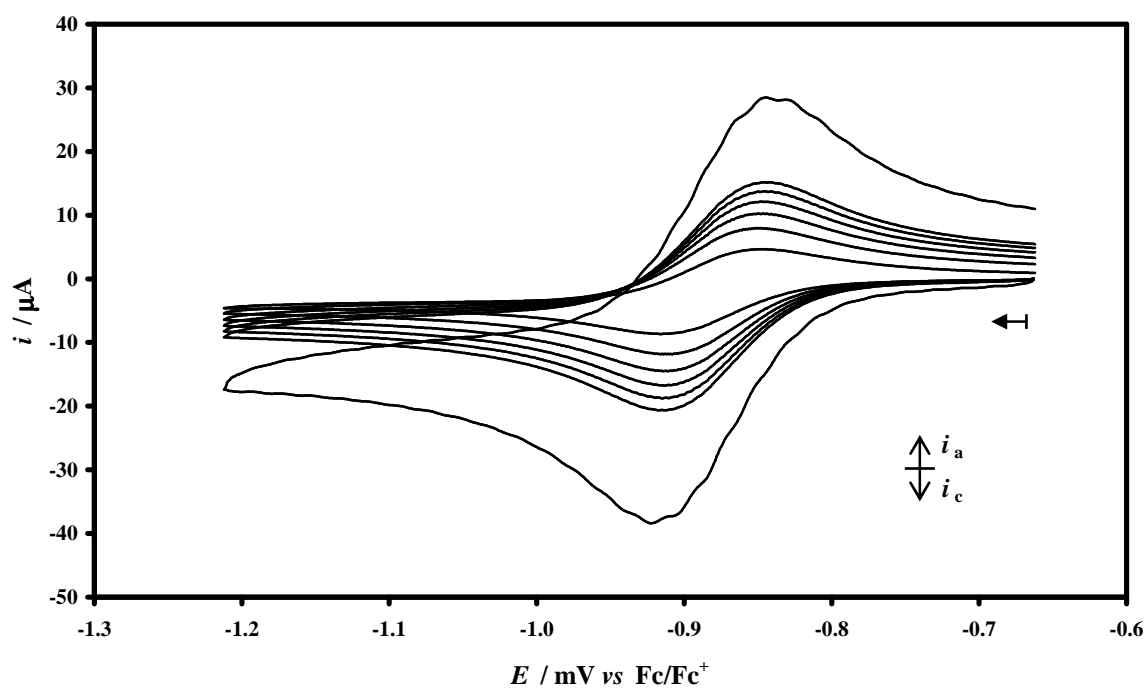


Figure A.31: Cyclic voltammograms (versus Fc/Fc⁺) of 1 mmol.dm⁻³ [Fe(bth)₃] {3} at scan rates 50, 100, 150, 200, 250, 300 and 1000 mV.s⁻¹. Scans initiated in the direction of the arrow. Measured in 100 mmol.dm⁻³ TBAPF₆/CH₃CN on a glassy carbon working electrode at 25 °C.

APPENDIX A

Table A.4: Electrochemical data of [Fe(dtm)₃] {4}. Solvent CH₃CN, supporting electrolyte TBAPF₆ ([NBu₄][PF₆]), versus Fc/Fc⁺, scan rate as indicated.

Scan Rate	E _{pa} / V	E _{pc} / V	ΔE / V	E ⁰ / V	i _{pa} / μA	i _{pc} / μA	i _{pa} /i _{pc}
50	-0.805	-0.882	0.077	-0.843	5.90	6.04	0.98
100	-0.809	-0.879	0.070	-0.844	7.90	7.98	0.99
150	-0.808	-0.880	0.072	-0.844	8.60	8.87	0.97
200	-0.807	-0.879	0.072	-0.843	9.29	9.29	1.00
250	-0.806	-0.880	0.074	-0.843	10.10	10.41	0.97
300	-0.807	-0.879	0.072	-0.843	18.81	19.19	0.98
1000	-0.806	-0.884	0.078	-0.845	23.53	24.01	0.98

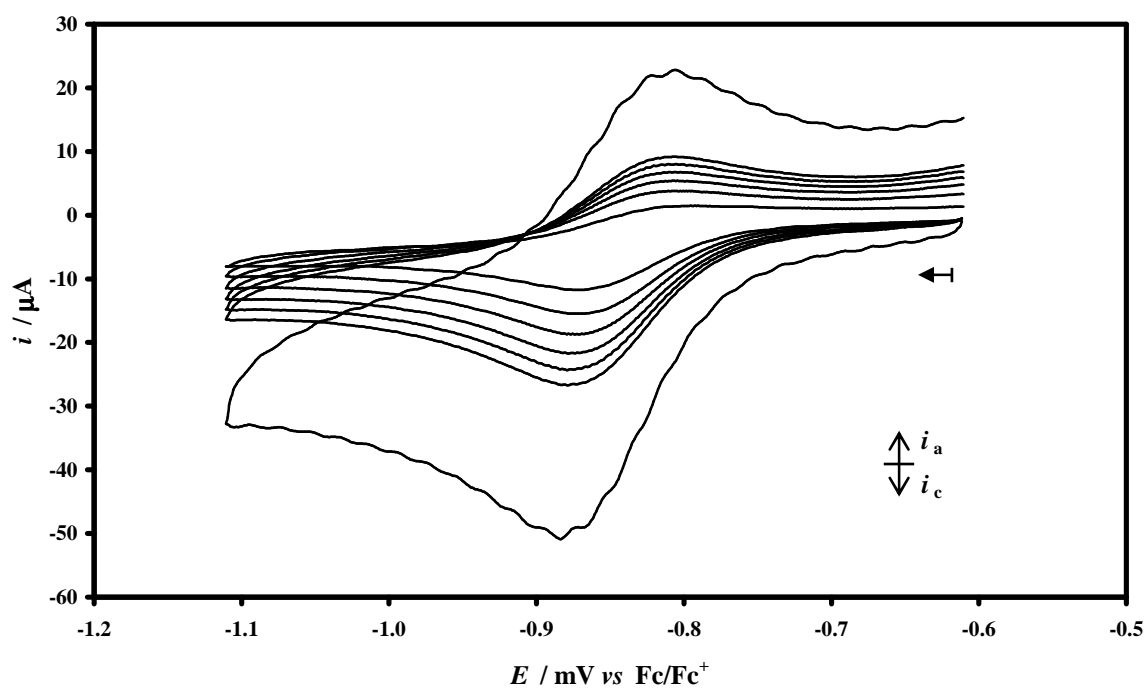


Figure A.32: Cyclic voltammograms (versus Fc/Fc⁺) of 1 mmol.dm⁻³ [Fe(dtm)₃] {4} at scan rates 50, 100, 150, 200, 250, 300 and 1000 mV.s⁻¹. Scans initiated in the direction of the arrow. Measured in 100 mmol.dm⁻³ TBAPF₆/CH₃CN on a glassy carbon working electrode at 25 °C.

APPENDIX A

Table A.5: Electrochemical data of [Fe(dbm)₃] {5}. Solvent CH₃CN, supporting electrolyte TBAPF₆ ([NBu₄][PF₆]), versus Fc/Fc⁺, scan rate as indicated.

Scan Rate	E _{pa} / V	E _{pc} / V	ΔE _p / V	E ^{0'} / V	i _{pa} / μA	i _{pc} / μA	i _{pa} /i _{pc}
50	-0.886	-0.954	0.068	-0.920	4.14	4.27	0.97
100	-0.887	-0.955	0.068	-0.921	7.39	7.54	0.98
150	-0.888	-0.951	0.063	-0.920	8.88	9.16	0.97
200	-0.886	-0.954	0.068	-0.920	9.99	10.09	0.99
250	-0.884	-0.953	0.069	-0.919	11.26	11.26	1.00
300	-0.885	-0.953	0.068	-0.919	12.30	12.43	0.99
1000	-0.883	-0.954	0.071	-0.919	23.17	23.65	0.98

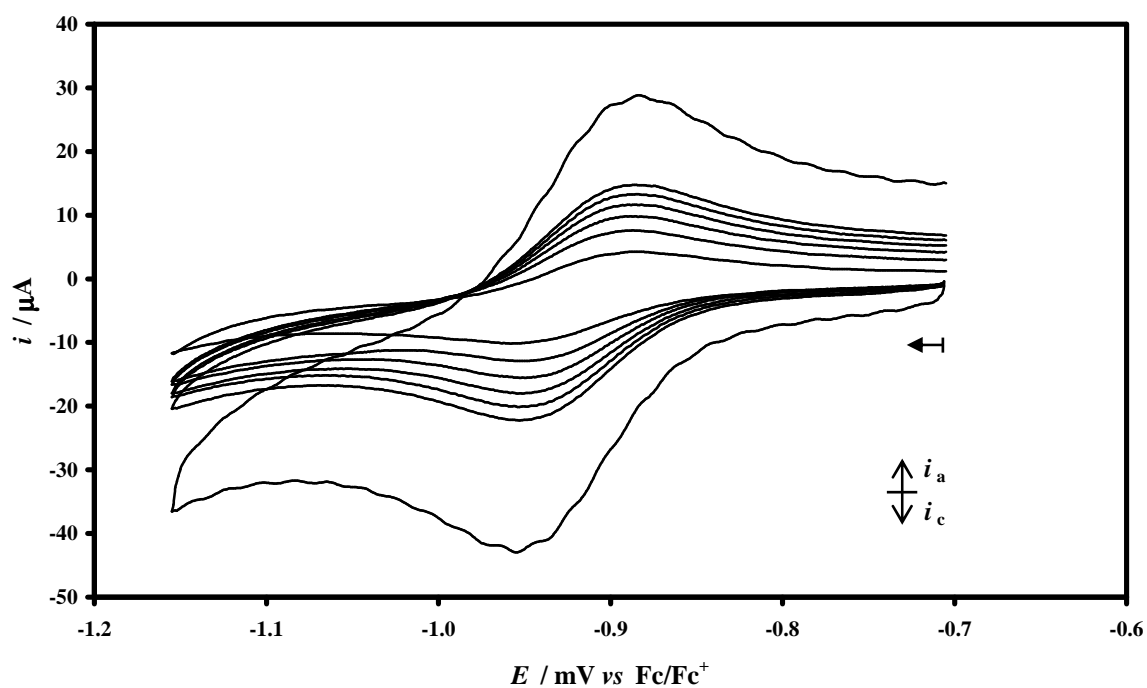


Figure A.33: Cyclic voltammograms (versus Fc/Fc⁺) of 1 mmol.dm⁻³ [Fe(dbm)₃] {5} at scan rates 50, 100, 150, 200, 250, 300 and 1000 mV.s⁻¹. Scans initiated in the direction of the arrow. Measured in 100 mmol.dm⁻³ TBAPF₆/CH₃CN on a glassy carbon working electrode at 25 °C.

APPENDIX A

Table A.6: Electrochemical data of [Fe(tfaa)₃] {6}. Solvent CH₃CN, supporting electrolyte TBAPF₆ ([NBu₄][PF₆]), versus Fc/Fc⁺, scan rate as indicated.

Scan Rate	E _{pa} / V	E _{pc} / V	ΔE _p / V	E ⁰ / V	i _{pa} / μA	i _{pc} / μA	i _{pa} /i _{pc}
50	-0.330	-0.426	0.096	-0.378	3.18	3.21	0.99
100	-0.333	-0.421	0.088	-0.377	5.64	5.75	0.98
150	-0.331	-0.426	0.095	-0.379	9.88	10.08	0.98
200	-0.326	-0.427	0.101	-0.377	11.40	11.52	0.99
250	-0.323	-0.431	0.108	-0.377	13.79	13.93	0.99
300	-0.324	-0.432	0.108	-0.378	17.04	17.04	1.00
1000	-0.304	-0.451	0.147	-0.378	26.45	27.27	0.97

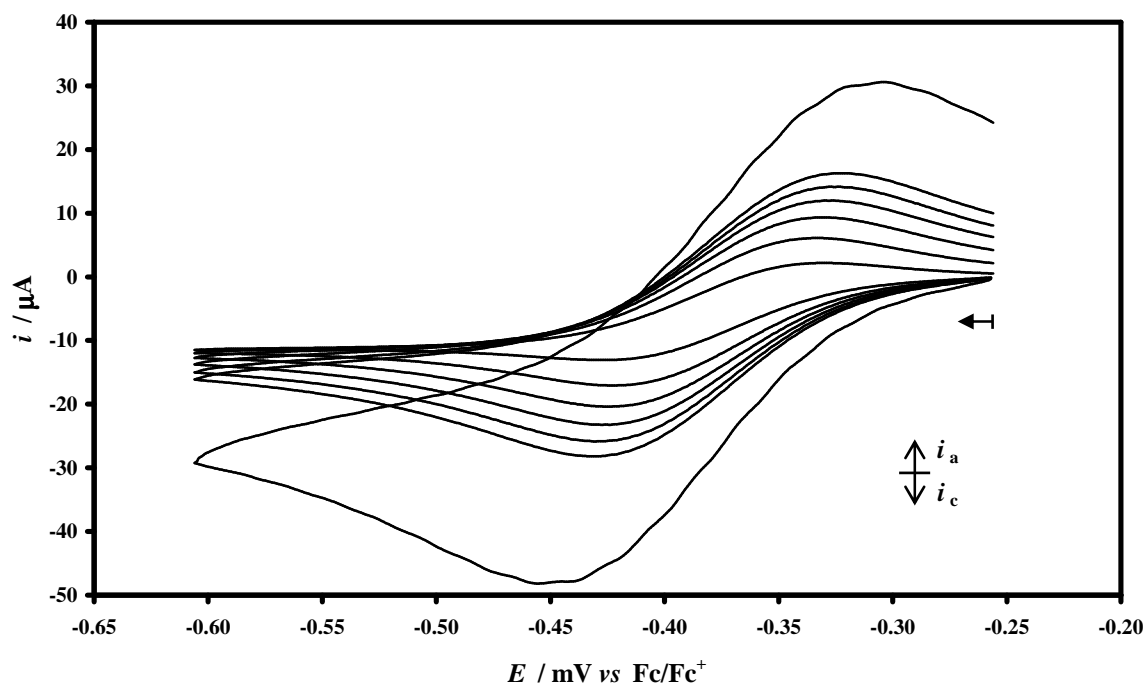


Figure A.34: Cyclic voltammograms (versus Fc/Fc⁺) of 1 mmol.dm⁻³ [Fe(tfaa)₃] {6} at scan rates 50, 100, 150, 200, 250, 300 and 1000 mV.s⁻¹. Scans initiated in the direction of the arrow. Measured in 100 mmol.dm⁻³ TBAPF₆/CH₃CN on a glassy carbon working electrode at 25 °C.

APPENDIX A

Table A.7: Electrochemical data of [Fe(tffu)₃] {7}. Solvent CH₃CN, supporting electrolyte TBAPF₆ ([NBu₄][PF₆]), versus Fc/Fc⁺, scan rate as indicated.

Scan Rate	E _{pa} / V	E _{pc} / V	ΔE _p / V	E ^{0'} / V	i _{pa} / μA	i _{pc} / μA	i _{pa} /i _{pc}
50	-0.311	-0.383	0.072	-0.347	6.00	6.06	0.99
100	-0.314	-0.381	0.067	-0.347	8.88	9.15	0.97
150	-0.313	-0.382	0.069	-0.347	10.06	10.16	0.99
200	-0.312	-0.383	0.071	-0.347	11.88	12.12	0.98
250	-0.312	-0.386	0.074	-0.349	14.50	14.95	0.97
300	-0.310	-0.388	0.078	-0.349	15.06	15.37	0.98
1000	-0.307	-0.390	0.083	-0.348	34.88	35.95	0.97

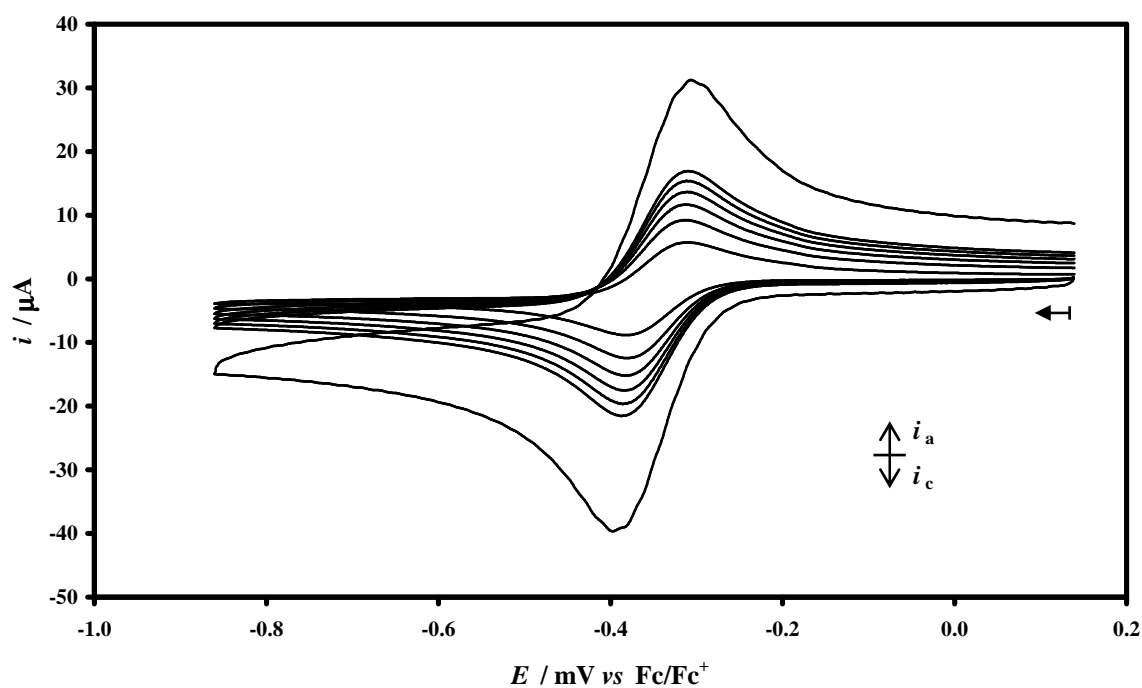


Figure A.35: Cyclic voltammograms (versus Fc/Fc⁺) of 1 mmol.dm⁻³ [Fe(tffu)₃] {7} at scan rates 50, 100, 150, 200, 250, 300 and 1000 mV.s⁻¹. Scans initiated in the direction of the arrow. Measured in 100 mmol.dm⁻³ TBAPF₆/CH₃CN on a glassy carbon working electrode at 25 °C.

APPENDIX A

Table A.8: Electrochemical data of [Fe(tfba)₃] {8}. Solvent CH₃CN, supporting electrolyte TBAPF₆ ([NBu₄][PF₆]), versus Fc/Fc⁺, scan rate as indicated.

Scan Rate	E _{pa} / V	E _{pc} / V	ΔE _p / V	E ⁰ / V	i _{pa} / μA	i _{pc} / μA	i _{pa} /i _{pc}
50	-0.317	-0.386	0.069	-0.352	10.58	10.80	0.98
100	-0.319	-0.383	0.064	-0.351	15.39	15.86	0.97
150	-0.318	-0.385	0.067	-0.352	17.09	17.44	0.98
200	-0.319	-0.387	0.068	-0.353	21.26	21.70	0.98
250	-0.317	-0.386	0.069	-0.352	26.80	27.07	0.99
300	-0.315	-0.387	0.072	-0.351	28.74	29.03	0.99
1000	-0.314	-0.390	0.076	-0.352	28.88	29.78	0.97

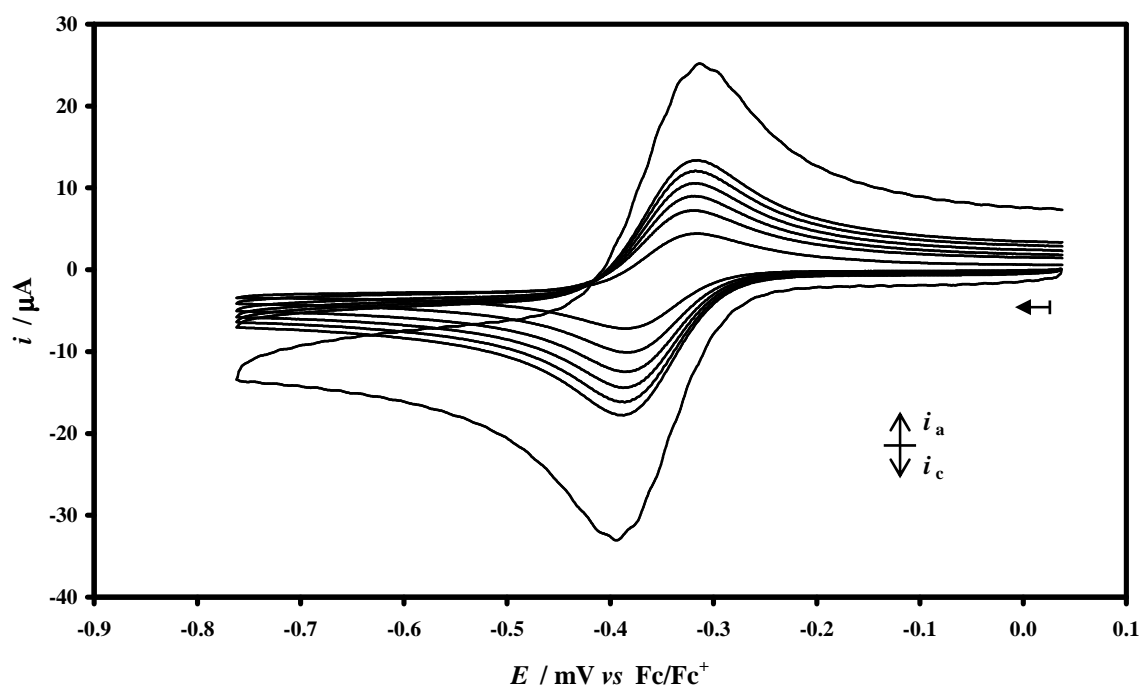


Figure A.36: Cyclic voltammograms (versus Fc/Fc⁺) of 1 mmol.dm⁻³ [Fe(tfba)₃] {8} at scan rates 50, 100, 150, 200, 250, 300 and 1000 mV.s⁻¹. Scans initiated in the direction of the arrow. Measured in 100 mmol.dm⁻³ TBAPF₆/CH₃CN on a glassy carbon working electrode at 25 °C.

APPENDIX A

Table A.9: Electrochemical data of [Fe(tta)₃] {9}. Solvent CH₃CN, supporting electrolyte TBAPF₆ ([NBu₄][PF₆]), versus Fc/Fc⁺, scan rate as indicated.

Scan Rate	E _{pa} / V	E _{pc} / V	ΔE _p / V	E ^{0'} / V	i _{pa} / μA	i _{pc} / μA	i _{pa} /i _{pc}
50	-0.319	-0.394	0.075	-0.356	4.64	4.68	0.99
100	-0.320	-0.390	0.070	-0.355	6.71	6.71	1.00
150	-0.319	-0.389	0.070	-0.354	9.13	9.22	0.99
200	-0.319	-0.393	0.074	-0.356	9.66	9.76	0.99
250	-0.317	-0.394	0.077	-0.355	11.59	11.83	0.98
300	-0.316	-0.392	0.076	-0.354	12.17	12.17	1.00
1000	-0.311	-0.400	0.089	-0.355	23.62	23.86	0.99

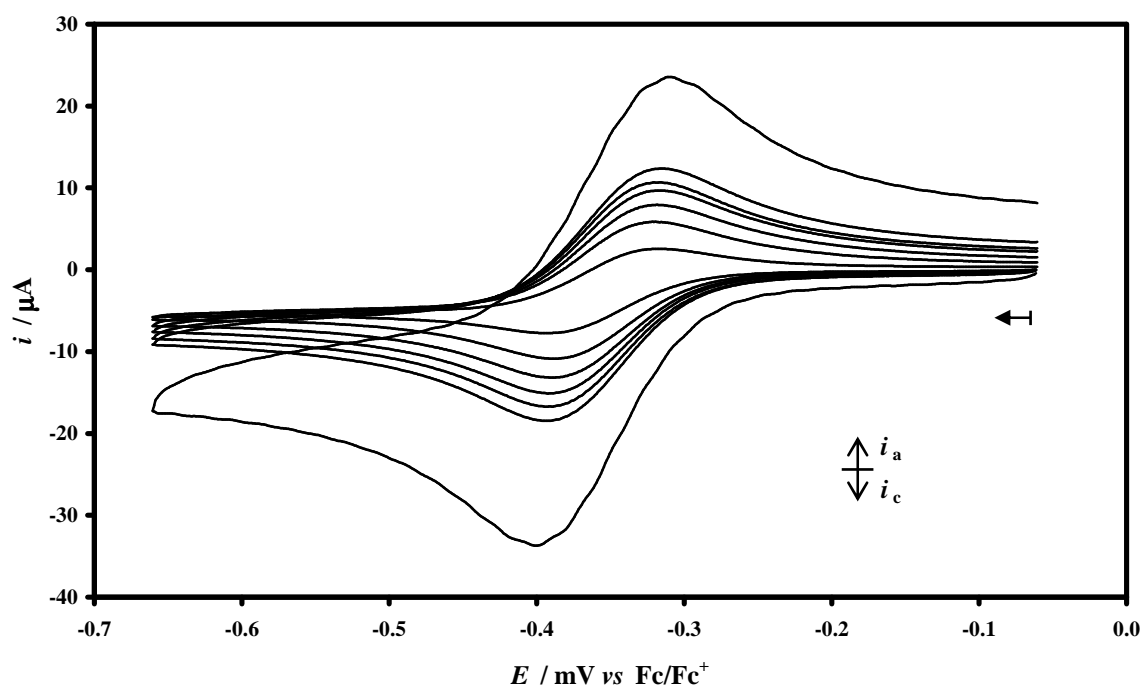


Figure A.37: Cyclic voltammograms (versus Fc/Fc⁺) of 1 mmol.dm⁻³ [Fe(tta)₃] {9} at scan rates 50, 100, 150, 200, 250, 300 and 1000 mV.s⁻¹. Scans initiated in the direction of the arrow. Measured in 100 mmol.dm⁻³ TBAPF₆/CH₃CN on a glassy carbon working electrode at 25 °C.

APPENDIX A

Table A.10: Electrochemical data of [Fe(hfaa)₃] {10}. Solvent DCM, supporting electrolyte TBAPF₆ ([NBu₄][PF₆]), versus Fc/Fc⁺, scan rate as indicated.

Scan Rate	E _{pa} / V	E _{pc} / V	ΔE _p / V	E ⁰ / V	i _{pa} / μA	i _{pc} / μA	i _{pa} /i _{pc}
50	0.238	0.168	0.070	0.203	2.07	2.14	0.97
100	0.237	0.167	0.070	0.202	4.34	4.39	0.99
150	0.238	0.164	0.074	0.201	5.37	5.42	0.99
200	0.240	0.163	0.077	0.201	6.40	6.53	0.98
250	0.244	0.159	0.085	0.201	7.01	7.08	0.99
300	0.244	0.159	0.085	0.201	7.91	8.15	0.97
1000	0.260	0.145	0.115	0.202	13.64	14.21	0.96

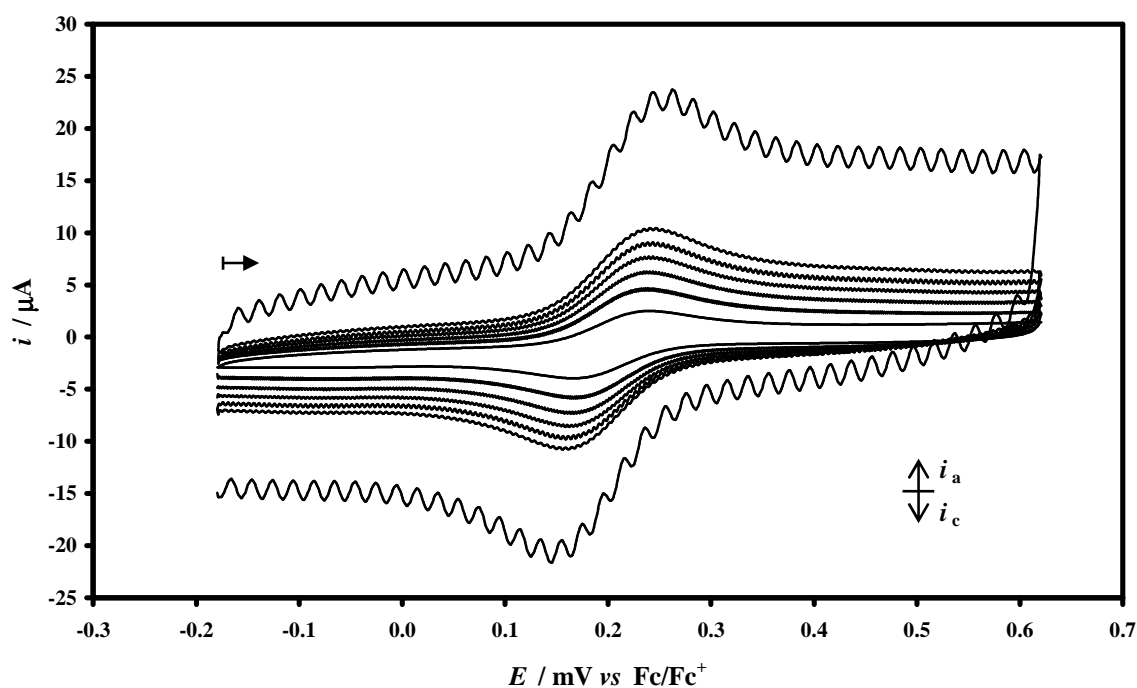


Figure A.38: Cyclic voltammograms (versus Fc/Fc⁺) of 1 mmol.dm⁻³ [Fe(hfaa)₃] {10} at scan rates 50, 100, 150, 200, 250, 300 and 1000 mV.s⁻¹. Scans initiated in the direction of the arrow. Measured in 100 mmol.dm⁻³ TBAPF₆/DCM on a glassy carbon working electrode at 25 °C.

Abstract

Fundamental properties of rhodium and iron catalyst have been researched in this study, by means of experimental and DFT computational techniques. Two types of rhodium complexes were studied: monocarbonyltriphenylphosphine rhodium complexes $[\text{Rh}(\beta\text{-diketonato})(\text{CO})(\text{PPh}_3)]$ and triphenylphosphite rhodium complexes $[\text{Rh}(\beta\text{-diketonato})(\text{P}(\text{OPh})_3)_2]$ (where $\beta\text{-diketonato}$ is a monoanionic bidentate ligand with two oxygen donor atoms $(\text{R}_1\text{COCHCOR}_2^-)$). The oxidative addition reaction of methyl iodide to both of these square planar rhodium(I) complexes has been studied. Three types of iron complexes were studied: tris($\beta\text{-diketonato}$) iron(III) complexes $[\text{Fe}(\beta\text{-diketonato})_3]$, a salen complex $[\text{Fe}(\text{salen})(\text{CH}_3)_2(\text{COCH}_3)_2(\text{py})_2]$ and porphyrin complexes $[\text{Fe}^{\text{III}}(\text{porphyrin})(\text{Ar})]$.

The reaction, $[\text{Rh}(\beta\text{-diketonato})(\text{CO})(\text{PPh}_3)] + \text{CH}_3\text{I}$ ($\beta\text{-diketonato} = \text{acac, tta, bth}$ and dtm), consists of many steps with numerous transition states, intermediate products and reaction products. On the grounds of an *in situ* ^1H NMR experimental study and a DFT computational study, a general reaction scheme with specific stereochemistry for the reaction $[\text{Rh}(\beta\text{-diketonato})(\text{CO})(\text{PPh}_3)] + \text{CH}_3\text{I}$ was constructed. The first step in the reaction, the oxidative addition of methyl iodide to the square planar rhodium(I) complex, was computationally studied for the series of $[\text{Rh}(\beta\text{-diketonato})(\text{CO})(\text{PPh}_3)]$ ($\beta\text{-diketonato} = \text{acac, tta, bth}$ and dtm) complexes. The transition state of the oxidative addition reaction corresponds to an $\text{S}_{\text{N}}2$ nucleophilic attack by the rhodium metal centre on the methyl iodide. The experimental kinetic rate constants (k_1) and the theoretical activation energies (ΔE^\ddagger) exhibited a linear relationship. A DFT computational study of the multistep reaction mechanism of the reaction $[\text{Rh}(\text{acac})(\text{CO})(\text{PPh}_3)] + \text{CH}_3\text{I}$ revealed that the reaction mechanism consists of fourteen distinctive steps with the formation of a second alkyl complex $[\text{Rh}(\text{acac})(\text{CH}_3)(\text{CO})(\text{PPh}_3)(\text{I})]$ as the rate-determining step.

A DFT computational study of the reaction $[\text{Rh}(\text{acac})(\text{P}(\text{OPh})_3)_2] + \text{CH}_3\text{I}$ was conducted. Simplified models, *viz.* $[\text{Rh}(\text{acac})(\text{P}(\text{OCH}_3)_3)_2]$ and $[\text{Rh}(\text{acac})(\text{P}(\text{OH})_3)_2]$, were also investigated. The various models have similar geometrical features and energy profiles of the reactants,

ABSTRACT

transition state and possible reaction products, but only the full model gave thermodynamic results in agreement with experimental data.

A series of $[\text{Fe}^{\text{III}}(\beta\text{-diketonato})_3]$ ($\beta\text{-diketonato} = \text{acac, ba, bth, dtm, dbm, tfaa, tffu, tfba, tta}$ and hfaa) complexes was synthesized and characterized with the aid of UV/vis spectrophotometry, mass spectroscopy, elemental analysis and by melting point measurements. A DFT computational study indicated that these complexes can occur as two isomers, the facial (*fac*) and meridional (*mer*) isomers. The $[\text{Fe}(\beta\text{-diketonato})_3]$ complexes were further electrochemically characterized by using cyclic voltammetry and spectroelectrochemistry. The redox process, $[\text{Fe}^{\text{III}}(\beta\text{-diketonato})_3] + e^- \rightleftharpoons [\text{Fe}^{\text{II}}(\beta\text{-diketonato})_3]^-$, was found to be electrochemically and chemically reversible at a scan rate of $100 \text{ mV}\cdot\text{s}^{-1}$. The formal reduction potential of the redox active metal Fe(III)/Fe(II) in the $[\text{Fe}^{\text{III}}(\beta\text{-diketonato})_3]$ complexes was correlated to parameters related to electron density of the iron centre, such as the acid dissociation constant of the uncoordinated $\beta\text{-diketone}$ ($\text{R}_1\text{COCH}_2\text{COR}_2$), the total group electronegativities of the R_1 and R_2 side groups on the $\beta\text{-diketonato}$ ligand ($\text{R}_1\text{COCHCOR}_2$)⁻ and the calculated ionization potentials of the $[\text{Fe}^{\text{III}}(\beta\text{-diketonato})_3]$ complexes. Electrochemical and spectroscopic techniques were combined in a spectroelectrochemistry study of the $[\text{Fe}^{\text{III}}(\beta\text{-diketonato})_3]$ complexes. The influence of the reduction reactions on the UV/vis absorption spectra was monitored. The intensity of the bands in the near ultraviolet region (200-600 nm) changed as the iron(III) complexes were reduced.

The performance of different DFT functionals in relation to the energetics of different spin states of iron complexes was tested. The spin crossover complex $[\text{Fe}(\text{salen})(\text{CH}_3)_2(\text{COCH}_3)_2(\text{py})_2]$ and the low/high spin complexes $[\text{Fe}^{\text{III}}(\text{porphyrin})(\text{Ar})]$ ($\text{Ar} = \text{aryl} = \text{Cl, Ph, C}_6\text{F}_5, 3,4,5\text{-C}_6\text{F}_3\text{H}_2$ and $2,4,6\text{-C}_6\text{F}_3\text{H}_2$) were used to conduct this research. For the spin crossover complex $[\text{Fe}(\text{salen})(\text{CH}_3)_2(\text{COCH}_3)_2(\text{py})_2]$, no single functional in the study could accurately reproduce the geometry of both the low and high spin states as well as provide an energy profile with equi-energetic low and high spin states. For the low/high spin complexes $[\text{Fe}^{\text{III}}(\text{porphyrin})(\text{Ar})]$, the newer pure functionals (OLYP and OPBE) performed the best in predicting the applicable spin states, closely followed by B3LYP.

Keywords

rhodium, iron, $\beta\text{-diketonato}$, salen, porphyrin, oxidative addition, spin crossover, DFT, NMR, CV, SEC

Samevatting

Fundamentele eienskappe van rodium en yster katalisators is met behulp van eksperimentele en kwantum-berekeningschemiese tegnieke ondersoek. Twee tipes rodium komplekse is ondersoek: monokarbonieltrifenielfosfien rodium komplekse $[\text{Rh}(\beta\text{-diketonato})(\text{CO})(\text{PPh}_3)]$ en trifenielfosfiet rodium komplekse $[\text{Rh}(\beta\text{-diketonato})(\text{P}(\text{OPh})_3)_2]$ (waar β -diketonato 'n monoanioniese bidentate ligande is met twee elektron skenkende suurstof atome $(\text{R}_1\text{COCHCOR}_2)^-$). 'n Studie van die oksidatiewe addisie-reaksie van metieljodied tot vierkantige planêre rodium(I) komplekse is uitgevoer. Drie tipes yster komplekse is ondersoek: tris(β -diketonato) yster(III) komplekse $[\text{Fe}(\beta\text{-diketonato})_3]$, 'n salen kompleks $[\text{Fe}(\text{salen})(\text{CH}_3)_2(\text{COCH}_3)_2(\text{py})_2]$ en 'n porfirien kompleks $[\text{Fe}^{\text{III}}(\text{porphyrin})(\text{Ar})]$.

Die reaksie, $[\text{Rh}(\beta\text{-diketonato})(\text{CO})(\text{PPh}_3)] + \text{CH}_3\text{I}$ (β -diketonato = acac, tta, bth en dtm), bestaan uit baie stappe met veelvuldige oorgangstoestande, intermediêre produkte en reaksieprodukte. Op grond van 'n *in situ* ^1H NMR eksperimentele studie en 'n kwantum-berekeningschemiese studie is 'n algemene reaksie skema met spesifieke stereochemie vir die reaksie $[\text{Rh}(\beta\text{-diketonato})(\text{CO})(\text{PPh}_3)] + \text{CH}_3\text{I}$ saamgestel. Die eerste stap van die reaksie, die oksidatiewe addisie van metieljodied tot die vierkantige planêre rodium(I) komplekse $[\text{Rh}(\beta\text{-diketonato})(\text{CO})(\text{PPh}_3)]$ (β -diketonato = acac, tta, bth en dtm), is in die kwantum-berekeningschemiese studie in diepte ondersoek. Die oorgangstoestand van die oksidatiewe addisie-reaksie toon 'n $\text{S}_{\text{N}}2$ nukleofieliese aanval deur die sentrale rodium atoom op die metieljodied molekule. Die eksperimentele kinetiese tempokonstante (k_1) en die teoretiese aktiveringsenergie (ΔE^\ddagger) toon 'n lineêre verwantskap. 'n Kwantum-berekeningschemiese studie van die stappe van die reaksie-meganisme van die reaksie $[\text{Rh}(\text{acac})(\text{CO})(\text{PPh}_3)] + \text{CH}_3\text{I}$ het getoon dat die reaksie-meganisme uit veertien afsonderlike stappe bestaan met die vorming van 'n tweede alkiel kompleks $[\text{Rh}(\text{acac})(\text{CH}_3)(\text{CO})(\text{PPh}_3)(\text{I})]$ as die tempobepalende stap.

'n Kwantum-berekeningschemiese studie van die reaksie $[\text{Rh}(\text{acac})(\text{P}(\text{OPh})_3)_2] + \text{CH}_3\text{I}$ is ook uitgevoer. Twee vereenvoudigde modelle, naamlik $[\text{Rh}(\text{acac})(\text{P}(\text{OCH}_3)_3)_2]$ en $[\text{Rh}(\text{acac})(\text{P}(\text{OH})_3)_2]$, is ook ondersoek. Die verskillende modelle het soortgelyke geometriese kenmerke en energieprofiel van die reaktante, oorgangstoestande en moontlike reaksieprodukte

SAMEVATTING

getoon, maar slegs die vol model kon termodinamiese resultate in ooreenstemming met eksperimentele data weergee.

'n Reeks $[\text{Fe}^{\text{III}}(\beta\text{-diketonato})_3]$ ($\beta\text{-diketonato} = \text{acac, ba, bth, dtm, dbm, tfaa, tffu, tfba, tta en hfaa}$) komplekse is gesintetiseer en gekarakteriseer met behulp van UV/vis spektrofotometrie, massa spektroskopie, element analise en smeltpunt metings. 'n Kwantum-berekeningschemiese studie het aangedui dat hierdie komplekse as twee isomere voorkom, die *fac*- en *mer*-isomere. Die $[\text{Fe}^{\text{III}}(\beta\text{-diketonato})_3]$ komplekse is verder gekarakteriseer deur 'n elektrochemiese studie met behulp van sikliese voltammetrie en spektro-elektrochemie. Daar is bevind dat die redoksproses, $[\text{Fe}^{\text{III}}(\beta\text{-diketonato})_3] + e^- \rightleftharpoons [\text{Fe}^{\text{II}}(\beta\text{-diketonato})_3]^-$, elektrochemies en chemies omkeerbaar is teen 'n skandeertempo van $100 \text{ mV}\cdot\text{s}^{-1}$. Korrelasies is gevind tussen die formele reduksie potensiaal van die redoksaktiewe metaal Fe(III)/Fe(II) in die $[\text{Fe}^{\text{III}}(\beta\text{-diketonato})_3]$ komplekse en parameters wat betrekking het op die elektrondigtheid van die sentrale yster, soos byvoorbeeld die suurdissosiasie konstante van die ongekoördineerde $\beta\text{-diketone}$ ($\text{R}_1\text{COCH}_2\text{COR}_2$), die totale groepelektronegatiwiteit van die R_1 en R_2 groepe van die $\beta\text{-diketonato}$ ligande ($\text{R}_1\text{COCHCOR}_2$)⁻ en die berekende ioniseringspotensiaal van die $[\text{Fe}^{\text{III}}(\beta\text{-diketonato})_3]$ komplekse. Elektrochemiese en spektroskopiese tegnieke is gekombineer in 'n spektro-elektrochemiese studie van die $[\text{Fe}^{\text{III}}(\beta\text{-diketonato})_3]$ komplekse. Die invloed van die reduksiereaksies op die absorbandsiespektra van die komplekse is met behulp van UV/vis spektrofotometrie gemonitor. Die intensiteit van die absorbandsiebande in die naby ultraviolet area (200-600 nm) het verander soos die Fe(III) komplekse gereduseer is.

Verskillende moduleringsdigtheidsfunksionele is geëvalueer met betrekking tot die energieë van verskillende spintoestande van yster komplekse. Die spinoorkruisingskompleks $[\text{Fe}(\text{salen})(\text{CH}_3)_2(\text{COCH}_3)_2(\text{py})_2]$ en die lae of hoë spin komplekse $[\text{Fe}^{\text{III}}(\text{porfyrin})(\text{Ar})]$ ($\text{Ar} = \text{aryl} = \text{Cl, Ph, C}_6\text{F}_5, 3,4,5\text{-C}_6\text{F}_3\text{H}_2 \text{ en } 2,4,6\text{-C}_6\text{F}_3\text{H}_2$) is in die toetsing gebruik. Nie 'n enkele moduleringsdigtheidsfunksionaal kon die geometrieë sowel as die gelyke energievlakke van die lae en hoë spin komplekse van $[\text{Fe}^{\text{III}}(\text{porfyrin})(\text{Ar})]$ akkuraat voorspel nie. Vir die lae of hoë spin komplekse $[\text{Fe}^{\text{III}}(\text{porfyrin})(\text{Ar})]$ het die moduleringsdigtheidsfunksionele OLYP en OPBE, gevolg deur B3LYP, goed geprester deur die toepaslike spintoestande akkuraat te voorspel.

Sleutelwoorde

rodium, yster, $\beta\text{-diketonato}$, salen, porfirien, oksidatiewe addisie, spinoorkruising, DFT, KMR, SV, SEC